Glottal motion and its impact on airflow and aerosol deposition in upper airways during human breathing

Adam Scheinherr

CENTRALE MARSEILLE

École Doctorale : Sciences pour l'Ingénieur (ED353)

Institut de Recherche sur les Phénomènes Hors Équilibre

THÈSE DE DOCTORAT

pour obtenir le grade de

DOCTEUR de l'ÉCOLE CENTRALE de MARSEILLE

Discipline : Mécanique et Physiques des Fluides

GLOTTAL MOTION AND ITS IMPACT ON AIRFLOW AND AEROSOL DEPOSITION IN UPPER AIRWAYS DURING HUMAN BREATHING

par

SCHEINHERR Adam

Directeur de thèse: BOIRON Olivier

Co-encadrante de thèse: BAILLY Lucie

Soutenue le 12 janvier 2015

devant le jury composé de :

DARQUENNE Chantal	Prof., University of California, San Diego, USA	Rapporteur
JÍCHA MIROSLAV	Prof., Brno University of Technology, Czech republic	Rapporteur
ISABEY Daniel	DR, INSERM, Paris, France	
MAURY Bertrand	Prof., Université Paris-Sud, France	
PICHELIN Marine	Dr., Air Liquide Healthcare, Jouy en Josas, France	
CAILLIBOTTE Georges	Dr., Air Liquide Healthcare, Jouy en Josas, France	
BOIRON Olivier	Prof., École Centrale de Marseille, France	Directeur
BAILLY Lucie	CR, CNRS, Marseille, France	Co-encadrante

To asthmatics.

GLOTTAL MOTION AND ITS IMPACT ON AIRFLOW AND AEROSOL DEPOSITION IN UPPER AIRWAYS DURING HUMAN BREATHING

Abstract

During inhaled therapies several factors limits the amount of drug delivered to the lungs. E.g. the upper airways morphology and in particular the glottis, defined by the vocal-fold aperture, causes upper airways to narrow in a minimal cross section, which is determinant on aerosol deposition by inertial impaction. This thesis aims to (i) investigate evolution of the glottal area during breathing, and (ii) predict the effects of a dynamic glottis and realistic airflow conditions on the aerosol deposition in upper airways using three-dimensional simulations.

First, a clinical study was conducted on 20 healthy volunteers (10 males and 10 females) to explore the glottal motion during several specific slow (below 20 cycles/min) and rapid breathing tasks (up to 90 cycles/min). The breathing was investigated simultaneously for the glottal area variations using laryngoscopic video recordings and for airflow rate using oral flowmeter.

The experimental measurements showed that the glottal geometry observed during a breathing cycle can be extremely variable depending on the respiratory phase, tidal volume, and breathing frequency. Testing the dynamic behaviour of the glottis during breathing, two groups of subjects were identified: one with relatively constant glottal area and other with significant variations. In average, the variations for the latter group of subjects was observed for males at 26% comparing maximale and minimal glottal opening during inspiration and expiration respectively.

The results of the clinical study together with anatomical morphological data served to create a model with idealised geometry of upper airways. This model represents the major geometrical characteristics of upper airways with special interest in the glottal region. Transport and deposition of aerosols was studied using 3D numerical cyclic simulations and parametrical analysis allowed to evaluate the influence of the cyclic flow, glottal dynamics, type of carrier gas (air or helium-oxygen mixture) and particle size on the deposition of aerosols in the upper airways.

The numerical simulations demonstrated significant decrease of respiration work with He-O_2 and jet-like flow with recirculation zone in the oro-pharynx and downstream the glottal plane. The principal deposition mechanism is inertial impaction (for the particle diameters 1 - 10μm) with most significant deposition region in the oro-pharynx. Important parameters for deposition are the particle size and the nature of carrier gas. For He-O_2 the deposition reaches two times smaller values than for air and the fraction of deposited particles increases significantly with diameter, reaching 80% of deposited efficiency for 10μm particles. Finally, the CFD results demonstrated negligible differences in aerosol transport and deposition between different glottal characteristics. Therefore, in normal breathing conditions the glottal motion can be neglected.

Key words

Glottal motion, respiration, flow, aerosol deposition, inhalation, upper airways, CFD simulation, air, Helium-Oxygen mixture.

IMPACT DU MOUVEMENT GLOTTIQUE SUR L'ÉCOULEMENT ET LE DÉPÔT D'AÉROSOLS DANS LES VOIES AÉRIENNES SUPÉRIEURES LORS DE LA RESPIRATION HUMAINE

Résumé La délivrance de médicaments lors de la mise en oeuvre de thérapies inhalées est dépendante de nombreux facteurs. Parmi ceux-ci la morphologie des voies aériennes supérieures (VAS) et en particulier celle de la région glottique est déterminante dans les mécanismes de dépôt de particules par impaction inertielle. Dans le cadre de ce travail, il est examiné d'une part la dynamique glottique durant différentes modalités de respiration et d'autre part déterminé numériquement l'effet de ces mouvements et des conditions de respiration associées sur le dépôt des aérosols dans les VAS.

Une étude clinique a été menée dans un premier temps sur un panel de 20 sujets sains (10 hommes et 10 femmes) au sein du service ORL de l'hôpital de la Timone à Marseille pour déterminer le mouvement glottique durant différentes tâches de ventilation allant d'une respiration normale avec moins de 20 cycles/min à une ventilation accélérée jusqu'à 90 cycles/min. L'acquisition des mouvements glottiques a été réalisée par imagerie numérique durant un examen de laryngoscopie avec mesure simultanée des débits associés aux différentes tâches de respiration.

Les mesures expérimentales montrent que la géométrie glottique varie pendant la respiration en fonction de la tâche de respiration, du volume courant et de la fréquence respiratoire. Une étude statistique a permis d'isoler deux comportements types l'un où l'aire glottique demeure sensiblement constante durant la respiration et l'autre ou une variation de cette même aire est observée. Sur ce dernier groupe d'individus la variation d'aire maximale observée sur les hommes est de 26%, l'ouverture maximale étant atteinte durant la phase d'inspiration et l'aire minimale durant l'expiration.

Ces résultats, ainsi que des données anatomiques, ont permis de construire un modèle géométrique idéalisé des VAS. Ce modèle reproduit fidèlement les principales singularités des voies extrathoraciques en apportant un grand soin à la description de la région glottique. Le transport et le dépôt d'aérosols dans ce modèle a été étudié en ayant recours à des simulations numériques 3D de l'écoulement cyclique. Une étude paramétrique a permis d'évaluer l'influence sur le dépôt de l'écoulement cyclique, de la nature du gaz porteur (Air vs mélange d'hélium-oxygène), de la prise en compte de la dynamique glottique et de la taille des particules.

Les résultats mettent principalement en évidence une nette diminution de la part extrathoracique du travail respiratoire lors de l'emploi du mélange He-O_2 et un écoulement de type jet en aval de la glotte durant l'inspiration associé à une recirculation sous le plancher glottique. Le mécanisme de dépôt principal étant l'impaction inertielle (pour les tailles des particules 1 - 10µm) le zone principale de dépôt est situé dans l'oropahrynx, quelles que soient les conditions pendant inspiration. La fraction de dépôt augmente rapidement avec le diamètre des particules atteignant près de 80% pour les particules de 10µm et diminuer deux fois pour He-O_2 en comparaison avec air. Finalement, la dynamique du dépôt ne varie pas de façon significative entre le modèle où la glotte est considérée comme statique et celle où elle est mobile. Donc, dans les conditions de respiration normal le mouvement de la glotte peut être négligé.

Mot clés

Mouvement glottique, respiration, écoulement, dépôt des aérosols, inhalation, voies aériennes supérieures, simulations CFD, air, mélange d'hélium-oxygène.

POHYB HLASIVEK A JEHO VLIV NA PROUDĚNÍ A DEPOZICI AEROSOLŮ BĚHEM DÝCHÁNÍ V HORNÍCH CESTÁCH DÝCHACÍCH

Abstrakt

Účinnost inhalačních terapií může být ovlivněna několika faktory, které limitují distribuci aerosolů do plic. Mezi ně patří například morfologie horních cest dýchacích a obzvláště hlasivek, které definují nejužší místo horních cest dýchacích, tzv. hlasivkovou štěrbinu. Tento region je tudíž určující pro depozici aerosolů vlivem setrvačného mechanismu. Cílem této disertační práce je (i) definovat pohyb hlasivek během dýchání a (ii) pomocí 3D numerických simulací predikovat vliv pohybu hlasivek a podmínek dýchání na depozici aerosolů v horních cestách dýchacích.

V první fázi této práce byla provedena klinická studie na 20 zdravých dobrovolnících (10 mužích a 10 žen) za účelem popsání pohybu hlasivek během uvolněného (pod 20 cyklů/min) a zrychleného (až 90 cyklů/min) dýchání. Během studie probíhala pozorování pohybu hlasivkové štěrbiny flexibilním laryngoskopem zároveň s měřením průtoku vzduchu orálním průtokoměrem.

Experimentální měření ukázaly, že pohyb hlasivek může být velice variabilní a záleží na dechovém objemu a režimu a frekvenci dýchání. Studií dynamiky hlasivek během dýchání byly identifikovány dvě skupiny pacientů: první s relativně nepodstatným pohybem a druhá s významným pohybem hlasivek. U druhé skupiny pacientů byl pozorován porovnáním maxima při inspiraci a minima při exhalaci v průměru 26% rozdíl velikosti hlasivkové štěrbiny.

Experimentální výsledky a morfologická data umožnili vytvořit idealizovaný model s geometrií horních cest dýchacích. Tento model reprezentuje hlavní geometrické charakteristiky horních cest dýchacích, se zvláštním detailem v oblasti hlasivek. Transport a depozice aerosolů byla studována pomocí 3D numerických cyklických simulací a parametrické analýzy umožnily ohodnotit vliv cyklického proudění, pohybu hlasivek, typu nosného plynu (vzduch nebo helium-kyslíková směs) a velikosti částic na depozici aerosolů v horních cestách dýchacích.

CFD výsledky ukázaly výrazný pokles dýchací práce se směsí He-O_2 a vzniku jet proudění s recirkulačními oblastmi v oropharynxu a za hlasivkami. Hlavním depozičním mechanismem je pro studované velikosti částic (1 - 10μm) setrvačný mechanismus s nejvýznamnějším depozitním regionem v oropharynxu. Důležitými parametry pro depozici je velikost částic a druh nosného plynu. V případě He-O_2 směsi depozice dosahuje 2krát nižších hodnot než pro vzduch a množství deponovaných aerosolů vzrůstá s velikostí partiklů, kdy dosahuje až 80% pro částice o velikosti 10μm. Konečně, výsledky ukázaly zanedbatelný rozdíl v transportu a depozici aerosolů mezi dvěma zjištěnými druhy pohybu hlasivek. Proto, v případě uvolněného dýchání, pohyb hlasivek je možno zanedbat.

Klíčová slova

Pohyb hlasivek, dýchání, proudění, depozice aerosolů, inhalace, horní cesty dýchací, CFD simulace, vzduch, směs helia a kyslíku.

Contents

Pursuing a PhD is both painful and enjoyable experience. It is like climbing a high peak, step by step, accompanied with bitterness, hardship, encouragement and trust. When I found myself at the top enjoying the beautiful scenery, I realized that it was the teamwork that got me here. Thus, I would like to express my gratitude to all those who gave me the possibility to complete this thesis.

I am deeply indebted to my supervisors Doctor Lucie Bailly and Professor Olivier Boiron. Their guidance has made this a thoughtful and rewarding journey. I am thankful for the constant trust, invaluably constructive criticism and friendly advice during the research work and writing of my thesis. Even through the language and cultural barrier they had always patience and understanding. Their encouragement was the driving force of my research. I always ended up with confidence and full of energy after our discussions.

I am also very grateful to our colleagues from Air Liquide company Doctor Marine Pichelin, Doctor Georges Caillibotte, Doctor Ira Katz and Benoit Piednoir for their constant availability in the most difficult steps of my thesis. I gratefully acknowledge Air Liquid for the funding that made my PhD work possible.

A great deal of the work was carried out in the collaboration with Doctor Aude Lagier, who gave fundamental scientific contribution to the clinical study. Also I would like to thank Thierry Legou for his willing assistance and availability and I can't forget to mention all 20 volunteers participating in this study.

A special thank to Professor Chantal Darquenne and Doctor Jan Jedelský, for their valuable suggestions and discussions during our meetings.

Many thanks to the scientists but also my great friends from our laboratory Yannick, Marjorie, Eric, Wei, Lionel, Jonathan and Guillaume.

I can't forget to explicit my love to all my Marseille friends Giova, Franchi, Elisa, Luca, Olivia, Floris, Fulvia, Brunella, Jessica, Zdenko, Dimitri, Karim.

A heartfelt thanks goes out to my girlfriend Cecilia for all her love, support and patience when I was only thinking about glottal images. Moreover, I can't forget her enormous help and precious discussions in the field of aerosol research.

Last, but not least, my family had to grudgingly learn to accept my separation from them and still gave me nothing but support, day after day, my love and gratitude for them can hardly be expressed in words.

PS: I can't forget my bicycle, for the whole three years carrying me everyday to the laboratory and passing with me over 12 000 kilometers. :-)

Preface

Already ancient man, inhaling smoke or odors of the plants, experienced inhalation therapy. In ancient Egypt nearly all respiratory problems were treated by inhalation. The Eper's medical papyrus dating back to 1550 B.C. includes several prescriptions for the use of snuffs, vapors and smoke for inhalation to treat nasal problems. The benefits of delivering medication *a priori* directly to the affected site (usually the lungs) have been understood for more than two hundred years. Aerosol therapy has dramatically improved the treatment of many respiratory diseases such as asthma and Chronic Obstructive Pulmonary Disease (COPD).

The human respiratory system and the breathing characteristics represent a complex biomechanical problem. During inhaled therapies, the upper airways' morphology can act as an unwanted filter, which limits the amount of drug delivered to the lungs. The glottis, defined by the vocal-fold aperture, causes upper airways to narrow in a minimal cross-section, which is determinant on aerosol deposition by inertial impaction. This thesis aims to (i) investigate evolution of the glottal area during breathing, and (ii) predict the effects of realistic glottal behavior and realistic airflow conditions on the aerosol deposition within the upper airways using flow simulations.

The thesis presents research and findings from two different domains: the human physiology and the mechanics of the two-phase flow in the upper airways. To gain understanding on the realistic breathing conditions, an *in vivo* study was performed. The characteristics of the airflow rate and the glottal dimensions variations were measured in collaboration with medical practitioners from *La Timone Adult Hospital* in Marseille, France and *Speech and Language Laboratory* (LPL) in Aix-en-Provence, France. Note that the experimental procedure was approved by the Committee on the Protection of People (CPP) in Biomedical Research (CPP Sud Méditerranée I, n°2012-A01390-13) and from all volunteers were obtained the informed consents. Afterwards, the measured data of the *in vivo* study were integrated into a complementary *in silico* study.

Computational Fluid Dynamics (CFD) simulations are an efficient tool to predict the respiratory airflow dynamics and aerosol transport and deposition in the human upper airways. Three-dimensional simulations were conducted implementing conditions resulting from *in vivo* measurements: (i) time-varying glottal wall motion of one breathing cycle; and (ii) unsteady oral airflow rates, together with unsteady aerosol injection of one breathing cycle.

The thesis is organized into 3 parts and 7 chapters. Part I summarizes the background and motivation for the study (chapter I.1), the state-of-the-art (chapter I.2), and the aims of the study (Summary and Aims).

Part II details the performed *in vivo* study. The methodology and the first preliminary experiments are pointed out in chapter II.3. Following chapter II.4 is divided into two sections. First section (section II.4.1) details the analysis of the clinical study, in terms of breathing aerodynamics. Second section (section II.4.2) details the analysis of the clinical study, in terms of glottal motion during breathing. Note that preliminary experiments in chapter II.3 were published in Scheinherr et al. [2012] and in Scheinherr et al. [2013a]. Both description and results of the final clinical study were submitted in July 2014 to *Medical Engineering & Physics* (Scheinherr *et al.*, *Realistic Glottal Motion and Airflow Rate during Human Breathing*).

Lastly, Part III describes the performed CFD simulations. The design of the glottal motion model as well as the preliminary numerical simulations are described in chapter III.5. The elaboration of the 3D idealized geometry of the upper airways is presented in chapter III.6, and finally, chapter III.7 presents the results of the different simulation cases introduced in chapter III.6. Note that preliminary 2D and 3D results of this chapter III.5 were presented in a conference paper of the 37^{th} Congress of the *Société de Biomécanique* (SB 2012) in Toulouse, France [Scheinherr et al., 2012], in a poster at 19^{th} Congress of the *International Society for Aerosol in Medicine* (ISAM 2013) in Chapel Hill, USA [Scheinherr et al., 2013b], and as an oral presentation at the 19^{th} Congress of the *European Society of Biomechanics* (ESB 2013) in Patras, Greece [Scheinherr et al., 2013a]. Finally the conclusions of the thesis are summarized (Conclusions).

Part I

General Context & Aims

NOMENCLATURE

Overline indicates time average.

A_{g}	glottal area [mm^2]
$\overline{A_{\mathrm{g}}^{\mathrm{E}}}$	the mean glottal area obtained during expiration [mm^2]
$\overline{A_{\mathrm{g}}^{\mathrm{I}}}$	the mean glottal area obtained during inspiration [mm^2]
$\overline{c}$	the average molecular velocity of the air [m/s]
AP_{g}	antero-posterior glottal diameter (glottal length) [mm^2]
C_{c}	the Cunningham slip correction factor
C_{C}	the BTPS conversion coefficient [-]
C_{D}	drag coefficient
D_{a}	particle aerodynamic diameter [m]
D_{e}	particle equivalent diameter [m]
D_{g}	particle geometric diameter [m]
D_{h}	hydraulic diameter [m]
D_{s}	particle Stokes diameter [m]
D_{p}	particle diameter [m]
E_{i}	impaction efficiency
f	breathing frequency [Hz]
F_{D}	drag force [N]
g	gravitational acceleration [m/s^2]
k	Boltzmann constant (1.38×10^{-23} J·K^{-1})
ℓ_{T}	turbulence length scale
l	length referring to dimensions of the model
m_{p}	particle mass [g]
n_{z}	number of collisions [-]
P	penetration [%]
P_{a}	ambient pressure [Pa]
$\overline{PEA_{\mathrm{g}}}$	the mean Peak Expiratory Area of glottis [mm^2]
$\overline{PEF}$	the maximum flow rate during exhalation [L/min]
$\overline{PIA_{\mathrm{g}}}$	the mean Peak Inspiratory Area of glottis [mm^2]
PIF	the maximum flow rate during inhalation [L/min]
P_{ws}	the saturation pressure of water vapor [Pa]
Q	flowrate [L/min]
R^2	linear regression
Re	Reynolds number [-]
Re_{p}	relative Reynolds number of a particle [-]
Stk	Stokes number [-]
T_{a}	ambient temperature [K]
T_{E}	expiratory period [s]
T_{I}	inspiratory period [s]
T_{t}	1 breathing cycle period [s]

u	mean flow velocity [m^3/s]
u_p	particle velocity [m^3/s]
V_{Dep}	deposition velocity [m/s]
V_E	exhaled volume [m^3]
V_I	inhaled volume [m^3]
V_p	particle volume [m^3]
V_t	tidal volume [m^3]

α	frequency parameter [s^{-1}]
$\alpha^\star$	low Reynolds number correction coefficient [-]
η	dynamic viscosity [Pa·s]
λ	mean free path [m]
μ	dimensionless deposition parameter [-]
μ_t	eddy viscosity [Pa·s]
ν	kinematic viscosity [m^2/s]
ρ_g	density of the gas [kg/m^3]
ρ_p	particle density [kg/m^3]
σ_p	geometric standart deviation (GSD) [m]

==========

Chapter I.1

Background and Motivation

1.1 Respiratory System

1.1.1 Introduction

This section provides a general description of the respiration process in humans. In physiology, the term "respiration" is defined as transport of Oxygen (O_2) from the ambient air to the cells within tissues and transport of Carbon dioxide (CO_2) in the opposite direction. The respiratory system is responsible for gas transfer between the tissues and the atmospheric air. Carbon dioxide produced by metabolism in the tissues is moved by the blood to the lungs where it is lost to the outside air. Oxygen that is supplied to the tissues is extracted from the outside air by the lungs. Atmospheric air is pumped in and out regularly through a network of pipes, called conducting airways, which connect the gas-exchange region inside the body with the environment outside the body.

The term "breathing", also referred as "ventilation" in organisms with lungs, is a part of respiration and considers the inhalation and exhalation of the gas inside and outside of the lungs. The diaphragm, as the main respiratory muscle, and the intercostal muscles of the chest wall play an essential role by generating, under the control of the central nervous system, the pumping action of the lung. The muscles expand and contract the internal space of the thorax, whose bony framework is formed by the ribs and the thoracic vertebrae [Rogers, 2011]. Therefore, breathing is an automated function in which nerve impulses sent from the brain stimulate the respiratory muscles to contract, thereby producing the mechanical forces associated with inhalation and exhalation.

The nose, mouth, pharynx, larynx, trachea, bronchial trees, lung air sacs and respiratory muscles are the structures that make up the respiratory system (see Figure I.1.1). The respiratory system can be divided into three regions, each consisting of several anatomical units:

i. the first region is the "upper airways" (UA) region, also referred as the extra-thoracic region,

ii. the second is the "tracheobronchial" region, which includes the airways from the trachea to the terminal bronchioles,

iii. and the last is the "alveolar" region, where proceeds the gas exchange.

These regions differ in airways structure, airflow patterns, function, retention time, and susceptibility to deposited inhaled aerosols. Readers interested in more detailed reviews can consult following works [West, 2007, 2008; Cotes et al., 2009].

In this thesis, focus is given to the flow dynamics occurring in the "upper airways" region during breathing, and specifically in the laryngeal area. The next part provides physiological and anatomical details on this area.

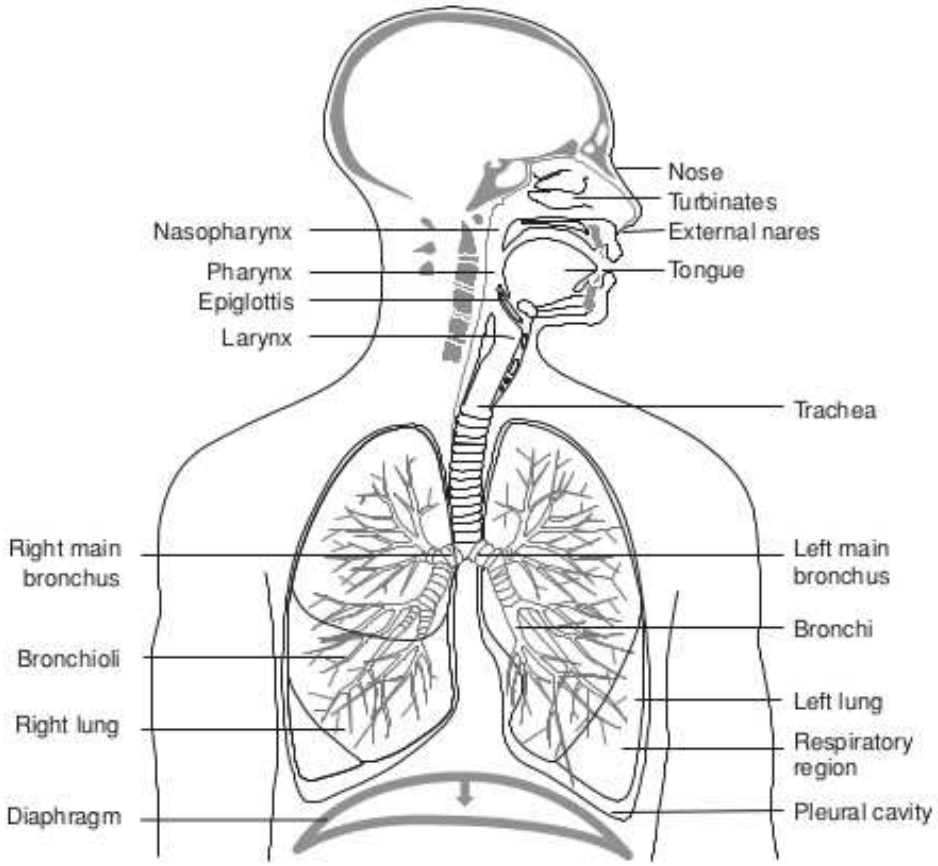

Figure I.1.1: Frontal view of the respiratory system (from Stocks and Hislop [2001]).

1.1.2 Upper Airways and Laryngeal Morphology

The upper airways have a complex geometry (see Figure I.1.1), that includes following components:

- the "oral cavity", sometimes called also the buccal cavity,

- the "nasal cavity", comprising the nose and paranasal cavities (sinuses),
- the "pharynx", divided into two parts including the pathway from the mouth to the larynx (oropharynx) and the nose (nasopharynx);
- the "larynx" (see Figure I.1.2), which forms a constriction at the entrance to the trachea that contains the vocal folds. The space between the vocal folds is called the glottis.

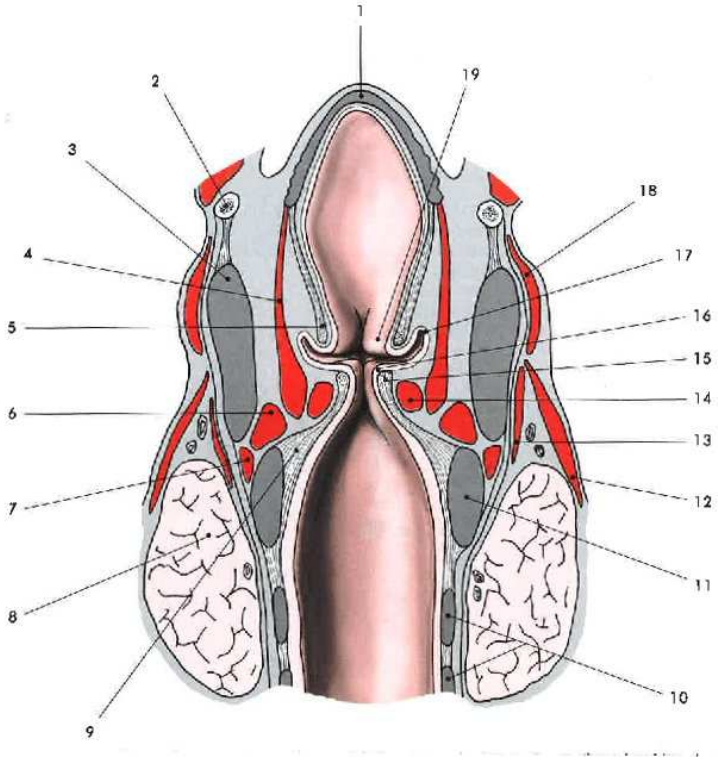

Figure I.1.2: **Frontal cut through larynx.** 1 - epiglottic cartilage, 2 - hyoid bone, 3 - thyroid cartilage, 4 - aryepiglottic muscle, **5 - false vocal fold**, 6 - lateral cricoarytenoid muscle, 7 - cricothyroid muscle, 8 - thyroid gland, 9 - cricovocal membrane, 10 - trachea cartilages, 11 - cricoid cartilage, 12 - sternothyroid muscle, 13 - inferior pharyngeal constrictor muscle, **14 - thyroarytenoid (vocalis) muscle**, 15 - vocal ligament, **16 - true vocal fold**, 17 - ventricle of the larynx, 18 - thyrohyoid muscle, 19 - vestibular fold or false vocal fold (image retrieved from Grim and Druga [2002]).

- the "trachea", lying downstream to the larynx. The trachea can be approximated by a tube of about 10 to 16 cm long and 2.0 to 2.5 cm wide.

The upper airways' morphology has a considerable intra-subject variability and inter-subject variations. In particular, these variations concern the shape of the oral cavity due to changes in the position of the tongue and jaws, and the motion of the vocal folds.

a/ Laryngeal Functions

The larynx is an organ of complex structure, displayed on Figure I.1.2. It serves three physiological functions [Hoh, 2010]:

- a respiratory function, as an air canal to the lungs. During inspiration, the air passes along the epiglottic cartilage, and further around a pair of "false" and "true" vocal folds.
- an airway protective function, which is phylogenetically the oldest function. This function is ensured during coughing, sneezing and swallowing. In that case, the epiglottis swings down and covers the opening into the larynx to avoid the aspiration of liquids or food into the lungs.
- a vocal function, as the organ of phonation.

b/ Laryngeal kinematics

Movements and muscular activity The main movement within the larynx is opening and closing of the glottis as displayed in Figure I.1.3. The vocal-fold movement is composed of rotation and translation of the arytenoids cartilages, in cricoarytenoids joints.

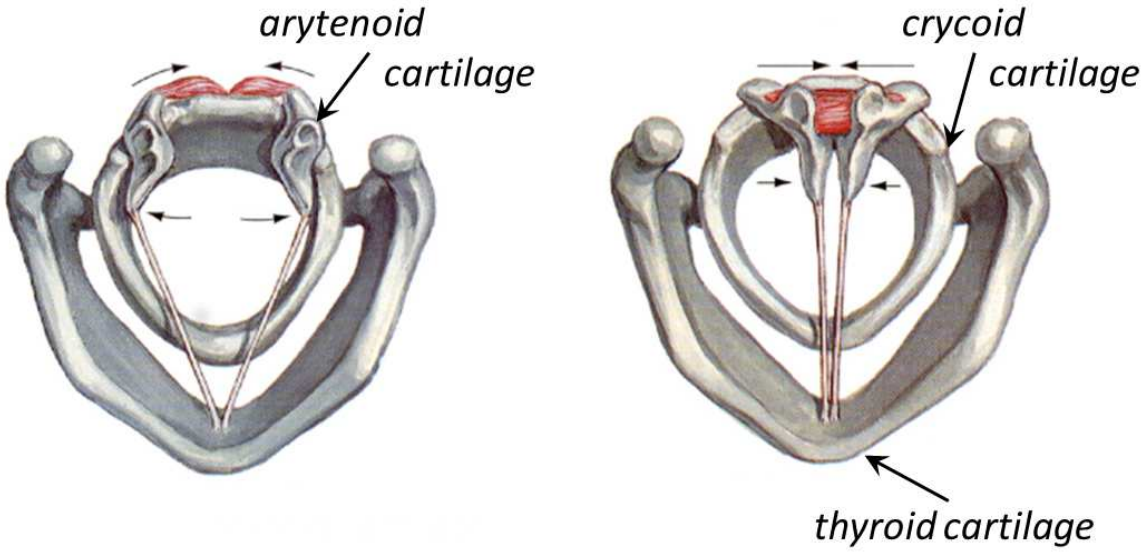

(a) Action of the posterior crico-arytenoid muscle - abduction of the vocal ligaments.

(b) Action of the inter-arytenoid muscle - adduction of the vocal ligaments.

Figure I.1.3: Superior view of the vocal folds movement (from [Hansen and Koeppen, 2002]). Note the crico-arytenoid joint action in abduction (left) and adduction (right).

The tension, altering the length and spatial orientation of the true vocal cords is managed by the intrinsic laryngeal muscles. Those are traditionally divided into three groups: vocal-fold adductors, one abductor and one tensor muscle. To the adductors belong:

- the lateral cricoarytenoid muscle (see Figure I.1.2, point *#6*),
- the thyroarytenoid muscle (see Figure I.1.2, point *#14*), which besides closing the vocal folds also modulates the sound quality,
- and the inter-arytenoid muscle (see Figure I.1.3b), which is found in the interarytenoid fold (see Figure I.1.4, point *#5*).

The tensor muscle is the cricothyroid muscle (see Figure I.1.2, point *#7*). The abductor muscle is the posterior cricoarytenoid (PCA) muscle (see Figure I.1.3a), thereby principally responsible for the control of the glottis (see Figure I.1.4).

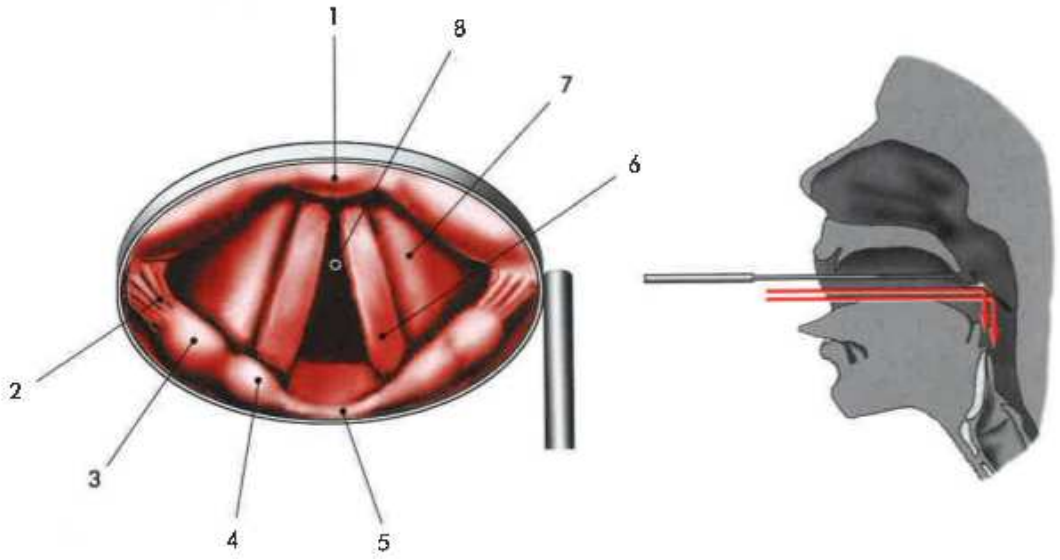

Figure I.1.4: **Laryngoscopic image (example of indirect laryngoscopy). 1 - epiglottis**, 2 - aryepiglottic fold, 3 - cuneiform tubercle, **4 - arytenoid (corniculate tubercle)**, 5 - interarytenoid fold, **6 - true vocal fold**, **7 - false vocal fold**, **8 - glottis** (from Grim and Druga [2002]).

The cricothyroid muscle is innervated by the superior laryngeal nerve, while all the others are innervated by the recurrent laryngeal nerve. Laryngeal muscles control breathing by adjusting the resistance to airflow to match respiratory frequency. The PCA dilates the glottis during inspiration to reduce the load on respiratory muscles, while the adductors contract during expiration to regulate expiratory airflow (see review of Hoh [2005]). The activity of these muscles is modulated by pressure receptors in the laryngeal mucosa [Sammon et al., 1993; Stella and England, 2001].

Means of Investigation The first *in vivo* observation of the glottal motion dates back to the 19th century, with Garcia's laryngeal mirror created in 1855 (see review of Henrich [2006]). The principle is displayed on Figure I.1.4. Thereby, one of the first studies describing the respiratory function of human larynx was done by Hooper [1885]. From the 1880s to the present time, the advances in the medical equipment have allowed a refined exploration of the vocal-fold dynamics, to characterize the vocal-fold vibrations

during phonation (see a review of Ziethe et al. [2011]) or their movement during breathing (see a review of Faber and Grymer [2003]). However, the vocal-fold specific anatomical location, surrounded by many laryngeal cartilages, makes them hardly discernible with ultrasound medical imaging. Instead, the current means of investigation are commonly referred as either "direct" or "indirect" tools, as follows:

- *Direct investigation tools* are used to perform invasive laryngoscopy [Karnell, 1989; Ouaknine et al., 2000; Švec et al., 2000], *i.e.*, a visual examination of the vocal folds thanks to a source of light and camera optics inserted in a tube. There are two types of laryngoscopies, using either a rigid endoscope inserted in the mouth, or a flexible nasofiberscope. Implemented transnasaly, the latter consists of bundles with flexible glassfibres conducting the image to camera optics and additional fiber to carry light from an external source. According to the spatio-temporal resolutions chosen during the examination mode (from 25 frames/s up to 10000 frames/s - full image or selected line), different methods can be conducted: classical videolaryngostroboscopy [Jackson et al., 1975; Baier et al., 1977; England and Bartlett, 1982; Brancatisano et al., 1983; Chen et al., 2013], high-speed cinematography [Childers et al., 1983, 1990; Bailly et al., 2010; Karakozoglou et al., 2012; Bailly et al., 2014], or videokymography [Švec and Schutte, 1996; Švec et al., 1999]. Aside from this classical tools in the voice scientific community, note that some recent studies rely on the use of Magnetic Resonance Imaging (MRI) [Pritchard and McRobbie, 2004].
- *Indirect investigation tools* do not allow a visual examination of the vocal folds. Instead, they yield to other quantities, measurable non-invasively, and related either to the vocal-fold contact variations - like electroglottography [Fourcin and Abberton, 1971; Rothenberg, 1992; Orlikoff, 1998] or photoglottography [Hess and Ludwigs, 2000; Honda and Maeda, 2008; Vaissière et al., 2010], or to the upper airway area like acoustic reflection technique [D'Urzo et al., 1988; Rubinstein et al., 1989; Martin et al., 1997; Busetto et al., 2009]. The latter is based on measurements of high-frequency sound waves which are emitted at the mouth and are reflected as they propagate along the respiratory tract. From the knowledge of reflected intensities and the times of arrival of reflections, the area at a given distance from the sensing microphone is computed, and a plot of airway cross-sectional area as a function of distance into the airway is constructed [Rubinstein et al., 1989].

c/ Laryngeal Major Dimensions

In the work of Eckel and Sittel [1995], 20 fresh larynges of human cadavers were investigated for laryngeal morphometry in horizontal sections. In the following, the main dimensions in the glottal plane are reported (see Figure I.1.5). Value *1* (female 2.1 mm, male 2.9 mm) gives the thickness of the thyroid cartilage about 1 cm from the mid-line on the left side. The greatest width of thyroid cartilage (the transverse distance between its posterior ends) is given by value *2* (female 31.6 mm, male 32.3 mm). The part of the glottis represented by the arytenoid cartilages is defined by value *3* (female 6.9 mm, male 8.6 mm). The ligament part of the glottis was measured as value *4* (female 10.6

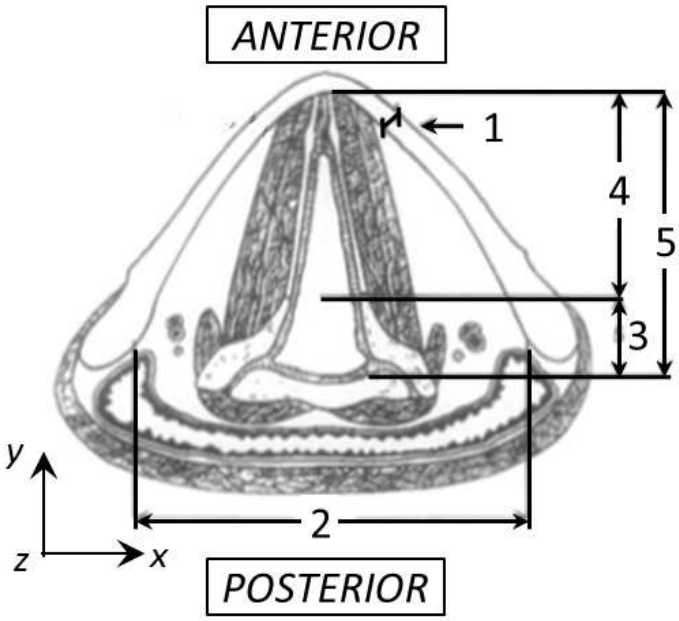

Figure I.1.5: Definitions of main distances in glottal level and posterior & anterior reference planes (image retrieved from Eckel and Sittel [1995]).

mm, male 13.6 mm). Value *5* is the *antero-posterior diameter* AP_g *of the glottis* (also called glottic length), defined as the distance between the intersection of the vocal folds in the thyroid cartilage and the dorsal mucosa-walled border of the glottis. For female, the length AP_g was in average measured at 17.6 mm, and for male at 22.1 mm. These values are comparable to the work of Friedrich and Lichtenegger [1997] who measured the length AP_g on 50 cadaver laryngeal specimens. They found 15.1 mm for female and 21.1 mm for male. Note that these previous data are consistent with the measurements performed by C. Darquenne from University of California, San Diego, USA (personal communication, May 7, 2014), who found $AP_g = 22.0$ mm using MRI on 1 male volunteer. Noticable are the differences of glottal dimensions depending on gender, that causes the male voices to be usually lower pitched influenced by larger glottal dimensions.

As typically observed during *in vivo* laryngoscopic investigation during tidal breathing (*e.g.*, Jackson et al. [1975]; Chen et al. [2013]), the glottis can be approximated by a triangular cross-section. Different values of the glottal cross-sectional area A_g can be found in the literature: $A_g = 45$ mm^2 is reported as the worst case scenario of glottal narrowing [Baier et al., 1977; Brouns et al., 2007b], while $A_g = 100$ mm^2 is reported as a realistic mean value in Brancatisano et al. [1983] (data obtained on 12 healthy subjects). These values are further detailed in section I.2.1. Note that typical dimensions of vocal folds and glottal channel during respiration differs from that during phonation (see Šidlof et al. [2008]).

1.1.3 Breathing Aerodynamics

This part introduces the composition of inhaled and exhaled gases, the lung volumes and the breathing airflow. For details on normal breathing aerodynamics available literature can be consulted (*e.g.*, Proctor and Hardy [1949]; Altman and Dittmer [1971]; Rodarte and Rehder [1986]; Chang [1989]).

a/ Nature of Gases Involved

Ambient air is composed primarily of the nitrogen N_2 (78.08%), oxygen O_2 (20.95%) and argon Ar (0.93%). Water vapor is the next most abundant constituent, and its concentration is highly variable. The remaining gaseous constituent of the ambient inhaled air are the trace gases, *i.e.*, carbon dioxide CO_2 (0.04%), methane CH_4, etc. They represent less than 1% of the global composition [Seinfeld and Pandis, 2012]. The levels of O_2 and CO_2 change in the exhaled air and correspond to 16.5% and 4.5%, respectively. Moreover, the exhaled air is expected to be nearly saturated (*i.e.*, with a relative humidity close to 100%)

b/ Lung Volumes and Capacities

Spirometres are devices to assess the ventilatory function [Miller et al., 2005], *i.e.*, to measure the volume of expired and inspired air in time. The earliest spirometers were water seal spirometers, first described by J. Hutchinson in 1846, and still used nowadays. Water seal spirometers measure the amount of water displaced in a sealed container when a patient exhales. The patient breathes into a hose, which is connected to a water-filled container (see Figure I.1.6). Inside the container is a lightweight plastic object, often called a bell, which rises as water is displaced during the patient's exhalation. A pen hooked up to the bell documents the exhalation and inhalation against time on a rotating chart carrier. The chart produced is called a spirogram, as illustrated in Figure I.1.6. On this chart, lung volumes and lung capacities refer to the volume of air associated with different phases of the respiratory cycle. Thus, several static lung volumes and capacities are commonly defined [Finlay, 2001; Guyton and Hall, 2003; West, 2008; Rogers, 2011]:

- the *total lung capacity* (TLC), that is the amount of air the lung can contain at the height of maximum inspiratory effort. The average total lung capacity of an adult human male is about 6 L of air, but only a small amount of this capacity is used during normal breathing. Therefore, all other volumes are natural subdivisions of TLC.
- the *residual volume*, that is the volume of gas which remains within the lung after maximum exhalation. Inhaled at birth, it is not exhaled until death because the rib cage prevents total lung collapse. Its average value is around 1.2 L.
- the *tidal volume* (V_t), that is the volume of air displaced between normal inhalation and exhalation. In a healthy adult, tidal volume is approximately 0.5 L under rest-

ing conditions. During exercise, the displaced volume may exceed three times this amount.

- the *vital capacity* (VC), that is the volume of air breathed out after the deepest inhalation. A normal adult has a vital capacity between 3 and 5 litres.
- the *functional residual capacity*, that is the volume in the lungs at the end-expiratory position under resting conditions. Its value is around 2.3 L in adults.

Note that typical values of these volumes and capacities depend on subject's age, height, weight and clinical status.

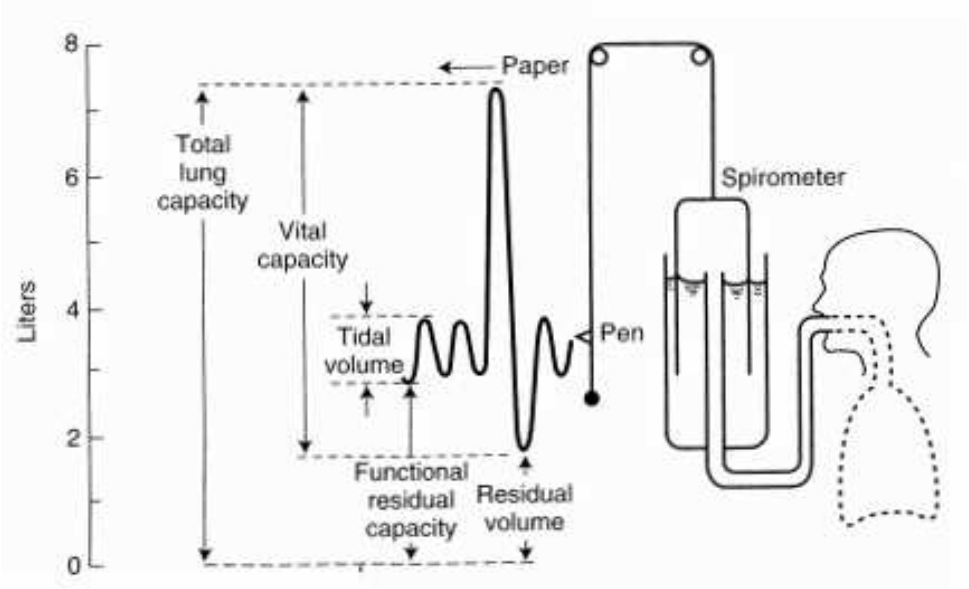

Figure I.1.6: Lung volumes and capacities, as displayed on a spirogram (image retrieved from West [2008]).

c/ Breathing Flow Rates

Note that a complete review on the breathing flow rate pattern, its parameters, diversity and individuality can be found in Benchetrit [2000] or Miller et al. [2005].

Definitions and typical values Typical variations of breathing flow rate Q are displayed as function of time in Figure I.1.7. Several ventilatory quantities are defined, such as:

- the total duration of one breathing cycle T_t [s], from which the breathing frequency is derived, $f = \dfrac{60}{T_\mathrm{t}}$ [breaths/min]. Typical values of f range between 12 and 15 breaths/min during normal breathing.
- the duration of inspiration phase, T_I [s];

- the duration of expiration phase, T_E [s]; note that, under normal conditions, the duration of the inspiration phase is always shorter in comparison with that of the expiration phase [Cain and Otis, 1949].
- the total volume inhaled during one breathing cycle, V_I [L];
- the total volume exhaled during one breathing cycle, V_E [L];
- the maximum flow rate during inhalation referred as "Peak Inspiratory Flow", PIF [L/min];
- the maximum flow rate during exhalation referred as "Peak Expiratory Flow", PEF [L/min].

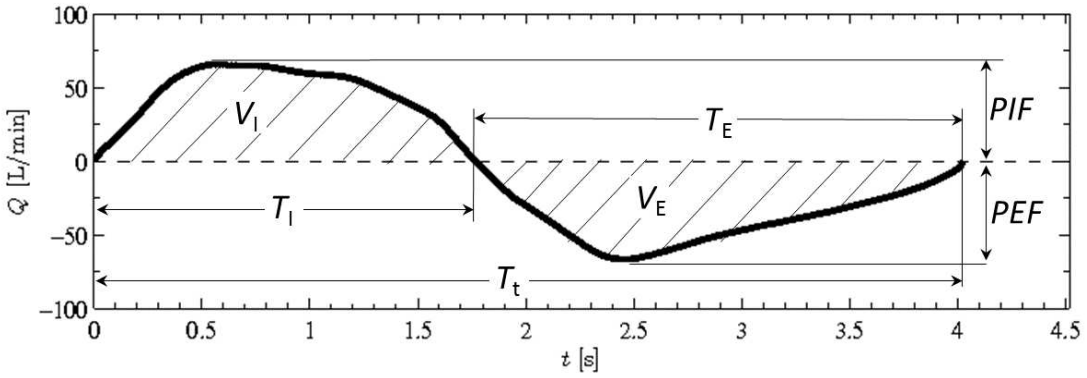

Figure I.1.7: Typical airflow rate pattern during one breathing cycle showing some of the quantities used to characterize breathing (airflow pattern shape).

Note that under quiet periodic breathing conditions, the tidal volume V_t corresponds to the average inhaled volume V_I (or equally to the average exhaled volume V_E). Knowing the tidal volume V_t and the breathing frequency f, minute ventilation can be calculated $\dot{V} = V_t f$, *i.e.*, the amount of gas inspired or expired per minute. Typically, the minute ventilation $\dot{V}$ is approximately 6 L/min in a healthy adult, compared to less than 1 L/min in an infant [Heyder and Svartengren, 2001]. Finally, different breathing regimes can be defined depending on the breathing frequency f or the depth of breathing:

- *eupnea*, characterized by *slow respiratory* rates ranging up to 20 breaths per minute (tidal breathing);
- *tachypnea*, characterized by *rapid respiratory* rates ranging from 20 to 90 breaths per minute;
- *hyperpnea*, which is a ventilation with increased depth of breathing;
- *apnea*, which is a temporary interruption in breathing; it can be voluntarily achieved by closing the vocal folds or it can occur as a consequence of sleeping disorders (sleep apnea) or trauma.

Intra-subject variations The flow-rate intra-subject differences are discussed by Benchetrit et al. [1989], from measurements of subjects' ventilation performed within 5 years. They showed that the individuality of breathing flow-rate pattern is maintained over a long period despite changes in smoking habit, weight, etc. Regarding inter-subject differences, Shea and Guz [1992] concluded that: (i) different people breath in different ways under strictly defined conditions of wakefulness; (ii) this is a relatively stable characteristic of an adult, being reproducible after a long period of time; (iii) identical twins breathe with similar patterns.
Other studies analyzed the variations of the respiratory flow-rate patterns related to different respiratory conditions [Cain and Otis, 1949; Proctor and Hardy, 1949; Painter and Cunningham, 1992]. In Cain and Otis [1949], the respiratory conditions were studied during *eupnea* with several added resistive loadings, whose influence is shown in Figure I.1.8 (see also Calabrese et al. [1998]). Whatever the case, they measured an airflow-rate higher during inspiration than during expiration. Painter and Cunningham [1992] showed that flow-rate shape during *hyperpnea* varies according to the exercise, or the elevated ratio of carbon dioxide CO_2 in blood (hypercapnia), or the lack of oxygen O_2 (hypoxia). Finally, Roth et al. [2003] studied the flow-rate pattern while breathing in a nebulizer drug delivery. Significant differences were observed in comparison with normal breathing, showing an increased tidal volume and lengthened period of breathing cycle.

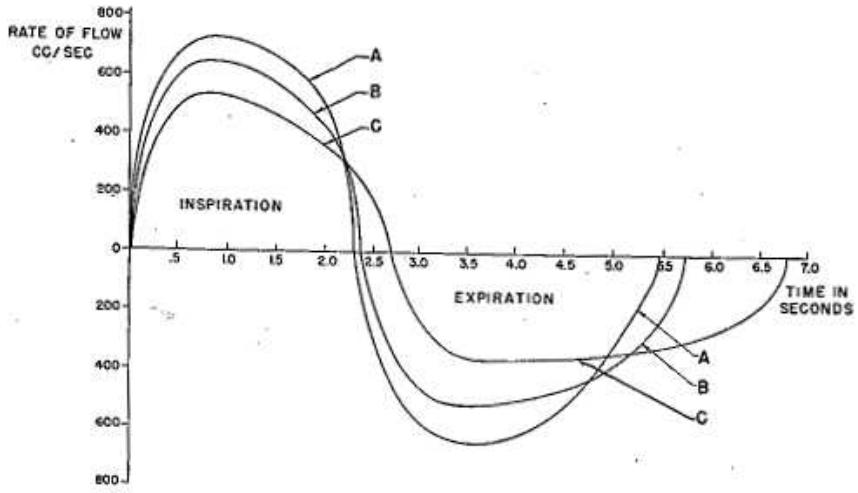

Figure I.1.8: Evolution of breathing pattern with added resistances. Measured by Cain and Otis [1949].

1.2 Lung Diseases and Aerosol Therapy

Lung diseases are often relentlessly progressive and represent an important public health problem. They usually cause a narrowing or blockage of the airways. Some of these diseases are characterized by a limitation of expiratory airflow in the lower airways (such as obstructive lung diseases), while others like chronic sinusitis affect the upper airways.

In this part, the common chronic lung diseases are presented, together with their current clinical treatment based on aerosol therapy.

1.2.1 Most Common Chronic Lung Diseases

a/ Pathogenesis

Tobacco smoke and exposure to indoor and outdoor air pollution are the most important risk factors. The incidence of lung diseases increases dramatically with the rise of airborne aerosol pollution. Numerous epidemiological studies showed that aerosol pollution is related to respiratory diseases [Schwartz, 1993; Dockery and Pope, 1994; Pope et al., 1995; Šrám et al., 2013]. The following health effects of undesirable aerosols have been observed: increased incidence of respiratory symptoms, decreased lung function, increased hospitalization rate.

b/ Obstructive Lung Diseases

Obstructive lung diseases limit flow of air in and out of the lungs. The main diseases within this group are Chronic Obstructive Pulmonary Disease (COPD), asthma and bronchiectasis.

- *COPD* is a serious long-term disease that mainly affects older people. It can lead to mild or severe shortness of breath that is not fully reversible even with treatment. Generally COPD embraces emphysema and chronic bronchitis. Emphysema is the destructive process of the alveolar structures that leads to the loss of lung elastic recoil. Chronic bronchitis affects both the large and the small airways, with hypertrophy (increase of the volume of the cells) or hyperplasia (cell proliferation).
- *Asthma* is a chronic inflammation with bronchoconstriction. Patients with asthma experience symptoms such as wheezing, breathlessness and chest tightness due to widespread narrowing of the airways.
- *Bronchiectasis* refers to an abnormal and irreversible widening of air passages in the lungs. Patients suffering from bronchiectasis are prone to infections as mucus accumulates in the airways and becomes stagnant. The symptoms can be coughing up blood, sputum production, chest pain and shortness of breath.

c/ Chronic Sinusitis

Chronic sinusitis is characterized by an inflammation of cavities around the paranasal sinuses. This inflammation can last for around eight weeks, despite treatment attempts. The most common symptoms are nasal congestion, increased secretions, facial pain and fatigue. Most cases are due to a viral infection, but it can also be caused by growths in the sinuses (nasal polyps) or by a deviated nasal septum. Young and middle-aged adults suffer most commonly from this disease.

1.2.2 Aerosol Therapy

Inhalation has been employed as a method for delivering medications for more than two thousands years [Sanders, 2007]. The benefits of delivering medication *a priori* directly to the affected site (oftenly the lungs) have been understood for more than two hundred years. Therefore, aerosol therapy has dramatically improved the treatment of many respiratory diseases such as asthma and COPD.

Advantages Basic advantage of aerosol therapy lies in the direct delivery of high local concentrations of the drug to the site of action, with minimized risks of systemic effects [Khilnani and Banga, 2008]. In comparison with other methods of treatment (oral delivery or injection), the improvement includes:

- ease and rapidity of administration;
- effectiveness with smaller doses of drug needed;
- faster pharmacokinetics of drug delivery to targeted area.

Drawbacks The efficiency of inhaled therapies depends on the ability of the subject (i) to produce an adequate inspiratory flow, and (ii) to properly use the delivery device:

i. During childhood, peak inspiratory flow (PIF) ranges from less than 0.05 to over 40 L/min, depending on age, maturity, and clinical status [Coates and Ho, 1998]. Most subjects older than 6 years are able to generate an adequate PIF (*i.e.*, $>$ 30 L/min), that is necessary for efficient inhalation from most commonly used delivery devices [Coates and Ho, 1998].

ii. The chosen device and its correct use have a major impact on aerosol delivery efficiency [Kovářová and Ždímal, 2009]. The medicament can be delivered in the form of a nebulized drug (nebulizers), a spray (pressurised Metered Dose Inhalers pMDI) or a powder (Dry Powder Inhalers (DPI). The device has to be chosen according to type of drug, patient's age and his mental/physical capacities.

In addition to these subject's abilities, several physical and anatomical factors such as particle characteristics, carrier gas flow properties or airways morphology can largely influence treatment efficiency [Finlay, 2001; Sandeau et al., 2010; Kleinstreuer and Zhang, 2010]. This can be explained by fundamental mechanics of aerosol transport and deposition, as detailed in next section.

1.3 Fundamental Mechanics of Aerosol Transport and Deposition

The inhaled pharmaceutical aerosols can be transported in the airflow stream by several mechanisms, including convection, diffusion, thermophoresis, etc. The delivery to the target site depends on the efficiency of these mechanisms, the geometry of the airways

and the aerosol properties. In this section, the aerosol geometrical and physical characteristics are presented, together with their effects on the particle transport and deposition mechanisms in human upper airways.

1.3.1 Aerosol Geometrical and Physical Characteristics

An aerosol is an assembly of solid or liquid particles suspended in a gaseous medium (*e.g.*, air), that is a two-phase system. In the following, we will focus on liquid particles suspended in a carrier gas. Manufactured and naturally produced particles may have a great diversity in size, shape, surface area, density and chemical composition. The particle size (noted as D_p) is the key property to characterize aerosol particles, since particle behavior is governed by different physical laws according to the size [Ruzer and Harley, 2005; John, 2011].

a/ Particle Shape and Size

Shape Aerosol particles like liquid droplets are spherical, while particles formed by crushing have irregular shape, and some crystalline particles can exhibit a regular geometric shapes. In the theoretical description of particle properties, a spherical shape is usually assumed. In the application of these theories to non-spherical particles, correction factors or equivalent diameters are used to estimate their properties.

Size Aerosol particle sizes range over 5 orders of magnitude, from about 1 nm to more than 100 µm. For a spherical particle of unit density, the size can be simply characterized by the geometric diameter. For particles of non-spherical shape and/or arbitrary density, an equivalent diameter D_e is used [John, 2011]. An equivalent diameter D_e is the diameter of a spherical particle that has the same property or characteristic as the non-spherical particle. Examples of such an equivalent diameter (see Figure I.1.9) can be:

- the aerodynamic diameter, D_a. It is defined as the diameter of a spherical particle of unit density having the same terminal settling velocity as that of the particle in question.
- the Stokes diameter, D_s. It is defined as the diameter of a spherical particle having the same density and settling velocity as the particle in question.

Both are the main diameters used in this thesis, and further detailed in section I.1.3.2.c. Note that numerous other diameters can be defined like diffusive diameter, electrical mobility diameter, optical diameter, etc.

b/ Aerosol Size Distribution

Two types of aerosols are defined, according to their size distribution:

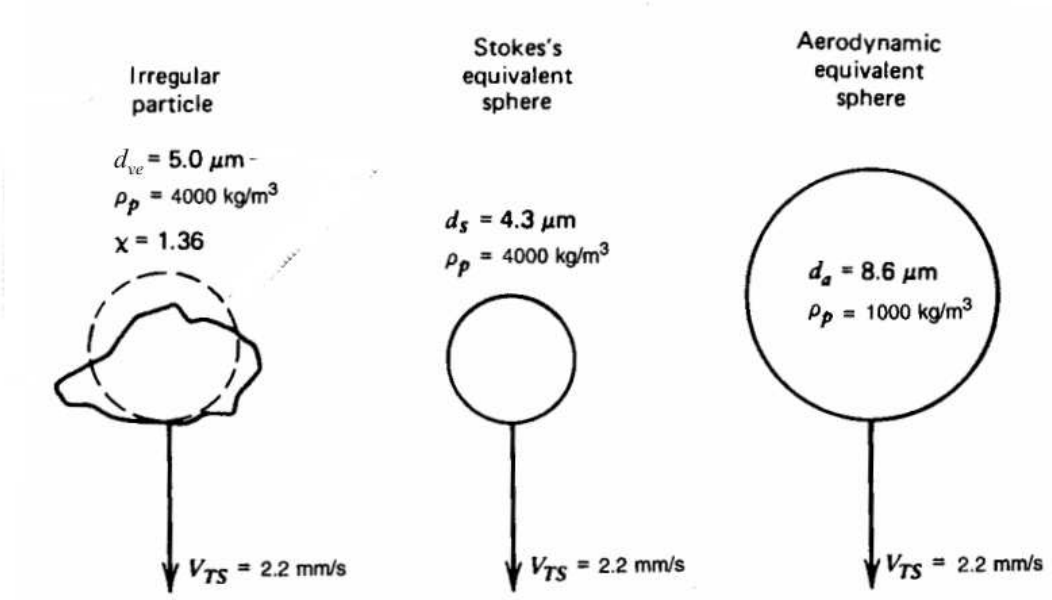

Figure I.1.9: Typical irregular particle and its equivalent spheres (retrieved from Hinds [1999]). See section I.1.3.2.c for definitions of shape factor χ, diameters D_a and D_s and settling velocity V_{TS}.

- *A monodisperse aerosol* has particles of uniform size and can be produced in the laboratory. In that case, a single number - such as the particle geometric diameter - suffices to describe the size of the particles. Note that conventionnally, a spread in particle diameter of less than about 10-20% (ie, with a geometric standard deviation of 1.1 to 1.2) is considered monodisperse.
- *A polydisperse aerosol* is composed of particles with different sizes. Most of the pharmaceutical aerosols belong to polydisperse type. The sizes of the particles in the aerosol are thus mathematically described by particle-size distributions, defining the relative amounts of the particles sorted according to the size. Typical particle-size distributions can be well characterized by the log-normal distribution or cumulative distribution [Olesik and Bates, 1995] for instance. The log-normal distribution approximates the size distribution in a log-normal scale and the cumulative distribution expresses the relative amount of particles below a specific size. In its simplest form, a lognormal distribution is completely defined by two parameters, its geometric mean diameter (D_g), and its geometric standard deviation (σ_g or GSD).

c/ Aerosol Hygroscopicity

Hygroscopicity is the ability of the particle to absorb or release water from the surrounding humid environment. The addition and removal of water can significantly affect the particle size. A hygroscopic aerosol that is delivered at relatively low temperature and humidity into higher humidity and temperature environment would be expected to increase

in size. The rate of growth is a function of the initial diameter of the particle, relative humidity, temperature of the surrounding air, and the relative speed between the particle and the surrounding gas.

More specifically, the hygroscopic growth of a particle strongly depends on the particle size relative to the mean free path of the carrier gas. The gas must be considered as an ensemble of rapidly moving molecules, colliding with the particles. The mean free path is defined as the average distance traveled by the air molecules between two successive collisions. The mean free path λ of a gas can be determined from the average number of collisions that a molecule undergoes in one second, n_z, and the average distance traveled in that second, so that:

$$\lambda = \frac{\overline{c}}{n_z}, \tag{I.1.1}$$

where $\overline{c}$ is the average molecular velocity of the air. The mean free path increases with increasing temperature or decreasing pressure. The growth rate for particles smaller than the mean free path is independent of droplet size, while for larger particles it is inversely proportional to the diameter [Barrett and Clement, 1988].
In the human respiratory tract, the air is nearly saturated. A value of relative humidity of 99% or 99.5% is generally accepted. The relative humidity increases rapidly in the upper airways region. When a particle is inhaled, it grows very rapidly, following an exponential time function, and then increases asymptotically to its equilibrium size [Xu and Yu, 1985]. To improve the lung delivery of inhaled medicines, the concept of controlled size increase was recently introduced by Longest and Hindle [2011]. In this approach, to significantly reduce device and extrathoracic depositional losses, the aerosol is delivered with an initially small size (submicrometer or nanometer) at all practical flow rates. Increasing the aerosol size as it enters the lungs is then used to ensure lung retention and to potentially target the site of delivery within the airways.

d/ Inhalability of Particles in the Respiratory System

The respiratory system is an effective size-selective aerosol sampler. Not all sizes of particle can be breathed in with 100% efficiency. The mass fraction of particles in an inhaled air volume that enters the nose or the mouth represents the *inhalable fraction*. The inhalability of the particle depends on the particle diameter and the airflow velocity and direction. Because particles transport and deposition depend on particle aerodynamic behavior in a flowing gas, the aerodynamic equivalent diameter is employed. Specific definitions of particles fraction according to the penetration in the respiratory tract are used (see Figure I.1.10) [Brown et al., 2013]:

- *Extrathoracic fraction*: the mass fraction of inhaled particles failing to penetrate beyond the larynx.
- *Thoracic fraction*: the mass fraction of inhaled particles penetrating beyond the larynx.

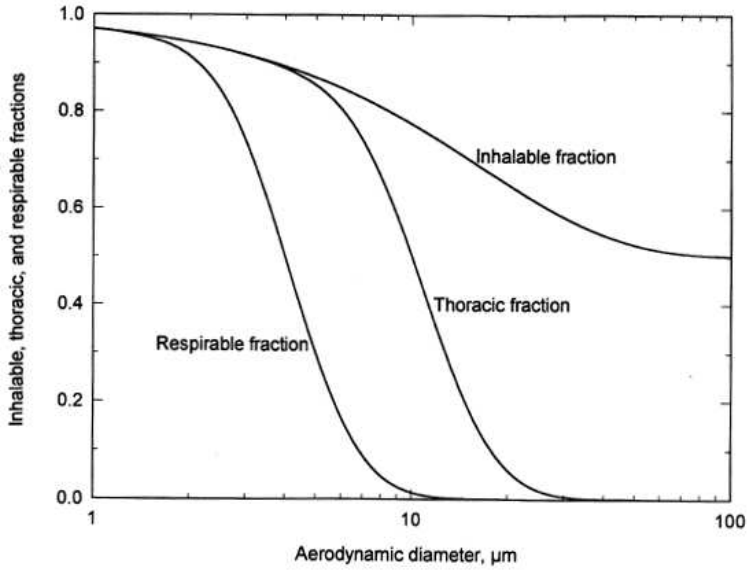

Figure I.1.10: The efficiency curves for inhalable, thoracic and respirable fractions (image retrieved from Hinds [1999]).

- *Respirable fraction*: the mass fraction of inhaled particles that can reach the lungs alveoli.

The graph on Figure I.1.10 shows the efficiency curves for *inhalable*, *thoracic* and *respirable fraction*, as proposed by International Standards Organization (ISO 7708). For inhalable, respirable and thoracic fractions, the particles having 50% penetration are 100 µm, 10 µm and 4 µm in diameter D_a, respectively [Hinds, 1999].

1.3.2 Aerosol Transport

From Newton's second law of motion, the basic equation of motion governing the trajectory of the particle with mass m_p and volume V_p is:

$$m_p \frac{d\boldsymbol{u}_p}{dt} = \boldsymbol{F}_D + V_p \boldsymbol{g}(\rho_p - \rho_g), \tag{I.1.2}$$

where $\boldsymbol{g}$ refers to gravitational acceleration, ρ_p to the particle's density, and ρ_g to the density of the surrounding gas. To solve this equation for particle velocity $\boldsymbol{u}_p$ in the flow of velocity $\boldsymbol{u}$, we must determine the drag force $\boldsymbol{F}_D$ and the buoyancy effect acting on the particle (second term on the right side). Note that Equation I.1.2 is only an approximate of the equation of motion of a particle (*i.e.*, in a fluid the drag force $\boldsymbol{F}_D$ is estimated by classical laws used and defined for steady flows). Therefore full equation, taking into

account the unsteadiness effects of the flow behavior was defined by [Hinze, 1975]:

$$m_\mathrm{p}\frac{\mathrm{d}\boldsymbol{u}_\mathrm{p}}{\mathrm{d}t} = \boldsymbol{F}_\mathrm{D} + V_\mathrm{p}\rho_\mathrm{g}\frac{\mathrm{d}\boldsymbol{u}}{\mathrm{d}t} + \frac{V_\mathrm{p}}{2}\rho_\mathrm{g}\left(\frac{\mathrm{d}\boldsymbol{u}}{\mathrm{d}t} - \frac{\mathrm{d}\boldsymbol{v}}{\mathrm{d}t}\right) + \\ + \frac{3{D_\mathrm{p}}^2}{2}\left(\pi\rho_\mathrm{g}\eta\right)^{\frac{1}{2}}\int_0^t \frac{(\mathrm{d}\boldsymbol{u}/\mathrm{d}t') - (\mathrm{d}\boldsymbol{v}/\mathrm{d}t')}{(t-t')^{\frac{1}{2}}}\mathrm{d}t' + V_\mathrm{p}\boldsymbol{g}(\rho_\mathrm{p} - \rho_\mathrm{g}) + \sum_i \boldsymbol{F}_\mathrm{i}, \quad \text{(I.1.3)}$$

where η is the dynamic viscosity of the surrounding gas. The second term on the right side is due to the pressure gradient in the fluid surrounding the particle, caused by acceleration of the gas by the particle. The third term on the right side is the force required to accelerate the apparent mass of the particle relative to the fluid. The fourth term on the right side, called the Basset history integral, accounts for the force arising due to the deviation of the fluid velocity from the steady state. The fifth term considers the gravity and the last term considers the additional external forces $\boldsymbol{F}_\mathrm{i}$ exerted on the particle. From the standpoint of liquid aerosols in the air, in most situations the second, third, and fourth terms on the right-hand side of the Equation I.1.3 may be neglected.

a/ Drag Force on Particle

The drag force $\boldsymbol{F}_\mathrm{D}$ is the resistance experienced by a particle moving in a fluid. When a particle is moving through the fluid, it deforms the fluid, causing layers of the fluid in the region around the particle to slide one over another. The drag force on a spherical particle is given by Finlay [2001]:

$$\boldsymbol{F}_\mathrm{D} = -\frac{1}{2}\rho_\mathrm{g}{v_\mathrm{rel}}^2\frac{\pi D_\mathrm{p}^2}{4}C_\mathrm{D}\boldsymbol{v}_\mathrm{drag}, \quad \text{(I.1.4)}$$

where C_D is the drag coefficient, v_rel is the velocity magnitude of the particle relative to the fluid motion:

$$v_\mathrm{rel} = |\boldsymbol{u}_\mathrm{p} - \boldsymbol{u}| \quad \text{(I.1.5)}$$

and $\boldsymbol{v}_\mathrm{drag}$ is the unit vector representing the direction of the drag force parallel to the relative velocity v_rel:

$$\boldsymbol{v}_\mathrm{drag} = \frac{\boldsymbol{u}_\mathrm{p} - \boldsymbol{u}}{v_\mathrm{rel}}. \quad \text{(I.1.6)}$$

Equation I.1.4 is the general form of the *Newton's resistance equation*, valid for all subsonic particle motions.

In 1851, Stokes derived an expression for the drag force, when inertial forces are negligible compared to viscous forces. The drag force on a spherical particle moving with velocity $\boldsymbol{u}_\mathrm{p}$ through a fluid is given by:

$$\boldsymbol{F}_\mathrm{D} = -3\pi\eta D_\mathrm{p}\left(\boldsymbol{u}_\mathrm{p} - \boldsymbol{u}\right). \quad \text{(I.1.7)}$$

This is *Stokes' law*, that contains dynamic viscosity η but not factors associated with inertia, such as the density of the fluid. Comparing Equation I.1.4 with Equation I.1.7

we can get the drag coefficient:

$$C_{\mathrm{D}} = \frac{24\eta}{\rho_{\mathrm{g}} v_{\mathrm{rel}} D_{\mathrm{p}}} = \frac{24}{Re_{\mathrm{p}}}, \quad \text{for} \quad Re_{\mathrm{p}} < 1 \tag{I.1.8}$$

where Re_{p} is the relative Reynolds number of the spherical particle defined as

$$Re_{\mathrm{p}} = \frac{\rho_{\mathrm{g}} D_{\mathrm{p}} v_{\mathrm{rel}}}{\eta}. \tag{I.1.9}$$

The use of Stokes' law is restricted to situations in which the particle Reynolds number is less than 1. Note that in case of transition region, $1 < Re_{\mathrm{p}} < 1000$, the frictional coefficient C_{D} can be calculated with empirical formula (see Table I.1.1). For high Reynolds numbers, $1000 < Re_{\mathrm{p}} < 200\ 000$, C_{D} has a nearly constant value of 0.424 (see Table I.1.1) [Liu et al., 1993]. The drag coefficient C_{D} in function of Re_{p} is shown in Figure I.1.11. The

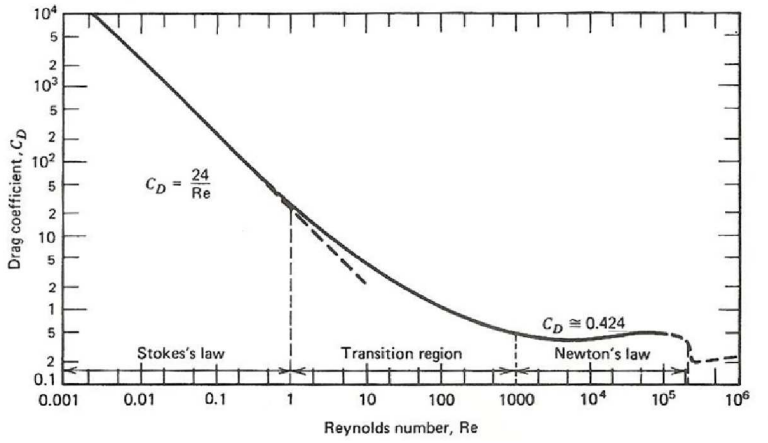

Figure I.1.11: Drag coefficient C_{D} in function of particle Reynolds number Re_{p} (image adapted from Hinds [1999]).

curve in the figure is representative for droplets, other particle shapes have similar curves. The correction for non-rigid spheres such as water droplets is generally insignificant.

Stokes' regime	**Transition - Empirical relationship**	**Newton's regime**
$C_{\mathrm{D}} = \frac{24}{Re_{\mathrm{p}}}$	$C_{\mathrm{D}} = \frac{24}{Re_{\mathrm{p}}}\left(1 + 0.15 {Re_{\mathrm{p}}}^{0.687}\right)$	$C_{\mathrm{D}} = 0.424$
$Re_{\mathrm{p}} < 1$	$1 < Re_{\mathrm{p}} < 1000$	$Re_{\mathrm{p}} > 1000$
Inertial forces negligible against viscous forces	Both inertial and viscous forces play a role	Viscous forces negligible against inertial

Table I.1.1: Equations for frictional coefficient C_{D} in function of Reynolds number.

The Stokes' law is valid only if the diameter of the particle is much greater than the mean free path of the fluid molecules surrounding the particle (*i.e.*, 0.067 μm for air at room temperature and 1 atmosphere pressure). Thus, a correction to Equation I.1.7 can be

applied to submicrometer particles, referred to as the Cunningham slip correction factor C_c, which is defined as [Ounis et al., 1991]:

$$C_c = 1 + \frac{2\lambda}{D_p}\left(1.257 + 0.4e^{-\frac{1.1D_p}{2\lambda}}\right). \tag{I.1.10}$$

The drag force is then:

$$\boldsymbol{F}_D = -\frac{3\pi\eta D_p \boldsymbol{v}_{drag}}{C_c}. \tag{I.1.11}$$

In that case, the drag coefficient for a sphere is replaced by:

$$C_D = \frac{24}{C_c \times Re_p}. \tag{I.1.12}$$

For particles with $D_p > 1\,\mu m$ the correction for slip can be neglected, and so Cunningham slip correction factor is equal to 1 [Hinds, 1999].

b/ Stokes Number

The equation of particle motion can be written in dimensionless form, by introducing U_0 as a characteristic velocity magnitude in the fluid flow, and D_h as a characteristic dimension of the geometry containing the fluid flow (*e.g.*, the hydraulic diameter of the airway the particle is in). Once the equation of motion Equation I.1.2 is non-dimensionalized, the Stokes number is obtained (Stk) as follows:

$$Stk = \frac{\rho_p {D_p}^2 u C_c}{18\eta D_h} = \frac{\tau U_0}{D_h}, \tag{I.1.13}$$

where ρ_p is the density of the particle, D_p its diameter, η is the dynamic viscosity of the gas and time τ is the particle relaxation time τ, defined by:

$$\tau = \frac{\rho_p {D_p}^2 C_c}{18\eta} \tag{I.1.14}$$

The particle relaxation time τ is the time required for the particle's velocity relative to the fluid to decay to $e^{-1} = 37\%$ of its initial value [Finlay, 2001], and the Stokes number is a dimensionless parameter that describes the ease of a particle to change its trajectory in the airflow. The value of the Stokes number determines whether a particle will undergo inertial impaction (see more in section I.1.3.3.a).

c/ Settling velocity

In the still air, the particle will settle under the action of gravity.

Spherical particles If the particle is spherical the gravity force is defined:

$$\boldsymbol{F}_{\mathrm{g}} = \rho_{\mathrm{p}} V_{\mathrm{p}} \boldsymbol{g}. \tag{I.1.15}$$

When the particle begins to move, the gas surrounding the particle exerts an opposite drag force (aerodynamic drag), which is equal to the gravitational force, and the particle reaches its terminal settling velocity (also called sedimentation velocity). Therefore, assuming $Re_{\mathrm{p}} < 1$, by equating the drag force defined by Stokes (Equation I.1.7 with a zero gas-velocity) to the gravitational force (Equation I.1.15) the magnitude of the settling velocity V_{TS} is obtained:

$$V_{\mathrm{TS}} = \frac{\rho_{\mathrm{p}} {D_{\mathrm{p}}}^2 g}{18\eta}. \tag{I.1.16}$$

Nonspherical particles A correction coefficient referred as dynamic shape factor χ can be applied to the Stokes' law, when particle has other than spherical shape. This will result in the modification of the drag force equation derived by Stokes (Equation I.1.7) applying the equivalent diameter D_{e}:

$$\boldsymbol{F}_{\mathrm{D}} = -3\pi\eta D_{\mathrm{e}} \left(\boldsymbol{u}_{\mathrm{p}} - \boldsymbol{u}\right) \chi \tag{I.1.17}$$

and the settling velocity will become:

$$V_{\mathrm{TS}} = \frac{\rho_{\mathrm{p}} {D_{\mathrm{e}}}^2 g}{18\eta\chi}. \tag{I.1.18}$$

According to definition given in section I.1.3.1, the aerodynamic diameter D_{a} can be calculated. The D_{a} is the diameter of a spherical particle, having a standard density ρ_w (that of a water droplet: 1000 kg/m^3), and having the same gravitational settling velocity as the particle in question, so that:

$$V_{\mathrm{TS}} = \frac{\rho_{\mathrm{p}} {D_{\mathrm{e}}}^2 g}{18\eta\chi} = \frac{\rho_w {D_{\mathrm{a}}}^2 g}{18\eta}. \tag{I.1.19}$$

Similarly, the particle's Stokes diameter D_{s} can be derived. It is the diameter of a spherical particle having the same density and settling velocity as the particle in question, so that:

$$V_{\mathrm{TS}} = \frac{\rho_{\mathrm{p}} {D_{\mathrm{e}}}^2 g}{18\eta\chi} = \frac{\rho_{\mathrm{p}} {D_{\mathrm{s}}}^2 g}{18\eta}. \tag{I.1.20}$$

From Equation I.1.19 and Equation I.1.20 can be derived as:

$$D_{\mathrm{a}} = D_{\mathrm{e}} \left(\frac{\rho_{\mathrm{p}}}{\rho_w \chi}\right)^{\frac{1}{2}} = D_{\mathrm{s}} \left(\frac{\rho_{\mathrm{p}}}{\rho_w}\right)^{\frac{1}{2}} \tag{I.1.21}$$

and for spheres:

$$D_{\mathrm{a}} = D_{\mathrm{p}} \left(\frac{\rho_{\mathrm{p}}}{\rho_w}\right)^{\frac{1}{2}}. \tag{I.1.22}$$

1.3.3 Aerosol Deposition

The aim of this section is to provide basic knowledge on the aerosol deposition within the human upper airways (see reviews *e.g.*, [Hinds, 1999; Finlay, 2001]). Particle deposition depends on:

- the airway geometries,
- the particle geometrical and mechanical properties (size, shape, density),
- the individual's breathing pattern (flow rate, frequency, tidal volume).

Deposition efficiency is defined as the ratio of the number of particles deposited within the respiratory tract to the total number of entering particles. Primary deposition mechanisms are: (a) inertial impaction, (b) turbulent mixing, (c) Brownian diffusion, (d) sedimentation. Secondary deposition mechanisms are: (e) electrostatic attraction, (f) interception, (g) cloud motion (see Figure I.1.12). Aerosol deposition in the extrathoracic and upper

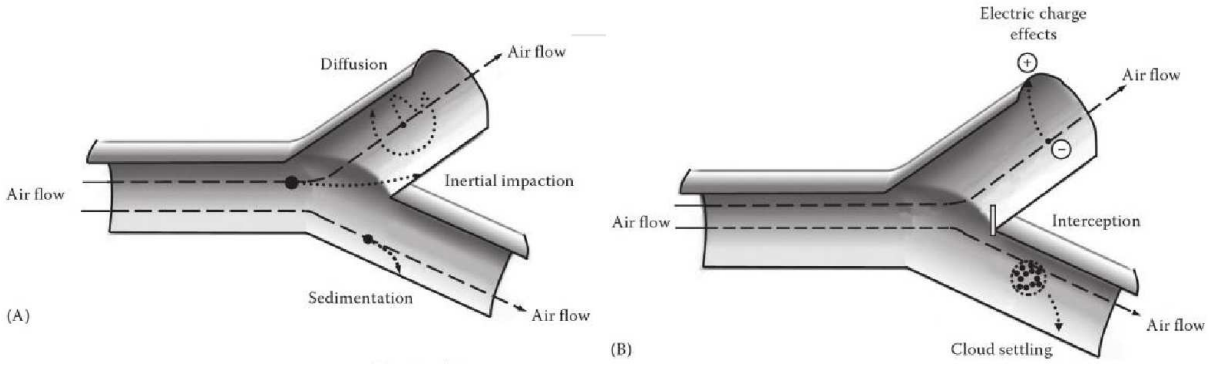

Figure I.1.12: Particle deposition mechanisms in a bifurcation airway (adapted from Martonen et al. [2000]).

bronchial regions is dominated by inertial impaction. For particles in the nanometer size range (with diameter $D_p < 200$ nm), diffusion also contributes. Lower bronchial and peripheral surfaces collect particles mainly by sedimentation. It is important to note that particles that contact the airway walls deposit in the mucus of the walls and generally are not reentrained. In the following, each deposition mechanism is detailed.

a/ Inertial Impaction

Inertial impaction occurs when particles have sufficient momentum to deviate from the fluid streamlines and thus, strike boundary surfaces. The principle of the mechanism is illustrated on panel *(A)* in Figure I.1.12. The effectiveness of this mechanism depends on the particles stopping distance at the air flow velocity u; consequently, this mechanism is limited to the large particles.

Important factor for this deposition mechanism is the Stokes number Stk defined in Equation I.1.13. Stokes number is characterizing whether the particle will undergo inertial

impaction in the fluid motion. When $Stk >> 1$, particles continue moving in a straight line when the flow turns. When $Stk << 1$, particles follow the gas streamlines perfectly. During inhalation, the incoming air often changes direction as it flows from the nose or mouth down through the branching airways system to the alveolar region. The greatest deposition by inertial impaction occurs in the regions, where the flow streamlines turn most sharply (*i.e.*, in the oropharynx, near glottal area, at the tracheal bifurcation and to a lesser degree at other bifurcations).

b/ Turbulent mixing

Turbulent mixing (also referred as turbulence diffusion) is the phenomenon when eddy structures and recirculation zones are created in the flow, which decreases the boundary layer on the walls and facilitates particles to deposit on the walls [Tian and Ahmadi, 2007]. As reported in previous studies *e.g.*, [Zhang et al., 2002]) particles basically follow the secondary airflow and are evidently affected by the intensity of turbulence and secondary flow. In such a case, the velocity of the particles and thus their trajectories are continuously undergoing changes in both magnitude and direction, which can result in their deposition on the walls. The turbulent flow for those reasons can be described in terms of its mean values over which are superimposed the instantaneous flow fluctuations. Therefore, on contrary from inertial impaction, that is produced by the mean flows, turbulent mixing is generated by the flow fluctuations. In human upper airways turbulent mixing plays a significant role in aerosol deposition in particular for high flows.

The turbulent flow in the respiratory tract is principally a function of the gas density [Darquenne and Prisk, 2004]. Therefore lowering the gas density can lead to converting of the flow regime to laminar flow. Within the respiratory system, turbulent mixing affects deposition mainly inside the upper airways region [Darquenne and Prisk, 2004; Darquenne, 2012].

c/ Brownian Diffusion

The Brownian motion is the irregular wiggling motion of an aerosol particle caused by the relentless bombardment of the gas molecules on the particle's surface. The principle of Brownian diffusion is illustrated on panel *(A)* in Figure I.1.12. Diffusion of aerosol particle is the net transport of the particles in a concentration gradient. The process is characterized by the particle diffusion coefficient D [Hinds, 1999]:

$$D = \frac{kTC_c}{3\pi\eta D_p}. \tag{I.1.23}$$

Here k is the Boltzmann constant (1.38×10^{-23} J·K^{-1}), T [K] is the temperature, η [Pa·s] is the air dynamic viscosity and D_p the particle diameter. The larger the value of D, the more vigorous the Brownian motion and the more rapid the mass transfer. A problem of great practical importance is the deposition by diffusion of aerosol particles to the walls of a tube as they flow through it. In the human respiratory tract, this deposition

mechanism is important for sub-micrometer particles. In the lung region diffusion is the main deposition mechanism for particles smaller than 0.5 µm in diameter and in the upper airways region for particles smaller than 0.01 µm in diameter [Hinds, 1999].

d/ Sedimentation

Sedimentation is the deposition of the particles by gravitational forces. The gravitational pull depends on the difference between the density of the particle and that of the surrounding medium. Mechanism by sedimentation in airway bifurcation is illustrated on panel *(A)* in Figure I.1.12. The particle sedimentation increases in importance with increasing particle size, and with low flow velocities causing increased particle residence time within the airway. Sedimentation has its maximum removal effect for particles in horizontally orientated airways. In human respiratory tract, sedimentation is a major factor affecting the particle deposition within the lung region, in particular for particles with Stokes number $Stk < 0.01$ [Darquenne et al., 2011]. In the upper airways region, high flow rates leads to insufficient time for particle to deposit by sedimentation [Cohen and Asgharian, 1990; Heyder and Svartengren, 2001].

e/ Interception

Interception is the process when a particle contacts the airway surface because of its physical size (see panel *(B)* on Figure I.1.12). Note that, on contrary from inertial impaction during deposition by interception particle does not deviate from the gas streamline. Thus the probability of the interception depends on the proximity of the gas streamline to the airway surface, and on the ratio of the particle size to the airway diameter, which is usually small even in the narrowest airways. For elongated particles (*e.g.*, fibers), interception is an important respiratory tract deposition mechanism. The chance of particle interception increases as the airway diameter becomes smaller.

f/ Electrostatic Deposition

Highly charged particles are attracted to the airway surface by the electrostatic charge that the particle induces in the airway surface by its presence (see panel *(B)* onFigure I.1.12). Unipolar charged aerosols with high number concentrations are also deposited because their mutual repulsion drives particles away from each other and towards the airway wall. Electrostatic deposition in human airways can be an important mechanism for submicron particles Cohen et al. [1998].

g/ Cloud Motion

Individual particles can, under certain conditions, form a cloud of particles (see panel *(B)* on Figure I.1.12). Such an entity will behave in the gas differently than individual particle. The movement of an entity is called cloud motion and can be significant for

example for deposition of cigarette smoke in the alveolar region [Martonen and Musante, 2000].

1.4 Current Clinical Needs and Challenges

As shown in previous parts, in addition to the chosen inhalation device, the characteristics of inhaled particles, airways morphology, carrier gas and flow properties can largely influence the aerosol transport-deposition mechanisms in upper airways. Thereby, they are key factors which determine the treatment efficiency of inhaled therapies [Finlay, 2001; Kleinstreuer and Zhang, 2010; Sandeau et al., 2010]. Some of these key factors can be monitored and optimized (*e.g.*, particles and flow properties), while others are not adjustable (airway anatomy).

1.4.1 Adjustable Key Factors

The influence of the particle aerodynamic diameter on deposition fraction in upper airways has already been described in section I.1.3.1.d. Therefore, in the following, the impact of gas-flow properties is detailed.

a/ Carrier Gas

Different gas mixtures may also affect particle transportation and deposition rate. For instance, a mixture of 78% of Helium and 22% of Oxygen (He-O_2) has a gas density about one third that of the air, and a viscosity about 8% higher than the air. Thus, at similar flow rates, the Reynolds number for Helium is approximately one third that of the air in any given airway. Accordingly, the use of He-O_2 mixture reduces turbulent flow in the trachea and secondary transitional flows in the conducting airways, thereby reducing deposition by turbulent mixing. The study of Peterson et al. [2008] reported a significant decrease in deposition within the mouth and throat and a significant increase in alveolar deposition when breathing He-O_2 compared to air. The comparison of the deposition fraction of monodisperse aerosol predicted in the extrathoracic region using air or He-O_2 as carrier gas is illustrated in Figure I.1.13, for several particle diameters. This prediction derives from the modeling described in Grgic et al. [2004a].

b/ Inhaled Flow Conditions

The effect of changes in breathing flow rates and volumes has direct influence on the efficiency of aerosol therapy [Agertoft and Pedersen, 1993; Bisgaard, 1995], as discussed in section I.1.1.3. High respiratory rates usually result in increased deposition in the more proximal airways. Shallow, rapid breathing should be avoided during inhalation therapy, since the smaller the tidal volume, the greater the proportion that will be wasted in the

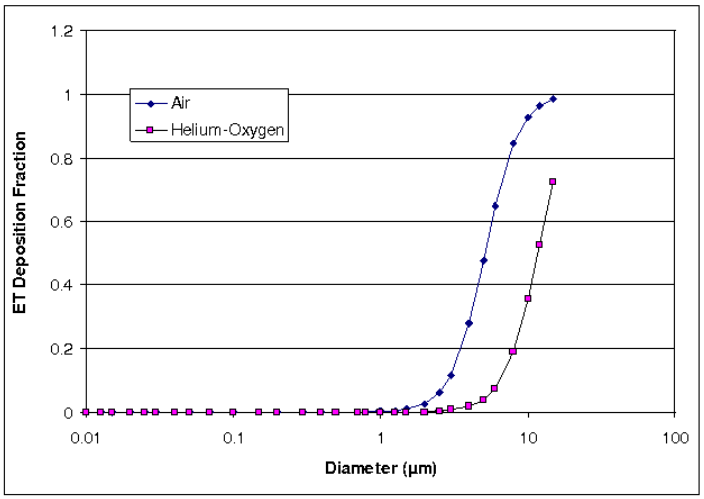

Figure I.1.13: Deposition fraction of monodisperse aerosol predicted in the extrathoracic region using air or He-O_2 as carrier gas. The prediction is derived from the modeling described in Grgic et al. [2004a].

dead space. On the contrary, during larger breaths, aerosol is likely to penetrate further into the lung, increasing peripheral deposition.

1.4.2 Unadjustable Key Factors

The major unadjustable factors altering treatment efficiency of inhalation therapy consist in airway anatomy of the subject. In fact, the upper airways anatomic arrangement can act as an unwanted filter, which limits the amount of drug delivered to the lungs. More specifically, the laryngeal area plays a key role not only in breathing airflow dynamics [Katz and Martonen, 1996; Martonen and Katz, 1993; Renotte et al., 2000; Brouns et al., 2007b], but also in aerosol transport mechanisms and deposition patterns [Grgic et al., 2004b; Gemci et al., 2003; Xi and Longest, 2008].

Thanks to three dimensional imaging data, recent clinical experiments have been conducted to measure the distribution of aerosol deposition in human subjects Fleming et al. [2011]; Conway et al. [2012]. Radioactive aerosol was administered to 11 healthy male subjects. The aerosol distribution was measured by combined Single Photon Emission Computed Tomography (SPECT) and X-ray Computer Tomography (CT). The distribution of deposition was described in terms of the percentage of inhaled aerosol deposited in different sections of the respiratory tract. Thereby, it is shown that particle deposition in upper airways region can reach as much as 40% of the total inhaled mass. A particular case is illustrated in Figure I.1.14, highlighting high deposition of radiolabelled aerosols detected in the laryngeal area, whereas target tissues were located in the lungs.

Therefore, this unwanted filter effect seems to be related to the glottal anatomy, which causes upper airways to narrow in a minimal transition cross-section. From this point of

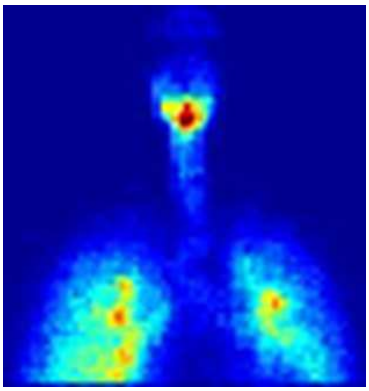

Figure I.1.14: Example of aerosol distribution measured on a heatlhy subject by single photon emission computed tomography (SPECT) after inhalation of radiolabelled particles. Extracted from the clinical study performed by Fleming et al. [2011] and Conway et al. [2012]. Illustration of the high deposition in the laryngeal region.

view, the knowledge of glottal motion during human breathing is of primary interest in order to assess the filtration efficiency of the upper airways.

Chapter I.2

Impact of the Glottis During Breathing

This chapter provides a state-of-the-art focused on the vocal-fold kinematics observed during human breathing (section I.2.1), its influence on the airflow occurring in the laryngeal/tracheal region (section I.2.2), and on the aerosols deposition in the upper airways (section I.2.3).

Note that the review covers the three common approaches in scientific research:

- *In vivo* studies, which provide experimental results from real living subjects. The applied methodology is often connected with strict legislation, high financial demands, inter- and intra-subject variability and needs to obtain informed consent.
- *In vitro* studies, which allow less expensive measurements, easier handling, feasibility and reproducibility through simplified laboratory experiments.
- *In silico* studies, which afford the possibility to set arbitrary boundary conditions, and to predict data not always reachable by the experiments, through numerical/theoretical modeling.

2.1 Glottal Motion Observed During Breathing

This section presents the current knowledge gained from *in vivo* studies, upon (1) the glottal kinematics observed under healthy and pathological breathing conditions, (2) the detected dimensions of the glottal area, and (3) the relationships between glottal opening and airflow rate.

2.1.1 Characterization of the Glottal Kinematics

a/ Under Healthy Conditions

General trends The general motion of the vocal folds during breathing is changing with the task:

- During *eupnea*, the glottal aperture is known to vary during the respiratory cycle, by widening during inspiration and narrowing during expiration [Baier et al., 1977; Higenbottam, 1980; England and Bartlett, 1982; England et al., 1982; Brancatisano et al., 1983; Templer et al., 1991; Chen et al., 2013]. Typical variations of the glottal width during eupnea is illustrated in the panel (a) of Figure I.2.1 as a function of percent tidal volume. From a study based on 5 subjects, England and Bartlett [1982]

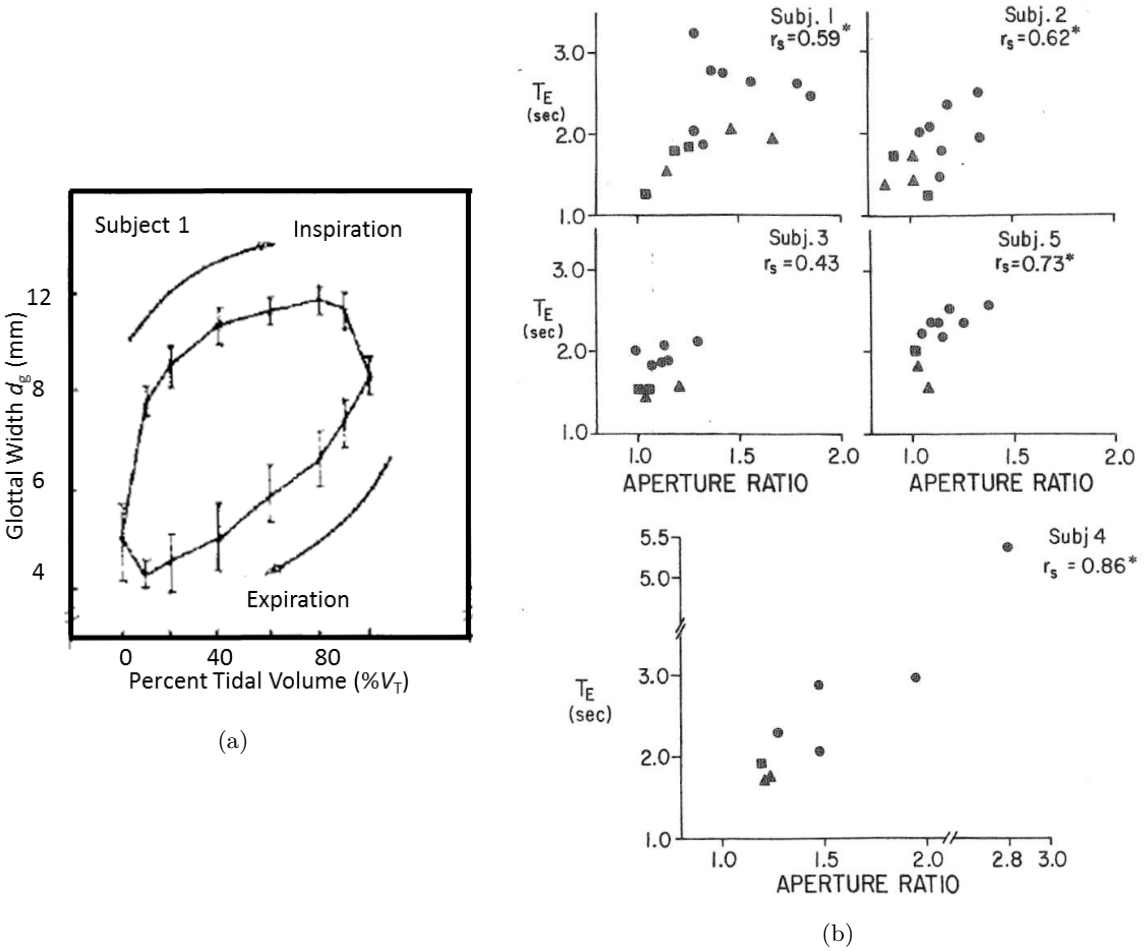

(a)

(b)

Figure I.2.1: (a) Glottic width variations measured on 1 subject plotted against percent tidal volume (%V_t) during an average breathing cycle (mean of 5-7 consecutive breaths). Extracted from Brancatisano et al. [1983]. (b) Average expiratory duration (T_E) against glottal aperture ratio measured on 5 subjects (circles: eupnea; triangles: hypercapnia; squares: exercise). Extracted from England and Bartlett [1982].

assessed the ratio of the glottal aperture measured at 50% of inspiratory duration

(T_I) to the same measurement at 50% of expiratory duration (T_E): it varied between 1 and 3 during eupnea as demonstated in panel (*b*) of Figure I.2.1. The glottal widening generally precedes the onset of inspiratory flow, and reaches a maximum value at approximately mid-inspiration. Similarly, the glottal narrowing generally precedes the onset of expiration, and goes on until nearly two-thirds of the tidal volume is expired. Noticeable inter-subject differences can be highlighted on the pattern of glottic motion, especially during inspiratory phase, whereas it appears to be reproducible in a given subject on different days [England and Bartlett, 1982; Brancatisano et al., 1983].
Note that some sparse studies have reported that this typical time-varying motion of the vocal folds is not systematic, even in healthy subjects. Indeed, Jackson et al. [1975] observed this motion in only two out of three subjects. For one of them instead, the glottis remained constantly opened whatever the breathing task. Semon [1895] saw time-varying glottal motions in only 10 out of 50 subjects. This result is generally explained by the stress stimuli generated by invasive laryngoscopy.

- During *hyperpnea*, Stănescu et al. [1972] measured a larger glottal area as compared to eupnea. Similarly, England and Bartlett [1982] observed a slight increase of glottal area during inspiration and a decrease in the extent of glottal narrowing occurring during expiration. The aperture ratio was measured smaller than during eupnea. They concluded that the braking of expiratory airflow by the vocal-fold motion is reduced during hyperpnea.

- During *panting*, the glottal area is larger as compared to tidal spontaneous breathing, at any lung volumes [Stănescu et al., 1972; Baier et al., 1977; Brancatisano et al., 1983]. The differences between inspiration and expiration were found much smaller. Similarly, Hurbis and Schild [1991] compared quiet and rapid breathing, and noticed an increase in glottal area during both inspiration and expiration with exercise.

Neuromuscular activity As the main abductor muscle of the vocal folds, the activity of the posterior crico-arytenoid muscle (PCA) has been investigated in sereval electromyographic studies during breathing. In healthy subjects, Payne et al. [1981] showed that the PCA phasic (*i.e.*, time-varying) activity was not registered during eupnea. Yet, PCA phasic activity was measured during inspiration in periods of voluntary hyperventilation (not in expiration). In that case, PCA activity increased with tidal volume, as shown in panel (*a*) of Figure I.2.2. Brancatisano et al. [1984] also registered an increased PCA activity together with increased widening of glottal aperture. According to Brancatisano et al. [1983]; England et al. [1982], the onset of glottic widening prior to the onset of inspiration is also consistent with neurophysiological observations. In particular, the electrical activity in the recurrent laryngeal nerve precedes the onset of phrenic nerve activity (*i.e.*, diaphragmatic activity) by around 100-200ms. The activation of the PCA continues until the end of inspiration and then declines.

These results support the idea that the PCA may be considered as an inspiratory muscle and that the regulation of ventilation may be linked with a motor control of the intrinsic laryngeal musculature. It is commonly agreed that the glottal widening may help the air

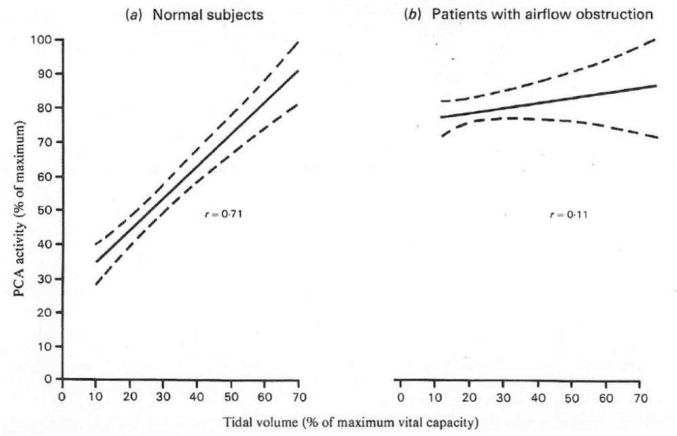

Figure I.2.2: Inspiratory electromyographic activity of PCA during hyperventilation in function of the tidal volume for (a) healthy subjects and (b) patients with airflow obstruction. From Payne et al. [1981].

intake during inspiration, to minimize the upper airways resistance to flow. By contrast, the glottal narrowing is interpreted as a metabolically inexpensive aid to modulate the expiratory airflow and control the rate at which the lungs return to their resting volume [England et al., 1982; Brancatisano et al., 1983; Templer et al., 1991].

b/ Under Pathological Conditions

General trends In the presence of experimentally induced bronchoconstriction or airflow obstruction due to lung disease, the vocal-fold narrowing during expiration is enhanced, as shown in Higenbottam [1980]. These observations are in agreement with the increased expiratory laryngeal resistance observed during eupnea in patients with airflow obstruction [Campbell et al., 1976], as also observed during pursed lip breathing. In healthy subjects, the resistance across the upper airways is reported around $1 cm H_20/L/s$ during quiet breathing, whereas it is on the order of 4 to 15 $\mathrm{mmH_20/L/s}$ in most patients with upper airway obstruction [Templer et al., 1991]. In the later study, it was shown that with a glottal area A_g below 50 mm^2, the pressures needed to generate normal airflows increase significantly, which is symptomatic of clinical trouble. Typically, for airflow rates ranging from 30 to 50 L/min, values of such "abnormal" pressures range from 10 to 29 mm H_20 for $A_g = 42.5\,\mathrm{mm}^2$, as shown on Figure I.2.3. Finally, it is interesting to note that *vocal fold dysfunction*, also referred to as paradoxical vocal fold motion (PVFM) in othorhinolaryngology, and defined as an intermittent, abnormal adduction of the vocal folds during respiration, frequently co-exits with asthma [Jain et al., 2006; Benninger et al., 2011].

Neuromuscular activity In constrast with healthy subjects, a time-varying PCA inspiratory activity was recorded by Payne et al. [1981] during eupnea in patients with airflow

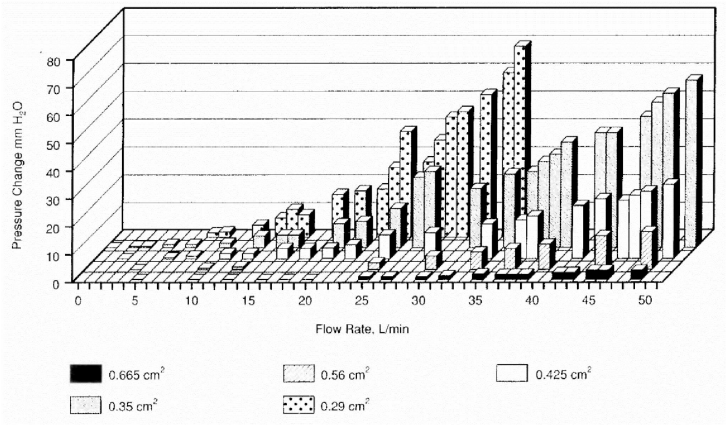

Figure I.2.3: Airflow rate against pressure difference across the vocal folds placed in breathing configuration for varying degrees of laryngeal obstruction. Glottal areas are parametrically varied between 29 mm^2 and 66.5 mm^2. Measurements performed on 5 fresh cadaveric larynges, extracted from Templer et al. [1991].

obstruction. In that case, the PCA activity failed to increase during voluntary hyperventilation, as shown in panel (*b*) of Figure I.2.2. Besides, at low tidal volumes, the PCA activity was measured nearly twice the value for healthy subjects at comparable tidal volumes.

2.1.2 Measurement of Glottal Dimensions

Depending on the subjects' characteristics (age, gender, body mass index, lung volumes), the breathing task and the chosen means of investigation (fibroscopy, MRI, acoustics reflection technique), different ranges of values have been measured for the glottal area A_g in adult healthy subjects (as defined in section I.1.1.2.c):

- *Average value in the order of* 50 mm^2 - Baier et al. [1977] provided one of the first direct dimensions of the vocal folds during eupnea and tachypnea (100 breaths/min) using fiberoptic cinelaryngoscopy (16Hz). Magnification of the camera optics was calculated using 1 mm diameter Teflon particles placed on the vocal folds as a reference. The measurements performed on 6 subjects (4 females, 2 males) are summarized in Table I.2.1, with a mean low value of 46 mm^2 for males in eupnea.
- *Average value in the order of* 100 mm^2 - Brancatisano et al. [1983] measured real dimensions of glottal area during eupnea on 10 males and 2 females using nasofibroscopy, assuming that the glottal antero-posterior diameter AP_g remains constant (see Figure I.1.5). Area A_g increased during inspiration up to 126 $\pm$ 8 mm^2 (mean value $\pm$ standard deviation), whereas during expiration it decreased down to 70 $\pm$ 7 mm^2. Thereby, according to this work, the glottic area oscillates about a mean of 98 mm^2 during eupnea. Recently, using nasofibroscopy, Chen et al. [2013] observed maximal peaks of glottal area during inspiration varying between 71 and 135 mm^2 on 8 subjects (mean value 98 $\pm$ 29 mm^2), and minimal peak areas during expiration

varying between 11 and 115 mm^2 (mean value 76 $\pm$ 28 mm^2). Finding a similar range of values, Pritchard and McRobbie [2004] used MRI to measure mean glottal area A_g on 10 females (A_g = 79.3 mm^2) and 10 males (A_g = 131.8 mm^2), near the point of maximum inflow.

- *Average value in the order of* 200 mm^2 - Rubinstein et al. [1989] measured changes in glottal cross-sectional area of 44 subjects using acoustic reflection technique. Subjects were instructed to inspire to total lung capacity (TLC) and then expire slowly to residual volume (RV) (hyperpnea task). The expiratory flow rate was kept relatively constant, between 500 and 700 mL/s. The authors found a value ranging between 137 and 207 mm^2 by 19 females (mean value of 194 $\pm$ 34 mm^2 at 50% of vital capacity (VC)), and between 144 and 231 mm^2 by 25 males (mean value of 185 $\pm$ 54 mm^2 at 50% of VC). The obtained data are summarized in Figure I.2.4, showing peak A_g values over 300 mm^2. Using the same investigation technique, a more recent study

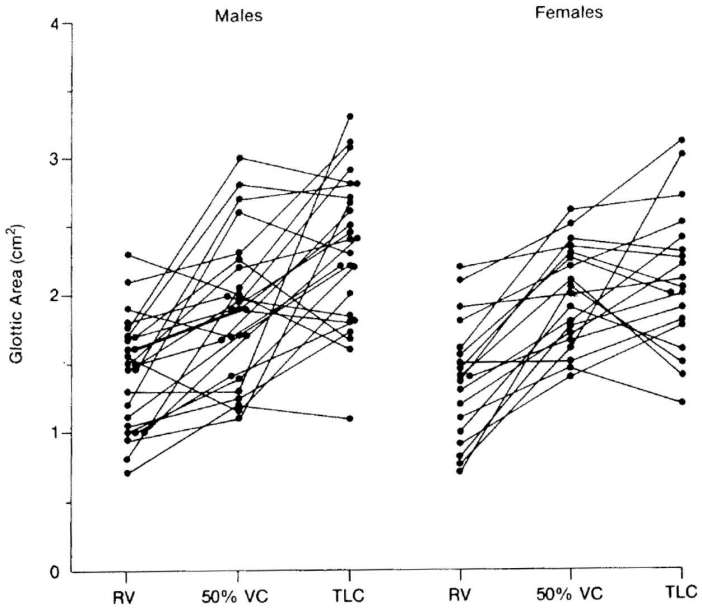

Figure I.2.4: Glottic cross-section area A_g measured by Rubinstein et al. [1989]. Measurements performed on 44 subjects, at total lung capacity (TLC), 50% of vital capacity (VC) and residual volume (RV). Extracted from Rubinstein et al. [1989].

has been performed on 60 male and 54 female subjects at the onset of inspiration (flow rate Q = 0 L/min) by Martin et al. [1997]. The mean area A_g was assessed at 170 mm^2 (at both seated and supine position). Note that in this latter work, the accuracy of the acoustic reflection technique was validated using both *in vitro* models and *in vivo* comparison with MRI technique, when area measurements were found to be within 10%.

In the literature, note that a mean A_g value ranging between 90-100 mm^2, as measured by Brancatisano et al. [1983] during eupnea, is often chosen as a reference, so as to conduct numerical simulations or *in vitro* measurements in upper airway models of healthy adult

Type of breathing	A_g [mm^2] - females			A_g [mm^2] - males		
	mean	range	N° of subjects	**mean**	range	N° of subjects
Eupnea	**76**	43 - 104	4	**46**	44 - 48	2
Tachypnea	**113**	87 - 138	2	**61**	53 - 69	2

Table I.2.1: Dimensions of glottal cross-section area A_g measured by Baier et al. [1977].

subjects (*e.g.*, Stapleton et al. [2000]; Heenan et al. [2003]; Brouns et al. [2007b]). Finally, to our knowledge, a single study has focused on the measurements of glottic areas on subjects with a history of glottic pathology (typically, surgery of the glottis or proximal trachea). This work has been conducted by D'Urzo et al. [1988], who compared measurements of the area A_g obtained by acoustic reflection technique and by computerized tomographic (CT) scans of the neck, on 11 adult subjects. Both measurements were performed in the supine position during eupnea at functional residual capacity. The mean A_g values determined for each subject are reported in Figure I.2.5, showing a good agree-

Subj No.	Acoustic Reflection	Computerized Tomography
1	2.1±0.3	2.4±0.6
2	1.4±0.2	1.6±0.3
3	1.9±0.2	1.6±0.5
4	2.1±0.1	1.9±0.3
5	2.7±0.2	2.3±0.5
6	2.9±0.3	3.4±0.4
7	2.0±0.1	2.2±0.5
8	1.9±0.1	1.8±0.1
9	0.7±0.3	0.6±0.2
10	0.4±0.1	0.3±0.1
11	1.2±0.2	0.8±0.3
Mean±SD	1.8±0.8	1.7±0.9

Values are expressed in cm^2.

Figure I.2.5: Comparison between measurements of glottic area A_g derived from acoustic reflection method and CT-scans, performed on 11 subjects with glottic pathology. Extracted from D'Urzo et al. [1988].

ment between both methods (average values of 180 ± 80 mm^2 for the acoustic method and 170 ± 90 mm^2 for the CT method).

2.1.3 Relationship between Glottal Area and Airflow Rate

The relationship between changes in glottal area and the inhaled airflow rate during breathing is not clearly known in the literature. It was investigated in few studies of reference in 1980s (*e.g.*, Stănescu et al. [1972]; Baier et al. [1977]; England et al. [1982]; Brancatisano et al. [1983]), which yielded to controversial results on that point.

In Stănescu et al. [1972], a positive significant correlation was found between glottis opening, lung volume and airflow rate. England et al. [1982] found a positive correlation between the average expiratory airflow from 75 to 25 % of the tidal volume and the mean glottal aperture during this interval. Therefore, according to the authors, a decrease in airflow is correlated with a decrease in the distance between the vocal folds.

By contrast however, Baier et al. [1977] did not find any correlation between inspiratory and expiratory flow with glottis dimensions during eupnea and breathing with increased frequencies. Similarly, no correlation was observed within a breath between airflow and glottic width in the reference study by Brancatisano et al. [1983]. In this latter work, during inspiration, both glottic width between the apexes of the arytenoid cartilages (d_g) and flow rate increased to a maximum value, and then decreased. However, the rise and fall of these two variables was not closely correlated. Furthermore, the volume corresponding to d_g^{max} and maximal flow rate rarely coincided. Similarly, during expiration, flow rate and d_g showed no consistent relationship.

2.2 Impact of the Glottis on Airflow in Upper Airways

The impact of the vocal-fold constriction on the airflow occurring in the human upper airways has been intensively investigated since the 1960s. In this section, a survey of the main *in vitro* and *in silico* studies which allowed to gain insight on this subject is presented.

2.2.1 *In Vitro* Studies

To overcome the limitations of *in vivo* test conditions, studies using artificial experimental larynges increased from the last 50 years. In 1957, Van den Berg et al. [1957] published a study of a static model of the vocal tract, in which flow resistance and Bernoulli effect within the glottal constriction were investigated. Since then (up to nowadays), many *in vitro* devices were developped to mimic the vocal-fold self-sustained vibrations as observed during human phonation, in order to better understand the fluid/structure interactions taking place within the laryngeal acoustical source. In comparison, the *in vitro* studies dealing with the glottis in breathing configuration are far less numerous. However, some pioneer studies in the 1960s-1980s allowed to highlight the impact of the glottis on breathing airflow properties. The main phonation- and breathing-related studies are summarized thereafter.

a/ Phonation-related Studies

Since 1960s, three main groups of mechanical replica of the larynx can be found in the phonation-related studies (*e.g.*, see a review in Ruty et al. [2007] and Kniesburges et al. [2011]):

- *Rigid fixed vocal-fold replica* [Van den Berg et al., 1957; Scherer et al., 1983, 2001; Pelorson et al., 1994; Hofmans et al., 2003] - These replica are used to explore the pressure-flow relationships under steady or unsteady flow conditions and fixed boundary conditions. For instance, pressure measurements conducted by Hofmans et al. [2003] allowed to characterize phenomena like glottal flow asymmetry due to the Coandă effect or transition to turbulence, the average subglottal phonatory pressure being around 800 Pa (range of values 300-1000 Pa). They demonstrated that those flow effects need a relatively long time to establish to the characteristic phonatory frequencies (typical range of values 100-300Hz), and are therefore unlikely to occur in real life.
- *Moving externally-driven vocal-fold replica* [Titze et al., 1995; Barney et al., 1999; Deverge et al., 2003; Cisonni et al., 2008; Mongeau et al., 1997; Shadle et al., 1991; Triep et al., 2005; Triep and Brücker, 2010] - these replica allowed to mimic the periodic medial-lateral motion of the glottal walls as well as their convergent/divergent shaped changes during the phonatory cycle. With optical fluid measurement techniques like particle image velocimetry, fundamental flow phenomena could be explored in supraglottal regions.
- *Deformable self-oscillating vocal-fold replica* [Ruty et al., 2007; Bailly et al., 2008, 2010; Becker et al., 2009; Drechsel and Thomson, 2008; Pickup and Thomson, 2010; Šidlof et al., 2011; Chisari et al., 2011; Krebs et al., 2012; Sciamarella et al., 2012] - these replica were elaborated to produce flow-induced vibrations at characteristic phonatory frequencies. They predominantly consist of polyurethane or silicone rubber, whose elasticity could be varied down to the very low Young's moduli that are characteristic of vocal fold tissue (on the order of a few kPa).

b/ Breathing-related Studies

Impact of the glottal presence on flow regime One of the reference works interested in the *in vitro* study of the flow regime occurring in human trachea has been performed by Dekker [1961]. Using flow visualization and hot-wire anemometer techniques, he measured the critical values of airflow/waterflow rate at which laminar flow in plastic casts of human tracheae changes into turbulent flow (see Figure I.2.6). Note that the volume flow rates were applied under steady conditions (with a constant head of pressure). The measurements were performed in casts of the trachea (1) with larynx in cadaveric position, (2) without the larynx, and also (3) in models with the glottis brought into a natural respiratory position. In case (1), he found critical airflow rate of 47 $\pm$ 14 mL/s (mean $\pm$ standard deviation) for inspiration, and 122 $\pm$ 38 mL/s during expiration. Critical values of flow rates for cases (2) and (3) during inspiration are reported in Figure I.2.6. With the vocal folds placed under "normal" configuration, the inspiratory critical airflow rate was measured at 96 $\pm$ 26 mL/s. Yet, in conclusion, because the vocal folds can be varied by both voluntary and reflex motions, he argued that it is highly improbable that critical flow in the trachea has a fixed value.

Another important reference work was done by Olson et al. [1973]. In their experimental

TABLE 2. *Critical flow in ml/sec through tracheal casts during inspiration*

Cast No.	Water Flow	Air Flow*	Air Flow†	Cast No.	Water Flow	Air Flow*	Air Flow†
A. Casts without larynx				*B. Casts with open glottis*			
13	28	420	422	*17*	8.1	122	108
14	16	240	355	*18*	7.6	114	86
15	23	345	389	*19*	6.2	93	113
16	24	360	367	*20*	9.9	148	120
				21	4.0	60	55
Mean	23	341	383	Mean	7.2	107	96
SD	±5	±75	±29	SD	±2.2	±33	±26

* Calculated equivalent air flow. † Direct measurement of air flow.

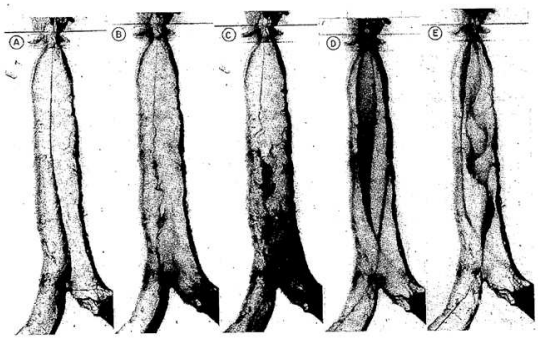

Figure I.2.6: Measurements of critical flow rate through transparent plastic casts of human tracheae for different fluid (air, water) and geometrical conditions (without larynx, with glottis included). Extracted from Dekker [1961].

study conducted on cast replicas of the human airway system (from the mouth to subsegmental bronchi) under steady flow conditions, it is reported that (i) the flow is generally laminar in the mouth for inspiratory rates below 200 mL/s; (ii) the onset of instabilities in the flow occurs at 700 to 800 mL/s in the pharynx; (iii) it occurs at 400 to 500 mL/s in the upper part of the larynx; (iv) and at 150 mL/s in the area just below the larynx. During eupnea at an inspiratory volume flow of 500 mL/s, they determined a mean Reynolds number of about 2000 in the larynx (peak value around 4000) and an average velocity varying from 5 to 7 m/sec, as shown in Figure I.2.7. Figure I.2.8 illustrates the velocity

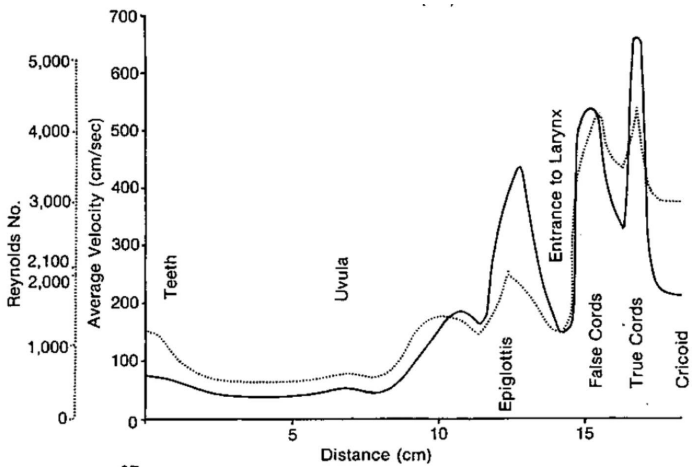

Figure I.2.7: Variations of the Reynolds number and the average airflow velocity in the upper airways during eupnea at an inspiratory volume flow of 500 mL/s. Extracted from Olson et al. [1973].

profiles measured in the larynx region for the lateral and antero-posterior planes during eupnea at 600 mL/s. Orders of magnitude of flow velocity are given, as well as main flow features, like the reversed flow pattern below each vocal fold.

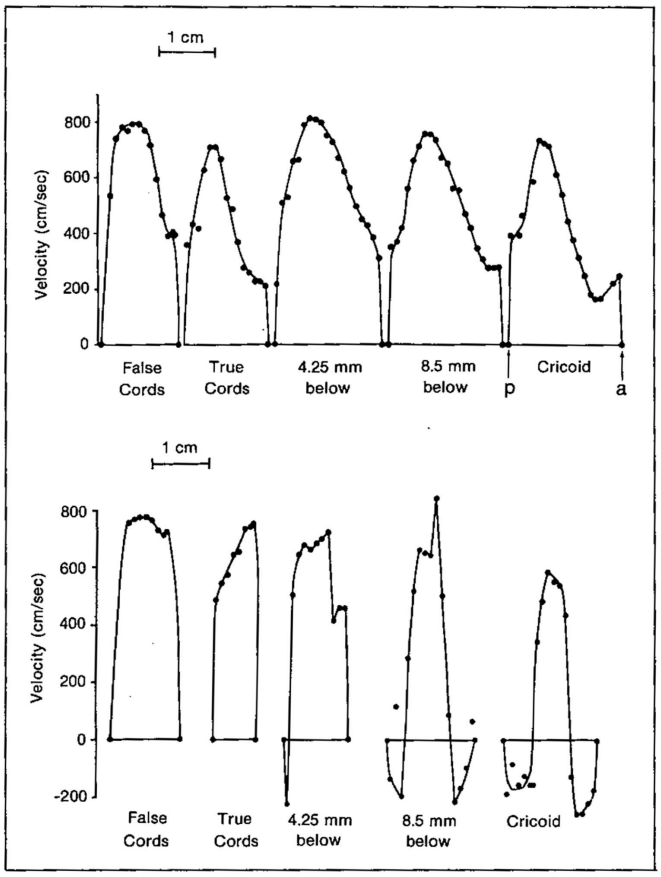

Fig 2.—Velocity profiles in the larynx for a quiet inspiration ($\dot{V} = 600$ ml/sec) through mouth. Note reversed flow below true cords in lateral plane. Right, A—P plane; inspiratory flow 600 ml/sec. Bottom, lateral plane; inspiratory flow, 600 ml/sec.

Figure I.2.8: Flow velocity profiles in the larynx during eupnea inspiration at 600mL/s (up: antero-posterior plane; bottom: lateral plane). Extracted from Olson et al. [1973].

Recently, the effects of turbulent flow conditions within the pharynx/larynx were further discussed by Shinneeb and Pollard [2012] using PIV measurements. The results showed that the flow is strongly three dimensional and is characterized by re-circulation, jet-like and sink-like mean flows. Bursting events (ejection, sweep and interaction events) were demonstrated in the epiglottal region.

Impact of the glottal geometry on the flow velocities From the anatomical observations made by Brancatisano et al. [1983] and England and Bartlett [1982], Menon et al. [1985] elaborated a model of the human central airways including a fixed glottis of parametrical aperture. Two apertures were used, corresponding to the shape and size at midinspiration and midexpiration (see Figure I.2.9). Sinusoidal airflows mimicking a tidal volume of 1500 mL and breathing frequencies of 0.25 and 1 Hz were studied using a pneumotachograph and hot-wire anemometry. Figure I.2.9 illustrates the normalized velocity profiles at peak inspiratory flow in the cross-section 1 of the model (2.5 tracheal diameters downstream

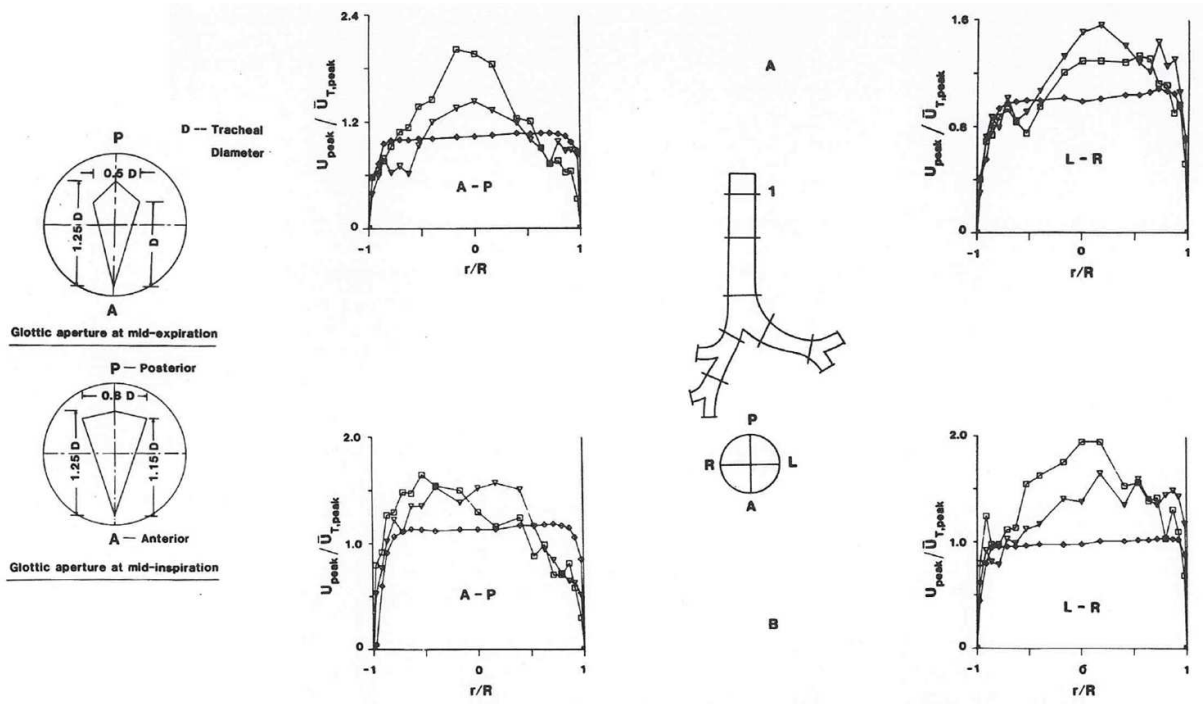

Figure I.2.9: Normalized peak inspiratory velocity profiles in the antero-posterior (panels *A-P*) and left-right (panels *L-R*) planes measured by Menon et al. [1985] in *in vitro* models of human upper airways with and without glottis (*squares*, narrow glottis aperture; *triangles*, wide glottic aperture; *diamonds*, measurements without the larynx model). **A**: tidal volume (V_t) of 1500mL and breathing frequency (f) of 0.25 Hz. **B**: V_t = 1500 mL, f = 1 Hz. Extracted from Menon et al. [1985].

from the vocal folds), in the antero-posterior (see panels *A-P*) and the left-right planes (see panels *L-R*). Comparison is made between the model without larynx, and the two models with narrow and wide glottic apertures. Without the larynx, the velocities are essentially flat, which is no more the case in the presence of the glottic aperture. The impact of glottic geometry on the velocity profiles measured in the trachea is also highlighted.

Impact of glottis on flow unsteadiness Using experimental models of the central airways without larynx included, several works have explored the assumption of quasi-steady flow behavior during breathing [Pedley, 1977; Isabey and Chang, 1981, 1982; Isabey et al., 1986]. In particular, Isabey and Chang [1981] studied the pressure-flow relationships in a cast of central airways including trachea and five generations of bronchi. Three different gas mixtures (air, HeO_2, and SF_6O_2) were employed. They found that the pressure drop is governed by the Reynolds number. Further in Isabey and Chang [1982] were discussed secondary velocity components. Secondary velocities did not exceed 18% of the mean axial velocity during inspiration and 21.5% during expiration. Afterwards, Isabey et al. [1986] measured the resistance during sinusoidal airflow oscillations (0.5 to 40 Hz) and for flow-rates up to 8 L/s. The work introduced alternative Strouhal number to explain unsteadiness in respiratory airflow. Regions of steadiness, "moderate" unsteadiness and

"dominant" unsteadiness were thereby identified.
The impact of the larynx inclusion in the models upon the quasi-steady flow properties was discussed in Menon et al. [1985]. They compared the peak oscillatory velocity profiles described in the previous section with the ones obtained in steady flow at the corresponding Reynolds number ($Re = 8830$). Figure I.2.10 Some differences in velocity magnitude

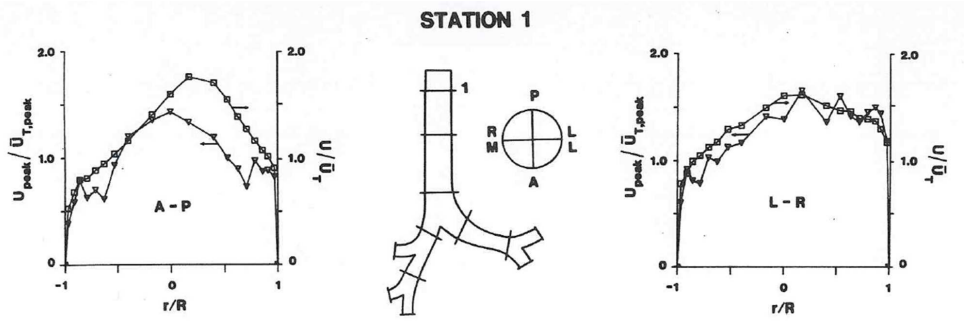

illustrates the comparison obtained on profiles at several stations of the *in vitro* model including the wide glottal aperture.

Figure I.2.10: Comparison between the peak inspiratory oscillatory velocity profiles with steady velocity profile at equivalent Reynolds number of 8830 ($V_t = 1500$ mL, $f = 1$ Hz; *squares*, steady flow; *triangles*, peak oscilatory flow). Extracted from Menon et al. [1985].

are demonstrated between steady and unsteady modes of breathing, albeit assigned to the inability to match the peak oscillatory flow exactly with the steady-flow value.

2.2.2 *In Silico* Studies

Similarly to the *in vitro* studies, there exists numerous works dedicated to the laryngeal flow from the standpoint of phonation, *i.e.*, during the vocal-fold vibrations. The fluid/structure models developed in this context are not directly usable to simulate breathing aerodynamics due to the high differences in the vocal-fold kinematics for both cases. Therefore, since the 1990s, another series of computational fluid dynamics (CFD) models has been implemented to investigate the flow field in human upper airways during breathing. A survey of the main phonation- and breathing-related *in silico* studies is summarized thereafter.

a/ Phonation-related Studies

During the last four decades, numerous theoretical and computational works have provided a detailed analysis of the glottal-jet spatio-temporal features during vocal-fold vibrations as observed in human phonation [Titze, 1994; Alipour et al., 2011]. In particular, the moving flow separation point at the glottal walls, the pulsatile glottal waveforms, flow unsteady properties, the cycle-to-cycle asymmetric deflection in the supraglottal region and the aerodynamic forces acting on the vocal-fold tissues have been extensively described. By order of complexity, the vocal-folds' dynamics were firstly simplified by

assuming either static [Scherer et al., 2001; Hofmans et al., 2003; Chisari et al., 2011], or driven mechanical rigid glottal boundaries [Barney et al., 1999; Kucinschi et al., 2006; Sciamarella and Le Quéré, 2008]. Vocal-fold flow-induced vibrations were then mimicked using low-dimensional lumped-mass models of self-sustained oscillations [Ishizaka and Flanagan, 1972; Wong et al., 1991; Pelorson et al., 1994; Steinecke and Herzel, 1995; Story and Titze, 1995; Ruty et al., 2007; Tao and Jiang, 2007; Bailly et al., 2008, 2010], or continuum-based finite-element models of deformable tissues [Berry et al., 1994; Alipour et al., 2000; Rosa et al., 2003; Decker and Thomson, 2007; Tao and Jiang, 2007; Luo et al., 2009; Zheng et al., 2011]. Similarly, the translaryngeal airflow has been largely described using variations of the simple *(un)steady* Bernoulli-based model [Ishizaka and Flanagan, 1972; Story and Titze, 1995; Ruty et al., 2007; Bailly et al., 2008]. Multiple Navier-Stokes formulations were then reported under the assumption of *quasi-steady* three-dimensional (3D) laminar incompressible flow conditions [Rosa et al., 2003], *unsteady* two-dimensional (in)compressible viscous flow-conditions [Zhang et al., 2002; Nomura and Funada, 2007; Zheng et al., 2009; Česenek et al., 2013], or even 3D *unsteady* models using direct numerical simulation [Zheng et al., 2011]. In the end, these previous works aimed to assess the acoustic correlates of each glottal-flow feature and the impact of flow/structure/acoustic interactions on voice quality. Thereby, most of physical models of the laryngeal source focused on the delay of lower and upper margins of the vocal-folds during phonation, which is not relevant in respiratory biomechanics.

b/ Breathing-related Studies

The specific influence of both laryngeal geometrical configuration and aerodynamics has been investigated in the field of breathing biomechanics [Martonen and Katz, 1993; Katz et al., 1997, 1999; Gemci et al., 2003; Brouns et al., 2007a,b; Lin et al., 2007; Xi and Longest, 2008].

Influence of Glottal Geometry Conditions *Static Glottis Conditions* - Most of the previous *in silico* studies were performed assuming static glottis conditions. Martonen and Katz [1993] performed 2D flow simulations through simplified model of larynx (including false and true vocal folds) and upper tracheobronchial airways. It was found that larynx is the key morphological factor affecting the character of air-stream and causing the laryngeal jet and re-circulation zone downstream of the vocal folds. Further, Katz and Martonen [1996] performed similar simulations using a 3D model and observed the creation of the circumferential secondary flow in the moment when the flow passes downstream of the ventricular folds and must turn to pass through the glottal aperture. Lin et al. [2007] observed curved sheet-like turbulent laryngeal jet with turbulent intensity between 10 and 20%, which leads to three times higher wall shear stress in trachea. Work concluded that the regions of high turbulence intensity are associated with Taylor-Götler-like vortices.

Regarding the effect of the glottal size and shape on the overall fluid dynamics behavior, a devoted description has been given very recently by Brouns et al. [2007b], using a 3D idealized model of the upper airways comprising a static glottis of parametrical aperture

(area of 45 or 90 mm^2). Three different laryngeal geometries with different shapes of glottal aperture - circular, elliptical and triangular were studied (see Figure I.2.11). Flow

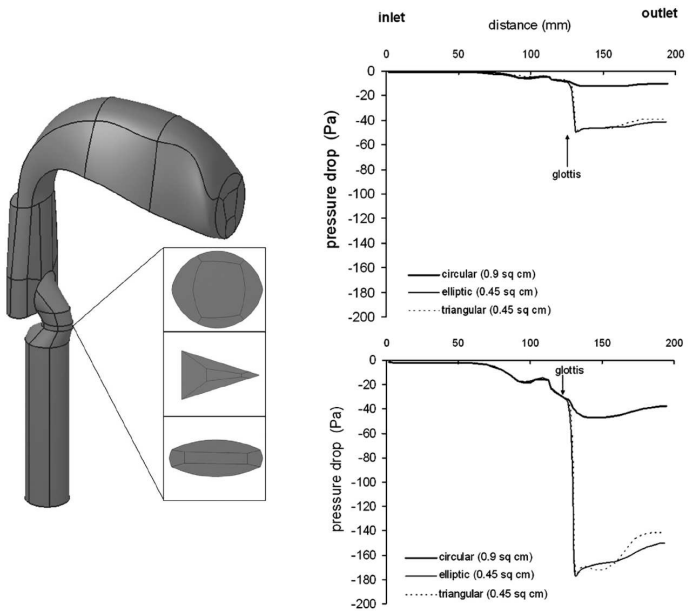

Figure I.2.11: Upper Airways geometry with different shapes of glottal aperture and resulting pressure drop variations found by Brouns et al. [2007b] (*upper panel*, steady flow at 15 L/min; *lower panel*, steady flow at 30 L/min).

rates of 15 and 30 L/min were simulated. This work shows that the interaction between the size and shape of the glottal aperture and the geometry of the mouth-throat model is crucial to the overall fluid dynamics. The predicted pressure drop along the oropharyngeal pathway is illustrated in Figure I.2.11. For the circular glottis (cross-section area of 90 mm^2), pressure drops at the glottis were predicted at 10 Pa (38 Pa) for the flow-rate of 15 L/min (30 L/min). Finally, Brouns et al. [2007b] suggested the needs for rendering more realistic geometry including moving boundaries in the glottal area.

Time-varying Glottis Conditions - To our knowledge, a single study considered an oscillatory flow simulated through driven glottal boundaries [Renotte et al., 2000], albeit in a 3D laryngeal tube isolated from the global upper airway geometry. Pseudo-time-varying glottic aperture and flow inlet conditions were set, with a peak flow rate of 0.75 L/s and oscillation frequency of 0.25 Hz. The respiratory cycle was modelled by a succession of 14 steady situations. The glottal area evolved between 66 and 112 mm^2 and the phase shift between flow rate and glottal area signal was set to 25°. Depending upon the Reynolds number, either laminar ($Re \leq 1500$) and/or turbulent ($Re > 1500$) flow equations were solved. Renotte et al. [2000] observed the jet-like behavior and a backflow region establishing in the sagittal plane at one diameter from the glottal constriction, extending over about 40 mm. Between inspiration and expiration profiles were found only minor differences.

Influence of flow properties *About the turbulence model* - Flow simulations in upper airways presented by Ball et al. [2008] showed $k-\omega$ model to be the most precise among other turbulence models. Wang et al. [2009] used on contrary $k-\epsilon$ model. Flow in the laryngeal area resulted in the jet, that impacts on the posterior trachea wall. The pressure drop was assesed at -80 Pa during inspiration and around 110 Pa during expiration (for flow rate of 6 L/min). Turbulence models were also studied by Cui and Gutheil [2011]. In the work was discussed the suitability of Large Eddy Simulation (LES). The results were compared with studies using other turbulent models and also with an experimental model. The models compared Reynolds-averaged Navier-Stokes (RANS) coupled with low Reynolds number (LRN) $k-\omega$ model used by Zhang and Kleinstreuer [2003], and LRN shear-stress transport $k-\omega$ model used by Jayaraju et al. [2007]. The results of LES model show improvement in particular in the transitional regime of the laminar-transitional-turbulent flow. The flow visualisation showed the impact of the laryngeal jet on the anterior wall of trachea, where a pair of smaller vortices is created. Location and length scale of the secondary vortices changed with the location of the laryngeal jet, which indicates that the vortices are also influenced by the laryngeal jet. Recently Elcner et al. [2013] simulated the flow in the respiratory system under steady inlet flow rate conditions (15, 30, and 60 L/min) using RANS coupled with LRN $k-\omega$ model. The laryngeal jet is discussed to impact tracheal anterior part and affect the flow in the entire trachea. Simulations were compared to experimental measurements and small differences were found in near-wall area. The study suggested that this can be influenced by chosen turbulence model.

About the unsteady properties - Two approximations are widely adopted in the numerical studies of breathing airflow and aerosol transport in upper airways: (i) a *mean constant inhalation flow rate* (typically 15, 30 and 60 L/min) is often applied at inlet conditions, considering that aerosols' inhalation only occurs for about one-half of the breathing cycle [Katz et al., 1997, 1999; Stapleton et al., 2000; Finlay, 2001; Brouns et al., 2007a,b; Jayaraju et al., 2007; Xi and Longest, 2007; Zhang and Kleinstreuer, 2011]; and (ii) *quasi-steady-state flow conditions* are frequently assumed, based on previous experimental data in the central airways showing that unsteadiness is important at the time of zero flow when exhalation stops and inhalation begins, *i.e.*, on a small portion of the tidal breathing cycle [Olson et al., 1973; Isabey et al., 1986; Finlay, 2001]. However, Jin et al. [2007] showed that the maximal inflow velocity in the upper airways is 60% higher in the unsteady respiration than in the steady mode.

2.3 Impact of the Glottis on Aerosol Transport and Deposition

2.3.1 *In vivo* Studies

A review summarizing some important *in vivo* studies related to aerosol deposition in human upper airways was published by Stahlhofen et al. [1989]. This work determined mathematical expressions of regional deposition in function of respiratory variables and particle size. A deposition of particles mostly located in the laryngeal area is already

suggested from these early works.

As mentioned in section I.1.4, a recent work was published by Fleming et al. [2011]; Conway et al. [2012], using Single Photon Emission Computed Tomography (SPECT) to describe the deposition of radionucleides in the respiratory system, in three dimensions, and in combination with X-ray computed tomography (CT) to relate deposition to lung anatomy. The results showed that the deposition in the upper airways can reach up to 40% of inhaled mass of aerosols in some cases.

2.3.2 *In vitro* Studies

In the previous experimental studies, the impact of the glottal geometry and kinematics on aerosol deposition was not extensively studied as such. A detailed review of the sparse earlier *in vitro* studies can be found in Xi and Longest [2008]. However, several works were dedicated to the measurement of total and regional deposition in idealized and patient-specific models of human upper airways (neglecting the larynx specificities). These studies were performed using either gamma scintigraphy [Grgic et al., 2004b; Heenan et al., 2004], gravimetry [Swift et al., 1992], Positron Emission Tomography (PET) [Lízal et al., 2013], fluorescence spectrometry [Cheng et al., 1999] or optical counting [Bělka et al., 2013]. Note that some works were dedicated to the characterization of particles' transport using Phase Doppler Particle Analyser (P/DPA) [Jedelský et al., 2012].

Grgic et al. [2004b] used gamma scintigraphy in several models of human upper airways, at flow rates of 30 and 90 L/min and particle diameters of $3 - 6.5\,\mu$m. They found that aerosols mostly deposit in laryngeal and upper trachea regions. The nasopharyngeal and glottal constrictions were the key morphological factors affecting downstream flow patterns and thus deposition. Using similar techniques in Heenan et al. [2004] together with PIV flow measurements, a strong connection was demonstrated between local deposition and local fluid velocity field, characterized at a constant inspiratory flow rate of 90 L/min. The authors concluded that local deposition levels correlate very strongly with local levels of velocity magnitude and flow curvature, which is consistent with an inertial impaction deposition mechanism.

Lízal et al. [2013] used PET technique in a model of the airways up to the 7^{th} generation of branching, with particle sizes of 2.5 µm and 4.3 µm and three steady flow regimes (15, 30 and 60 L/min). Highest deposition was measured in oral cavity and trachea. A moderate increase was observed for regimes with higher Stokes numbers.

2.3.3 *In Silico* Studies

A large amount of *in silico* studies has been proposed to simulate aerosol deposition in the upper airways, with varying nano- or micrometric particles, carrier gases and flow models and inlet flow conditions (*e.g.*, Stapleton et al. [2000]; Zhang and Kleinstreuer [2004]; Jin et al. [2007]; Xi and Longest [2008]; Sandeau et al. [2010]; Miyawaki et al.

[2012]; Huang et al. [2013]). In the following, only the aspects focused on the deposition of microparticles in the larynx area and on the influence of unsteady flow properties are highlighted.

About the deposition in the larynx area - The effects of the laryngeal jet on microparticle transport and deposition have been recently pointed out in Xi and Longest [2008]. In this work, two breathing conditions were studied to approximate sedentary and light activity breathing conditions. The associated mean tracheal inhalation flow rates were 15 and 30 L/min respectively (steady inhalation conditions). The glottal aperture was varied accordingly: a glottal area of 67 mm^2 was considered under sedentary conditions, while an area of 125 mm^2 was chosen under light activity conditions. The low Reynolds number $k-\omega$ flow model was selected and a Lagrangian tracking method was used to predict deposition data of particles ranging from 2.5 nm to 12 µm. The results are presented in Figure I.2.12 It is shown that inclusion of the laryngeal model increases the tracheal

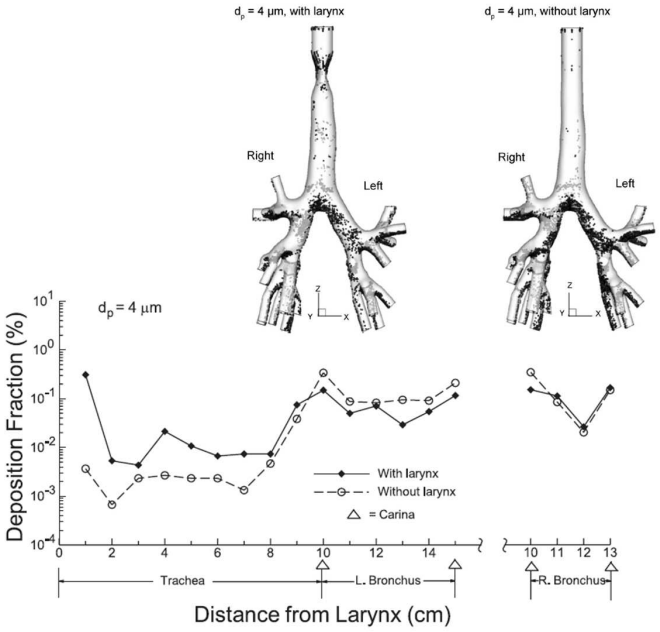

Figure I.2.12: Averaged deposition fractions of microparticles in a model with larynx and without larynx ($Q = 15$ L/min, $D_p = 4\,\mu m$), predicted per unit centimer length in the trachea. Extracted from Xi and Longest [2008].

deposition of micro-particles by factors ranging from 2 to 10.

About the influence of unsteady flow properties - A few studies have highlighted noticeable effects of transient inlet conditions and time-dependent flow calculations on aerosols local deposition [Zhang and Kleinstreuer, 2004; Grgic et al., 2006; Jin et al., 2007; Xi and Longest, 2008]. For instance, Zhang et al. [2002] showed that particle deposition efficiencies are larger for cyclic flow than for constant flow at the mean flow rate due to the enhanced particle impaction during peak flows. [Grgic et al., 2006] suggested, that higher deposition efficiencies in unsteady mode are result of higher particle velocity reached due

to the accelerating flow rate. Similarly, Jin et al. [2007] showed that about 7.5% higher deposition efficiencies of micron-size particles is found, when unsteady respiration mode is selected (see Figure I.2.13). Recently, Huang et al. [2013] simulated the flow in up-

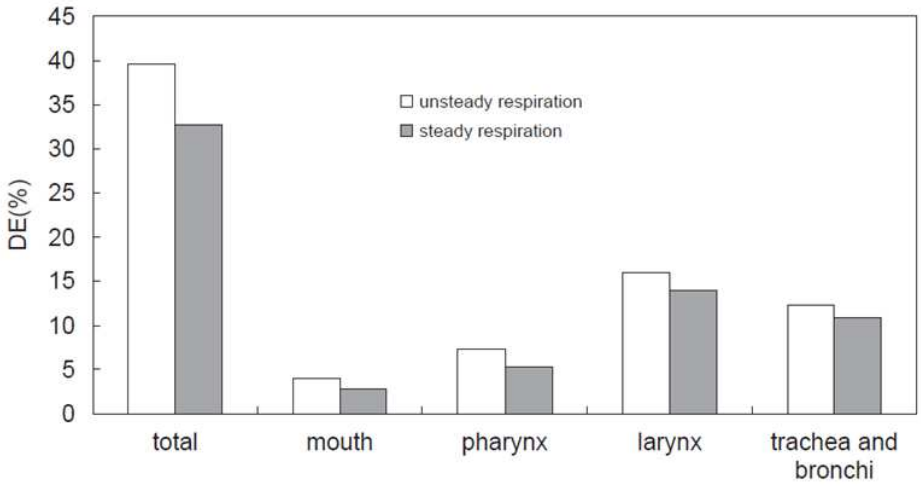

Figure I.2.13: Comparison of particle deposition efficiencies DE simulated in an upper airway model, assuming unsteady or steady respiration modes. $D_p = 5\,\mu m$, $Q = 60$ L/min, particle density of 600 kg/m^3. Extracted from Jin et al. [2007].

per airways employing a realistic breathing condition - expansion of the pleural cavity. Comparison with fixed boundary conditions showed that: "(i) the velocity profiles at the inlet are not uniform or axially symetric, but askew with high-speed flow shifted to upper wall, (ii) the pressure drop and turbulence intensity are lower, but the secondary intensity is higher, (iii) at different flow rates (30, 40.8 and 60 L/min) the secondary intensities characteristics are identical before larynx, because low turbulent fluctuations, but in trachea were observed discrepancies caused by high level turbulence intensity and different pattern of recirculation, (iv) the length of recirculation zones increases with flow rate, (v) the peaks of secondary flow intensity in the trachea are found near the flow separation and reattachment points and the peaks of turbulence intensity in the trachea seem to correspond to the separation and reattachment area".

A summary of the main results from this state-of-the-art, together with the main issues, is proposed in the next chapter.

Summary and Aims

Characterisation of Glottal Motion during Breathing

Regarding the glottal kinematics during human breathing, the current knowledge gained from previous *in vivo* studies can be summarized as follows:

- Under healthy conditions, the vocal-fold geometry is generally unsteady during a breathing cycle: the glottal area progressively increases during inspiration and narrows during expiration. The ratio of the glottal aperture measured at 50% of inspiratory duration to the same measurement at 50% of expiratory duration can vary between 1 and 3 during eupnea. The glottal widening generally precedes the onset of inspiratory flow. The opening of the vocal folds is connected with an increased activity of the posterior crico-arytenoid (abductor) muscle of the larynx. The onset of glottic widening prior to the onset of inspiration is consistent with neurophysiological observations.
- However, some sparse studies have reported that the typical time-varying glottal motion is not systematic: in some cases, the glottis can remain constantly opened whatever the breathing task.
- In the presence of airflow obstruction due to lung disease, the glottal narrowing during expiration is enhanced.
- A mean glottal cross-section area (A_g) of 90-100 mm^2 is often chosen as a reference in the literature during eupnea [Brancatisano et al., 1983]. However, it is important to note that numerous studies found an average value around 200 mm^2.
- Whereas the qualitative observations and average/peak glottal area dimensions are often provided in the previous works, the quantitative description of the glottal motion in time has been barely studied in details. In particular the glottal dynamics and its interaction with the breathing airflow rate is generally poorly described. It was investigated in few early reference studies, which yielded to controversial results however. That is why, currently this research interest is still subject of active investigations [Brouns et al., 2007a; Chen et al., 2013; Xi et al., 2014].

Therefore, the first general purpose of this thesis was to investigate the time-variations of the glottal area during breathing, together with the synchronized breathing airflow pattern. To this end, a clinical study was conducted on 20 healthy volunteers to explore

the glottal motion during several specific *slow* and *rapid breathing* tasks. The glottal area variations were investigated using laryngoscopic video recordings and synchronized airflow measurements. The methodology and the results are detailed in Part II.

Impact of Glottal Motion on Airflow & Aerosol Deposition

The impact of glottal motion on airflow and aerosol deposition in the human upper airways is often discarded from the experimental and numerical studies. The current knowledge on this point can be summarized as follows:

- Many studies have been developed to better mimic and model the vocal-fold self-sustained vibrations as observed during human phonation, in order to better understand the fluid/structure interactions taking place within the laryngeal acoustical source. However, in comparison, the studies dealing with the impact of glottal kinematics on breathing airflow and aerosol deposition are far less numerous.
- Early *in vitro* studies were mainly carried out under steady flow conditions, with a static glottis. They showed that the inspiratory critical airflow rate at the laminar-turbulent transition is around 100 mL/s; the mean Reynolds number is of about 2000 in the larynx (peak value around 4000), with an average velocity varying from 5 to 7 m/s at the glottis.
- Most of the previous *in silico* studies were performed assuming static glottis conditions. Furthermore, two approximations are widely adopted: (i) a mean constant inhalation flow rate (15 to 60 L/min) applied at inlet conditions; (ii) quasi-steady flow conditions. However, some recent studies showed that the maximal inflow velocity in the upper airways is 60% higher in unsteady respiration than in steady mode; and that about 7.5% higher deposition efficiencies of microparticles are obtained when unsteady mode is selected [Jin et al., 2007; Xi and Longest, 2008].
- Finally, to our knowledge, a single study considered an oscillatory flow simulated through a mobile glottis during breathing [Renotte et al., 2000]. However, the respiratory cycle was modelled by a succession of steady situations, and the breathing pattern was approximated by a simple sinusoidal function, as well as the glottal motion.

Therefore, the second general purpose of this thesis was to predict the effects of a dynamic glottis and realistic airflow conditions on the aerosol deposition within the upper airways using three-dimensional simulations. To this end, measured geometrical variations of the glottal area (see Part II) were used to develop a 3D dynamic model of the glottal aperture. Two-phase flow simulations were then conducted within a 3D average geometry of the upper airways, using experimental unsteady airflow conditions and dynamic glottal configurations. The methodology and the results are detailed in Part III.

Part II

Breathing Aerodynamics & Glottal Motion: In Vivo Study

Introduction

In section I.2.1 was introduced a large number of studies that extensively characterize the vocal-fold vibrations during human phonation. By contrast, however, the glottal variations during different human breathing regimes have been barely investigated so far. Despite a few reference studies [Baier et al., 1977; England and Bartlett, 1982; Brancatisano et al., 1983], the relationship between the glottal area and the inhaled airflow rate is still poorly understood.

For that reason was initiated a collaboration with the *Speech and Language Laboratory* (LPL, Aix Marseille University, CNRS, UMR 7309, Aix-en-Provence, France - A. Lagier, T. Legou, A. Giovanni) together with the ENT Department of the *La Timone Adults Hospital* (AP-HM, Marseille, France - A. Lagier, A. Giovanni). The main objective of this work was to explore and to characterize the glottal dynamics during human respiratory phase by means of an *in vivo* exploratory approach. The physiological mechanisms of the respiratory cycles were investigated using synchronized video-recording of laryngofiberscopic examination and oral airflow measurements. A quantitative characterization of the glottal motion was derived from the processing of the recorded laryngeal images. In this part, the recorded clinical database is presented as follows:

- the methodology is detailed in chapter II.3. First, preliminary experiments are described. Then, the final clinical study performed on 20 healthy volunteers and comprising 144 breathing sequences of 30s is presented.
- the chapter II.4 is divided into two sections. First section (section II.4.1) details the analysis of the clinical study, in terms of breathing aerodynamics. Second section (section II.4.2) details the analysis of the clinical study, in terms of glottal motion during breathing. Combining these anatomical observations with variations of airflow pattern of section II.4.1, the aerodynamic impact of the glottal motion is discussed as a function of breathing task and subject gender.

Note that preliminary experiments in chapter II.3 were published in Scheinherr et al. [2012] and in Scheinherr et al. [2013a]. Both description and results of the final clinical study were submitted in July 2014 to *Medical Engineering & Physics* (Scheinherr *et al.*, *Realistic Glottal Motion and Airflow Rate during Human Breathing*).

Chapter II.3

Methodology

All the recording sessions took place at the Otolaryngology Department of the *La Timone Adults Hospital*. The experimental procedure was approved by the Committee on the Protection of People (CPP) in Biomedical Research (CPP Sud Méditerranée I, n°2012-A01390-13).

3.1 Preliminary Experiments

Several preliminary measurements were performed so as to test the feasibility of the clinical study and to design the whole measurement protocol.

3.1.1 Videoscopy & Air-flowrate measurements

Two healthy female subjects - S1 (29 year-old), S2 (33 year-old), and two healthy male subjects - S3 (48 year-old), S4 (24 year-old), were involved in preliminary measurements of glottal area and airflow rate. These experiments enabled:

i. the test and validation of the measurement equipment,

ii. the development of a graphical interface to describe the breathing tasks the subject is asked to produce [NI LabWindows™/CVI],

iii. the development of a customized methodology to synchronize airflow measurement and laryngeal images acquisition [Acquisition tool - NI LabWindows™/CVI],

iv. the development of a customized methodology to process the recorded data [Matlab®],

v. preliminary CFD simulations [ANSYS® Fluent Academic Research] (see chapter III.5).

Test and validation of the measurement equipment. The measurement equipment consists of:

i. a flexible videonasofibroscope, as used in clinical routine to perform video laryngoscopy;

ii. the EVA2^{TM} system developped at the *Laboratory Speech and Language* to perform oral airflow measurements during vocal production, *i.e.*, during expiratory phase (S.Q.Lab). The EVA2^{TM} system consists in a two-grid flowmeter (pneumotachograph) characterized by a small dead space, specific linearized response for the inhaled and exhaled flow, and an accuracy of 1 cm^3/s [Ghio and Teston, 2004].

Preliminary *in vitro* experiments were conducted to calibrate the EVA2^{TM} system under unsteady flow conditions (*i.e.*, during both inspiratory and expiratory phases). To this end, a device reproducing mechanical ventilation under unsteady sinusoidal regimes was used, based on the set-up developped in Fahd [2012] for dynamic calibration of pressure sensors. The latter is equipped with a cylinder comprising a mobile piston of controllable kinematics. The displacement of the piston is driven by a numerically controlled electrical rod. This device allowed to reproduce sinusoidal flow conditions, with a controlled airflow rate varied from 200 to 500 mL/s, and a breathing period varied from 1.5 to 4s. This step showed a quantitative agreement in frequency and amplitude between the time-variations of the reference airflow rate generated by the ventilation device and the sensor EVA2^{TM}. Figure II.3.1 illustrates this quantitative agreement on four cycles of sinusoidal ventilation characterized by a period of 2.5s and a maximal airflow rate of 290 mL/s. The relative discrepancy between the airflow rate amplitudes as measured by the two devices is assessed around 1% in average over an acquisition of 30s.

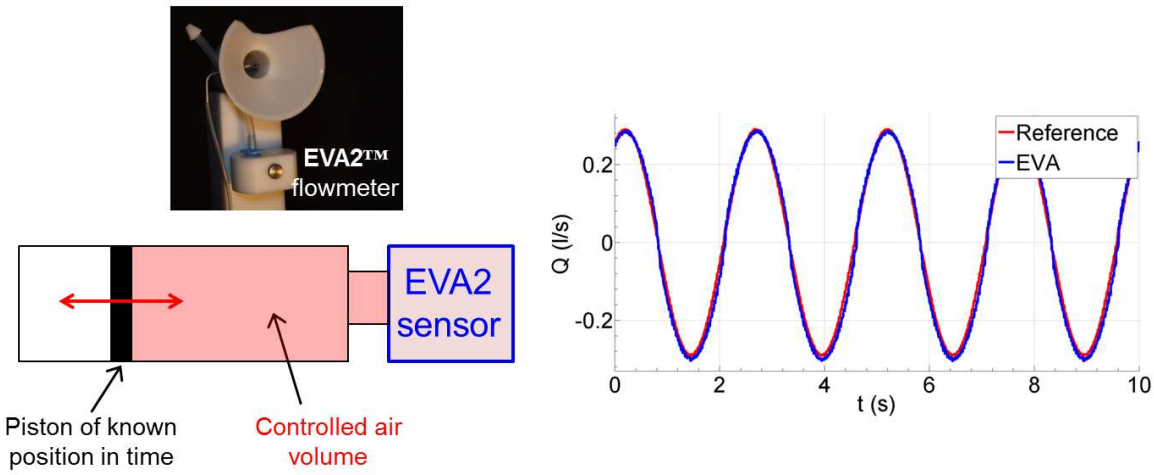

Figure II.3.1: *(left)* Schematic illustration of the device reproducing sinusoidal mechanical ventilation using a piston of known position in time. *(right)* Typical time-variations of the airflow rate Q during unsteady flow conditions, as measured by the EVA2^{TM} sensor and derived from the piston displacement (reference signal).

Development of a graphical interface to define the breathing tasks. The interface developed to describe the instructions to the subject during the preliminary experiments is displayed in Annex A - Instruction Interface for Clinical Study. In particular, this interface comprises the list of the breathing tasks to realize (see the list detailed in next section), a metronome to help the subject breathing at the target frequency when necessary, and

a progress bar to show her/him the duration of the target task.

Other aspects of the methodology (synchronization set-up, post-processing of data) are detailed in section II.3.2, in the scope of the final clinical study.

Finally, results from these preliminary experiments are valorized in chapter III.5, where they are used as boundary conditions for airflow simulations.

3.1.2 Direct Transglottal Pressure Drop Measurements

During this exploratory approach, direct measurement of subglottal air pressure was also performed on one subject (a 59-years-old male) to assess the transglottal pressure drop changes during several breathing tasks. Thanks to the EVA2^{TM} system, subglottal pressure P_{sub} and intraoral pressure P_{io} measurements were recorded simultaneously to the oral airflow signal Q (see Figure II.3.2). This step was performed in collaboration with the LPL (B. Amy de la Bretèque, T. Legou, A. Giovanni), and the Department Speech and Cognition of GIPSA-lab (Images, Speech, Signal, Automation Laboratory - Grenoble UMR 5216, N. Henrich-Bernardoni).

The subglottal pressure was directly measured via puncture of the cricothyroid membrane, while the intraoral air pressure was measured using a catheter located into the subject's mouth [Plant and Hillel, 1998]. These measurements allowed to determine the transglottal pressure drop changes during breathing. Two tasks were investigated: tidal breathing (*eupnea*) and task with an increasing breathing frequency and amplitude (panting).

Different results can be highlighted in Figure II.3.2:

- the order of magnitude of the transglottal pressure during tidal breathing is around 40 Pa. This pressure drop can reach as much as 600 Pa in specific forced breathing regimes (panting).
- a small hysteresis is measured in the (Q, ΔP) loop during tidal breathing. This hysteresis increases notably during the panting task, showing either a change in flow regime and/or a change in the anatomical configuration during the breathing cycle.

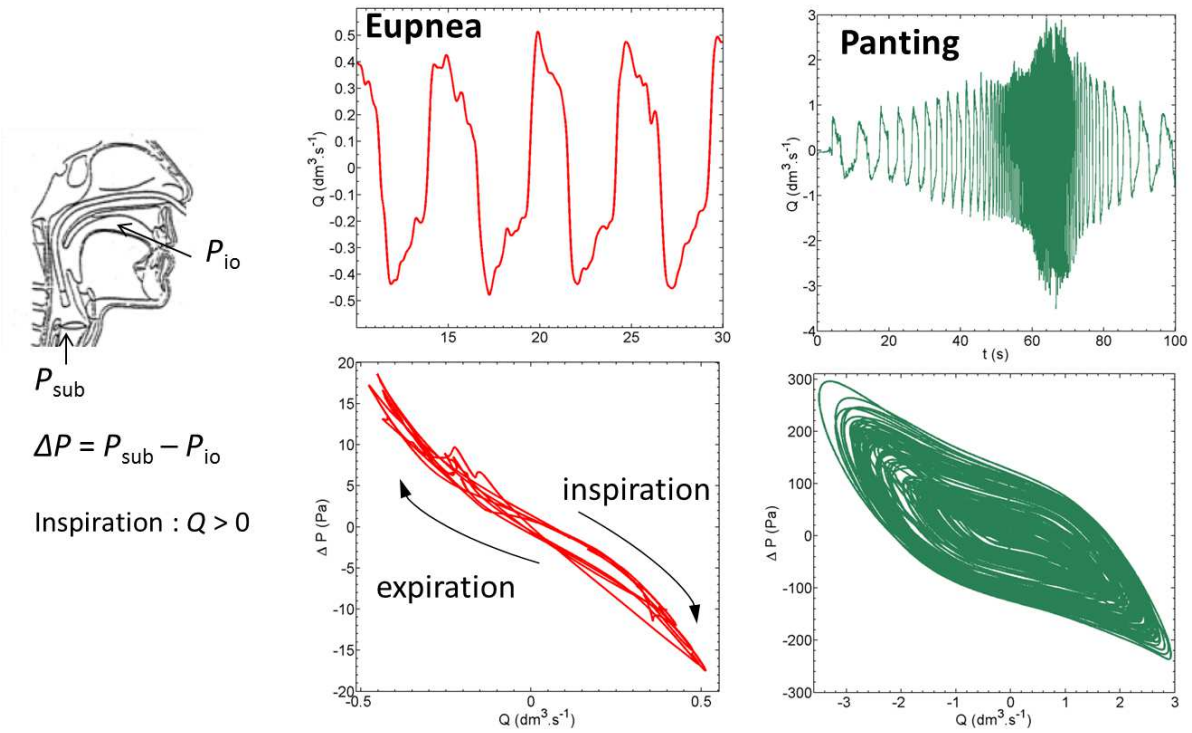

Figure II.3.2: *(left)* Schematic illustration of the subglottal pressure (P_{sub}) and intraoral pressure (P_{io}) measurements location. *(middle)* Typical variations of the airflow rate Q with time during eupnea, and transglottal pressure drop $\Delta P = P_{\text{sub}}$ - P_{io} in function of Q *(right)* Same as *(middle)* during panting.

3.2 Clinical Study

The preliminary experiments described in the previous section yielded to the elaboration of a clinical study, as a biomedical research project promoted by the Marseille Public University Hospital System (AP-HM).

3.2.1 *in vivo Recordings*

a/ Subjects

The study was conducted on 20 healthy volunteers, including 10 females (Fi, i ∈ [01..10]) and 10 males (Mi, i ∈ [01..10]) who delivered informed consent. All subjects were non-smokers, without any professional sportive activity, aging between 22 and 28 years. Volunteers with previous laryngeal or respiratory disorder were excluded from the study. Table II.3.1 lists the subjects' characteristics.

Females					Males				
Subject	Age [yr]	Weight [kg]	Height [cm]	BMI [kg/m^2]	Subject	Age [yr]	Weight [kg]	Height [cm]	BMI [kg/m^2]
F01	27	55	162	21.0	M01	25	75	188	21.2
F02	24	55	166	20.0	M02	26	76	177	24.3
F03	24	50	170	17.3	M03	24	65	170	22.5
F04	22	70	182	21.1	M04	28	63	176	20.3
F05	25	55	160	21.5	M05	25	75	180	23.1
F06	23	65	170	22.5	M06	27	65	168	23.0
F07	25	59	172	19.9	M07	26	65	178	20.5
F08	23	60	160	23.4	M08	26	63	173	21.0
F09	23	51	170	17.6	M09	26	65	180	20.1
F10	26	60	168	21.3	M10	27	70	179	21.8
Mean	**24.2**	**58**	**168**	**20.6**	**Mean**	**26**	**68.2**	**177**	**21.8**
SD	1.5	6.2	6.6	1.9	SD	1.2	5.3	5.7	1.4

Table II.3.1: General physical characteristics of the subjects. (BMI: Body Mass Index; SD: standard deviation of the data)

b/ Breathing Tasks & Database

Each subject was asked to produce eight 30s-tasks of quiet and rapid breathing, described as follows:

(A) *Slow breathing tasks - below 20 cycles/min:*

(a) $\mathbf{Eup}_{\mathrm{f}}$: task of free *eupnea*

(b) Repetition of $\mathbf{Eup}_{\mathrm{f}}$

(c) $\mathbf{Eup}_{15}$: task of *eupnea* with a controlled breathing frequency at 15 cycles/min.

(d) $\mathbf{Hyper}_{\mathrm{f}}$: task of free *hyperpnea* (deep breathing with maximal respiratory volume)

(B) *Rapid breathing tasks - above 20 cycles/min:*

(e) $\mathbf{Tachyp}_{30}$: task of *tachypnea* with a controlled breathing frequency at 30 cycles/min.

(f) $\mathbf{Tachyp}_{60}$: task of *tachypnea* with a controlled breathing frequency at 60 cycles/min.

(g) $\mathbf{Tachyp}_{90}$: task of *tachypnea* with a controlled breathing frequency at 90 cycles/min.

(C) *Specific inhalation task:*

(h) **Aerosol**: task mimicking the breathing gesture typically performed when using a dry powder inhaler (or a metered dose inhaler) to deliver medication (quick and deep inspiration followed by slow expiration).

For all tasks, the subject's nose was closed to ensure that the subject breathed only through her/his mouth. Note that both tasks of free *eupnea* ($\mathbf{Eup}_{\mathrm{f}}$) were intentionally presented to the subject as a phase of acquisition trials. This aimed to prepare her/him before the recording of the controlled tasks, which were described as the target of the

study. Thereby, by reducing the effect of a motor control focused on the breathing, tasks (A)a and (A)b were acquired in the condition closer to spontaneous breathing. By contrast, the other tasks correspond to cases of controlled breathing, for which the subjects were asked to synchronize their breathing frequency with a metronome projected on an instruction computer. These tasks intended to explore the extent of glottal motion and breathing capacity in specific respiratory contexts. In the end, 18 volunteers only (9 females and 9 males) successfully performed the entire protocol, thus yielding to a database comprising 144 sequences of 30s.

c/ Measurements

All measurements were done in the seated posture. The measurement set-up is displayed on Figure II.3.3. The glottis was observed using a flexible nasofiberscope equipped with a

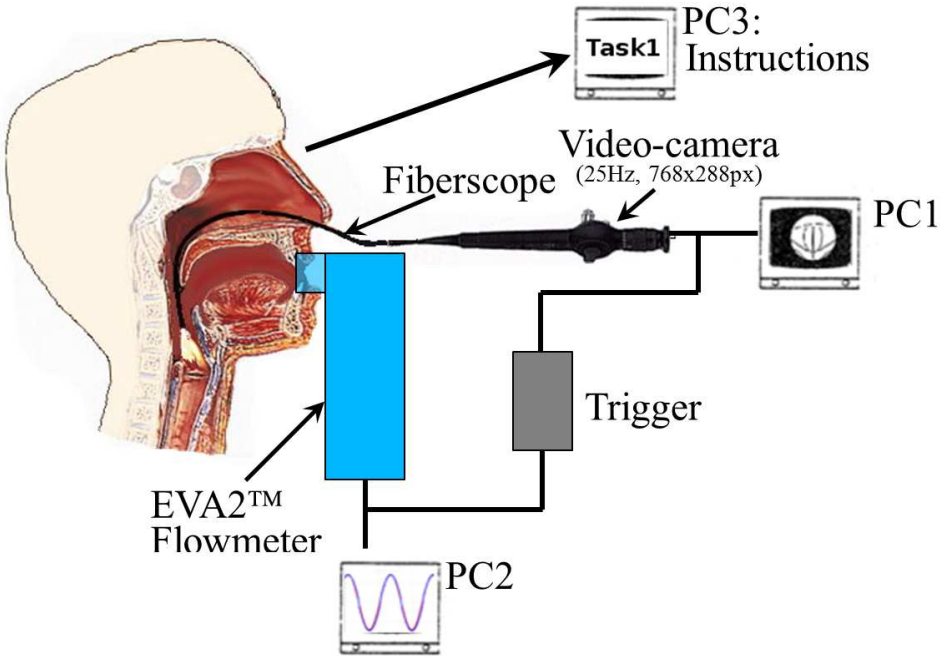

Figure II.3.3: Setup of the measurement (image of nasal endoscopy adapted from Akerlund et al. [2014]).

PAL camera (Storz endovision XL 202800) and a continuous cold light source. Laryngeal images were captured at a frequency of 25 frames/s with a resolution of 768×288 pixels. The airflow rate was simultaneously registered by means of a pneumotachograph placed at the mouth, the EVA2™ system (see section II.3.1), that enables flow rate signal measurements with the sampling frequency of 6250 Hz. A trigger generated by an acquisition tool developed in NI LabWindows™/CVI (National Instruments Corporation, USA) was used to synchronize the recordings of laryngeal images and flow rate signal. Note that for several subjects (7 females and 6 males), a local anesthetic (Lidocaine Aguettant 5%) was

sprayed in the naris before the fiberscope introduction, so as to provide a better comfort during the invasive examination. Ambient temperature T_a was also measured.

3.2.2 Data Processing

All data were processed so that any point in the upper airways is located by the (x, y, and z) coordinates as introduced in Figure II.3.4.

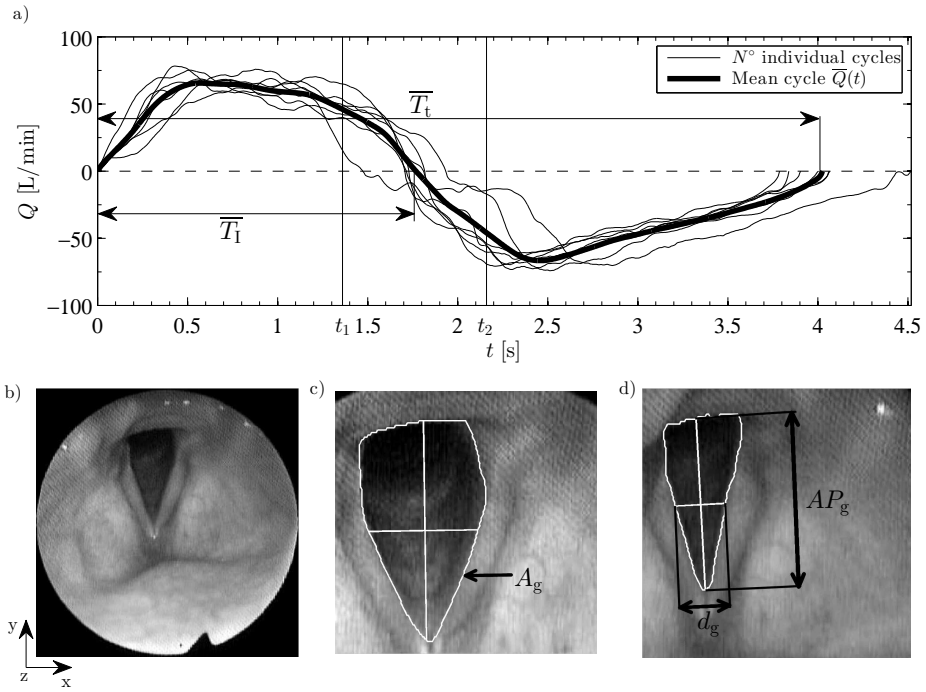

Figure II.3.4: *(a)* Superposed individual breathing cycles $Q(t)$ (subject M01, task Eup_{15}) and resulting mean breathing cycle $\overline{Q}$ in function of time t [s]. *(b)* Example of laryngoscopic image with detected glottal area A_g, antero-posterior diameter AP_g and glottal width d_g at the time of maximum glottal opening t_1 *(c)*, and at the time of minimum glottal opening t_2 *(d)*.

a/ Airflow-rate

Within each recorded 30 seconds sequence, every respiratory cycle was detected on the airflow signal, Q, using a zero-tracking method. Conventionally, positive and negative flow rate values correspond to inspiration and expiration, respectively. A so-called BTPS (Body Temperature, Pressure, Water vapor Saturated) correction factor C_C was applied to convert the flow measured at the ambient conditions to the thermodynamic conditions expected within the extrathoracic region [Hankinson and Viola, 1983; Juroszek, 2006].

For each sequence, the Q-zero axis was updated so that

$$\overline{V}_{\mathrm{E}} = C_{\mathrm{C}}\overline{V}_{\mathrm{I}}, \tag{II.3.1}$$

where $\overline{V}_{\mathrm{E}}$ [L] is the average expired volume, $\overline{V}_{\mathrm{I}}$ [L] is the average inspired volume and the conversion coefficient C_{C} [-] is defined by Juroszek [2006]:

$$C_{\mathrm{C}} = \frac{310}{T_{\mathrm{a}}}\frac{P_{\mathrm{a}} - P_{\mathrm{ws}}}{P_{\mathrm{a}} - 6.26}, \tag{II.3.2}$$

where pressure P_{ws} is the saturation pressure of water vapor at ambient temperature T_{a} [K], and ambient pressure P_{a} [kPa]. Coefficient C_{C} was quasi-constant over the whole database, equal to 1.07 (see Table II.3.2, column #7). Each corrected sequence was averaged into one mean flow rate

$$\overline{Q}(t) = \frac{1}{\mathrm{N}^{\circ} - 1}\sum_{\mathrm{j}=0}^{\mathrm{N}^{\circ}} Q\left(t + \mathrm{j}\overline{T}_{\mathrm{t}}\right), \tag{II.3.3}$$

where time $\overline{T}_{\mathrm{t}}$ [s] (see Table II.3.2, column #2) is the average period of N° cycles (see Table II.3.2, column #8). Number of cycles N° stands for the total number of breathing cycles of all subjects within the breathing task and gender group. An illustrative example is displayed on panel *(a)* in Figure II.3.4.

b/ Glottal Motion Detection

This procedure was limited to the analysis of two major tasks, $\mathbf{Eup}_{15}$ and $\mathbf{Tachyp}_{30}$, altogether representing *slow* and *rapid breathing* tasks, respectively. At first, breathing cycles with hidden glottis aperture (by the epiglottis or the arytenoid cartilages) were removed from the video processing. Finally, about 126 (252) respiratory cycles out of 149 (291) were associated to task $\mathbf{Eup}_{15}$ ($\mathbf{Tachyp}_{30}$ respectively). For these retained sequences, the glottal motion was extracted from every laryngoscopic image k taken at the shot-instant (t_{k}) as follows:

i. Correction of the x- and y-motions of the fiberscope and focus on a region of interest (ROI) using a cross-correlation technique. Initially, on the first image the ROI is chosen by hand. When proceeding next image, the cross-correlation coefficient of the precedent ROI is calculated at all possible positions in actual image. The coordinates with the highest cross-correlation coefficient value are then chosen for new ROI.

ii. Smoothing of the resized image using a Gaussian bandpass filtering [Iheme, 2011]. Gaussian bandpass filter is a frequency filtering, which is based on Fourier Transform. A bandpass attenuates very high and very low frequencies, but retains a middle range of frequencies. The advantage of the Gaussian filter is that when Gaussian is transformed between the frequency and spatial domains, it remains Gaussian. Therefore it does not incur the ringing effect in the spatial domain of the filtered image as can be significant in case of Ideal bandpass filter or Butterworth bandpass

Task	$\overline{T}_t$ [s]		$\overline{T}_t/\overline{T}_I$ [-]		$\overline{PIF}$ [L/min]		$\overline{PIF}/\overline{PEF}$ [-]	$\overline{V}_I$ [L]		C_C [-]	N°
	mean SD	range	**mean** SD	range	**mean** SD	range	**mean** SD	**mean** SD	range	**mean** SD	sum
Males											
Eup$_f$	**2.96** 0.78	1.5 - 5.8	**2.10** 0.16	1.43 - 3.45	**42.7** 11.7	11.5 - 84.8	**0.88** 0.19	**0.66** 0.15	0.12 - 1.42	**1.08** 0.05	256
Eup$_{15}$	**3.99** 0.03	3.7 - 4.5	**2.26** 0.21	1.82 - 3.04	**49.3** 14.2	30.8 - 86.6	**1.11** 0.17	**0.98** 0.34	0.52 - 2.11	**1.07** 0.01	68
Tachyp$_{30}$	**2.00** 0.01	1.8 - 2.4	**2.13** 0.16	1.69 - 2.55	**72.4** 28.0	37.6 - 167.6	**0.98** 0.16	**0.81** 0.44	0.42 - 1.99	**1.07** 0.01	145
Tachyp$_{60}$	**1.02** 0.06	0.8 - 1.3	**2.10** 0.13	1.72 - 2.99	**93.2** 51.1	49.3 - 271.5	**1.02** 0.15	**0.55** 0.32	0.20 - 1.66	**1.07** 0.01	327
Tachyp$_{90}$	**0.75** 0.02	0.6 - 0.9	**2.11** 0.18	1.70 - 3.02	**102.6** 63.8	45.9 - 343.8	**1.02** 0.16	**0.45** 0.29	0.18 - 1.47	**1.07** 0.01	393
Hyper$_f$	**7.39** 2.50	3.5 - 12	**2.20** 0.19	1.73 - 2.67	**125.7** 62.0	56.1 - 329.4	**1.11** 0.30	**3.82** 1.44	2.38 - 8.90	**1.07** 0.01	38
Aerosol	**3.29** 1.15	1.4 - 5.8	**3.55** 0.92	2.09 - 6.82	**263.1** 126.3	118.5 - 586.7	**3.58** 1.09	**1.83** 0.72	1.19 - 3.96	**1.07** 0.01	38
Females											
Eup$_f$	**4.00** 1.04	2.2 - 3.5	**2.36** 0.22	1.56 - 2.36	**32.2** 7.2	15.5 - 32.0	**1.12** 0.17	**0.64** 0.18	0.29 - 0.56	**1.07** 0.02	217
Eup$_{15}$	**3.99** 0.03	3.6 - 4.1	**2.21** 0.10	1.94 - 2.15	**42.9** 8.4	23.4 - 35.5	**1.06** 0.09	**0.94** 0.23	0.38 - 0.71	**1.07** 0.02	81
Tachyp$_{30}$	**1.99** 0.00	1.8 - 2.1	**2.12** 0.12	1.81 - 2.55	**50.9** 9.1	30.0 - 75.8	**0.99** 0.11	**0.61** 0.13	0.27 - 0.98	**1.07** 0.02	146
Tachyp$_{60}$	**1.00** 0.00	0.8 - 1.2	**2.10** 0.11	1.59 - 2.84	**60.0** 13.2	31.0 - 97.9	**1.04** 0.12	**0.36** 0.08	0.14 - 0.64	**1.08** 0.02	332
Tachyp$_{90}$	**0.73** 0.04	0.4 - 1.1	**2.10** 0.15	1.63 - 3.55	**59.9** 15.4	33.8 - 99.2	**1.03** 0.16	**0.26** 0.08	0.11 - 0.60	**1.07** 0.01	476
Hyper$_f$	**8.00** 2.53	5.1 - 13.4	**2.32** 0.19	1.80 - 2.77	**75.3** 22.2	46.4 - 112.6	**1.11** 0.09	**2.54** 0.57	1.35 - 3.70	**1.07** 0.01	43
Aerosol	**3.19** 1.05	1.9 - 5.5	**4.74** 1.92	2.49 - 13.04	**161.6** 35.9	89.3 - 252.6	**3.10** 0.92	**1.12** 0.24	0.57 - 1.84	**1.07** 0.01	46

Table II.3.2: Measured airflow rate parameters in function of gender and breathing task. Rows are highlighted for tasks further used for the glottal motion analysis.

filter. On Figure II.3.5 can be seen subsequently the original image (Figure II.3.5a), its Fourier spectrum (Figure II.3.5b), the image of frequency domain filter function (Figure II.3.5c) and the filtered image (Figure II.3.5d).

iii. Detection of the vocal-fold contours applying a geometric active contours function proposed by Caselles et al. [1997]. This algorithm is an edge-based active contour method, using the image gradients to identify object boundaries. This model requires to choose an initial contour before any automatic computation (the initial position and convergence time of the method being closely linked). Therefore, for each image processing of a recorded 30s-sequence, a first approximative contour of the vocal-folds was drawn by hand on the laryngeal images acquired during one single breathing cycle (see yellow curve in Figure II.3.6 for instance). On each image, these initial curves were then automatically driven to regions with highest gradient as illustrated in Figure II.3.6, where the red lines show some contours typically detected during

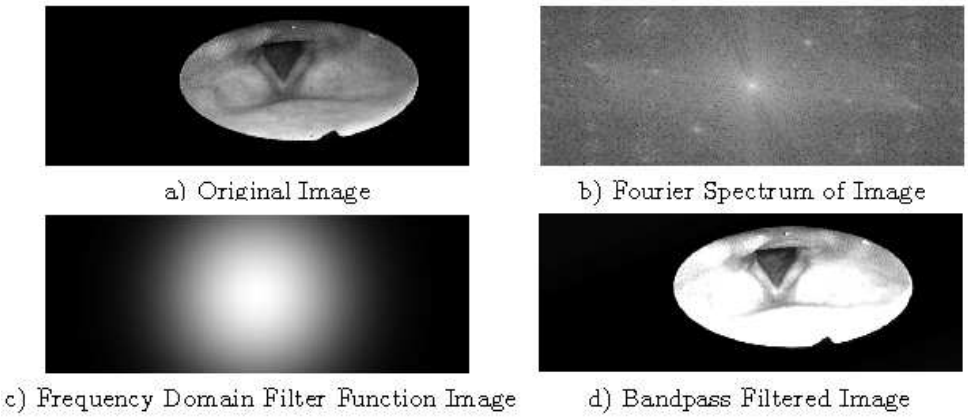

Figure II.3.5: Example of filtering function using Gaussian bandpass filter.

the technique's convergence. The final contour, after the algorithm's convergence, is displayed in Figure II.3.4c. This final contour was chosen as initialization to process the end of the sequence. In the end, the glottal area $A_g^{px}(t_k)$ was extracted from this contour dectection in function of time t_k, and assessed in px^2 .

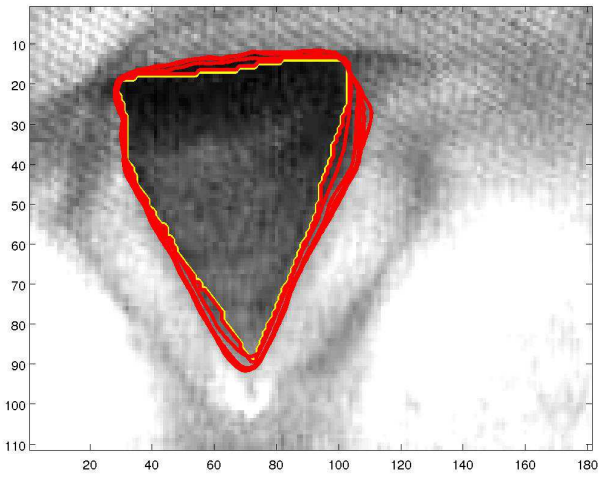

Figure II.3.6: *Example of geometric active contours function* [Caselles et al., 1997]. Image [px] of glottal area with detected yellow curve representing the initial contour and the red curves representing the active contours function.

iv. Determination of the glottal antero-posterior diameter $AP_g^{px}(t_k)$ (see Figure II.3.4d) at each shot-instant t_k in pixels: at first, 2 points were detected on left and right vocal-fold contour to identify the left and right glottal border lines. From the intersection of those border lines, a centerline was derived. At last, the distance AP_g^{px} was defined by the 2 cross points of the centerline with the vocal fold contour, and assessed in pixels.

v. Determination of the glottal width $d_g^{px}(t_k)$ at each shot-instant t_k in pixels: this distance was determined by a perpendicular line to AP_g at its mid-level (see Figure II.3.4d).

vi. Correction of possible vertical movement of the larynx and z-motion of the fiberscope by assuming the glottal antero-posterior diameter as a geometrical invariant during breathing [Higenbottam, 1980], labelled AP_g^o. Thereby, the distance AP_g^{px} assessed in pixels after step iv) is updated to sastisfy this condition.

vii. Finally, conversion of the measured data from pixels to millimeters, assuming $AP_g^o =$ 22.1 mm for males and 17.6 mm for females [Eckel and Sittel, 1995]. The conversion of glottal area is done using equation:

$$A_g(t_k) = A_g^{px}(t_k) \left(\frac{AP_g^o}{AP_g^{px}(t_k)} \right)^2 . \tag{II.3.4}$$

c/ Methodology Accuracy

The measurement of the distance between the camera extremity and the glottal plane would enable direct conversion from pixels to millimeters. However, touching the glottal plane was not allowed by the protocol as it could cause laryngospasm. That is why we chose the hypothesis of AP_g as a geometrical invariant [Higenbottam, 1980], as an alternative to convert the pixels measurements. This approach has been previously applied by several authors [Brancatisano et al., 1983; Hurbis and Schild, 1991; Beaty et al., 1999], and it seemed a reasonable assumption during our experiment, as the AP_g borders were relatively fixed. In the future, this problem could be overcome using other endoscope designs, like used by Kobler et al. [2006], where a grid of light projected from the endoscope makes it possible to determine the distance between camera optics and the observed tissue.

The accuracy of the protocol was tested by recording a printed glottal image of known area A_g =930 mm^2 and distance AP_g^o = 47 mm. During the recording, several motions of the camera were applied along x-, y- and z-directions, so as to mimic the possible motions of the fiberscope during the laryngoscopy. Figure II.3.7 shows two curves derived from the image processing of these recordings, following the steps described in previous section: the green curve (with crosses) shows the detected area $A_g^{px}(t)$ in px^2, before application of step vi); the other one shows the deduced area $A_g(t)$ in mm^2, according to Equation II.3.4 (red curve with triangles). From this latter case, the time-averaged value of $A_g(t)$ could be calculated and assessed at: 972 mm^2. Therefore, the average error of the detection procedure was found around 4.5%. This procedure was repeated on several glottal images of the database. The error of the detection depended on the recorded laryngoscopic image quality (*e.g.*, variable light contrast). In the end, the maximal error reached by the detection procedure was assessed at 10%.

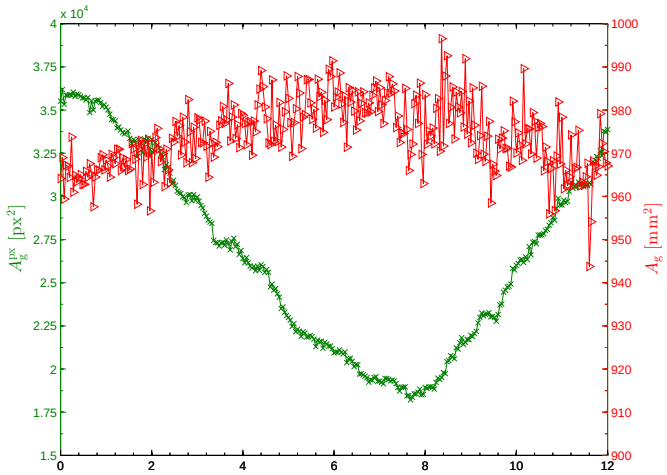

Figure II.3.7: Evaluation of the detection procedure. The green curve with crosses represents the variations of the detected area $A_g^{px}(t)$ in px^2. The red curve with triangles represents the converted values in mm^2.

Chapter II.4

Results

In the followings, if X is a function of time t, $X_{\max}$ refers to the maximum value of X over duration t.

4.1 Breathing Aerodynamics

For each task and subject gender of the database, the previous Table II.3.2 summarizes the measured primary respiratory variables: mean period length $\overline{T}_{\mathrm{t}}$ [s] (see Figure II.3.4), mean Peak Inspiratory Flow $\overline{PIF}$ [L/min] and mean inspired volume $\overline{V}_{\mathrm{I}}$ [L]. Furthermore, Table II.3.2 reports the derived variables $\overline{T}_{\mathrm{t}}/\overline{T}_{\mathrm{I}}$ ($\overline{T}_{\mathrm{I}}$ [s] is the mean inspiration period, see Figure II.3.4a) and $\overline{PIF}/\overline{PEF}$ ($\overline{PEF}$ [L/min] is the mean Peak Expiratory Flow), and the BTPS correction factor, C_{C}. All variables are averaged over the number of processed breathing cycles, N°.

Figure II.4.1 and Figure II.4.2 present the corresponding normalized mean flow-rates $\overline{Q}/\overline{PIF}$ as a function of ωt [rad], where ω is the pulsation of the average cycle defined as $\omega = 2\pi/\overline{T}_{\mathrm{t}}$. The flow rates obtained for the *slow breathing* tasks (A)a to (A)d (see Figure II.4.1a and Figure II.4.1c for males and females respectively), and *rapid breathing* tasks (B)e to (B)g (see Figure II.4.1b and Figure II.4.1d for males and females respectively) are displayed. The flow rate obtained for the specific inhalation task (C)h is plotted separately in Figure II.4.2.

4.1.1 General Airflow Features

For each case, the measured airflow pattern was confronted to the sinusoidal evolution $sin(\omega t)$, commonly used as an idealized breathing pattern [Renotte et al., 2000; Jin et al., 2007; Jedelský et al., 2012]. For *slow* and *rapid breathing* tasks, Figure II.4.1 shows that the quasi-sinusoidal approximation can be *a priori* usable as a whole. Yet, several discrepancies can be highlighted. First, the Euclidean distance between measurements and this harmonic signal (noted ε_{k} [−] at instant t_{k}) is smaller for male than female subjects

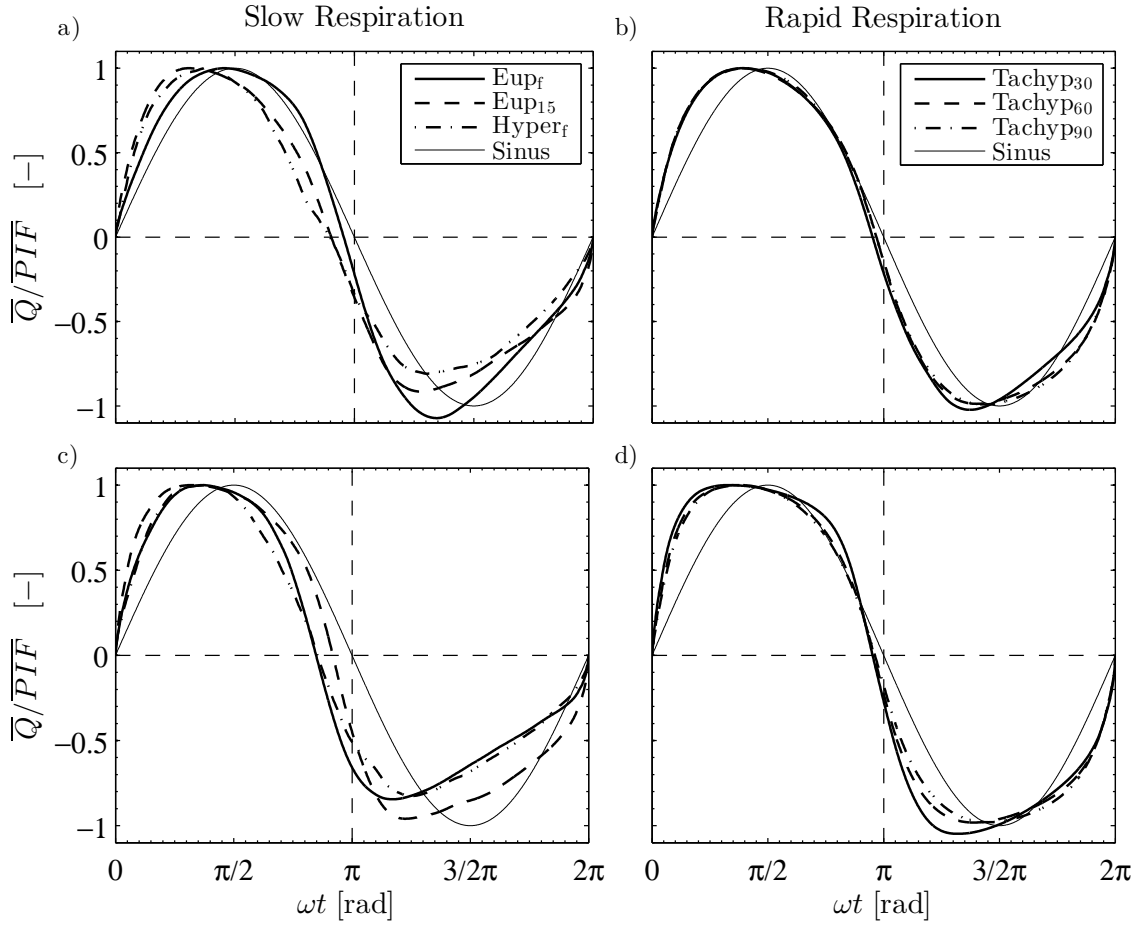

Figure II.4.1: Normalized mean flow rates $\overline{Q}/\overline{PIF}$ as function of ωt [rad] for *slow breathing* tasks (**Eup**$_f$, **Eup**$_{15}$, **Hyper**$_f$) (Panels *(a)* and *(c)* for males and females, respectively) and *rapid breathing* tasks (**Tachyp**$_{30}$, **Tachyp**$_{60}$, **Tachyp**$_{90}$) (Panels *(b)* and *(d)* for males and females, respectively). For comparison a sinus curve is added.

($\varepsilon = 5.45$ versus 6.89, mean value over breathing cycle). Furthermore, the approximation is closer to measurements during inspiration ($\varepsilon = 5.04$) than during expiration phase ($\varepsilon = 7.31$). Note that smallest distances ε_k were found during inspiratory phases of tasks **Eup**$_f$, **Tachyp**$_{30}$, **Tachyp**$_{60}$ and **Tachyp**$_{90}$ ($\varepsilon \approx 3.88$), whereas largest ε_k were found for the **Aerosol** task (9.09 and 17.15 for inspiration and expiration, respectively). Now, whatever the task, a phase difference in maximal flow rate occurrences has been measured between sinusoid and realistic patterns. We found a phase angle smaller for male subjects than female (27.1° in comparison with 36.0°), and smaller for inspiration than for expiration (26.8° in comparison with 36.3°). Over the whole database, the smallest phase difference is found for task **Eup**$_f$ (8.0° for males, inspiration). Considering males and females together, over the whole cycle, a phase difference around 21.1° was measured for tasks **Eup**$_f$, **Tachyp**$_{30}$, **Tachyp**$_{60}$, **Tachyp**$_{90}$, and **Hyper**$_f$, and around 39.3° for **Eup**$_{15}$ task. At last, for both genders, the phase difference for **Aerosol** task reaches the highest

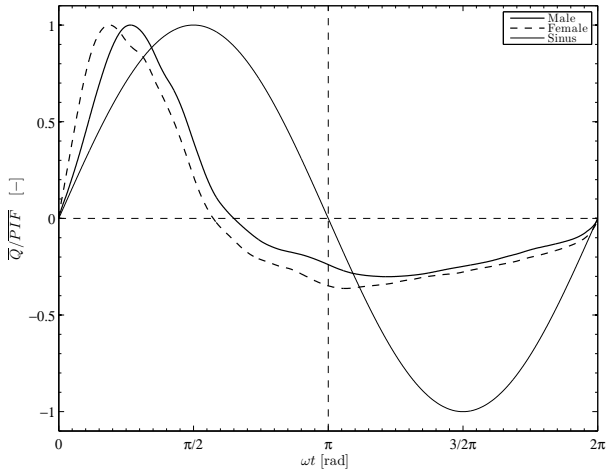

Figure II.4.2: Normalized mean flow rates $\overline{Q}/\overline{PIF}$ as function of ωt [rad] for the *specific inhalation* task **Aerosol**, for males and females. For comparison a sinus curve is added.

values (up to 79°) and thus the sinusoidal hypothesis is no more valuable in case of *specific inhalation* task (Figure II.4.2).

4.1.2 Breathing frequency

From $\overline{T}_{\mathrm{t}}$ in Table II.3.2 can be deduced that spontaneous slow breathing (**Eup**$_{\mathrm{f}}$) was achieved at a mean frequency of 20 cycles/min for males and 15 cycles/min for females. The measured frequencies of tasks **Eup**$_{15}$, **Tachyp**$_{30}$, and **Tachyp**$_{60}$ correspond to the target values, which validates the protocol for this range of breathing rates. Note that the target value chosen for task **Tachyp**$_{90}$ (90 cycles/min) was too high for most of the subjects, who worked out with a breathing frequency around 80 cycles/min instead. All the tasks were performed so that in average $\overline{T}_{\mathrm{t}}/\overline{T}_{\mathrm{I}} > 2$, thereby yielding to an inspiratory duration shorter than the expiratory one, which is in agreement with previous studies made on healthy subjects [Cain and Otis, 1949; Benchetrit, 2000]. In particular, Proctor and Hardy [1949] found a ratio $\overline{T}_{\mathrm{t}}/\overline{T}_{\mathrm{I}}$ in the range 1.57 - 2.9 during *quiet breathing* (including patients with pulmonary disease), versus 1.43 - 3.45 in our case (mean value 2.10 and 2.36, for male and female groups, respectively).

4.1.3 Breathing amplitude

Values of the flow rate maximal amplitudes $\overline{PIF}$ are very different inter-tasks and inter-subjects, as detailed in Table II.3.2. Over the whole database, the amplitudes are 30% higher for male than for female subjects. During spontaneous breathing, the typical peak values ranged between 29 L/min and 68 L/min, with a mean value of 43 L/min for males, and 32 L/min for females. These results are in line with previous studies (see range of values between 13 L/min and 78 L/min in Proctor and Hardy [1949]).

4.2 Glottal motion during breathing

Table II.4.1 summarizes the primary and derived parameters of glottal dimensions measured during *slow breathing* (**Eup**$_{15}$) and *rapid breathing* (**Tachyp**$_{30}$). The primary variables are $\overline{A}_g$, $\overline{A}_g^I$ and $\overline{PIA}_g$, where $\overline{A}_g$ is the mean glottal area obtained over the average cycle $\overline{Q}$, $\overline{A}_g^I$ is the mean glottal area obtained during inspiration (resp. $\overline{A}_g^E$ during expiration), and $\overline{PIA}_g$ is the Peak Inspiratory Area of glottis (resp. $\overline{PEA}_g$ is the peak expiratory value). The derived variables $\overline{A}_g^I/\overline{A}_g^E$ (resp. $\overline{PIA}_g/\overline{PEA}_g$) represent the ratio of the mean (resp. peak) $\overline{A}_g$ amplitude during inspiratory and expiratory phases.

The variations of $\overline{A}_g$ in function of $\overline{Q}$ for all subjects are shown in Figure II.4.3 and Figure II.4.4, for *slow* and *rapid breathing* respectively. Please note that values in Table II.4.1 are derived from average cycles represented on Figure II.4.3 and Figure II.4.4. Therefore, first an average cycle from N° individual cycles of each group is characterized and after its mean parameters are noted.

Slow Breathing **- Eup**$_{15}$												
Group	$\overline{A}_g$ [mm^2]	$\overline{A}_g^I$ [mm^2]		$\overline{PIA}_g$ [mm^2]		$\overline{A}_g^I/\overline{A}_g^E$ [-]		$\overline{PIA}_g/\overline{PEA}_g$ [-]	N°
	mean SD	**mean** SD	range	**mean** SD	range	**mean** SD	range	**mean** SD	sum
M - 1st group	**187.15** 4.5	**190.57** 9.2	184.8 - 197.9	**193.57** 15.1	200.0 - 221.4	**1.03** 0.05	1.01 - 1.08	**1.08** 0.07	14
F - 1st group	**185.70** 27.3	**186.55** 29.5	149.7 - 241.1	**189.10** 33.8	158.9 - 362.4	**1.01** 0.03	0.96 - 1.04	**1.03** 0.05	47
M - 2nd group	**198.74** 48.0	**213.90** 49.3	154.4 - 299.4	**224.20** 58.7	194.3 - 348.0	**1.15** 0.09	1.00 - 1.24	**1.26** 0.30	45
F - 2nd group	**157.95** 13.4	**182.56** 26.3	156.9 - 209.6	**190.26** 32.5	181.3 - 246.2	**1.33** 0.24	1.20 - 1.61	**1.46** 0.35	20
M - all	**196.14** 41.9	**209.01** 44.0	154.4 - 299.4	**217.32** 53.8	194.3 - 348.0	**1.12** 0.10	1.00 - 1.24	**1.22** 0.31	59
F - all	**177.37** 26.7	**185.31** 27.2	149.7 - 241.1	**189.21** 31.6	164.5 - 274.5	**1.08** 0.20	0.96 - 1.61	**1.12** 0.32	67
Rapid Breathing **- Tachyp**$_{30}$									
M - 1st group	**208.96** 5.7	**210.89** 9.5	200.0 - 216.7	**213.68** 10.0	222.1 - 241.1	**1.02** 0.04	0.97 - 1.05	**1.07** 0.05	41
F - 1st group	**178.81** 13.7	**179.41** 12.5	161.9 - 195.9	**180.68** 17.6	176.5 - 230.1	**1.00** 0.04	0.94 - 1.05	**1.02** 0,05	98
M - 2nd group	**214.31** 5.7	**227.24** 9.5	174.7 - 293.6	**235.73** 10.0	201.7 - 318.7	**1.11** 0.04	1.01 - 1.25	**1.24** 0.05	85
F - 2nd group	**174.78** 57.1	**188.60** 46.7	157.2 - 223.2	**196.43** 53.7	175.7 - 251.6	**1.17** 0.18	1.08 - 1.34	**1.39** 0.08	28
M - all	**212.53** 38.9	**221.07** 41.5	174.7 - 293.6	**227.81** 43.5	201.7 - 318.7	**1.08** 0.09	0.97 - 1.25	**1.17** 0.22	126
F - all	**177.92** 23.5	**181.55** 20.3	157.2 - 223.2	**184.09** 25.2	175.7 - 251.6	**1.04** 0.11	0.94 - 1.34	**1.08** 0.22	126

Table II.4.1: Parameters of glottal dimensions measured in function of gender, group of subjects, and breathing task. Highlighted rows represent groups with progressive glottal movement.

4.2.1 General Features

Identification of two groups in the database. In a first approach, a statistical analysis of the database was conducted to test the common assumption of a linear correlation between the area $A_g(t)$ and the airflow rate $Q(t)$ time-variations. A linear regression coefficient R^2 between those two variables was calculated. Closer the value R^2 is to 1, more significant is this linear relationship between $A_g(t)$ and $Q(t)$. The values of regression for all subjects and tasks **Eup**$_{15}$ and **Tachyp**$_{30}$ are summarized in Table II.4.2. Two groups of subjects can be distinguished (see Figure II.4.3 and Figure II.4.4 for **Eup**$_{15}$ and **Tachyp**$_{30}$, respectively):

- The "1st group" of subjects is characterized by a linear regression coefficient close to 0, such as $R^2 < 0.3$ (see Table II.4.2). In this case, no linear correlation between $Q(t)$ and $A_g(t)$ is evidenced. Note however that this result does not imply that the glottal aperture is constant in time.
- The "2nd group" of subjects is characterized by a non-negligible linear regression coefficient, such as $R^2 \geq 0.3$ (highlighted cells in Table II.4.2). In this case, the non-zero R^2-values show that the area $A_g(t)$ varies according to the breathing phase. However, the assumption of a linear correlation between $Q(t)$ and $A_g(t)$ seems very inaccurate, as shown by the low R^2-values.

FEMALES										
Task	F01	F02	F03	F04	F05	F06	F07	F08	F09	F10
Eup$_{15}$	0.05	0.78	0.41	0.08	0.02	0.01	0.01	0.08	0.45	0.18
Tachyp$_{30}$	0.11	0.08	0.53	0.01	0.01	0.01	0.11	0.17	-	0.12
MALES										
Task	M01	M02	M03	M04	M05	M06	M07	M08	M09	M10
Eup$_{15}$	0.51	0.56	0.59	0.02	0.30	0.47	-	0.45	0.01	0.18
Tachyp$_{30}$	0.54	0.50	0.73	0.01	0.05	0.10	-	0.01	0.05	0.33

Table II.4.2: R^2 values of linear regression between area $A_g(t)$ and $Q(t)$. Highlighted cells are those with important value of $R^2 \geq 0.3$.

In a second approach, this criterion based on R^2-value was completed by the analysis of the glottal amplitudes measured for each subject during a mean cycle. Every mean breathing cycle of the database can be characterized by a mean ratio $\overline{A}_g^I/\overline{A}_g^E$ greater or roughly equal to 1 (see Table II.4.1, column #5). In some cases, the glottal amplitudes were quite important, although not in linear proportion with the inspired airflow rate. Yet, the detected glottal area time-variations demonstrate a substantial inter-subject variability.

Therefore, within each gender and task category, the subjects were finally divided into two groups, depending on both R^2-value and the glottal aera amplitude, relatively to the accuracy of the glottal motion detection procedure assessed at 10% (see section II.3.2.2.c).

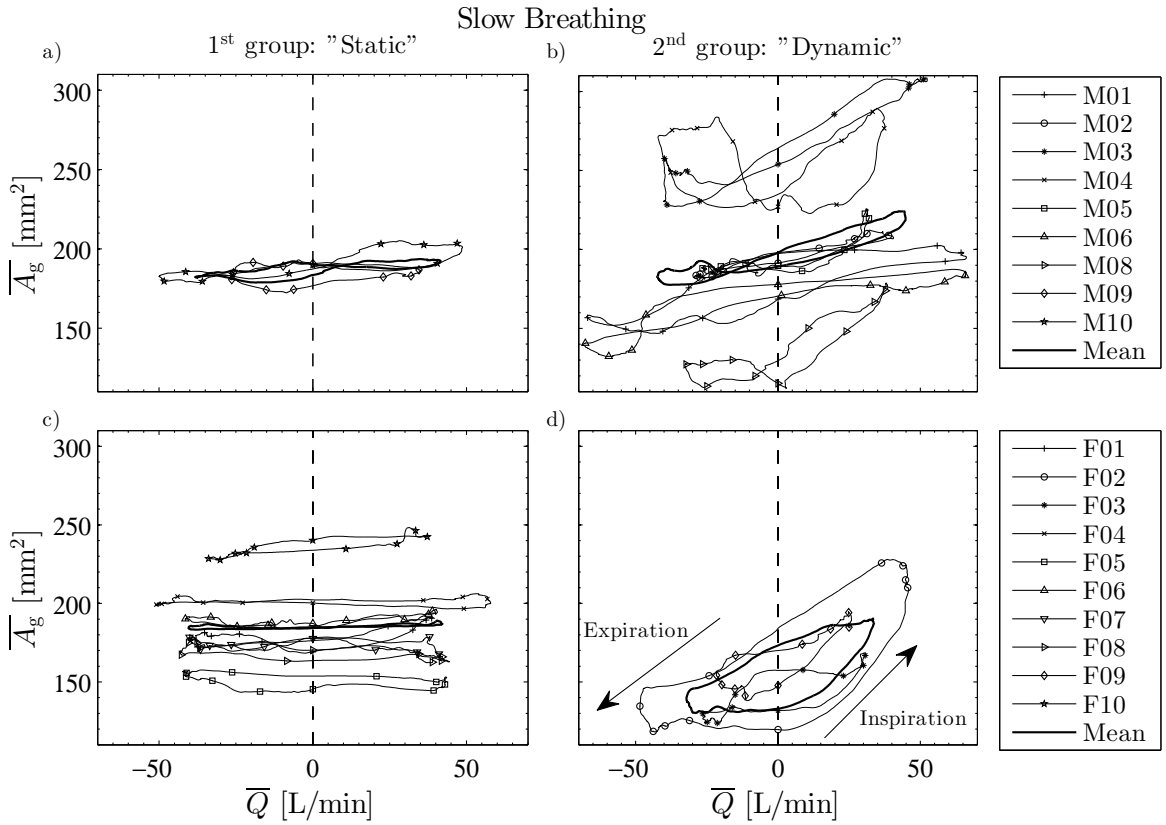

Figure II.4.3: Glottal area $\overline{A}_g$ variations during *slow breathing*. Upper panels (*a*, *b*) represent male subjects and lower panels (*c*, *d*) female subjects. Left panels (*a*, *c*) are dedicated to the 1st group (with "static" glottal movement) and right panels (*b*, *d*) are dedicated to the 2nd group (with "dynamic" glottal movement).

The final classification of the subjects into two groups is represented in Table II.4.1 (column #1):

- The 1st group (labelled as "static") gathers the subjects with a quasi-constant glottal area detected during the average breathing cycle. This group is characterized by (i) a quasi-zero linear regression coefficient R^2 in Table II.4.2 and (ii) by a mean glottal area variation smaller than 10%. In Figure II.4.5 are shown the evolutions of the mean, normalized glottal area $\overline{A}_g/\overline{PIA}_g$ in function of the normalized time ωt for all groups and tasks $\mathbf{Eup}_{15}$ and $\mathbf{Tachyp}_{30}$. This "static" glottal evolution during breathing has been reported in Hyatt and Wilcox [1961] and in 1 subject from 3 in Jackson et al. [1975].

- The 2nd group (labelled as "dynamic") gathers the subjects with a time-varying glottal area during the average breathing cycle, so that (i) the regression coefficient R^2 is non-zero ($R^2 \geq 0.3$) in Table II.4.2 and (ii) the mean glottal area variation is higher than 10% (see Figure II.4.5). This group is characterized by a progressive glottal widening (resp. narrowing) during inspiration (resp. expiration), in agreement with previous reference studies [Baier et al., 1977; England et al., 1982; Brancatisano et al.,

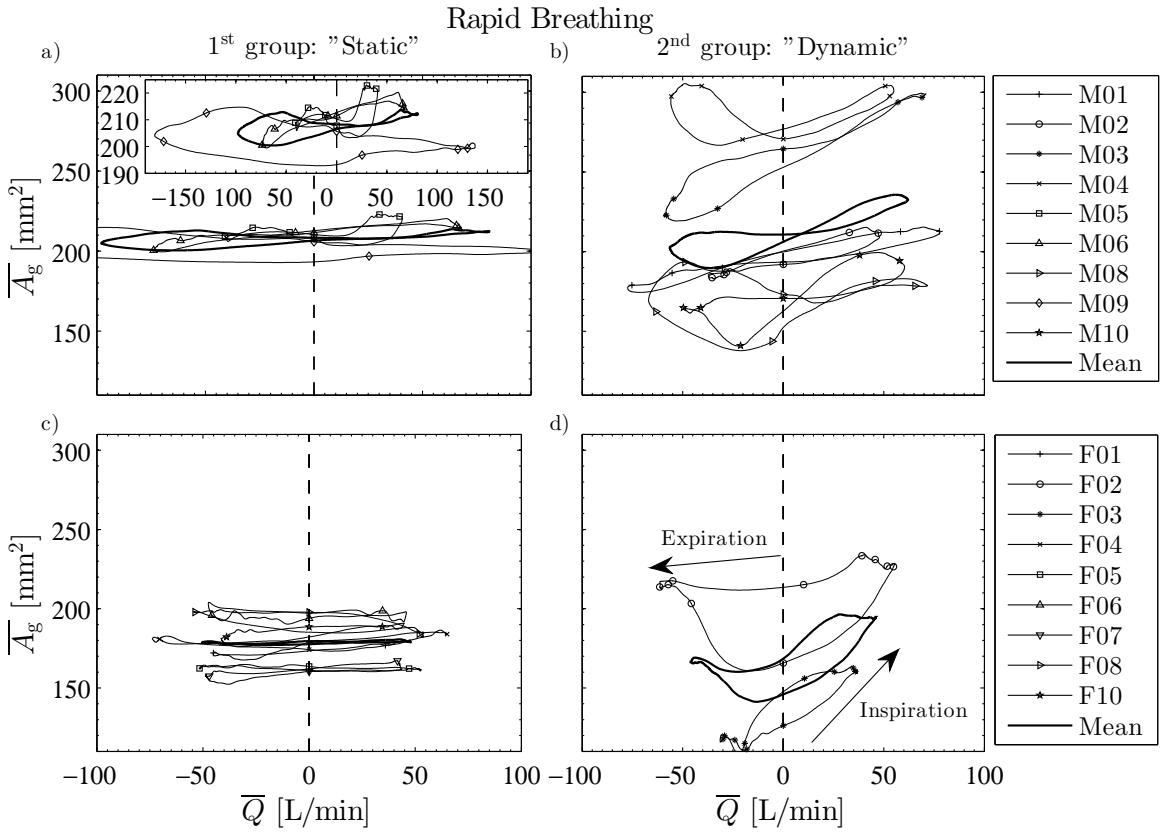

Figure II.4.4: Glottal area $\overline{A}_g$ variations during *rapid breathing*. Upper panels (*a*, *b*) are for male subjects and lower panels (*c*, *d*) are for female subjects. Left panels (*a*, *c*) are dedicated to the 1st group (with "static" glottal movement) and right panels (*b*, *d*) are dedicated to the 2nd group (with "dynamic" glottal movement). Panel *(a)* includes a detail of subject M09 for its high airflow rate variations.

1983]. The peak values reached during inspiration have been measured around 1.26 and 1.46 times higher than the minimum value achieved during expiration for males and females respectively. During *slow breathing*, the 2nd group is composed of 52.6% of studied subjects, against 44.4% of subjects during *rapid breathing*.

Characteristic amplitudes and ratios. In the group as a whole, a glottal narrowing during expiration was observed. The average peak ratio $\overline{PIA}_g/\overline{PEA}_g$ was ranging from 1.21 (subject F04) to 2.31 (subject M08). (Note that this ratio is assessed from the time-averaged cycle of one volunteer. Later those cycles of the volunteers in a selected group are again time-averaged to get final cycle, from which are deduced values in Table II.4.1.) This ratio was evaluated at 1.8 in Brancatisano et al. [1983] and between 1.16 and 1.54 for 5 subjects studied by England et al. [1982]. This glottal narrowing is supported by the activity of the thyroarytenoid muscle during expiration [Kuna et al., 1991], which is an adductor muscle of the vocal folds.

In our database, during *slow breathing*, the peak glottal area changes for males from **217.32** ± 53.8 mm^2 (**mean** ± SD) during inspiration ($\overline{PIA}_g$) to **178.1** ± 34.6 mm^2

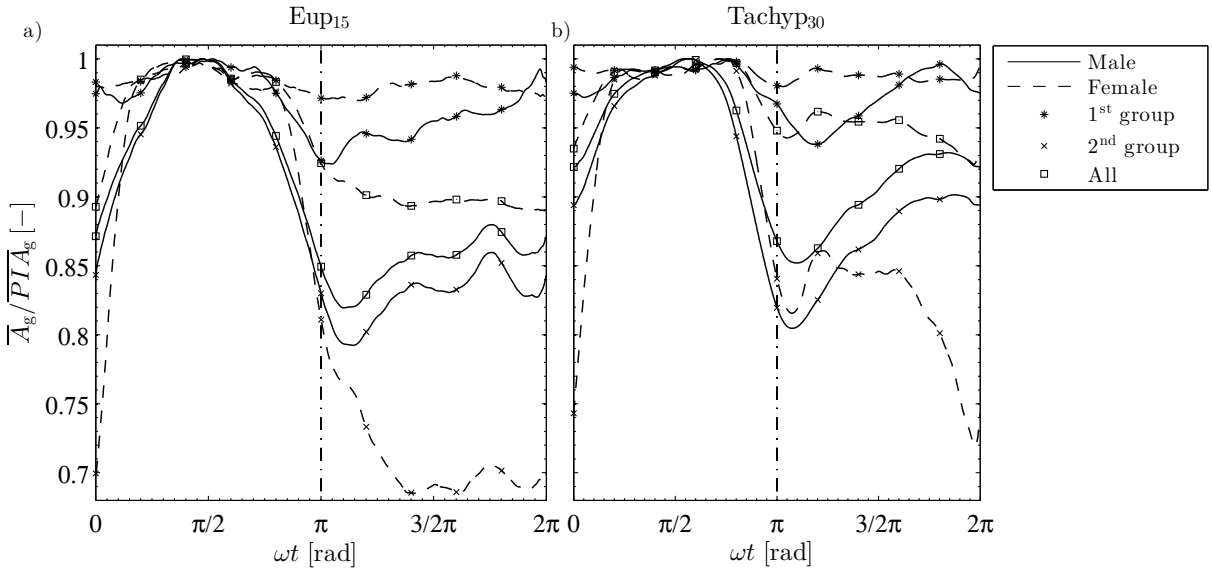

Figure II.4.5: Comparison of the mean, normalized glottal area evolution $\overline{A}_g/\overline{PIA}_g$ [–] in function of the normalized time ωt [–] for different groups of subjects and tasks **Eup**$_{15}$ *(a)* and **Tachyp**$_{30}$ *(b)*.

during expiration ($\overline{PEA}_g$). Similarly, for females the peak glottal area changes from **189.21** ± 31.6 mm^2 during inspiration to **168.23** ± 30.8 mm^2 during expiration. The mean value over the whole cycle, $\overline{A}_g$, was found at **196.14** ± 41.9 mm^2 for males, and **177.37** ± 26.7 mm^2 for females. The corresponding values for *tachypnea* breathing are reported in Table II.4.1.

Another important feature can be highlighted from the clinical study. In average on our database, the measured glottal areas are much higher than those measured with equivalent method in other works [Baier et al., 1977; Brancatisano et al., 1983]. In comparison, Baier et al. [1977] measured a value $\overline{A}_g$ of 44 mm^2 and 48 mm^2 for 2 males, while ranging from 43 mm^2 to 104 mm^2 for 4 females. Similarly, Brancatisano et al. [1983] measured a value $\overline{A}_g$ of 98 mm^2 (peak value $\overline{PIA}_g$ **126** ± 8 mm^2, 12 subjects, 2 females). However, our results are in agreement with previous studies based on the acoustic reflection [D'Urzo et al., 1988; Rubinstein et al., 1989; Martin et al., 1997] or MRI technics [Pritchard and McRobbie, 2004]. In particular, D'Urzo et al. [1988] used both acoustic reflection and Computerized Tomography (CT) methods to measure glottal area at functional residual capacity on 11 subjects. The results derived from CT and acoustic reflection methods were similar. The values of A_g were measured in the range between 40 to 290 mm^2 (mean value of **180** ± 80 mm^2). Similarly, in Martin et al. [1997] was measured A_g of 170 mm^2 at the onset of inspiration by 114 subjects. Note that Rubinstein et al. [1989] measured values of glottal area A_g during hyperpnea, ranging between 144 and 211 mm^2 on 25 males, and between 137 and 207 mm^2 on 19 females.

4.2.2 Influence of subject gender

a/ "Static" and "dynamic" group of subjects

The influence of the subject gender on glottal variations during *slow breathing* is clearly highlighted in Figure II.4.3. Indeed the male group has much more representatives in the 2nd group "dynamic" (7/9) relative to the 1st "static" group (2/9), whereas female subjects are gathered together in majority in the 1st "static" group (7/10) compared with the 2nd "dynamic" group (3/10). These trends are similar in *rapid breathing*, as displayed in Figure II.4.4 (6/9 males against 2/9 females only in the 2nd "dynamic" group).

b/ Glottal motion amplitudes & time-variations

Despite their minimal proportion within the 2nd group, females in this group demonstrate glottal motion amplitudes larger than males. This result yields to higher ratios $\overline{A}_{\mathrm{g}}^{\mathrm{I}}/\overline{A}_{\mathrm{g}}^{\mathrm{E}}$ and $\overline{PIA}_{\mathrm{g}}/\overline{PEA}_{\mathrm{g}}$ for females, whatever the task (see Table II.4.1, darkened rows). However, for both genders, the mean $\overline{A}_{\mathrm{g}}\left(\overline{Q}\right)$ loops plotted in Figure II.4.3 panels *(b)* and *(d)* do not exhibit ellipsoidal shapes, which would have been observed in case of sinusoidal glottal dynamics during a breathing period. Instead, the shape-differences observed on the $\overline{A}_{\mathrm{g}}\left(\overline{Q}\right)$ loops of males and females mainly derive from the different time-variations of the glottal area recorded during inspiration for both genders: a plateau in $\overline{A}_{\mathrm{g}}$ evolution occurs during this phase for females, while a quasi-sinusoidal variation is measured for males (see Figure II.4.6). Note that during *slow breathing*, the glottal dynamics during expiration is similar for males and females: the glottis tends to stay opened in the narrowest posture (panels *(a)* and *(c)* on Figure II.4.6).

4.2.3 Influence of breathing task

The comparison of the $\overline{A}_{\mathrm{g}}\left(\overline{Q}\right)$ loops given in Figure II.4.3 and Figure II.4.4 shows similar tendencies and orders of magnitude for *eupnea* and *tachypnea*.

From our results, the influence of the breathing task on glottal motion is far less emphasized than the one of the subject gender. The glottal aperture is larger during the whole cycle for *tachypnea* than for *eupnea*. This is in agreement with Baier et al. [1977], who measured larger glottal areas for men and women during *tachypnea* in comparison with *quiet breathing*.

Furthermore, during hyperpnea, England and Bartlett [1982] observed an area A_{g} slightly increasing during inspiration and narrowing during expiration. Also they found smaller aperture ratio in comparison with *quiet breathing*. Those observations are confirmed by measurements of upper airways resistance. Spann and Hyatt [1971] measured a decrease in the average laryngeal resistance with *hyperpnea*. Stănescu et al. [1972] measured a 43% decrease in airway resistance during inspiration, and a 26% decrease during inspiration

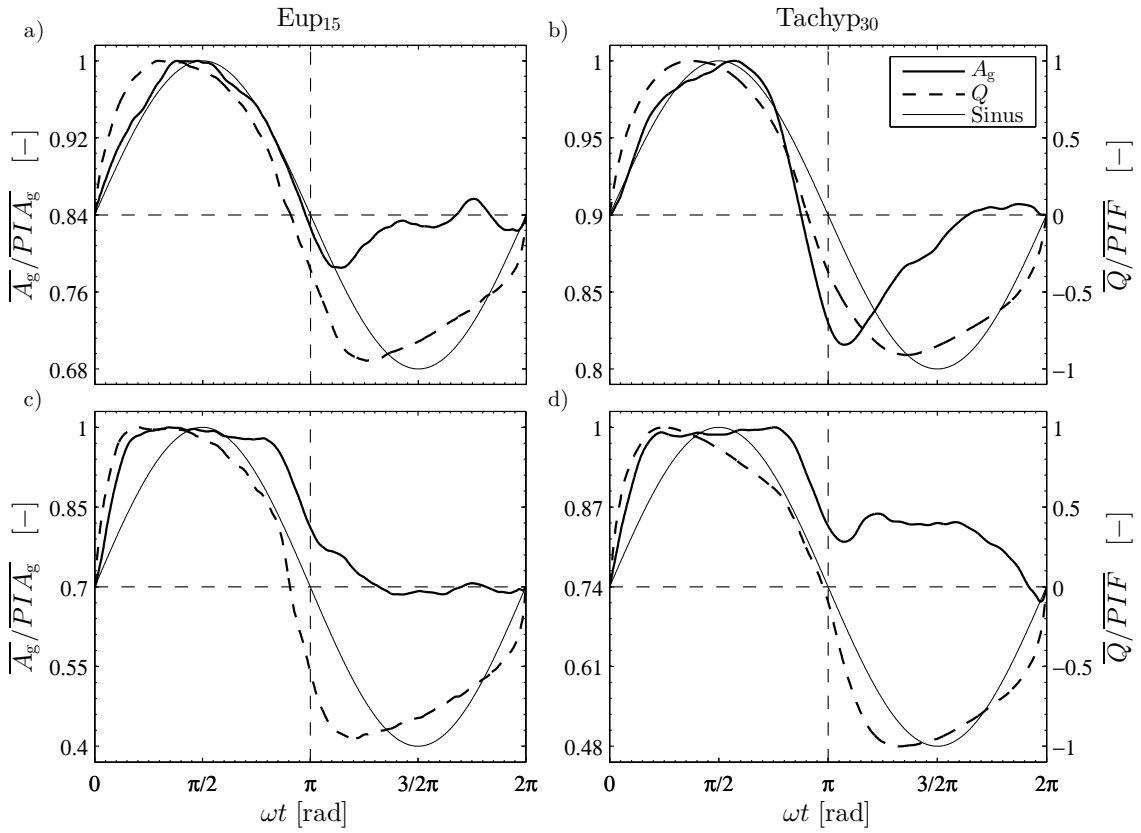

Figure II.4.6: Comparison of mean normalized glottal area $\overline{A}_g/\overline{PIA}_g$ [–], mean normalized flow rate $\overline{Q}/\overline{PIF}$, and sinusoidal pattern for males (panels *(a)* and *(b)*, tasks **Eup**$_{15}$ and **Tachyp**$_{30}$, respectively) and females (panels *(c)* and *(d)*, tasks **Eup**$_{15}$ and **Tachyp**$_{30}$, respectively). Results given for subjects with "dynamic" glottal variations (2nd group).

during *hyperpnea*. Finally, Insalaco et al. [1990] confirmed those results by measuring a decrease in thyroarytenoid muscle activity during *hyperpnea*.

4.2.4 Correlation between airflow rate pattern & glottal motion

Figure II.4.6 shows the mean normalized glottal area dynamics ($\overline{A}_g/\overline{PIA}_g$) in function of normalized time (ωt) for subjects classified within the 2nd group only. The 1st group is not presented here as the glottal dynamics is steady and the resulting normalized pattern would be a straight line close to 1. Upper (resp. lower) panels correspond to male (resp. female) subjects. On the figures are superposed the mean normalized airflow rate patterns ($\overline{Q}/\overline{PIF}$), to analyze the correlation between airflow rate and glottal area time-variations.

For all subjects of the 2nd group and for all tasks, the glottal widening starts with the onset of inspiration, whereas the glottal narrowing precedes the expiration phase. For males, the opening of $\overline{A}_g$ reaches the Peak Inspiratory glottal Area $\overline{PIA}_g$ after the Peak

Inspiratory Flow $\overline{PIF}$ is achieved. This phase difference is assessed at about 15.6°. For females, this delay is reduced and both peaks occur rather simultaneously. If the glottal motion seems related to the airflow dynamics during inspiratory phase, no correlation is brought out from the data registered during expiratory phase. Therefore, the same absolute airflow amplitude is associated to (at least) two different glottal openings. Note that Figure II.4.7 presents these results for subjects of 1st and 2nd group as a whole, yielding to similar conclusions.

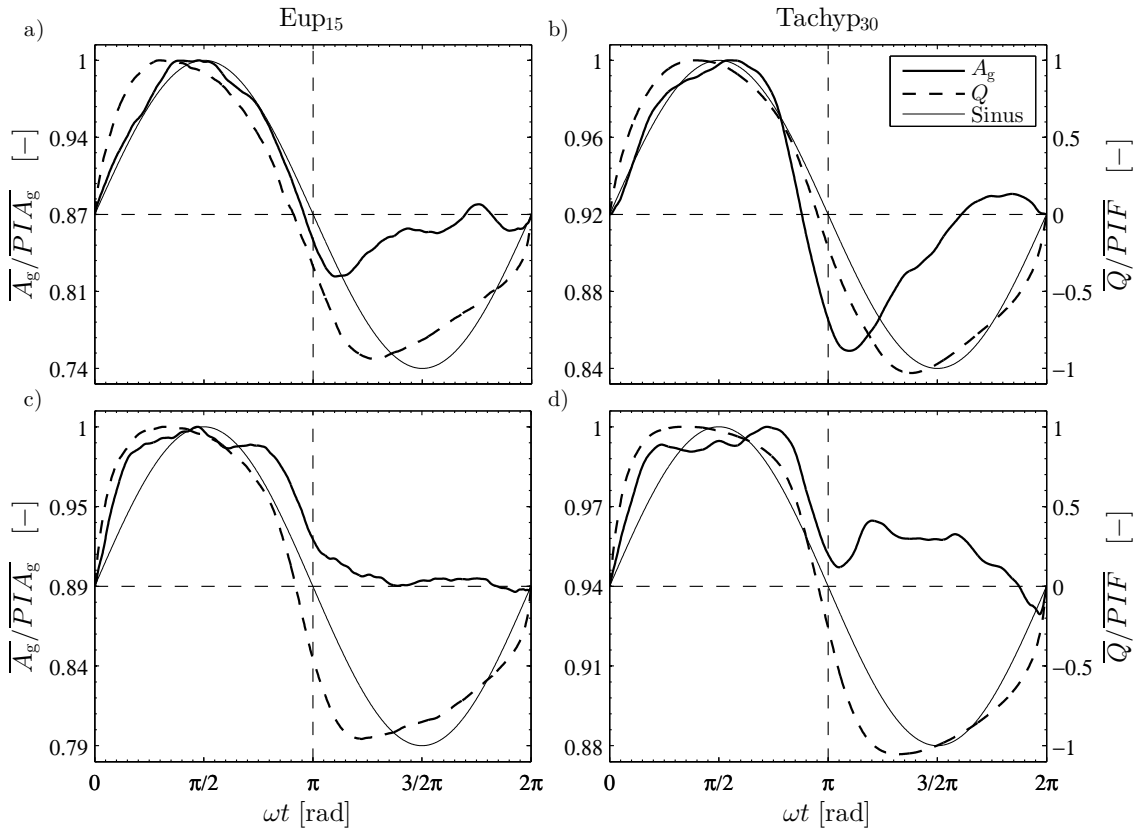

Figure II.4.7: Comparison of mean normalized glottal area $\overline{A}_g/\overline{PIA}_g$, mean normalized flow rate $\overline{Q}/\overline{PIF}$ and sinusoidal pattern for males (panels *(a)* and *(b)* represent tasks **Eup**$_{15}$ and **Tachyp**$_{30}$, respectively) and females (panels *(c)* and *(d)* represent tasks **Eup**$_{15}$ and **Tachyp**$_{30}$, respectively). Results given for all subjects within the gender (both 1st and 2nd group of subjects together).

4.3 Discussion

4.3.1 Towards the reasons for glottal motion and aerodynamics

Although the primary adductor muscles of the larynx (lateral cricoarytenoid, thyroarytenoid, interarytenoid) induce a control of vocal-fold length, tension and vocal frequency

during human phonation, the glottal self-sustained vibrations result from complex interactions between the laryngeal airflow and the mechanical behavior of vocal-fold soft tissues [Titze, 1994]. In fact, these vibrations can typically be reproduced on excised larynges or *in vitro* synthetic models of vocal folds [Dollinger et al., 2011]. Thereby, once installed, the sound-related glottal motion is not driven by a neuromotor control. By contrast, the respiratory-related glottal motion is generated by contractions of intralaryngeal muscles, and is highly affected by laryngeal reflex responses [Widdicombe and Tatar, 1988; Shiba, 2009]. More specifically, the vocal fold abductor (posterior cricoarytenoid muscle) dilates the glottis during inspiration by abduction rotation of the arytenoid cartilages, while the adductor muscles narrow the glottis during expiration by adduction-rotation of the arytenoid cartilages. There is general agreement that this controlled motion is carried out in order:

i. to help the air intake during inspiration by glottis widening, which lowers the upper airways resistance to flow,

ii. to brake the passive expiratory airflow by glottis narrowing, which enables a control of the end-expiratory lung volume and pressure in order to prevent alveoli from collapse [Rattenborg, 1961; Brancatisano et al., 1983; Roux, 2002; Shiba, 2009].

Note that several studies are dedicated to the restoration of an optimal laryngeal geometry after a surgical change of the vocal folds, which would minimize the airflow resistance in the upper airways [Templer et al., 1991; Hundertmark-Zaušková et al., 2013]. Thus, the results obtained in our study on glottal motion and aerodynamics during breathing were further analyzed to interpret the data in terms of energy efficiency. To this end, the power dissipated by an airflow (volume airflow rate $Q^0(t)$) through a circular diaphragm ("glottis" of cross section area A_g^0) across a cylindrical tube ("trachea" of cross section area A_t with diameter equal to glottal antero-posterior distance AP_g) was calculated in two comparative cases:

(a) a realistic case, mimicking the measured unsteady flow and glottal conditions, where:

$$Q^0(t) = \overline{Q}(t), \tag{II.4.1}$$

$$\text{and} \quad A_g^0(t) = \overline{A}_g(t), \tag{II.4.2}$$

(b) an idealized case assuming unsteady sinusoidal flow conditions and steady glottis, where:

$$\begin{aligned} Q^0(t) &= \overline{PIF}\sin(\omega t), \\ \text{with} \quad \overline{PIF} &= \frac{\pi \overline{V}_I}{\overline{T}_t}, \end{aligned} \tag{II.4.3}$$

$$\text{and} \quad A_g^0(t) = \overline{A}_g. \tag{II.4.4}$$

Considering the air as an incompressible Newtonian gas with typical flow Reynolds number $\mathrm{Re} < 10^5$ and neglecting unsteady effect, the power P_w [W] dissipated through a circular

diaphragm is given by:

$$P_{\mathrm{w}} = \Delta p\, Q^0 = \frac{1}{2}\rho U^2 \lambda \mid Q^0 \mid, \tag{II.4.5}$$

where Δp [Pa] is the pressure drop through the singularity, $\rho = 1.2$ kg/m^3 is the air density, $U = 2\overline{V}_{\mathrm{I}}/\left(\overline{T}_{\mathrm{t}} A_{\mathrm{g}}^0\right)$ [ms^{-1}] is the mean flow velocity during inspiration phase and λ [-] is the singular head loss coefficient calculated by Idel'cik and Meury [1978] as:

$$\lambda = \left(1 + 0.707\sqrt{1 - \frac{A_{\mathrm{g}}^0}{A_{\mathrm{t}}}} - \frac{A_{\mathrm{g}}^0}{A_{\mathrm{t}}}\right)^2. \tag{II.4.6}$$

Figure II.4.8 shows a comparison of the power P_{w} [mW] obtained from the data registered for female and male subjects, in the illustrative case of *rapid breathing* (**Tachyp**$_{30}$). Over

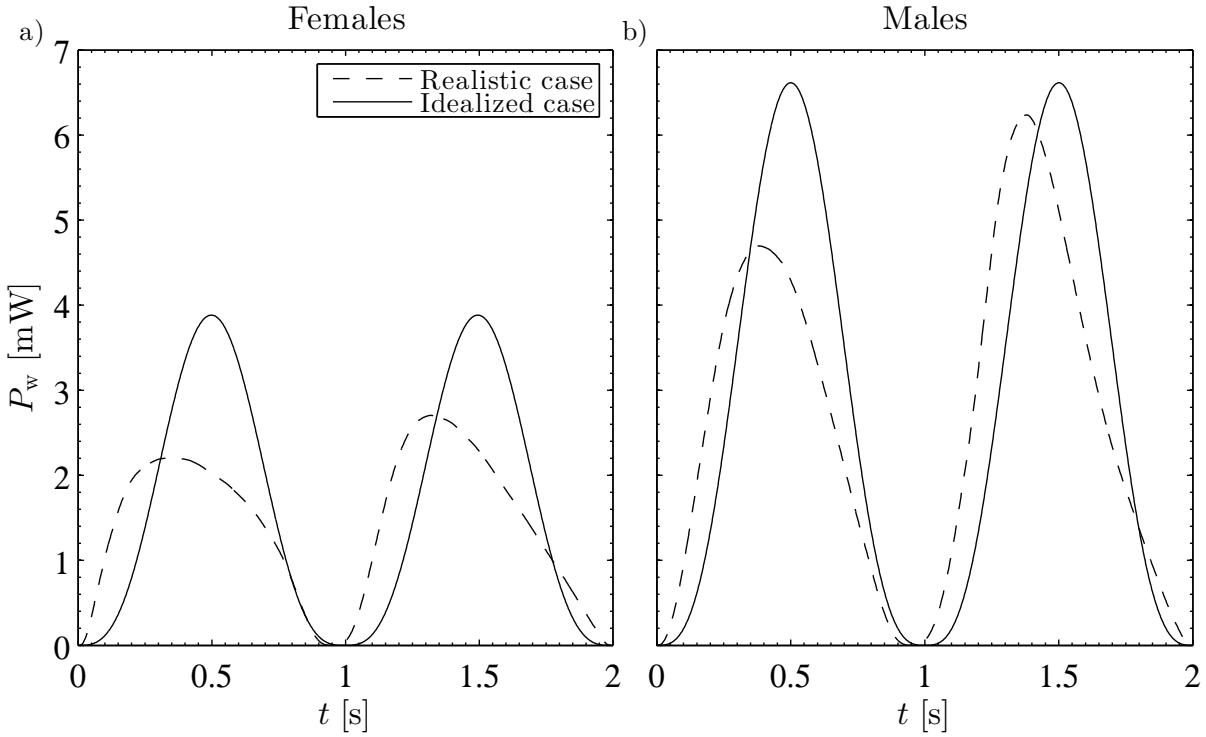

Figure II.4.8: Power P_{w} [mW] comparison of idealized and realistic cases, obtained from the data registered for female and male subjects, in the illustrative case of *rapid breathing* (**Tachyp**$_{30}$). First peak corresponds to inspiration and second peak to expiration.

the whole, it is interesting to note a substantial decrease of the power dissipated during the average breathing cycle in realistic case (a) as compared to idealized case (b). The energy dissipated by head loss within the "glottal" diaphragm over a cycle, E [J], is defined as:

$$E = \int_0^{\overline{T}_{\mathrm{t}}} P_{\mathrm{w}} \mathrm{d}t. \tag{II.4.7}$$

Average values are presented in Table II.4.3 in function of gender and breathing task.

***Slow Breathing* - Eup$_{15}$**		
Group	Realistic case	Idealized case
Males All	2.73	2.84
Females All	2.73	3.10
***Rapid Breathing* - Tachyp$_{30}$**		
Males All	5.28	5.62
Females All	2.86	3.28

Table II.4.3: Energy loss E [mJ] within a circular diaphragm in two breathing modes: (a) mobile glottis, non-sinusoidal airflow and (b) steady glottis, sinusoidal airflow.

During *slow breathing* (resp. *rapid breathing*), the relative decrease between idealized and realistic cases equals 4% (resp. 6%) and 12% (resp. 13%) for males and females group, respectively. Therefore, it is shown that the realistic breathing mode (mobile glottis, non-sinusoidal airflow rate) is an energy saving maneuver in comparison with an idealized mode (steady glottis, sinusoidal airflow rate).

4.3.2 Towards the aerodynamic impact of glottal motion

The database was also exploited to evaluate the impact of the measured glottal motion and airflow rates on characteristic flow parameters within the glottis. These flow parameters are listed below:

- the maximum and mean flow velocity during inspiration, noted $u_{\max}$ and u_{mean}, respectively;
- the local Reynolds numbers $Re_{\max}$ and Re_{mean} based on $u_{\max}$ and u_{mean}, respectively;
- the frequency parameter, given by:

$$\alpha = R_{\text{h}}\sqrt{\frac{\omega}{\nu}}, \qquad \text{where} \quad R_{\text{h}} = \frac{D_{\text{h}}}{2}, \tag{II.4.8}$$

  where D_{h} [m] stands for the hydraulic diameter and ν [m^2/s] for the air kinematic viscosity.

For each group, these parameters are a function of the inspiratory volume $\overline{V}_{\text{I}}$, the breathing period $\overline{T}_{\text{t}}$ and the glottal cross-section area $\overline{A}_{\text{g}}(t)$. Table II.4.4 presents the values obtained in conditions of *slow* and *rapid breathing* for males and females (based on data from Table II.3.2 and Table II.4.1). The mean Reynolds numbers Re_{mean} range between 1900 and 3100 (peak values below 5000), corresponding to moderate mean velocity values expected within the glottis (peak values between 4-6 m/s). Low values of the frequency

	Females		**Males**	
Flow parameter	*Slow breathing*	*Rapid breathing*	*Slow breathing*	*Rapid breathing*
u_{max} [m/s]	4.17	5.41	3.93	5.99
u_{mean} [m/s]	2.66	3.45	2.50	3.81
Re_{max} [−]	3069	4001	3088	4852
Re_{mean} [−]	1954	2547	1966	3089
α [−]	1.76	2.51	1.88	2.74
D_h [mm]	10.7	10.8	11.44	11.8

Table II.4.4: Glottal airflow parameters derived from the database as function of gender and breathing rate.

parameter α (in the range 1.8 - 2.7) are indicators of a flow comprising notable viscous effects, and whose time duration of the boundary layer development is comparable to the breathing cycle period. These parameters provide information which is used as input data to conduct realistic numerical simulations of laryngeal airflow (see Part III). Finally, it is important to note that the fraction of aerosol deposited on the laryngeal walls is highly dependent on the Stokes number (Stk), defined as:

$$Stk = \frac{\rho_p D_p^2 u}{18 \eta D_h}, \tag{II.4.9}$$

where ρ_p is the particle density, D_p the particle diameter, η the air dynamic viscosity, u the air inlet velocity and D_h the glottal hydraulic diameter. Thus, the deposition dynamics in the larynx is likely to be influenced by:

i. unsteady flow velocity (as demonstrated in Jin et al. [2007]),

ii. unsteady glottal dimensions during breathing.

From this point of view, the clinical database reported in this study seems of primary interest to better evaluate the aerosol transport and deposition mechanisms.

Summary

Several items can be highlighted to summarize the methodology and results presented in the Part II:

- A clinical study was conducted in collaboration with the ENT Department of the *La Timone Adults Hospital* to examine the glottal motion during eight breathing tasks by means of an *in vivo* exploratory approach. This study was realized on 20 healthy non-smoking volunteers in the range of 20 and 30 years old, including 10 women and 10 men. Laryngofibroscopy was realized using a flexible nasofibroscope. Synchronized oral airflow measurements were achieved by means of EVA2^{TM} system developed at the *Speech and Language Laboratory* (LPL). The breathing tasks were divided in *slow breathing* tasks (below 20 cycles/min) and *rapid breathing* tasks (above 20 cycles/min). In total, 144 breathing sequences of 30s were recorded.
- The data processing comprised: (i) the detection of a mean breathing airflow rate per gender for the "slow" and "rapid" breathing tasks; (ii) the extensive analysis of the laryngeal images recorded during two major tasks for all subjects: the task of *eupnea* performed at 15 cycles/min; and the task of *tachypnea* performed at 30 cycles/min. These tasks are altogether representative of "slow" and "rapid" breathing tasks. A customized methodology was developed to extract time-variations of the glottal area in each case.
- In addition, some preliminary experiments allowed to measure the transglottal pressure drop during several breathing tasks, *i.e.*, an information which completes the clinical study and which is rarely available in the literature. The transglottal pressure during eupnea was found around 40 Pa; it can reach as much as 600 Pa in specific forced breathing regimes (*panting*).
- Regarding the whole database, two cases of glottal time-variations were found: "static" and "dynamic" ones. Thus, testing the correlation of glottal and flow-rate time-variations, subjects with “static” or “dynamic” glottis during an average breathing cycle were sorted. Whatever the breathing regime, male have much more representatives in the "dynamic" group, while female are gathered together in majority in the "static" group. Yet, despite their minimal proportion in the "dynamic" group, females demonstrate glottal motion amplitudes larger than males.
- During "slow" breathing, for males, the peak value of glottal area narrowed from 217.32 $\pm$ 53.8 mm^2 (mean $\pm$ SD) during inspiration, to 178.1 $\pm$ 34.6 mm^2 during

expiration. For females, the peak glottal area changes from 189.21 ± 31.6 mm^2 during inspiration to 168.23 ± 30.8 mm^2 during expiration. The mean value over the whole cycle, $\overline{A}_g$, was found at 196.14 ± 41.9 mm^2 for males, and 177.37 ± 26.7 mm^2 for females.

- If the glottal motion seems related to the airflow dynamics during inspiratory phase, no correlation is brought out from the data registered during expiratory phase. The same absolute airflow amplitude is associated to at least two different glottal openings.
- Regarding flow unsteadiness, this study showed that the that the realistic breathing mode (mobile glottis, non-sinusoidal airflow rate) is an energy saving maneuver in comparison with an idealized mode (steady glottis, sinusoidal airflow rate).
- These measurements provided input data to conduct the realistic numerical simulations of laryngeal airflow and particle deposition, as presented in the following Part III.

Part III

Flow & Aerosol Transport in Upper Airways: In Silico Study

Introduction

As reported in Part I, some previous Computational Fluid Dynamics (CFD) studies showed that the laryngeal area can play a key role in airflow dynamics (see section I.2.2.2). More specifically, the glottis causes human upper airways to tighten and narrow in a minimal transition cross-section (see section I.2.1). This anatomical singularity yields to a complex jet-like tracheal flow, characterized by important recirculation zones and a locally turbulent behavior, which can be determinant on particle deposition by inertial impaction [Katz and Martonen, 1996; Katz et al., 1997; Renotte et al., 2000; Brouns et al., 2007b].

However, as summarized in section I.1.3.2, most of the studies dedicated to the glottal impact on the respiratory biomechanics and aerosol deposition patterns within the upper airways are still limited. Indeed, several assumptions often adopted are: a mean constant inhalation flow rate applied at inlet conditions, quasi-steady respiratory flow conditions, and a parametric static glottal cross-section [Katz et al., 1997; Brouns et al., 2007b; Zhang and Kleinstreuer, 2011].

Therefore, the aim of this part is to exploit the results of the *in vivo* study detailed in Part II, and to elaborate an original CFD model employing the measured data as dimensions of upper airways geometry, and unsteady input conditions. Thereby considering: realistic cyclic breathing airflow rates at the inlet area, unsteady flow conditions and aerosol delivery, and mobile glottal walls. To this end, a step-by-step methodology was adopted, comprising (i) the elaboration of a glottal motion model derived from the *in vivo* data, (ii) numerical modeling in preliminary 2D and 3D geometries including both mobile glottal walls and unsteady breathing conditions, (iii) the elaboration of a 3D average idealized geometry of the upper airways, and (iv) numerical simulations of two-phase flow conducted in the complete 3D geometry using experimental unsteady airflow conditions and dynamic glottal configurations. Hence, this part is divided in three chapters as follows:

- The design of the glottal motion model as well as the preliminary numerical models (steps i and ii) are described in chapter III.5. The methodology used to elaborate dynamic meshes is pointed out. The results obtained in a simple 3D tube geometry including a mobile diaphragm are presented.
- The elaboration of the 3D idealized geometry of the upper airways (step iii) is presented in chapter III.6. This chapter describes the chosen geometry, the mesh properties, the solution method and the different simulation cases implemented in ANSYS®

Fluent Academic Research (Release 15.0). The glottal wall conditions (static or dynamic group), the breathing type (eupnea or tachypnea) and the nature of carrier gas (air or Helium (He) - Oxygen (O_2) 78% - 22% mixture) are the three parameters varied in the simulation cases.

- Finally, chapter III.7 presents the results of the different simulation cases introduced in chapter III.6 (step iv).

Note that preliminary 2D and 3D results of this chapter III.5 were presented in a conference paper of the 37^{th} Congress of the *Société de Biomécanique* (SB 2012) in Toulouse, France [Scheinherr et al., 2012], in a poster at 19^{th} Congress of the *International Society for Aerosol in Medicine* (ISAM 2013) in Chapel Hill, USA [Scheinherr et al., 2013b], and as an oral presentation at the 19^{th} Congress of the *European Society of Biomechanics* (ESB 2013) in Patras, Greece [Scheinherr et al., 2013a].

Chapter III.5

Preliminary CFD Models with Mobile Glottis and Unsteady Breathing Conditions

This chapter details the design of a glottal motion model derived from the *in vivo* data reported in Part II, and its implementation in simplified preliminary CFD models with aerosol transport. As pilot studies, two simple geometries including glottal mobile walls were created: (i) a 2D rectangular moving constriction placed in a 2D rectangular channel, and (ii) a 3D cylindrical tube including a mobile 2D diaphragm representing the glottal constriction. The first 2D case is described in Annex B - 2D Model. Present chapter is fully dedicated to the 3D case.

In comparison with realistic geometry of the larynx, the geometry considered in this chapter only comprises a realistic glottal area, derived from previous part. However, this first rough approximation enabled to understand the problematics connected to unsteady 3D flow simulations with unsteady boundary conditions. It allowed to provide basic qualitative information and first orders of magnitude relative to the airflow occurring in the glottal region, while performing low time-consuming computational calculations. More specifically, the elementary design of the model (tube) was chosen to focus on the settings of the mobile walls and the mesh deformation in time, by allowing an easier adjustment of dynamic mesh geometries in the CFD solver, an easier choice of the mesh properties and an easier assessment of the relevance of the moving mesh settings.

In the following, the design of geometry is described in section III.5.1, the solution method in section III.5.2, and the initial and boundary conditions are detailed in section III.5.3 together with the different cases of simulations. The mesh properties are presented in III.5.4. The numerical results of CFD simulations on the flow field and aerosol transport and deposition are discussed in section III.5.5.

5.1 Geometry

The model was designed using GAMBIT 2.4.6 (Fluent, Inc.). The geometry consists in a 3D tube with a 2D constriction (plane Ω_g) representing the glottis, as illustrated in Figure III.5.1 and Figure III.5.2.The tube was divided into four parts, two upstream the glottal constriction ($\Omega_1 + \Omega_2$) and two downstream the glottal constriction ($\Omega_3 + \Omega_4$). In detail, volumes $\Omega_2 + \Omega_3$ are attached to the glottal plane Ω_g and has to be remeshed every time step of the calculation according to the motion of the glottal constriction. Therefore, the division of the tube into four volumes assures less time-consuming procedure to generate the mesh every time step.

The tube diameter d_{inlet} was set to 17.6 mm, corresponding to the mean female glottal antero-posterior diameter AP_{g}, as measured by Eckel and Sittel [1995] (note that female dimension was chosen, because data on female airflow rate will be implemented for the simulations - see section III.5.3). To ensure stabilization of the jet formed at the glottal constriction during simulation of both inspiration and expiration, the regions upstream the glottis $\Omega_1 + \Omega_2$, and downstream the glottis $\Omega_3 + \Omega_4$, were designed with a length of $10d_{\text{inlet}}$.

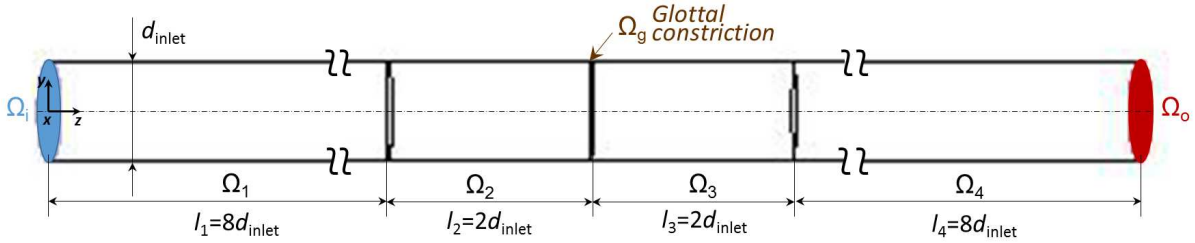

Figure III.5.1: Sketch of the simplified glottal area geometry with the total length of $20d_{\text{inlet}} = 352$ mm.

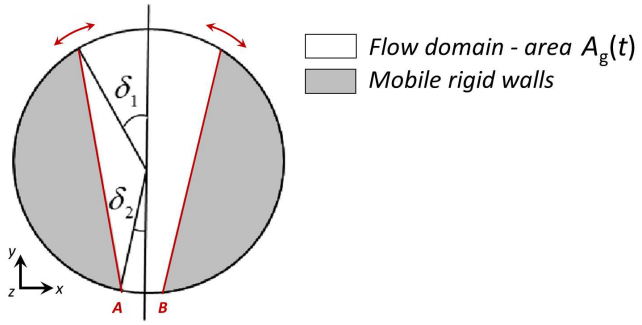

Figure III.5.2: Detail of the simplified glottal geometry (see section III.5.1 for definition of angles δ_1 and δ_2).

As shown in Figure III.5.2, the glottal simplified geometry was approximated by a nearly triangular cross-section of area A_{g}. This shape was typically observed during *in vivo*

laryngoscopic investigation of quiet breathing in Part II, and was already applied in the literature [Renotte et al., 2000]. The middle part proximates the glottis and the gray side parts correspond to the vocal folds. Points A and B are fixed in the geometry, symmetric with respect to the glottal median axis (that of AP_g). Their position is defined by the angle δ_2, chosen constant in time, at a value of 5° (see Figure III.5.2). This value was chosen in agreement with typical measurements performed on laryngeal images recorded in the clinical study (Part II). The glottal motion is parametrized by the angle δ_1 (see Figure III.5.2) whose values can be varied as a function of time. Thereby, the glottal area variations are obtained through the rotation of the side parts around points A and B. To simulate a glottal area variation $A_g(t)$ as measured in Part II, the value of angle $\delta_1(t)$ at shot-instant t was calculated as follows:

$$A_g(t) - \frac{AP_g}{2}\left(\delta_1(t) + \delta_2 + \frac{1}{2}\sin(\pi - \delta_1(t) - \delta_2)\right) = 0. \tag{III.5.1}$$

Equation III.5.1 was solved using Matlab® function *fsolve* in the frame of non-linear equations. Further, details on the mobile boundary conditions for the simulated cases are given in section III.5.3.

5.2 Solution Method

5.2.1 Mechanical model

Flow regime. For realistic inhalation conditions in slow and rapid breathing, the orders of magnitude of the flow parameters in the laryngeal region have been detailed in previous part (see Table II.4.4). In particular, the local mean Reynolds number obtained at the glottis is moderate, ranging between 1900 and 3100, with peak values around 5000. The prior measurements conducted by Dekker [1961] on casts of human trachea (see section I.2.2.1) showed that the critical value of Reynolds number corresponding to the transition between laminar and turbulent regimes is around 460, under steady conditions. Based on that experiment, most of the CFD studies dealing with breathing airflow in the literature assume a turbulent regime in the upper airways geometry (see *e.g.*Sandeau [2010]).
Due to the moderate values of the Reynolds number, and to the different values of flow rates occurring during a mean breathing cycle (see Table II.3.2), it is likely that the flow regime can stand close to the laminar-turbulent transition at some instants in the cycle. By analogy with hemodynamic pulsatile flows of similar characteristic patterns, the flow unsteadiness induces internal stabilization effects, so that laminar regimes can be observed in spite of peak Reynolds number larger than 4000 [Boiron et al., 2007]. Therefore, a turbulence flow model was chosen for the following 3D CFD model, keeping in mind that transitional flows are likely to occur.

Mechanical formulation. In the following, it is assumed that studied gas behaves as a Newtonian incompressible gas. With respect to dynamic meshes, the integral form of the Navier-Stokes flow governing equations in turbulent regime on a volume Ω_i is moving can be written in primitive variables formulation as:

$$\left.\begin{array}{rcl} \nabla \cdot \boldsymbol{u}(\boldsymbol{x},t) & = & 0 \\ \rho\left[\frac{\partial \boldsymbol{u}(\boldsymbol{x},t)}{\partial t} + \left(\left(\boldsymbol{u}\left(\boldsymbol{x},t\right) - \boldsymbol{u}_{\text{grid}}\right)\cdot\nabla\right)\boldsymbol{u}(\boldsymbol{x},t)\right] & = & -\nabla p(\boldsymbol{x},t) + \nabla\cdot\boldsymbol{\tau} \end{array}\right\} \begin{array}{l}\forall[\boldsymbol{x},t] \\ \in \Omega_i \times [0,+\infty[\end{array} \quad \text{(III.5.2)}$$

where variables $\boldsymbol{u}$, p, ρ, τ stand respectively for the Reynolds averaged gas velocity vector, the static pressure, the fluid density, and the viscous tensor. The latter depends on the eddy viscosity coefficient μ_t (Equation III.5.4). Vector $\boldsymbol{u}_{\text{grid}}$ represents the grid velocity of the moving mesh, which is determined for all mesh elements as:

$$\boldsymbol{u}_{\text{grid}} = \frac{\Delta \boldsymbol{y}}{\Delta t}. \quad \text{(III.5.3)}$$

This approach to describe the evolution of fluid domain is referred as Arbitrary Lagrangian-Eulerian (ALE) mapping. The ALE formulation combines the advantage of both classical kinematical descriptions: the Lagrangian and the Eulerian description. In the ALE description, the nodes of the computational mesh may be moved with the continuum in normal Lagrangian fashion, or be held fixed in Eulerian manner, or be moved in some arbitrarily specified way to give a continuous rezoning capability. The advantages are (i) in comparison with a purely Lagrangian method, greater distortions can be afforded; and (ii) in comparison with a purely Eulerian approach, the distortions are handled with higher resolution [Donea et al., 2004].

5.2.2 Numerical method

With respect to the assumption of transitional flows (see previous paragraphs), the Shear-Stress Transport (SST) $k-\omega$ turbulence model was chosen to describe the turbulent flow regime, based on its ability to capture the air flow structures in the transitional flow regimes (*e.g.*, Zhang and Kleinstreuer [2003]; Xi and Longest [2007]; Sandeau et al. [2010]). The Shear-Stress Transport (SST) $k-\omega$ turbulence model combines the advantage of the standard $k-\omega$ model [Wilcox, 1998] in the near wall region and the robustness of the $k-\epsilon$ for the free-stream flow [Menter et al., 2003]. This results in a more complex formulation of the eddy viscosity (Equation III.5.4) that includes two main variables, k the turbulent kinetic energy, and ω the dissipation per unit turbulence kinetic energy. The model was developed by Menter [1993], where can be found its standard formulation. It is a model with two governing equations (Equation III.5.5 and Equation III.5.6), based on the eddy viscosity μ_t [Menter, 1993]:

$$\mu_t = \frac{\rho k}{\omega}\frac{1}{\frac{SF_2}{a_1\omega}}, \quad \text{(III.5.4)}$$

where S is the invariant measure of the strain rate magnitude, F_2 the second blending function (explained below), and the model constant a_1 is the Bradshaw's structural parameter (for details, see definitions in Menter [1993]).

The transport equations are derived from Reynolds Averaged Navier-Stokes equations (RANS) and, applied to dynamic mesh, are written for k as:

$$\rho_{\mathrm{g}}\frac{\partial k}{\partial t}+\rho_{\mathrm{g}}\frac{\partial\left(k\left(\overline{u}_{\mathrm{j}}-u_{\mathrm{grid_j}}\right)\right)}{\partial x_{\mathrm{j}}}=\frac{\partial}{\partial x_{\mathrm{j}}}\left[\left(\eta_{\mathrm{g}}+\frac{\mu_{\mathrm{t}}}{\sigma_{\mathrm{k}}}\right)\frac{\partial k}{\partial x_{\mathrm{j}}}\right]+ \\ +\min\left[-\rho_{\mathrm{g}}\overline{u_{\mathrm{i}}'u_{\mathrm{j}}'}\frac{\partial\left(\overline{u}_{\mathrm{i}}-u_{\mathrm{grid_i}}\right)}{\partial x_{\mathrm{j}}},\ 10\rho_{\mathrm{g}}\beta^{\star}k\omega\right]-\beta^{\star}\rho_{\mathrm{g}}k\omega \quad \text{(III.5.5)}$$

and correspondingly for ω as:

$$\rho_{\mathrm{g}}\frac{\partial\omega}{\partial t}+\rho_{\mathrm{g}}\frac{\partial\left(\omega\left(\overline{u}_{\mathrm{j}}-u_{\mathrm{grid_j}}\right)\right)}{\partial x_{\mathrm{j}}}=\frac{\partial}{\partial x_{\mathrm{j}}}\left[\left(\eta_{\mathrm{g}}+\frac{\mu_{\mathrm{t}}}{\sigma_{\omega}}\right)\frac{\partial\omega}{\partial x_{\mathrm{j}}}\right]-\frac{\alpha}{\mu_{\mathrm{t}}}\overline{u_{\mathrm{i}}'u_{\mathrm{j}}'}\frac{\partial\left(\overline{u}_{\mathrm{i}}-u_{\mathrm{grid_j}}\right)}{\partial x_{\mathrm{j}}}-\beta\rho_{\mathrm{g}}\omega^{2}+ \\ +2\left(1-F_{1}\right)\rho_{\mathrm{g}}\sigma_{\omega,2}\frac{1}{\omega}\frac{\partial k}{\partial x_{\mathrm{j}}}\frac{\partial\omega}{\partial x_{\mathrm{j}}}. \quad \text{(III.5.6)}$$

The first term on the right side of each equations stands for effective diffusivity of k and ω respectively, composed of the diffusion caused by turbulent flow fluctuations and by molecular diffusion. The second (source) term represents the production of k and ω respectively, and the third (sink) term stand for the dissipation of k and ω, respectively. Finally the fourth term on the right side of Equation III.5.6 includes the first blending function F_1. This and the second blending function F_2 ensure that close to boundary is valid the $k-\omega$ model and in distance the $k-\epsilon$ model.

The flow mean velocity $\overline{u}_{\mathrm{i}}$ is composed from mean (ensemble-averaged or time-averaged) and fluctuating components, and the velocity $u_{\mathrm{grid_{i,j}}}$ is the instantaneous velocity of the moving mesh boundaries. Details and definitions on the turbulent Prandtl numbers σ_{k} and σ_{ω} for k and ω respectively, the coefficients in dissipation terms of transport equations $\beta^{\star}$ and β, and other model constants can be found in Menter [1993] and Menter et al. [2003].

5.2.3 Simulation setting

The equations were solved by means of a finite volume method using first-order time, spatial discretization schemes, and time step set to 2.5×10^{-3}s. The unsteady calculation had 1260 time steps. Iterative convergence was achieved when the dimensionless RMS residuals over the entire flow field were inferior to 10^{-4}, which occurred at each time-step after about 50 iterations. The Courant-Friedrich-Lewy (CFL) criterion

$$CFL_{\mathrm{inlet}}=\frac{\overline{u}_{\mathrm{inlet}^{\max}}\Delta t}{\Delta x_{\mathrm{inlet}}}=14.5[-], \quad \text{(III.5.7)}$$

is derived for the inlet area using the inlet velocity $\overline{u}_{\mathrm{inlet}}$

$$\overline{u}_{\mathrm{inlet}}(t)=\frac{\overline{Q}(t)}{A_{\mathrm{inlet}}}, \quad \text{(III.5.8)}$$

where the inlet area is

$$A_{\text{inlet}} = \frac{\pi {d_{\text{inlet}}}^2}{4}, \tag{III.5.9}$$

. In the present solution for the shot-instant $t(\overline{Q}_{\max})$ the $CFL = 10$. Even if $CFL > 1$, calculation converged, so neither mesh dimensions and neither Δt had to be changed.

5.3 Initial & Boundary Conditions

As for the 2D CFD model (see Boundary Conditions in Annex B - 2D Model), the airflow rate input conditions and glottal geometry kinematics were based on the data from the preliminary *in vivo* study (see section II.3.1.1).

All boundary conditions were set and the simulation was conducted for one breathing cycle. The computational process of this transient calculation is illustrated by a flow chart on the Figure III.5.3. At first, the initial conditions (items ((a) and (b)) are applied and the boundary conditions are set (items (c)) to (k)). Next, the CFD equations are processed until convergence is achieved and particles touching the walls of the model are post-processed (item (l)). New time step is passed, mesh nodes in domain Ω_{g} are recalculated (item (h)) and the attached domains Ω_2 and Ω_3 are smoothed and remeshed if skewness or size of the elements exceeds preassigned limits (item (i)). Finally, the inlet velocity (item (c)) and particles injection (item (k)) are set.

Initial and boundary conditions were set for different domains of the model Ω_{i}, Ω_1, Ω_2, Ω_3, Ω_4, Ω_{g}, and Ω_{o} (see Figure III.5.1) as follows:

Initial conditions

(a) Initial conditions with zero velocities $u_{(t=0)} = 0$ and pressures $p_{(t=0)} = 0$ were assumed at all points.

(b) At the inlet wall Ω_{i}, the initial values for the turbulent kinetic energy k and the specific dissipation rate ω were assigned, assuming a fully developed flow, using the empirical relation as follows:

$$k_{inlet} = \frac{3}{2}(u_{\text{z}}^{\max} I)^2 \qquad \text{and} \qquad \omega_{inlet} = \frac{2u_{\text{z}}^{\max} I}{3\ell_{\text{T}}}, \tag{III.5.10}$$

where I is the turbulence intensity chosen at 2% (low intensity) and ℓ_{T} the turbulence length scale:

$$\ell_{\text{T}} = 0.07 d_{\text{inlet}}. \tag{III.5.11}$$

The factor 0.07 is based on the maximum value of the mixing length in fully-developed turbulent pipe flow [Schlichting, 1968, p. 568].

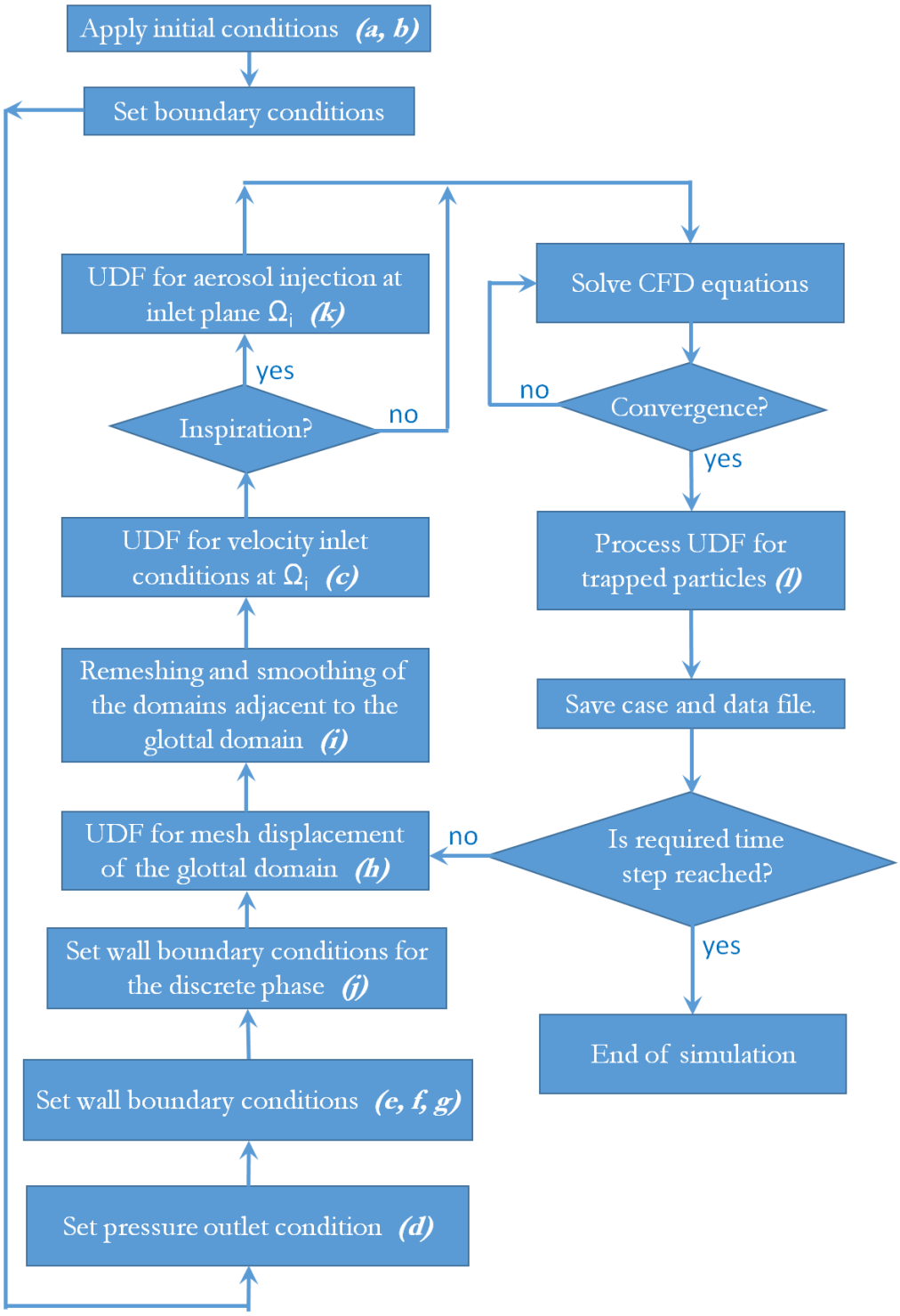

Figure III.5.3: A flow chart of the numerical process. See list in the Initial & Boundary Conditions section for details on the items in brackets.

Flow boundary conditions

(c) The inlet velocity $\overline{u}_{inlet}(t)$ is set at the inlet face Ω_i. The time-variations were evaluated in agreement with the *in vivo* recordings of female subject S1 (section II.3.1.1) using the airflow rate $Q(t)$ (see Equation III.5.8). The mean flow rate $Q(t)$ cycle (see Figure III.5.4a) was calculated from 54 quiet breathing cycles. The unsteady boundary condition was coded in C programming language using a User Defined Function (UDF) with DEFINE_PROFILE macro.

(d) A pressure outlet boundary condition $p(t)$ was set at outlet domain Ω_o to 0 Pa.

Wall boundary and dynamic mesh conditions

(e) On solid walls of Ω_1, Ω_2, Ω_3, and Ω_4 domains, a no slip shear boundary condition $\boldsymbol{u}_\mathrm{wall} \cdot \boldsymbol{n} = 0$ was applied, where $\boldsymbol{u}_\mathrm{wall}$ is the velocity vector of the wall motion, here equal to zero and $\boldsymbol{n}$ is the outward normal vector.

(f) The wall boundary conditions at Ω_1, Ω_2, Ω_3, and Ω_4 domains for the $k-\omega$ model equations correspond to the wall function approach for wall-function meshes and to the appropriate low-Reynolds number boundary condition for the fine meshes. The value of ω is specified at the wall as:

$$\omega_\mathrm{w} = \frac{\rho_\mathrm{g}(u^*)^2}{\eta}\omega^+, \tag{III.5.12}$$

where u^* is the friction velocity (for definition see Equation III.5.14 in the following chapter), η is the fluid dynamic viscosity and ω^+ is defined for both laminar sublayer and logarithmic region (see Launder and Spalding [1974] for details).

(g) The wall boundary conditions for the inlet Ω_i and outlet face Ω_o were imposed as:

$$\frac{\partial k}{\partial n} = \frac{\partial \omega}{\partial n} = 0, \tag{III.5.13}$$

where n is the normal to the boundary.

(h) The deforming motion of solid boundaries in glottal domain Ω_g was set according to the area of the glottal constriction A_g (for definition see Figure II.3.4c in section II.3.2.2) as measured in the clinical preliminary study (section II.3.1). The chosen kinematics are the ones registered during the typical quiet breathing cycle of subject S1 (see Figure III.5.4a). Two different cases were simulated for comparison:

- **Case 1** considers a steady glottal geometry with a glottal area $A_\mathrm{g}(t) = 90.2$ mm^2 (see Figure III.5.4a). This value corresponds to the initial inspiration value at $Q = 0$ L/min obtained during typical quiet breathing cycle of subject S1 from preliminary *in vivo* study: $A_{\mathrm{g(t=0)}} = 90.2$ mm^2 (section II.3.1.1). Note that this glottal area dimension is in agreement with the glottal aperture used by Brouns et al. [2007a] in their CFD study.

- **Case 2** considers a glottal area moving in time, $A_g(t)$. Time-variations are the ones measured during typical quiet breathing cycle of subject S1, and displayed in Figure III.5.4a. The corresponding evolution of angle δ_1 [°] is displayed on III.5.4b. Angle δ_1 varies between 10 and 40° and was defined by resolving the Equation III.5.1 for given values $A_g(t)$.

  The resulting geometry of the glottal model in case 2 can be compared with real laryngoscopic images acquired for female subject S1 in Figure III.5.5. This figure shows two shot-instants chosen during one typical breathing cycle of subject S1, as displayed on the airflow rate signal Q: the first one corresponds to peak inspiration (Figure III.5.5a), and the second one to peak expiration (Figure III.5.5b).

  The movement in the glottal plane Ω_g was assured by rotation of the rigid walls around the points A and B in Figure III.5.2. The movement of each node in glottal plane was accomplished every time-step by UDF loaded and compiled within the ANSYS Fluent solver. The UDF was based on the DEFINE_GRID_MOTION macro and the movement was determined solving a cross-multiplication. Resulting mesh at peak inspiration and peak expiration is shown at Figure III.5.6.

(i) Volumes Ω_2 and Ω_3, attached to the glottal plane, were updated every time-step applying the smoothing and remeshing function of the ANSYS Fluent solver, if the skewness or size of the mesh elements exceeds specified values. This ensured adequate mesh quality over the entire calculation. The quality of the mesh over the whole breathing cycle is reported later for final model of upper airways.

Discrete phase boundary condition

(j) The wall boundary conditions for the discrete phase are set: "*escape*" at the inlet Ω_i and outlet Ω_o faces, and UDF for trapped particles at all the other faces (see item (l)). This ensures that a particle passing the outlet boundary Ω_o during inspiration or passing the inlet boundary Ω_i during expiration (leaving the computational domain) is lost for further calculation and a particle touching all the other walls is post-processed according to conditions set in the UDF (see (l)).

(k) A monodisperse aerosol was injected from inlet area Ω_i into the model during the inspiration phase (between $t = 0$ and $t = 1.5$ s). The particles were composed of liquid water with density 998.2 kg/m^3 and had a spherical shape with diameter $D_p = 5.7$ µm. Those values correspond to large particles utilized in *in vivo* study of Conway et al. [2012] (note that the diameter was evaluated as the volume median diameter). The particle's injection speed and direction were chosen identical to the inlet airflow velocity ($\boldsymbol{u}_p = \boldsymbol{u}$). Thus, the Stokes number Stk (Equation I.1.13) varied between 0 and 0.45. The particles were injected from the center of each mesh element at the inlet face. So, the number of particles injected at one instant corresponds to the number of cells in the inlet surface. The time step is equal to the time step of the calculation, *i.e.*, 2.5×10^{-3}s. This results to face-uniformly injected particles in accordance with linear function (see linear injection curve at Figure III.5.13).

In the present case, the density of the particle is much larger than the density of the gas $\rho_p >> \rho_g$. So, the only non-negligible force on the particle is the drag force $\boldsymbol{F}_D$ [Crowe et al., 2011]. Thus, the equation of motion for a single particle (see Equation I.1.2 in section I.1.3.1.d) is used for the present simulation in the form without the second term on the right side. For the final simulation with realistic upper airways model, the importance of Brownian diffusion will be discussed (see section III.6.2.2).

(l) The discrete phase boundary condition for particles touching the wall (walls of Ω_1, Ω_2, Ω_g, Ω_3, and Ω_4 domains) was programmed using an UDF with DEFINE_DPM_BC macro. The UDF removes such a particle from the computational domain and saves information about its position and velocity.

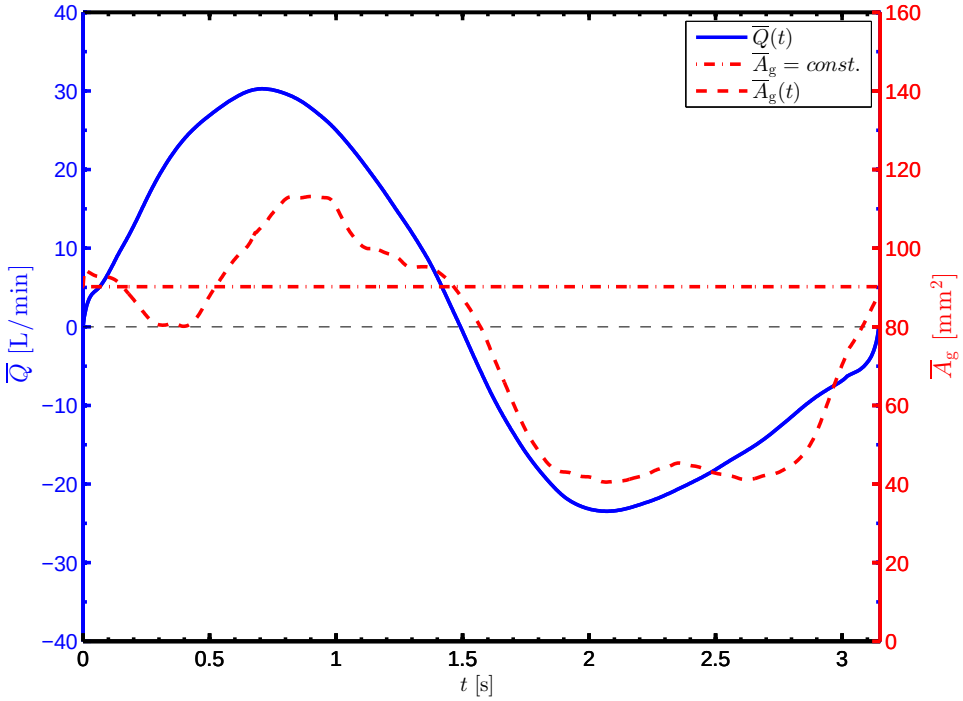

(a) Evolution of airflow rate $\overline{Q}$ and glottal area A_g in function of the time t. Flow rate $\overline{Q}$ is mean of 54 quiet breathing cycles and positive axis corresponds to inspiration, negative to expiration. Area $A_g(t)$ corresponds to a typical quiet breathing cycle and area $A_g = const.$ corresponds to the initial value $A_g(t = 0) = 90.2$ mm^2.

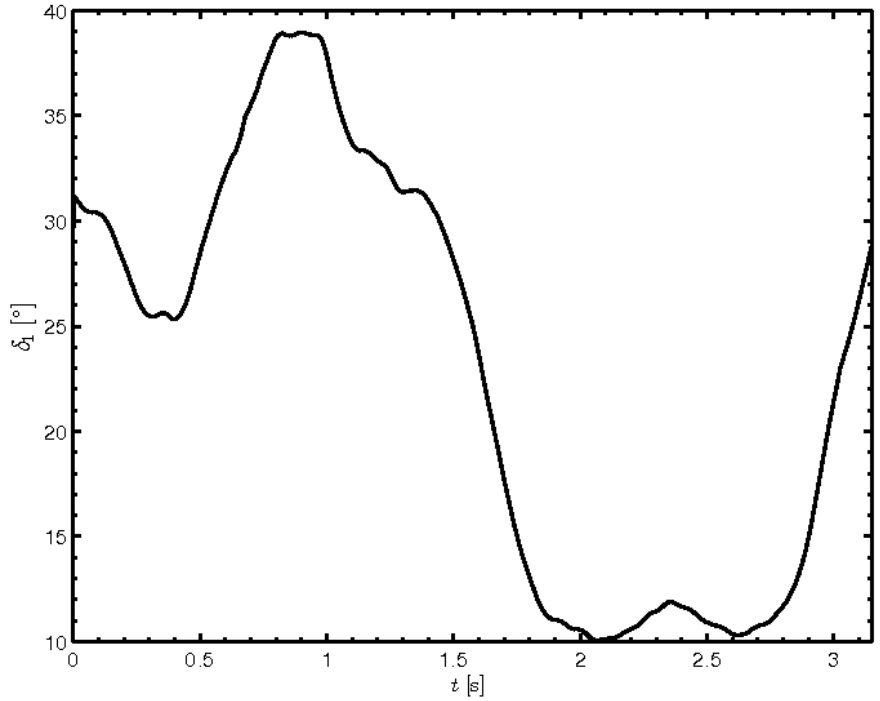

(b) Evolution of angle δ_1 [°] derived from glottal area A_g.

Figure III.5.4: Reference data for the unsteady boundary conditions measured on female subject S1 in preliminary *in vivo* study (see section II.3.1.1).

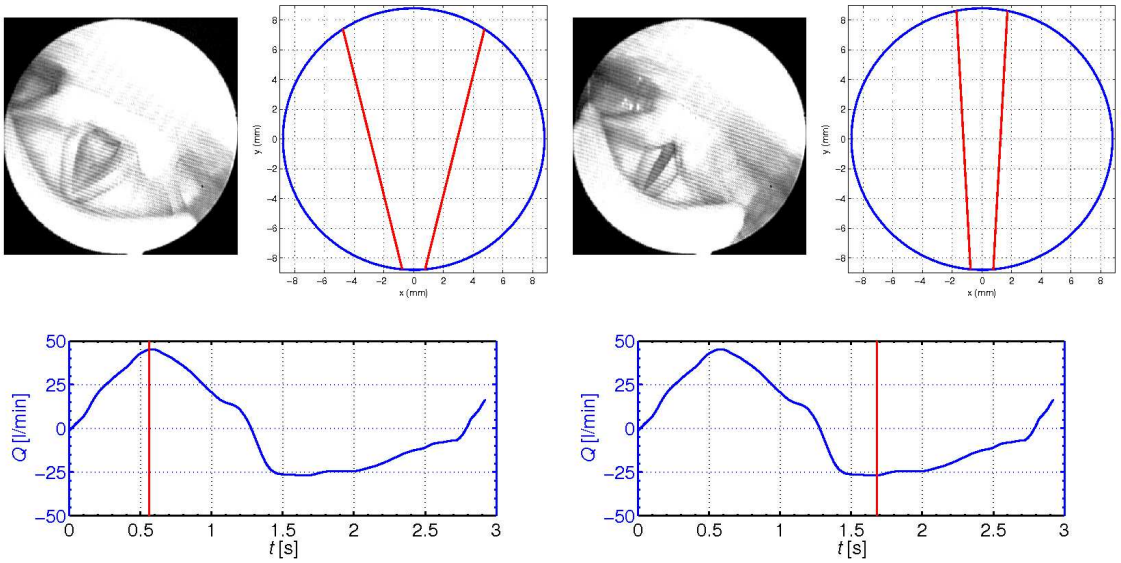

(a) A shot-instant at the peak inspiration.

(b) A shot-instant at the peak expiration.

Figure III.5.5: Laryngeal images of glottal area, with corresponding proposed glottal geometry of the model and corresponding measured airflow rate Q [L/min](subject S1 from preliminary experiments - see section II.3.1.1).

5.4 Mesh Properties

The unstructured grid of the model was created in GAMBIT 2.4.6 (Fluent, Inc.). Two different mesh elements were used:

i. The volumes Ω_1 and Ω_4 (see Figure III.5.1) were meshed using hexahedral elements and only where appropriate, also wedge elements. Elements were stretched in the neighborhood of the walls using layering meshing technique.

ii. For the middle parts Ω_2 and Ω_3 (the regions connected to the moving glottal diaphragm) the tetrahedral grid elements advisable for regions with dynamic meshes were chosen. The mesh was generated primarily with tetrahedral elements, but, if appropriate, also hexahedral, pyramidal, and wedge elements were used. Mesh elements were refined at the walls and thus, density of the mesh was not homogeneous on the whole computational field.

Detail of the mesh in the glottal area is given in Figure III.5.6. Here panel (a) represents the largest opening (inspiration phase) and panel (b) the narrowest constriction of the glottal geometry (expiration phase).

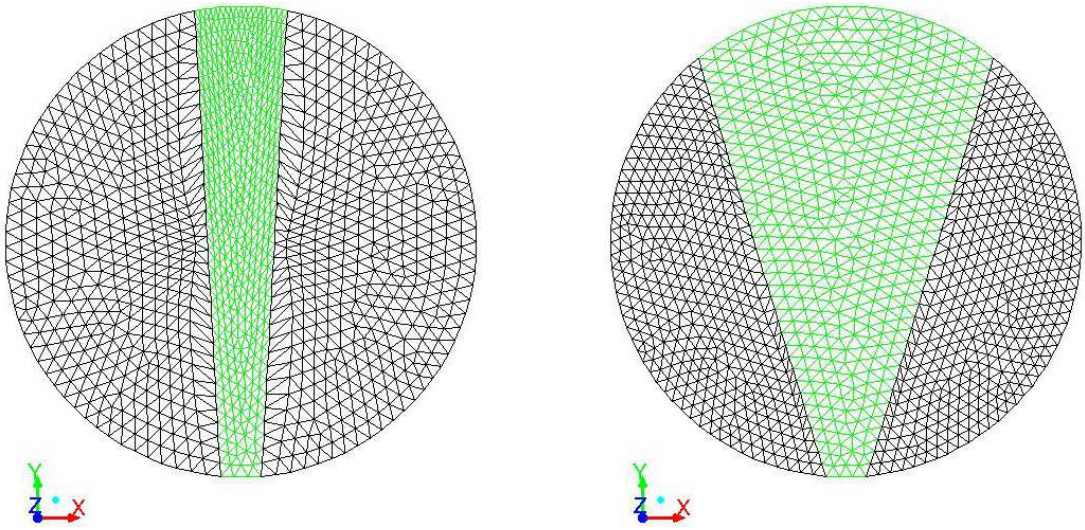

(a) A shot-instant at the peak inspiration. The geometry corresponds to laryngoscopic image at Figure III.5.5a

(b) A shot-instant at the peak expiration. The geometry corresponds to laryngoscopic image at Figure III.5.5b.

Figure III.5.6: A snapshot of the surface mesh in glottis constriction (green part corresponds to interior wall and black parts to wall boundary condition).

In total, three meshes with different refinement levels were tested for the future calculations. The transient simulations were realized in ANSYS Fluent solver (ANSYS® Fluent Academic Research, Release 14.0) with steady boundary conditions (velocity inlet $u_{\text{inlet}} = 2$ m/s corresponding to peak inspiration flow PIF in Figure III.5.4a). The main mesh characteristics are summarized in Table III.5.1.

	Mesh 1	Mesh 2	Mesh 3
N° of elements	284289	608130	1369071
$\Delta x^{\min}_{\text{glottis}}$ [mm]	1.00	0.75	0.5
$\Delta x^{\min}_{\text{tube}}$ [mm]	0.25	0.19	0.13
u^*_{glottis} [m/s]	0.490	0.490	0.490
u^*_{tube} [m/s]	0.288	0.288	0.288
y^+_{glottis}	33.4	25.1	16.7
y^+_{trachea}	4.9	3.7	2.45

Table III.5.1: The main characteristics of the three meshes.

Parameter $\Delta x^{\min}$ is the smallest mesh element size, u^* is the friction velocity:

$$u^* = \sqrt{\frac{\tau_{\text{w}}}{\rho}}, \tag{III.5.14}$$

where τ_{w} is the wall shear stress defined as:

$$\tau_{\text{w}} = \frac{1}{2}\rho u^2 c_{\text{f}}, \tag{III.5.15}$$

c_{f} is the friction coefficient solved from equation [Launder and Spalding, 1974]:

$$c_{\text{f}} = 2 \cdot 0.039 \cdot Re^{-\frac{1}{5}}. \tag{III.5.16}$$

Using friction velocity u^* the dimensionless distance from wall y^+ can be calculated:

$$y^+ = \frac{u^* \Delta x^{\min}}{\eta}. \tag{III.5.17}$$

Comparison of the results obtained for the three meshes is plotted in Figure III.5.7. Panel (a) represents the velocity magnitude simulated along the center-line of Ω_2 and Ω_3 domains (see Figure III.5.1). Panel (b) represents the velocity magnitude simulated along the antero-posterior line of the glottis plane. All three curves converge to same values of velocity magnitude. This is validated by comparison of Mesh 3 chosen as a reference mesh, with Mesh 2 and Mesh 1 using Error Norm L2:

$$\varepsilon = \frac{\sqrt{\sum_{i=1}^{n} \frac{1}{n} \left(u_{\text{i}}^{\text{ref}} - u_{\text{i}}\right)^2}}{\sqrt{\frac{1}{n} {u_{\text{i}}^{\text{ref}}}^2}} \tag{III.5.18}$$

There was found only 3.4% difference between Mesh 3 and Mesh 2 and 4.3% between Mesh 3 and Mesh 1. Therefore, in order to achieve the best accuracy of the CFD solution, the finest Mesh 3, with the smallest y^+ number, was chosen.

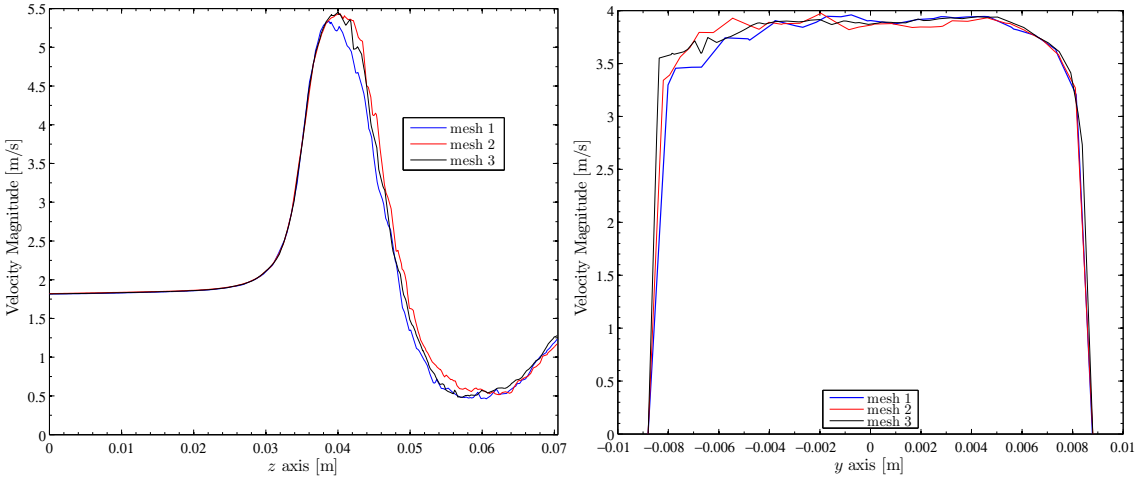

(a) Velocity magnitude $|\,u\,|$ along the center-line of Ω_2 and Ω_3 domains.

(b) Velocity magnitude $|\,u\,|$ at the glottal antero-posterior line.

Figure III.5.7: Comparison of the results obtained with the three tested meshes.

5.5 Results

Simulations were performed in ANSYS Fluent solver (ANSYS® Fluent Academic Research, Release 14.0) for both cases 1 and 2 presented in the previous section. First simulation (case 1) was performed considering unsteady experimental flow inlet conditions together with glottal static wall boundaries. Second simulation (case 2) was performed using unsteady conditions for both airflow and glottal moving walls (see section III.5.3 and Figure III.5.4a). The results on the flow field are presented in the first part and on the aerosol deposition in the second part.

5.5.1 Study of Flow in Case 1 & 2

In the following, the flow is studied in details mainly at the instant of peak inspiratory flow PIF, where the effects should be important on the particle deposition by inertial impaction.

Figure III.5.8 shows the velocity magnitude $|u|$ contours for peak inspiration PIF and peak expiration PEF, respectively. The cut through the model in the plane $y = 0$ points out the laryngeal jet formed at the glottal constriction area. The flow passing the glottal constriction is not furthermore axially symmetrical and the jet formed shifts towards the wall of the tube. The attraction of the fluid jet to the nearby wall is often referred as the Coandă effect. It was observed in the 2D simulations (see Annex B - 2D Model) and also found in the literature (*e.g.*, see Česenek et al. [2013]). This phenomenon is noteworthy in particular during peak expiration flow PEF (Figure III.5.8b) for the case 2 with moving glottal constriction.

The maximum streamwise velocity reached by the flow during PIF is around 4.0 and

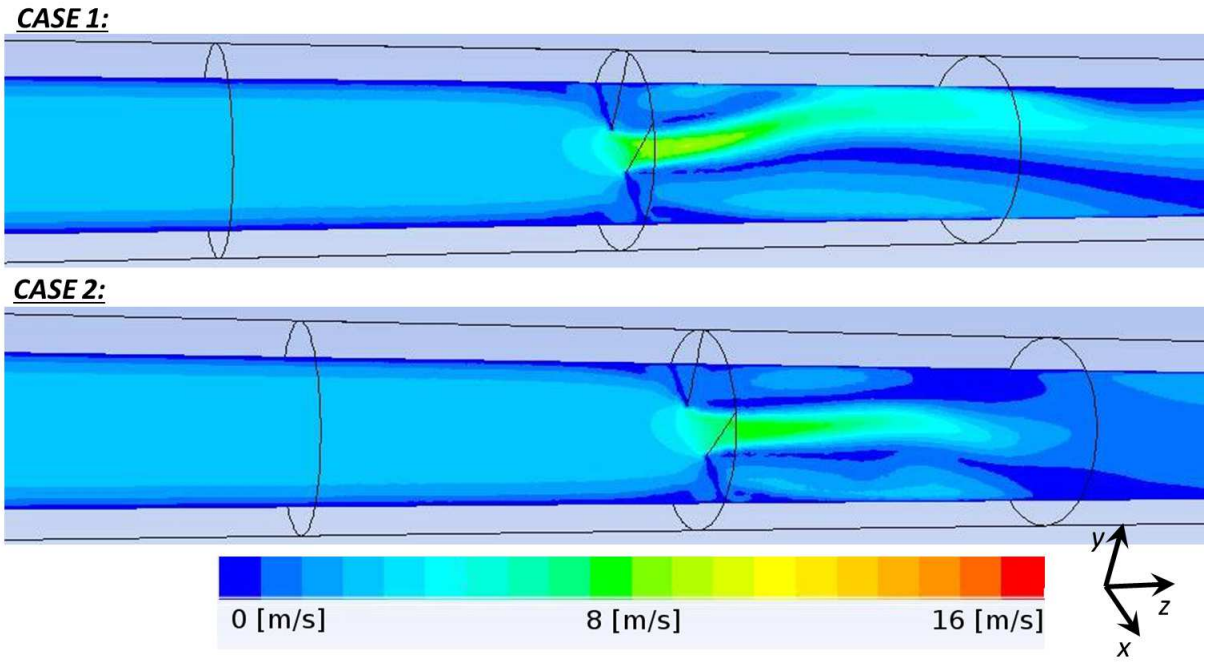

(a) Inspiration peak (PIF).

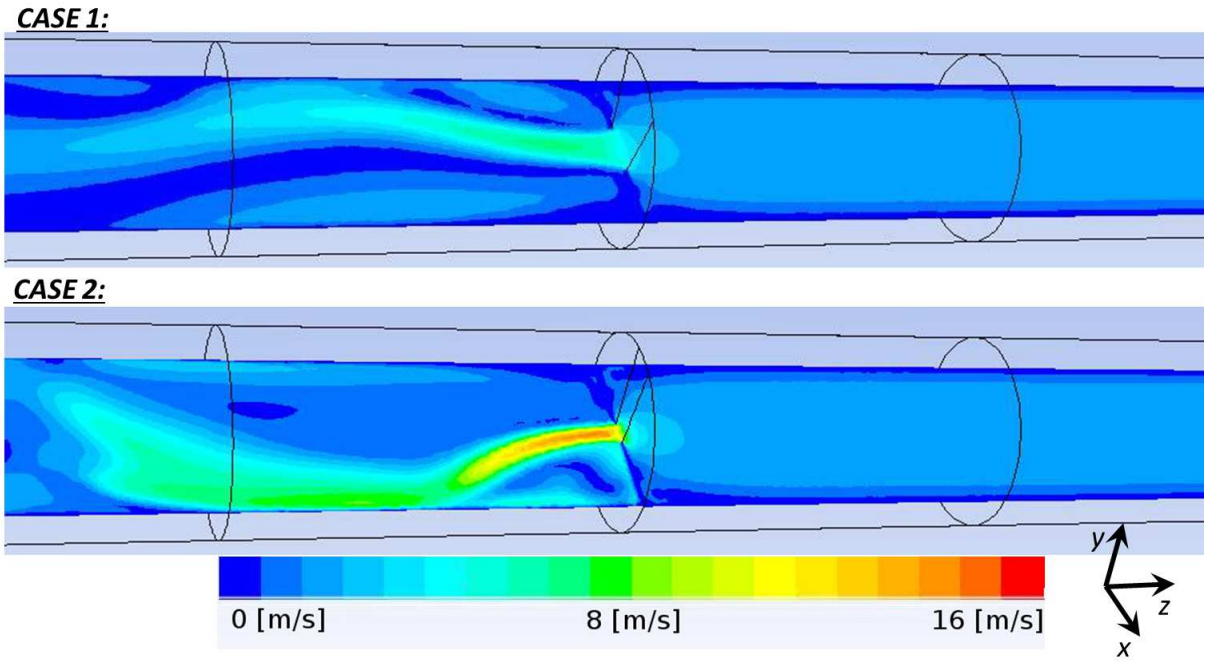

(b) Expiration peak (PEF).

Figure III.5.8: Contours of velocity magnitude $|u|$ [m/s] at the plane $y = 0$. Comparison of case 1 and case 2 at peak inspiration (panel a) and peak expiration (panel b).

$3.5u_{\text{inlet}}$ for case 1 and 2 respectively, that is within the range of amplitudes found also by Renotte et al. [2000]. During PEF the flow reaches velocity up to 3.8 and $9.3u_{\text{inlet}}$ for case 1 and 2, respectively. High value for case 2 is caused by the very narrow glottis aperture measured during expiration.

Figure III.5.9a illustrates the velocity magnitude $|u|$ contours in the plane $x = 0$, per-

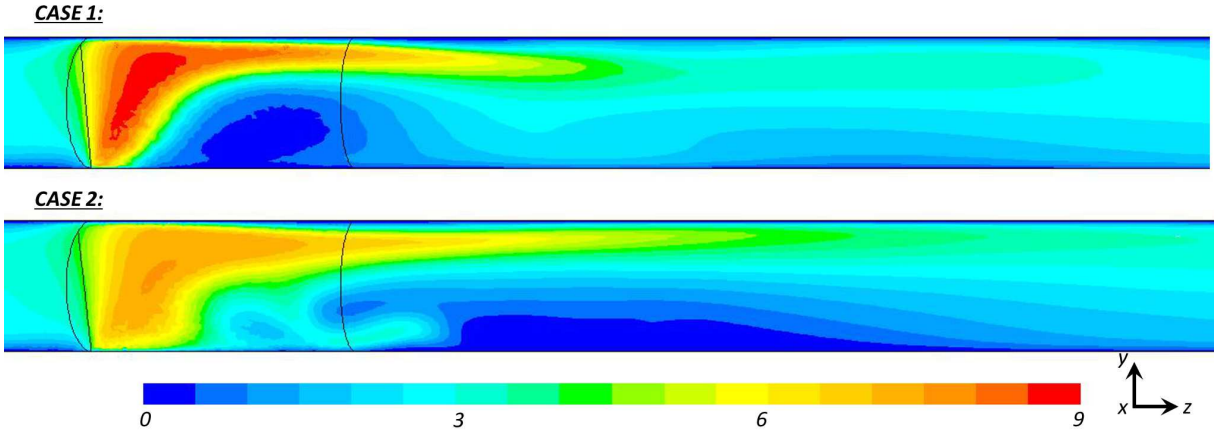

(a) Velocity magnitude $|u|$ [m/s].

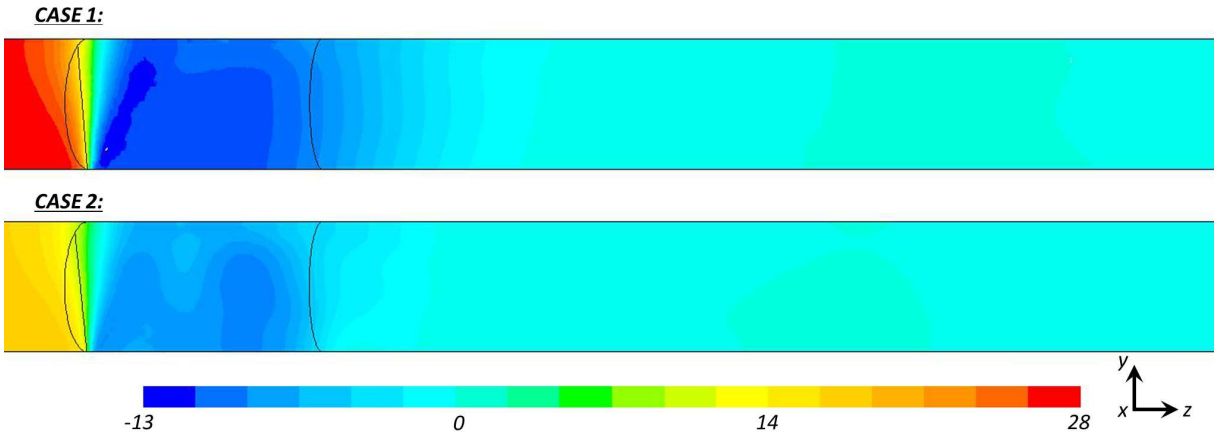

(b) Static pressure [Pa].

Figure III.5.9: Contours of different flow dynamics parameters at the plane $x = 0$ and shot-instant of peak inspiration (PIF). Comparison of case 1 and 2.

pendicular to plane displayed in Figure III.5.8. The chosen shot-instant corresponds to the peak inspiration flow, PIF. The important feature is the shift of the jet towards the upper (posterior part in sense of glottal plane) wall of the tube, in agreement with the simulations of the flow through glottal region performed by Gemci et al. [2000]; Renotte et al. [2000]. The static pressure contours presented on Figure III.5.9b can explain the shift of the jet towards the widest opening of the glottis. Likewise in perfect fluid, the flow is following the direction towards regions with lower pressure. In our case, in the section before glottal plane, the flow starts to orientate towards the low pressure region,

which is found in the upper part of the glottal plane.

Further description of the laryngeal jet during PIF is given in Figure III.5.10. The generated contours represent the axial velocity u_z and the superposed vectors are scaled according to the magnitude of the secondary flow, here represented as the tangential velocity. The profiles presented are perpendicular to model z-axis. The first panel represents the profile in the glottal plane $z = 0$. Further panels correspond to the subsequent planes in the tube. In both cases 1 and 2, at the glottal plane the flow reaches axial velocity around 6 m/s. The vectors show that the pressure gradient force induces strong secondary flows, forming the flow direction towards the central plane $x = 0$. In subsequent levels, the flow shifts towards the posterior wall and until the distance $z = 1.5\, d_{\text{inlet}}$ the importance of secondary vectors is noteworthy. As the high-speed flow is moving downstream the glottal plane, it is being slowed down and a backflow up to -3 m/s is generated. Renotte et al. [2000] observed similar recirculation zone downstream the glottal orifice. Finally, at a distance $z = 5\, d_{\text{inlet}}$ the secondary flow is negligible, the laryngeal jet losses its kinetic energy, the flow stabilizes and becomes uniform. These observations are also in agreement with results by Renotte et al. [2000]. Therefore, it may be concluded that the flow is well predicted by the proposed model and the selected geometrical and numerical models are adequate.

The importance of laryngeal jet and secondary flow with recirculation zones is crucial for particle deposition efficiency. The recirculation zones are formed in the location where the jet impacts the walls of the tube. This can be observed on Figure III.5.8 in the plane $y = 0$. On Figure III.5.10 is explained the velocity composition of the laryngeal jet and the importance of tangential velocity. The secondary flow is pushing the high-speed flow towards the anterior wall as shown on Figure III.5.9a.

Another important parameter from the physiological point of view is the transglottal pressure drop. Figure III.5.11 presents the results obtained along the center-line of the 3D model. The figures compare the two simulation cases with/without moving boundaries, showing the importance of the mobile glottal geometry, located at $z = 0$ and representing the realistic conditions. In particular, the narrow constriction during expiration demonstrates the influence of glottal variations on pressure drop dynamics (see Figure III.5.11b). Curves on III.5.11a representing the PIF are in agreement with previous other studies concerned with the inspiratory flow [Kleinstreuer and Zhang, 2003; Brouns et al., 2007b]. The pressure drop dynamics is visualized on Figure III.5.12 for the entire cycle. The curves represent the total pressure drop through the model in function of the airflow rate. The order of magnitude is in accordance with the preliminary *in vivo* study (see Figure II.3.2 detailed in section II.3.1.2), and confirms the significance of realistic glottal movements for the airflow.

5.5.2 Aerosol Deposition

On Figure III.5.13 are demonstrated the particles injected into the model and their ratio of deposition on the model walls and the ratio of particles escaped by the outlet face in

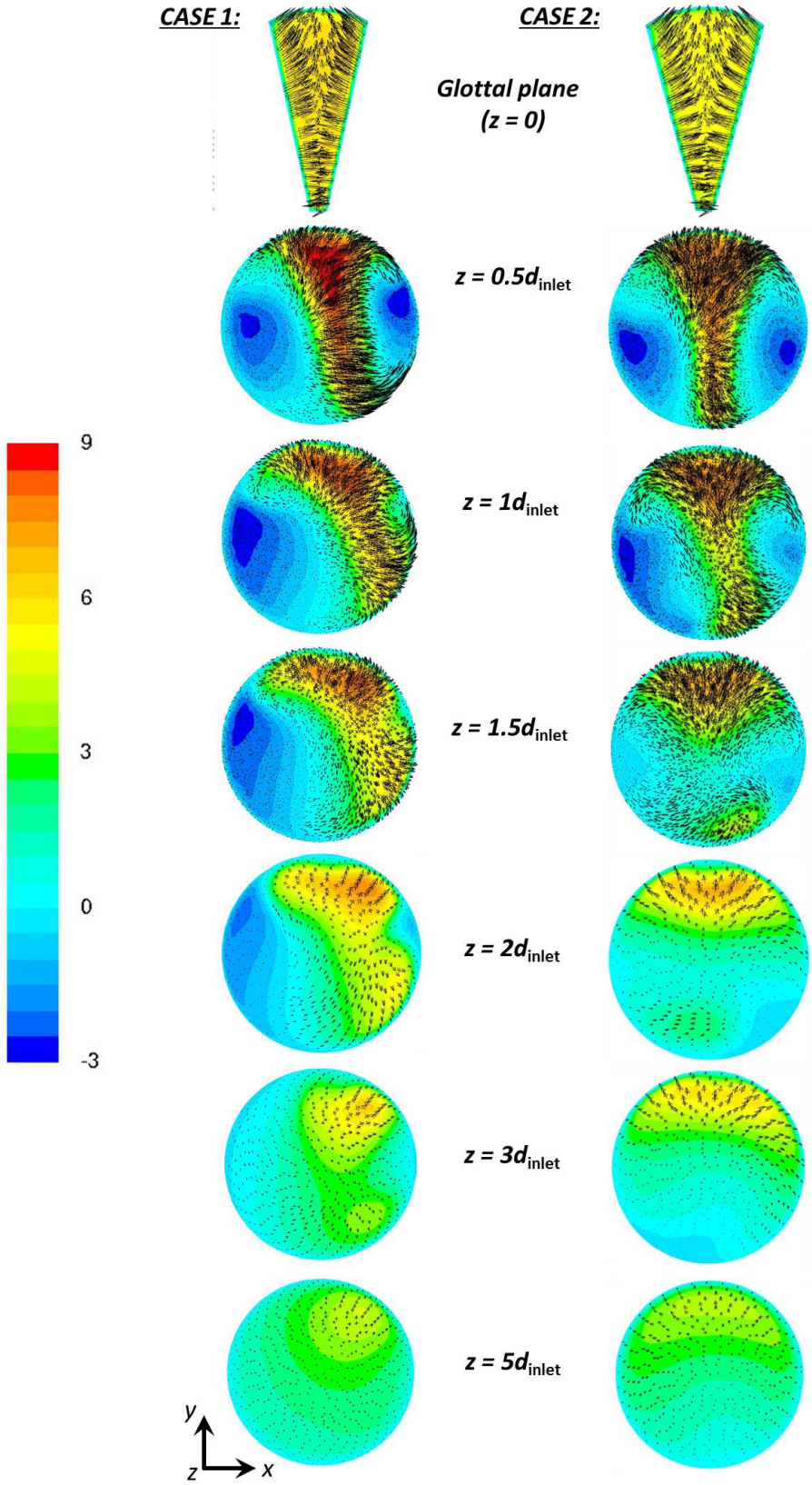

Figure III.5.10: Contours of axial velocity u_z [m/s] and vectors of secondary flow (tangential velocity) for glottal plane and subsequent cross-sections at the shot-instant of peak inspiration. Comparison of case 1 and 2.

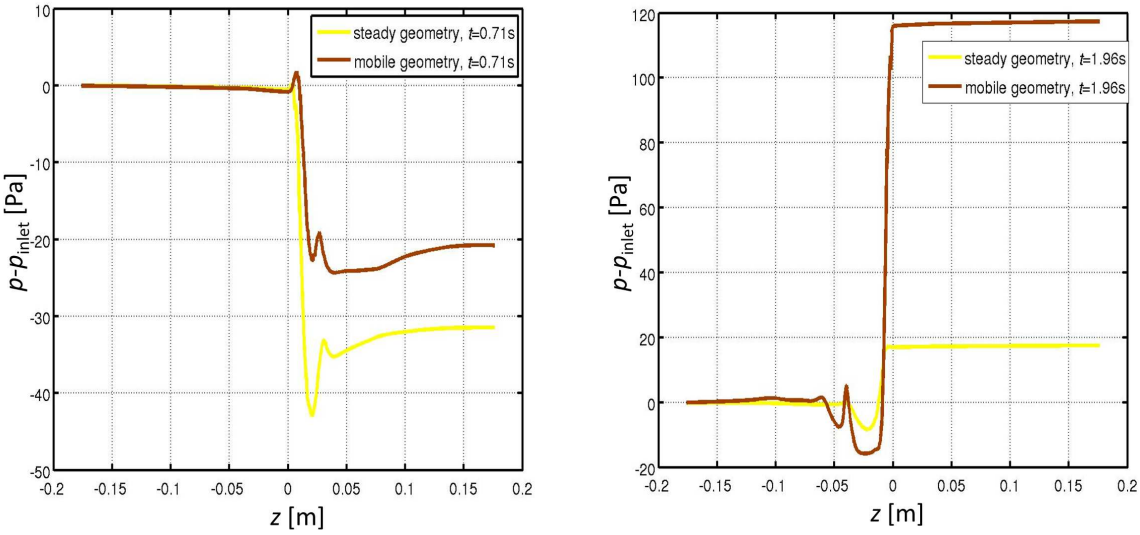

(a) At the instant of peak inspiration ($t = 0.71$ s).

(b) At the instant of peak expiration ($t = 1.96$ s).

Figure III.5.11: Variations of pressure drop as a function of the axial distance from the inlet. Comparison of case 1 and 2. Note that the glottal diaphragm is found at $z = 0$ m.

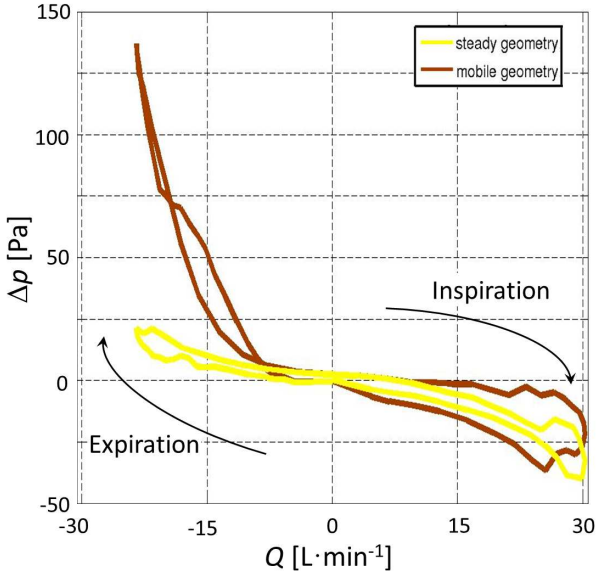

Figure III.5.12: Total pressure drop Δp through the model in function of the flow rate Q. Comparison of case 1 and case 2.

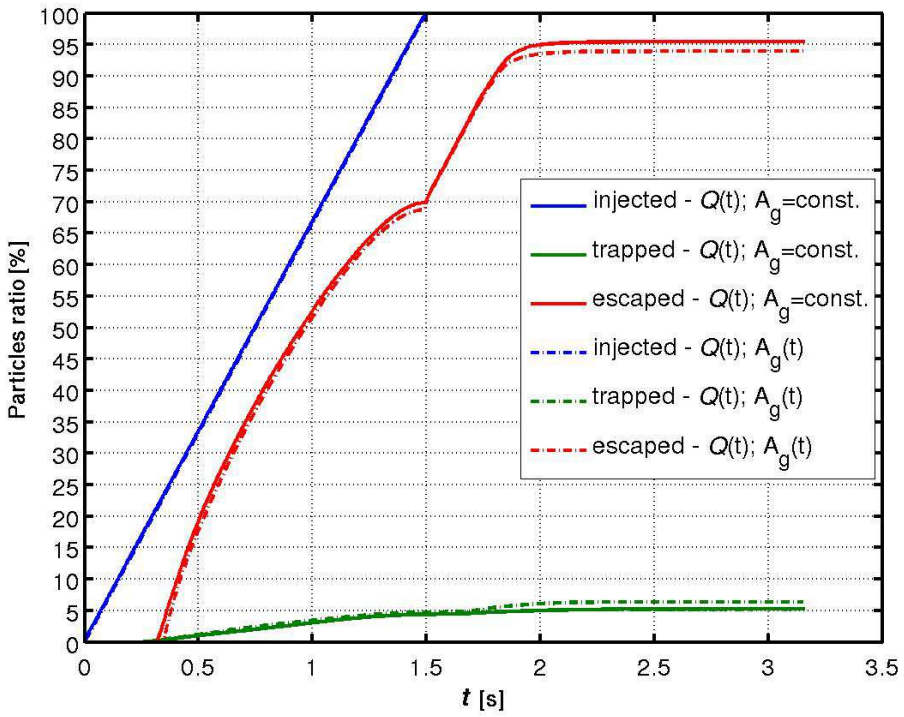

Figure III.5.13: Ratio of particles injected, deposited and escaped from the model in function of the time.

function of the time t. Comparing the resulting curves with the inlet flow rate curve $Q(t)$ on Figure III.5.4a we can deduce the particle flow and deposition dynamics assumptions.

Only a few particles is deposited on the walls of the model before the instant $t = 0.25$s. Indeed, in the beginning of the inspiration the flow speed is low and only few particles is present in the model. Later, at the instant $t = 0.3$s first particles were transported through the entire model and start to escape by the outlet face Ω_o. The number of particles escaping from the model as well as number of deposited particles increases with the airflow velocity. However, around the instant $t = 1.5$s the flow is changing from the inspiration to the expiration, the injection stops and the flow speed is low. Hence, only few particles are deposited or escaped around this instant. Next, during expiration no particles are being injected into the model and thus only remaining particles are being transported with the airflow stream. As the flow speed rises, the deposition and number of particles escaped (in this time by face Ω_i) rises, until all of the particles leave the computational domain. The results of one breathing cycle show that only minor part (less than 10%) from the total number of the injected particles is deposited within the model. The realistic case 2, with mobile glottal walls enhanced 2% in the deposited fraction. Nevertheless, this effect of the moving glottal constriction is negligible in comparison to total number of injected particles.

The deposition sites are displayed on Figure III.5.14 and both cases can be compared. Two

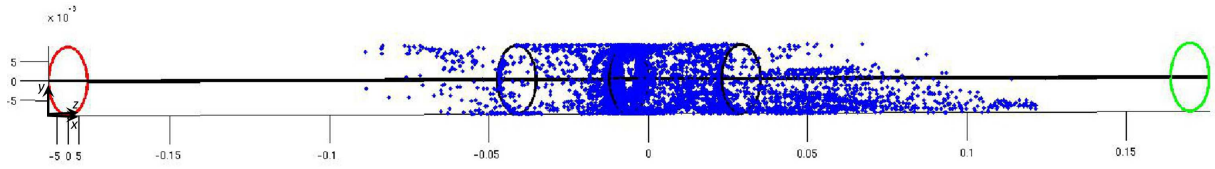

(a) Case 1 - steady glottal geometry model.

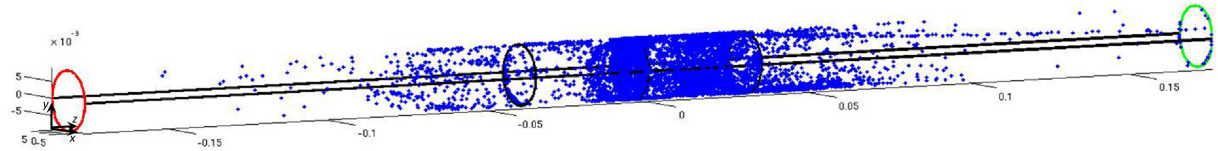

(b) Case 2 - dynamic glottal geometry model.

Figure III.5.14: Illustration of the deposited particles after 1 breathing cycle simulation. Comparison of case 1 and case 2. Note that inlet Ω_i and outlet Ω_o faces are found on the left and right end of the tube, respectively.

main deposition regions are observed: (i) particles are deposited due to inertia effects at the wall of glottal constriction and (ii) downstream the glottal plane the particles deposit at the side of the airflow jet impaction. Thus, the deposition downstream the glottis depends on the creation of the laryngeal jet and the influence of the secondary flows described in previous section.

In conclusion, the glottal geometry has an important influence on the creation of the laryngeal jet and subsequent deposition of the particles in this region. Nevertheless, the differences between steady and dynamic geometries are found negligible and hence, does

not play a significant role on overall deposition in the present geometry of the glottal area.

Chapter III.6

3D CFD Model of Upper Airways with Mobile Glottis and Unsteady Breathing Conditions

---

This chapter describes the elaboration of the final 3D CFD model used in this thesis to study the airflow and the aerosol transport and deposition in the upper airways. Starting from the preliminary 3D CFD model presented in chapter III.5, the final methodology is detailed in the next sections. The chosen idealized geometry is described in section III.6.1 and the mechanical formulation in section III.6.2. Next follows section III.6.3 on the applied boundary conditions, defined according to the clinical measurements reported in Part II. section III.6.2.2 deals with the discrete phase model, while the mesh properties are detailed in section III.6.4. The results obtained from the simulations are presented in the next chapter (chapter III.7).

6.1 Geometry

6.1.1 3D upper airways idealized geometry

A volumetric male upper airways (UA) geometry was built from the processing of a medical database obtained using High Resolution Computed Tomography (HRCT) as described in Conway et al. [2012]. A typical example of the UA HRCT-scan from this study is given in Figure III.6.1 (left panel), in median saggital view. This example corresponds to a male adult. From these scans, an average idealized model was reconstructed to be representative of the major geometrical characteristics of UA in a male adult, yet made of basic shapes of adjustable parameters. Note that the specific shape and position of the tongue apex in the HRCT-scan (Figure III.6.1) was not reproduced in the model geometry. The identified main geometrical singularities are summarized in Figure III.6.1.

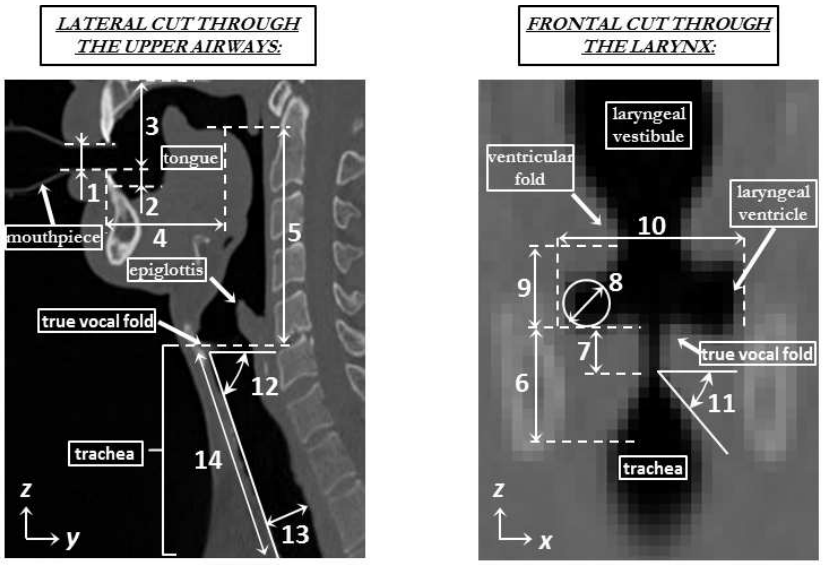

N°	Definition	Value
1	Mouthpiece diameter	10.00 mm
2	Oral cavity depth	5.08 mm
3	Oral cavity height	35.92 mm
4	Oral cavity length	65.81 mm
5	Oropharynx+ Laryngeal vestibule height	123.30 mm
6	Vocal fold thickness	10.00 mm
7	Height of the minimal glottal constriction	4.00 mm
8	Ventricular sinus diameter	2.49 mm*
9	Ventricular sinus height	5.30 mm*
10	Ventricular sinus width	19.15 mm
11	Vocal fold inclination degree	40°
12	Trachea inclination degree	70°
13	Trachea diameter	22.10 mm
14	Trachea length	175.00 mm

Figure III.6.1: **Reference average upper airways dimensions during breathing.** HRCT-scan saggital and frontal view of a male adult UA, images obtained from the pilot study described in Conway et al. [2012] (* measurement extracted from Agarwal et al. [2003], mean value, male data).

For each singularity, the aspect ratio measured in average from the segmented images was preserved. Several cross-sections A_i were defined along the upper airways geometry, as well as a central sagittal line (see Figure III.6.2a). Dimensions of each cross section A_i along the centerline are displayed in the graph on Figure III.6.2b. The main dimensions summarized in Figure III.6.1 and the cross-section variations presented in Figure III.6.2b

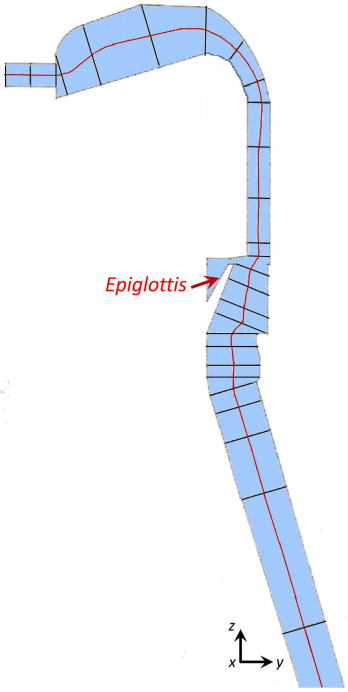

(a) Centerline of the model in median sagittal view and cross-section areas A_i averaged along the centerline.

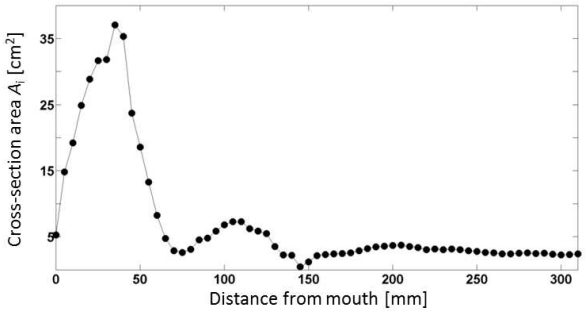

(b) Variations of cross-section areas A_i along the model center-line.

Figure III.6.2: Main dimensions for upper airways model reconstruction.

were utilised to reconstruct the average geometry of the upper airways model.

The meshing software Gambit (Fluent Inc.) was used to generate the 3D geometry. The obtained idealized 3D UA geometry built from the mouth to the end of the trachea and including a nebulizer mouthpiece - as in the scan in Figure Figure III.6.1 - is displayed in Figure III.6.3.

6.1.2 3D Laryngeal region idealized geometry

This part focuses on the laryngeal region of the model described in previous section. The main laryngeal dimensions in the 3D reconstructed geometry are summarized on Figure III.6.1 (values 6 - 11) and in Figure III.6.2b. For illustration, the final 3D laryngeal geometry is also detailed in Figure III.6.4a. The main glottal and supraglottal dimensions were reconstructed based on the HRCT-scans from the pilot study described in Conway et al. [2012] (see values 6, 7, and 11 on Figure III.6.1), on the measurements presented in the *in vivo* study (section II.3.2), but also on previous reference studies in the literature [Eckel and Sittel, 1995; Agarwal et al., 2003].

Glottal region The dimension chosen for the antero-posterior length (AP_g = 22.1 mm) was taken from the measurements by Eckel and Sittel [1995] on male adults (see sec-

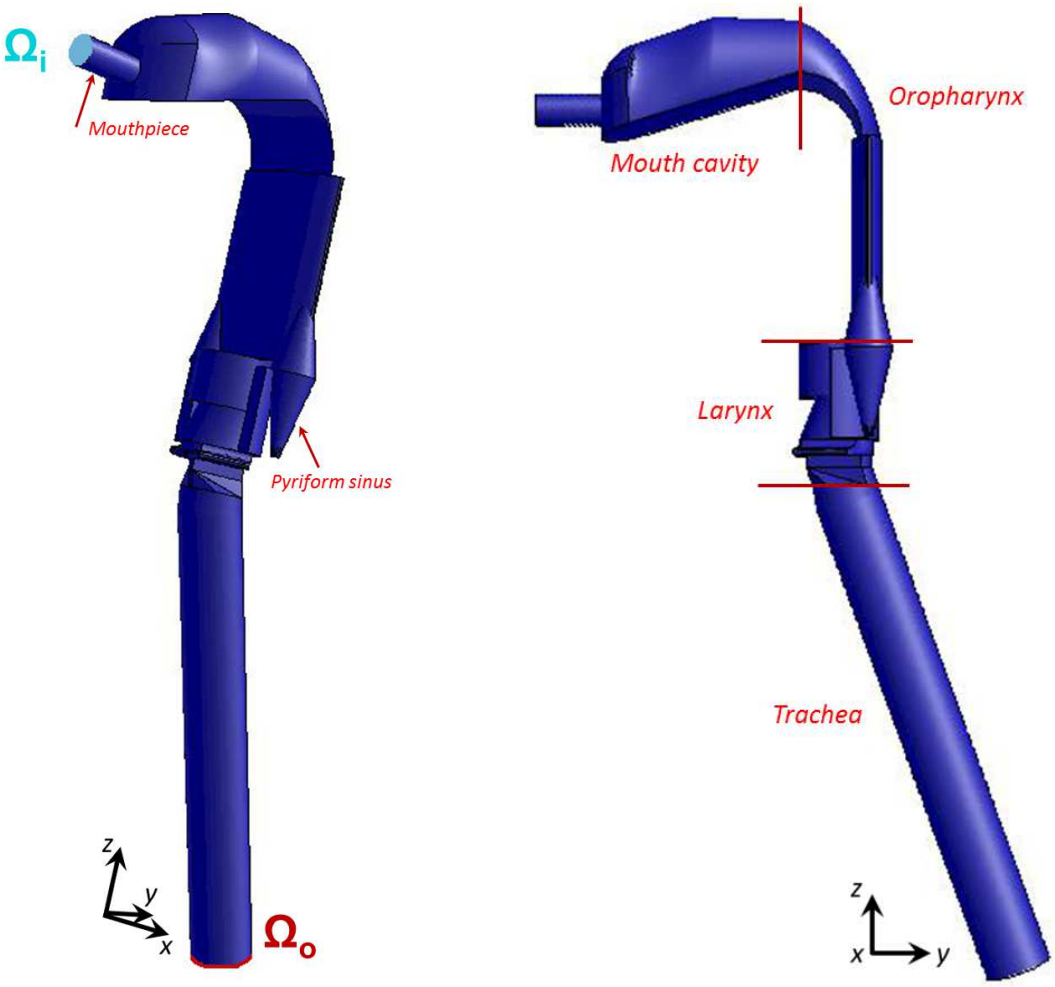

(a) Isometric view.

(b) Saggital view.

Figure III.6.3: Resulting model of the upper airways geometry.

tion I.1.1.2 and Figure III.6.1). This value was compared with the study of C. Darquenne from the University of California, San Diego (personal communication, May 7, 2014), who found a glottal antero-posterior diameter $AP_g = 22.0$ mm on male volunteers, using Magnetic Resonance Imaging (MRI). The shape of the glottal region (Ω_g) and its movement in time were designed in accordance with the *in vivo* observations and the pilot geometry presented in the 3D simplified laryngeal model study (see Figure III.5.2). In particular, the glottal plane, displayed by the face $ACFE$ in Figure III.6.4b, is identical to the 2D diaphragm built in Figure Figure III.5.2. The motion of the whole glottal region Ω_g was controlled by the rotation of the faces highlighted with red edges in Figure III.6.4b. The face $ACFE$ was moved by rotation of CF around AE, and axisymmetrically on the opposite side. As presented in previous chapter, the glottal kinematics was parametrized by the angle $\delta_1(t)$, defined in Figure III.5.2. The time-evolution of $\delta_1(t)$ was calculated from the corresponding glottal area time-variations $A_g(t)$ as measured in Part II, using Equation III.5.1. On the 2D glottal plane, the resulting motion is illustrated in Figure III.5.5,

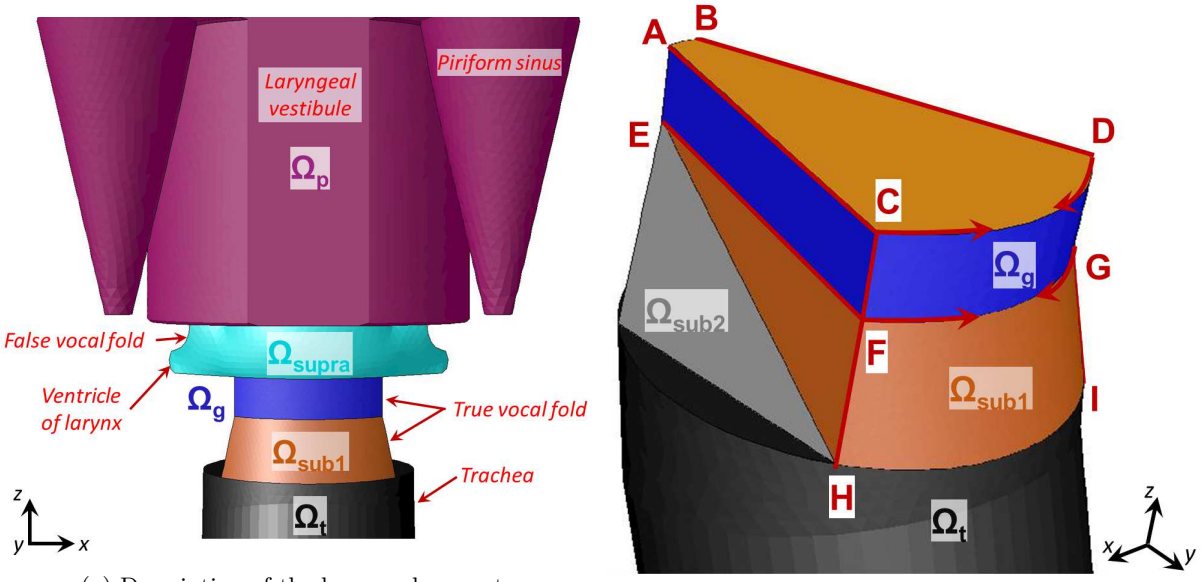

(a) Description of the laryngeal geometry in the 3D UA model.

(b) Scheme of the glottal geometry movement.

Figure III.6.4: Detail of the 3D laryngeal geometry.

where the cases of maximal and minimal opening can be compared with laryngoscopic images of the glottal area. Below the volume Ω_g, the movement of the subglottal area (Ω_{sub1}) was controlled by the rotation of the point F around point E, point H being fixed. This yielded to the inclination of the HF edge in time, and the axisymmetric movement on the opposite side. At the begining of inspiration, the inclination of the HF edge corresponds to the value 9 derived from the HRCT images (see Figure III.6.1). Finally, Figure III.6.5 provides a 3D illustration of the laryngeal zone as deformed at peak inspiration and peak

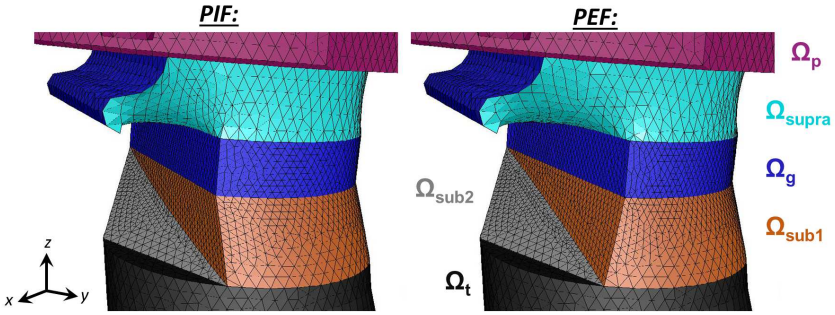

Figure III.6.5: Isometric view of the laryngeal region. Comparison of the mesh at PIF and PEF.

expiration during a typical breathing cycle.

Supraglottal region Regarding the supraglottal region Ω_{supra} (see Figure III.6.4a) which comprises the ventricular folds and the laryngeal ventricle, its geometrical configuration has been previously well characterized during voice production (see a review in Bailly [2009]). This supraglottal geometrical configuration was assumed to be close to the one observed during tidal breathing. Thus, the ventricular sinus shapes and dimensions (see values 8 and 9 on Figure III.6.1) were chosen from a reference statistical analysis of 28 laminagraphic tracings (from 4 males) of the larynx during modal register phonation [Agarwal et al., 2003]. The area between the ventricular folds was designed according to the measured *in vivo* ratio of false and true glottal opening, equal to 2.3 (typical value determined in average on a male subject during tidal breathing). The other supraglottal dimensions were measured on the HRCT-scan of the upper airways obtained from the pilot study described in Conway et al. [2012].

6.2 Solution Method

The numerical solution of the airflow and aerosol transport was obtained using the commercial CFD code (ANSYS® Fluent Academic Research, Release 15.0). In the following, the mechanical assumptions, parameters and formulation are presented for the flow model in a first step, and for the discrete phase in a second step.

6.2.1 Mechanical flow model

Simulation cases In the following, the CFD input data are based on the clinical measurements described in Part II. Accounting for the several results highlighted in these processed data, three parameters were varied in the simulation cases:

- the breathing type - In the clinical study, two breathing tasks were extensively studied: the task of *eupnea* performed at 15 cycles/min ($\mathbf{Eup}_{15}$), and the task of *tachypnea* performed at 30 cycles/min ($\mathbf{Tachyp}_{30}$). These tasks are altogether representative of *slow* and *rapid* breathing. Finally, the inlet flowrate conditions imposed for both tasks during one breathing cycle are presented on Figure III.6.8a for *slow* breathing and on Figure III.6.8b for *rapid* breathing.
- the glottal wall conditions - In the clinical study, two groups of subjects were identified (Group 1 and 2), with static or dynamic glottal walls during an average breathing cycle (see section II.4.2.1). So, both conditions were implemented for each breathing task. The glottal geometry time-variations imposed as an input parameter are displayed in Figure III.6.8a and Figure III.6.8b, along the inlet flowrates.
- the nature of the carrier gas (air or Helium (78%)-Oxygen(22%) mixture).

Finally, Table III.6.1 summarizes the different cases of simulation, associated to a number in the following.

In total, 4 simulation cases were carried out with air, and 2 simulation cases with He-O_2 mixture.

Breathing type	Group	A_g dynamics	Air	He-O_2 mixture
Eup$_{15}$	"Static"	A_g = const.	case **1**	case **3**
- see Figure III.6.8a	"Dynamic"	$A_g(t)$	case **2**	
Tachyp$_{30}$	"Static"	A_g = const.	case **4**	case **6**
- see Figure III.6.8b	"Dynamic"	$A_g(t)$	case **5**	

Table III.6.1: Description of the 6 CFD simulations (and their case numbers) performed during this study, depending on: the breathing type, the glottal wall conditions, and the type of carrier gas.

Flow parameters and model Table III.6.2 summarizes the main flow parameters for both carrier gases: air (with density $\rho_g = 1.225$ kg/m^3 and dynamic viscosity $\eta = 1.7894 \times 10^{-5}$ Pa·s), and He-O_2 mixture (with density $\rho_g = 0.422$ kg/m^3 and dynamic viscosity $\eta = 2.152 \times 10^{-5}$ Pa·s). The table considers face-uniform flow and gives its maximal values at the peak inspiration flow PIF and mean values calculated from mean velocity u_{mean}:

$$u_{mean} = \frac{\overline{V}_I}{\overline{T}_I}, \tag{III.6.1}$$

where $\overline{V}_I$ is the mean inspired volume and $\overline{T}_I$ is the mean period of the inspiration phase (data retrieved from *in vivo* study, section II.4.1).

	Air						He-O_2					
	Eup$_{15}$			**Tachyp**$_{30}$			**Eup**$_{15}$			**Tachyp**$_{30}$		
	Inlet	Glottis	Outlet	Inlet	Glottis	Outlet	Inlet	Glottis	Outlet	Inlet	Glottis	Outlet
D_h [m]	0.01	0.0121	0.0221	0.01	0.0124	0.0221	0.01	0.0121	0.0221	0.01	0.0124	0.0221
u_{max} [m/s]	9.55	3.42	1.96	13.16	4.44	2.69	9.55	3.42	1.96	13.16	4.44	2.69
u_{mean} [m/s]	6.91	2.47	1.41	9.57	3.23	1.96	6.91	2.47	1.41	9.57	3.23	1.96
Re_{max} [-]	6538	2833	2947	9009	3769	4070	1866	807	844	2583	1084	1169
Re_{mean} [-]	4728	2044	2139	6549	2748	2963	1354	585	612	1876	787	849
I [%]	5.34	5.93	5.89	5.13	5.71	5.59	6.2	6.93	6.89	5.99	6.68	6.62

Table III.6.2: Aerodynamic parameters at the inlet, glottal area and outlet for mean and peak inspiration flows.

Accounting for these flow parameters, in case of air, a turbulent $k - \omega$ SST transport model was applied, as done in previous 3D simulations (chapter III.5). However, based on the low Reynolds number Re values expected in case of He-O_2 mixture, the equations for laminar flow were implemented (for details see Equation III.7.5 in Annex B - 2D Model).

6.2.2 Discrete Phase Model

The Lagrangian discrete phase model in ANSYS Fluent solver follows the Euler- Lagrange approach. The fluid phase is treated as a continuum by solving the Navier-Stokes equations, while the dispersed phase is solved by tracking a large number of particles through the calculated flow field. Thus, the trajectory of a discrete phase particle is solved by

integrating the force balance on the particle, which is written in a Lagrangian reference frame. This force balance equates the particle inertia with the forces acting on the particle. The purpose of this section is to evaluate forces on the particle within the upper airways using very simple approximations. Consequently the full equation of particle transport (Equation I.1.3 in section I.1.3.2) derived by Hinze [1975] is reduced to essentials and the simplified form is afterwards implemented in ANSYS Fluent solver.

Evaluation of forces on the particle As presented in section I.1.3.3, the principal mechanisms influencing the transport of aerosols in human airways: (a) inertial impaction, (b) turbulent mixing, (c) Brownian diffusion, (d) sedimentation:

a/ Inertial impaction

The inertial impaction mechanism can be described using the dimensionless Stokes number Stk as defined in Equation I.1.13.

The deposition by inertial impaction was evaluated using an approximation of the mouth-throat airway area as a circular pipe with a bend. The angle $\beta = 90°$ was measured from oro-pharynx curvature of our model. The flow parameters used were those of $\mathbf{Eup}_{15}$ breathing (Male, Group 2 "dynamic"), assuming the peak flow velocity at PIF $u = 5.68$ m/s and the hydraulic diameter of the narrowest oropharynx cross-section $D_\mathrm{h} = 9.17$ mm.

Pui et al. [1987] derived a relationship to calculate the penetration fraction P (the fraction of entering particles that exit the model), in a tube bend of a circular cross-section for laminar flow ($Re = 1000$) as:

$$P = \left[1 + \left[\frac{Stk}{0.171}\right]^{0.452\frac{Stk}{0.171}+2.242}\right]^{-\frac{2}{\pi}\beta}, \tag{III.6.2}$$

and for turbulent flow (independently of Reynolds number) as:

$$P = \exp\left[-2.823\, Stk\, \beta\right], \tag{III.6.3}$$

where β $[rad]$ is the angle of the curve geometry.

For our purpose, the penetration fraction P was calculated in the case of turbulent regime with air (density $\rho_\mathrm{g} = 1.225$ kg/m^{-3} and dynamic viscosity $\eta = 1.7894 \times 10^{-5}$ Pa·s) and in the case of laminar regime with He-O_2 mixture (density $\rho_\mathrm{g} = 0.422$ kg/m^{-3} and dynamic viscosity $\eta = 2.152 \times 10^{-5}$ Pa·s). The resulting curves on Figure III.6.6 show that, in this configuration, the deposition by inertial impaction is more efficient in turbulent regime than in laminar flow regime.

In laminar flow the penetration fraction starts to decrease with the particle diameter $D_\mathrm{p} > 4\,\mu$m, in turbulent flow with particle diameter $D_\mathrm{p} > 1\,\mu$m. In conclusion, the bend geometry of the oro-pharynx within the upper airways causes inertial impaction to have significant influence on micro-particle transport and deposition.

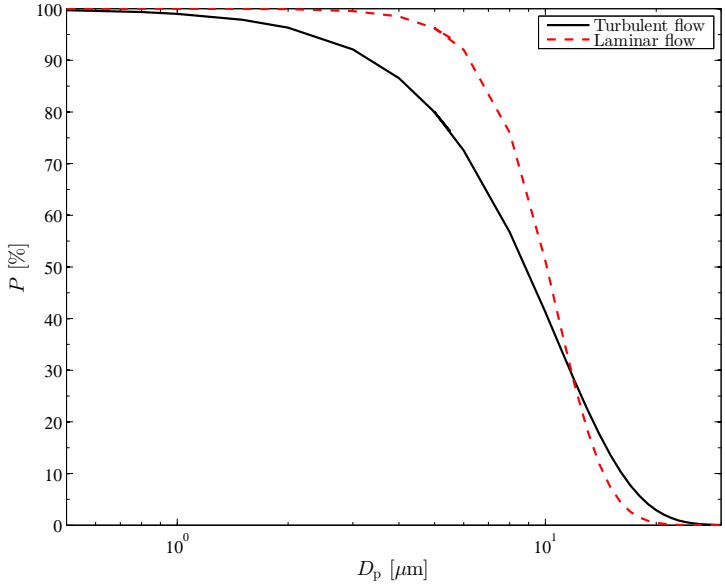

Figure III.6.6: Penetration P versus particle diameter D_p in log-normal scale for a simplified bend geometry of an oropharynx considering deposition by inertial impaction.

b/ Turbulent mixing

Turbulent mixing depends on the flow regime developed within the model. When the flow is turbulent, ANSYS Fluents solver predicts the trajectories of particles using the mean fluid phase velocity $\overline{u}$.

c/ Brownian diffusion

The Brownian diffusion is characterized by the diffusion coefficient D (see Equation I.1.23). This coefficient is estimated differently for turbulent and laminar flow regimes. Considering a steady laminar flow through a tube having circular cross-section, the penetration P is a function of the dimensionless deposition parameter μ,

$$\mu = \frac{DL}{Q}, \tag{III.6.4}$$

where L [m] is the length of the tube and Q is the volume flow rate [m^3/s]. The penetration P as a function of μ is given by [Hinds, 1999]:

$$\begin{aligned} P &= 1 - 5.50\mu^{\frac{2}{3}} + 3.77\mu \text{ for } \mu < 0.0009, \\ P &= 0.819\,\exp(-11.5\mu) + 0.0975\,\exp(-70.1\mu) \text{ for } \mu \geq 0.0009. \end{aligned} \tag{III.6.5}$$

Diffusion of the particles in the turbulent flow is more complicated. Wells and Chamberlain [1967] defined the diffusive deposition velocity V_dep through the laminar boundary

layer for turbulent flow:

$$V_{\mathrm{dep}} = \frac{0.04u}{Re_{\mathrm{p}}^{\frac{1}{4}}} \left(\frac{\rho_{\mathrm{g}} D}{\eta} \right)^{\frac{2}{3}}, \tag{III.6.6}$$

where u is the average flow velocity in the tube and ρ_{g} the density of the gas. Using the diffusive deposition velocity V_{dep} can be further calculated the penetration through the tube:

$$P = \exp\left(\frac{-4 V_{\mathrm{dep}} L}{D_{\mathrm{h}} u} \right). \tag{III.6.7}$$

The main parameter of the deposition by diffusion is the length L of the model. Therefore, in the case of our upper airways geometry, an approximation was made and the length L was evaluated as the total length of the upper airways model, $L = 0.42$ m. Further turbulent flow conditions were assumed for air (dynamic viscosity $\eta = 1.85 \times 10^{-5}$ Pa·s), while laminar flow conditions were assumed for the He-O_2 mixture (dynamic viscosity $\eta = 2.152 \times 10^{-5}$ Pa·s). The hydraulic diameter D_{h} was assumed as the glottal hydraulic diameter for the mean glottal geometry (inspiration, Male, Group 2 "dynamic") and the peak glottal velocity (at PIF) of $\mathbf{Eup}_{15}$ breathing $u = 5.68$ m/s (inspiration, Male, Group 2 "dynamic").

Results on Figure III.6.7 show that for our approximation the penetration P is higher in

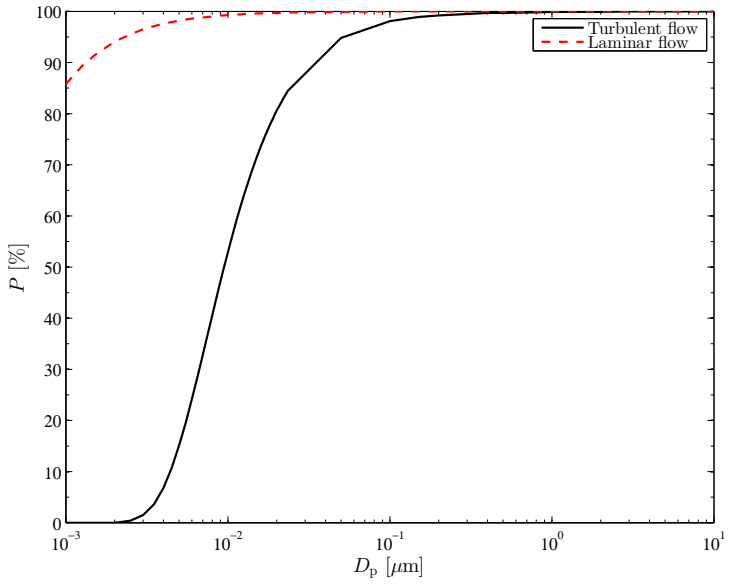

Figure III.6.7: Penetration P versus particle diameter D_{p} for a circular tube of a length $L = 0.42$ m considering deposition by diffusion.

laminar flow of He-O_2 mixture, because in this flow regime occurs lower diffusional deposition. Nevertheless, for particles greater than 0.1 μm, the Brownian diffusion mechanism is negligible in both flow regimes. Thus, since in the following simulations, particles with $D_{\mathrm{p}} > 1$ μm are used, the term with Brownian force is negligible in the equation of motion (see Equation I.1.2).

d/ Sedimentation

In the upper airways region, high flow rates lead to insufficient time for particle to deposit by sedimentation [Cohen and Asgharian, 1990; Heyder and Svartengren, 2001]. Thus, force of gravity is not included and the gravitational acceleration in the gravity term of Equation I.1.3 (in the fifth term on the right hand side) is set to zero.

Final Form of the Equation of Particle Motion Finally, the equation of particle motion, Equation I.1.3 in section I.1.3.2, can be expressed in the following form:

$$m_{\mathrm{p}}\frac{\mathrm{d}u_{\mathrm{p}}}{\mathrm{d}t} = -\frac{1}{2}\rho_{\mathrm{g}}|u_{\mathrm{p}}-\overline{u}|^2\frac{\pi D_{\mathrm{p}}^2}{4}C_{\mathrm{D}}\frac{u_{\mathrm{p}}-\overline{u}}{|u_{\mathrm{p}}-\overline{u}|} \tag{III.6.8}$$

Hence, for the simulations within the ANSYS Fluent environment the equation of particle motion includes only the drag force term.

6.2.3 Numerical method

The numerical method is similar to the one presented in the case of previous 3D simulations (chapter III.5). Yet, in the following, some details are given on the turbulent $k-\omega$ SST transport model applied to simulate the airflow. An additional option with low Reynolds number correction (LRN) was set to capture the airflow structures at low Reynolds numbers. This is assured by reduction of turbulent viscosity using the coefficient $\alpha^\star$:

$$\alpha^\star = \frac{\alpha_0^\star + Re_{\mathrm{t}}/R_{\mathrm{k}}}{1+Re_{\mathrm{t}}/R_{\mathrm{k}}}, \tag{III.6.9}$$

where the turbulent Reynolds number Re_{t} is defined as:

$$Re_{\mathrm{t}} = \frac{\rho k}{\eta\omega}, \tag{III.6.10}$$

and constants $R_{\mathrm{k}} = 6$, $\alpha_0^\star = \frac{0.072}{3}$ [ANSYS®, 2013b]. Thus, the formulation of eddy viscosity (Equation III.5.4) considers the low Reynolds coefficient:

$$\mu_{\mathrm{t}} = \frac{\rho k}{\omega}\frac{1}{\max\left[\frac{1}{\alpha^\star}, \frac{SF_2}{a_1\omega}\right]}. \tag{III.6.11}$$

The kinetic turbulent energy k and specific dissipation rate ω were solved using Equation III.5.5 and Equation III.5.6, respectively. The turbulence intensity I at the inlet and outlet face were set according to:

$$I = 0.16{Re_{\max}}^{-\frac{1}{8}}, \tag{III.6.12}$$

and the turbulent length scale as defined in Equation III.5.11. The Reynolds number was calculated using equation:

$$Re_{D_{\mathrm{h}}} = \frac{\rho_{\mathrm{g}}u_{\max}D_{\mathrm{h}}}{\eta}, \tag{III.6.13}$$

where D_h is the hydraulic diameter of the inlet surface, u_{max} the maximal surface-averaged speed of the flow derived from the inlet airflow rate $\overline{Q}$ and η the dynamic viscosity of the air.

6.2.4 Simulation setting

In low Mach numbers, in the limit of incompressible flows, the linkage between density-pressure is weak. Thus, pressure is treated as an independent variable, and the continuity equation is replaced by a pressure equation, obtained from the continuity and momentum equations. Such a solution is in ANSYS Fluent called as pressure-based (see ANSYS® [2013b]). The form of the Navier-Stokes equations shows linear dependence of velocity on pressure and vice-versa. Here was applied the PISO (Pressure Implicit with Splitting of Operator) algorithm (originally proposed by Issa [1986]), where the estimated velocity field is corrected with the pressure correction field to derive a divergence-free velocity field. The PISO was chosen because it is supposed to better resolve the simulations with moving computational meshes [Ferziger and Peric, 2001].

To avoid start-up effects and obtain a periodic solution of the flow field, all simulations were solved during three consecutive breathing cycles. The results of the flow field at different periods are within the same range ($u(x, t) = u(x, t + T)$) and so 3 periods calculation is shown to be sufficient. The equations were solved by means of a finite volume method using first-order time, spatial discretization schemes, and time step set to 3.167×10^{-3} s or 1.587×10^{-3} s for $\mathbf{Eup}_{15}$ and $\mathbf{Tachyp}_{30}$, repectively. This yields to the Courant-Friedrich-Lewy (CFL) criterion defined in Equation III.5.7 about 20 and 13.5 in the glottal region, respectively. The unsteady calculation had 1260 time steps. Iterative convergence was achieved when the dimensionless RMS residuals over the entire flow field were inferior to 10^{-3}.

6.3 Initial & Boundary Conditions

The boundary conditions setting are similar to the ones detailed in the previous CFD model (section III.5.3). However the data for the airflow inlet and the glottal kinematics were taken from the *in vivo* measurements realized on 9 male volunteers (see section II.3.2). All boundary conditions were set and the simulation was conducted for 3 consecutive breathing cycles. The computational process of such a transient calculation is illustrated by the flow chart on Figure III.5.3 (see section III.5.3 for details).

The computational process of this transient calculation is illustrated by a flow chart on the Figure III.5.3. At first, initial conditions (items ((a) and (b)) are applied and all the boundary conditions are set (items (c)) to (k)). Next, the CFD equations are processed until convergence is achieved and particles touching the walls of the model are post-processed (item (l)). New time step is passed, mesh nodes in domains Ω_g and Ω_{sub1} are recalculated (item (h)) and the attached domains Ω_{supra} and Ω_{sub2} are smoothed and

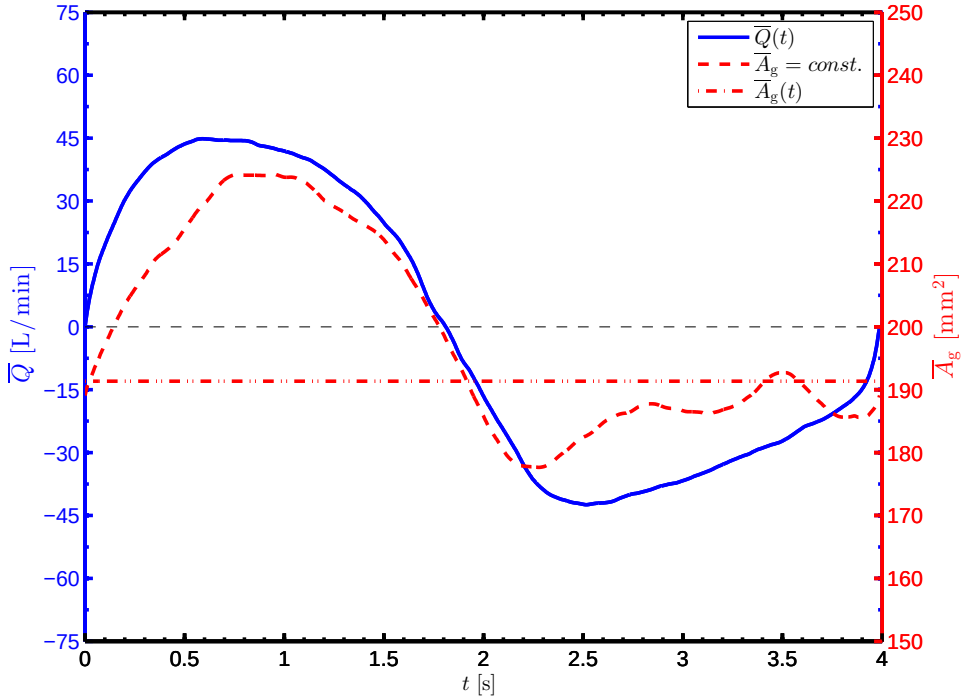

(a) **Eup**$_{15}$.

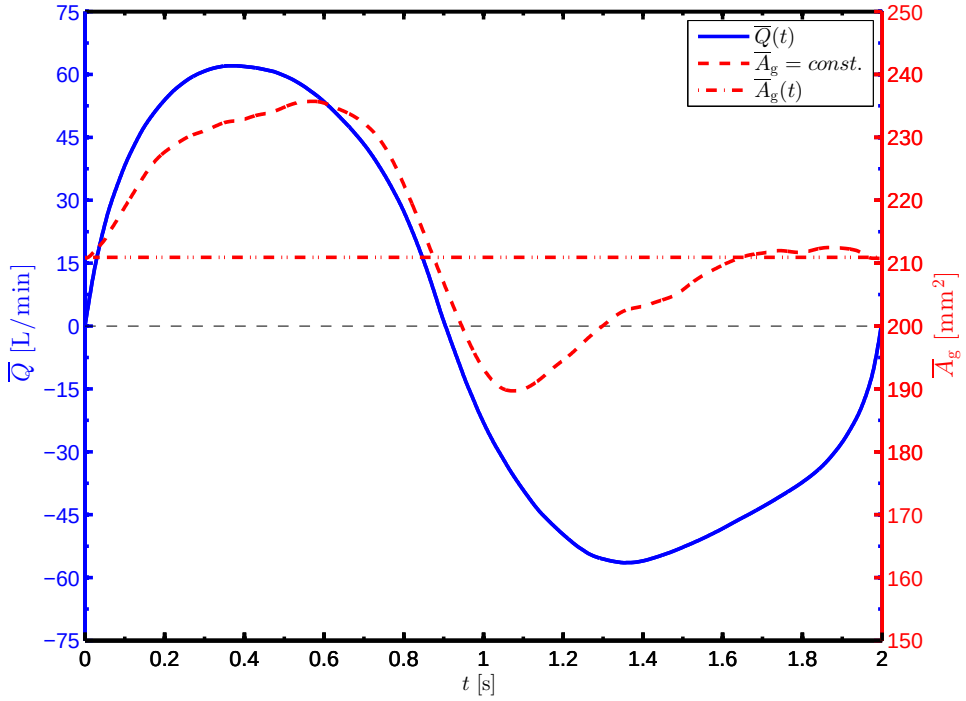

(b) **Tachyp**$_{30}$.

Figure III.6.8: **Airflow and glottal geometry boundary conditions.** Evolution of airflow rate $\overline{Q}$ [L/min] and glottal area A_g [mm^2] in function of the time. Plotted area $A_g(t)$ and flow rate $\overline{Q}$ correspond to the mean cycle for males, Group 2 "dynamic" (see section II.3.2). Area $A_g = const.$ is mean of inspiration phase of male cycle, Group 1 "static" ($A_g = 210.91$ mm^2). Panels a and b correspond to different breathing tasks.

remeshed if skewness or size of the elements exceeds preassigned limits (item (i)). Finally velocity inlet (item (c)) and particle injection (item (k)) are set.

The unsteady boundary conditions were coded in C programming language using the User Defined Functions (UDFs). The UDF is a function that can be dynamically loaded within the ANSYS Fluent solver (ANSYS® Fluent Academic Research, Release 15.0) to enhance the standard features of the code. All UDFs were compiled within the ANSYS Fluent solver and executed every time step during the simulation.

The conditions for different domains Ω_i, Ω_o (see III.6.3a) and Ω_p, Ω_{supra}, Ω_g, Ω_{sub1}, Ω_{sub2}, Ω_t (see Figure III.6.5) were set as following:

Initial conditions

(a) Initial conditions with zero velocities $u_{(t=0)} = 0$ and pressures $p_{(t=0)} = 0$ were assumed at all points.

(b) At the inlet wall Ω_i, the initial values for the turbulent kinetic energy k and the specific dissipation rate ω were assigned, assuming a fully developed flow, using the empirical relation from Equation III.5.10.

Flow boundary conditions

(c) At the inlet face Ω_i the inlet velocity u_{inlet} was derived from Equation III.5.8 using the flow rate $\overline{Q}(t)$ and inlet area A_{inlet}. Variation of the flow rate $\overline{Q}(t)$ was taken from the results of male Group 2 "dynamic" (see section II.4.2). A mean of all quiet breathing cycles was calculated (see Figure III.5.4a) for two breathing tasks, $\mathbf{Eup}_{15}$ and $\mathbf{Tachyp}_{30}$ (see Figure III.6.8). The unsteady boundary condition was coded in C programming language using an UDF with DEFINE_PROFILE macro.

(d) A pressure outlet boundary condition $p(t)$ was set at outlet domain Ω_o to 0 Pa.

Wall boundary and dynamic mesh conditions

(e) On solid walls of Ω_p, and Ω_t domains, a no slip shear boundary condition was applied :$\boldsymbol{u}_{wall} \cdot \boldsymbol{n} = 0$, where $\boldsymbol{u}_{wall}$ is the velocity vector of the wall motion, here equal to zero and $\boldsymbol{n}$ is the outward normal vector.

(f) The wall boundary conditions at Ω_t, Ω_{supra}, Ω_g, Ω_{sub1}, Ω_{sub2}, and Ω_t domains for the $k-\omega$ model equations correspond to the wall function approach for wall-function meshes (see Launder and Spalding [1974] for details).

(g) Wall boundary conditions for the inlet Ω_i and outlet face Ω_o were imposed using the Equation III.5.13.

(h) The geometry in the glottal and subglottal domain, respectively Ω_g and Ω_{sub1} were set according to the dimensions of the glottal constriction A_g (for definition see Figure II.3.4c in section II.3.2.2) measured in the *in vivo* study (section II.4.2).

Two different cases for two breathing regimes, **Eup**$_{15}$ and **Tachyp**$_{30}$ (Figure III.6.8), were simulated:

- **Cases 1, 3, 4, and 6** consider a steady glottal geometry with a mean glottal area $\overline{A}_g = 190.6$ and 210.9 mm^2 for **Eup**$_{15}$ and **Tachyp**$_{30}$, respectively. These values correspond to the mean value during inspiration phase of male subjects, Group 1 "static" (see Table II.4.1 in section II.4.2).
- **Cases 2 and 5** consider a moving glottal geometry according to $\overline{A}_g(t)$, observed during the mean cycle of male subjects, Group 2 "dynamic" (see Figure III.6.8). Corresponding unsteady boundary conditions for the rigid walls of those domains were compiled to ANSYS Fluent solver using an UDF with DEFINE_GRID_MOTION macro. The kinematics was programmed similarly to the solution showed for previous CFD model (section III.5.3). The walls were rotating according to the angle δ_1 calculated from the Equation III.5.1, to recalculate the position of each mesh node a cross-multiplication was applied. Detail of the UDFs utilized is given in the Annex (see Annex C - User Defined Functions for the UDFs of glottal Ω_g and subglottal Ω_{sub1} domain).

(i) Volumes Ω_{supra} and Ω_{sub2}, attached to the glottal region, were updated every timestep applying the smoothing and remeshing methods of the ANSYS Fluent solver, if the skewness or size of the mesh elements exceeds specified values.

Disperse phase boundary condition

(j) The wall boundary conditions for the discrete phase are set: "*escape*" at the inlet Ω_i and outlet Ω_o faces, and UDF for trapped particles are set at all the other faces. This ensures that a particle passing the outlet boundary Ω_o during inspiration or passing the inlet boundary Ω_i during expiration (leaving the computational domain) is lost for further calculation and a particle touching all the other walls is post-processed according to conditions set in the UDF (see (l)).

(k) The aerosol injection from inlet surface Ω_i was programmed using an UDF with DEFINE_DPM_INJECTION_INIT macro (see details in section III.6.2.2). Since 3 consecutive breathing cycles were carried out for each simulation, the aerosol was injected into the model during the inspiration phase of the third cycle. The particles were composed of liquid water with density of 998.2 kg/m^3 and spherical shape. Monodisperse aerosol of four different particle diameters, $D_p = 1$, 3, 5, and 10 µm, were injected into the model. The size range was chosen to comprise the aerosol particle sizes typically used for inhalation therapy (*e.g.*, see particles with mass median diameter in the range from 2.90 µm up to 6.05 µm measured in Conway et al. [2012]). The injection was programmed using an UDF, so that the particle injection speed and direction correspond to the inlet airflow ($\boldsymbol{u}_p = \boldsymbol{u}$). The particles were injected from the center of each mesh element at the inlet face. The number of particles injected at an instant corresponded to the number of cells in the inlet surface. The injection time step was equal to the time step of the calculation. This resulted to the face-uniformly injected particles in accordance with linear function.

The particles were assumed deposited when they approached the solid wall to a distance equal to the half of their diameter.

(l) The discrete phase boundary condition for particles that touch the wall (walls of Ω_t, Ω_{supra}, Ω_g, Ω_{sub1}, Ω_{sub2}, and Ω_t domains) was programmed using an UDF with DEFINE_DPM_BC macro. The UDF removes such a particle from the computational domain and saves information about the position of injection and deposition, about the time of injection and deposition and about the particle velocity and size characteristics.

6.4 Mesh Properties

The unstructured grid of the model was generated in Gambit 2.4.6 (Fluent Inc.). Findings from previous preliminary simulations (chapter III.5) were applied. In correspondence to previous 3D model, the complex geometries including dynamic meshes were meshed preferably using tetrahedral elements.

i. The volumes from the mouthpiece up to the end of the larynx (see Figure III.6.3) were meshed with tetrahedral elements. The Tet/Hybrid element scheme with TGrid option in GAMBIT assures that mesh is generated primarily with tetrahedral elements. Yet, where appropriate, also hexahedral, pyramidal, and wedge elements can be used. Density of the mesh was not homogeneous on the whole computational field. At first, mesh elements were refined at the walls all over the model and second, special interest was put to glottal Ω_g and subglottal Ω_{sub1} regions (see Figure III.6.5) including moving walls. Those were meshed with smaller mesh element size (Table III.6.3).

ii. The volume of trachea (see Figure III.6.3) was meshed using primarily hexahedral elements and where appropriate also wedge elements were utilised (Hex/Wedge meshing option in GAMBIT). Elements were stretched in the neighborhood of the walls using layering meshing technique. Table III.6.3 summarizes the mesh element size used.

6.4.1 Grid dependence

The dependence of the results on the chosen computational grid was tested on 3 different meshes. Table III.6.3 summarizes the main parameters (see Equation III.5.14 and Equation III.5.17) corresponding to the meshes under test. One testing simulation for each mesh was held with stationary boundary conditions. The calculation was solved using $k-\omega$ SST turbulence model. The velocity inlet was set to 7.2256 m/s (mean inlet velocity during quiet breathing $\mathbf{Eup}_{15}$, male) and the glottal geometry corresponded to area $A_g = 190.6$ mm^2 equal to mean glottal area during $\mathbf{Eup}_{15}$ breathing, male Group 1. Other simulation parameters were similar to those explained in next section.

	Mesh 1	Mesh 2	Mesh 3
N° of elements	464409	900180	2002748
$\Delta x^{\min}_{\text{glottis}}$[m]	0.00075	0.00052	0.00035
$\Delta x^{\min}_{\text{trachea}}$[m]	0.00025	0.00025	0.00019
u^*_{glottis}[m/s]	0.302	0.302	0.302
u^*_{trachea}[m/s]	0.175	0.175	0.175
y^+_{glottis}	11.3	10.7	7.2
y^+_{trachea}	3.0	3.0	2.2
CPU time [s]	16 800	30 900	96 720

Table III.6.3: The main characteristics of the three meshes.

Because the main purpose of this study is put on particle transport and deposition in upper airways, the deposition fraction was chosen as the most relevant parameter to test the accuracy of the meshes. Deposition fraction gives the ratio of total number of particles deposited in the given region to the total number of particles injected to the model. Therefore, the quality of the meshes was assessed by comparing the resulting deposition fractions in the mouth region for 4 different particle diameters D_p = 1, 3, 5, and 10 µm (see Figure III.6.9a). The results show that "Mesh 1" results in up to 2 times

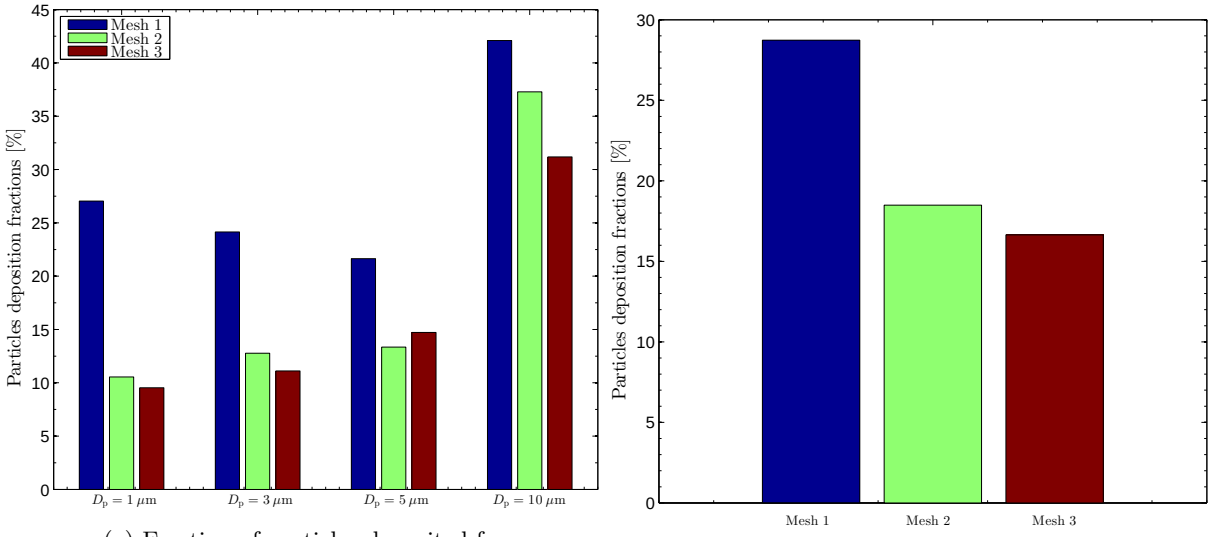

(a) Fraction of particles deposited for different particle diameters D_p.

(b) Total fraction of particles deposited.

Figure III.6.9: Comparison of deposition fractions in the oral region for the 3 tested meshes.

higher deposition fraction in comparison with other two meshes (in case of D_p = 1 µm). On contrary, results of "Mesh 2" and "Mesh 3" differ in total (see Figure III.6.9b) only 2% from each other. "Mesh 2" does not show significant discrepancies from "Mesh 3" and yield to almost identical results. In conclusion, with respect to computational efficiency (see CPU times in Table III.6.3) and accuracy, mesh-independent results may be achieved using "Mesh 2". Thus all of the UA models considered in this study were meshed with

the minimal count of 900 000 elements.

6.4.2 Quality of Dynamic mesh

A key element for accuracy and stability of the simulations is the mesh quality. ANSYS Fluent allows mesh checking evaluating the orthogonal quality. In order to determine the orthogonal quality of a given cell, ANSYS Fluent [ANSYS®, 2013a] calculates the following quantities for each face i:

- the normalized dot product of the area vector of a face ($\boldsymbol{A}_i$) and the vector from the centroid of the cell to the centroid of that face ($\boldsymbol{f}_i$):

$$\frac{\boldsymbol{A}_i \cdot \boldsymbol{f}_i}{|\boldsymbol{A}_i|\,|\boldsymbol{f}_i|} \tag{III.6.14}$$

- the normalized dot product of the area vector of a face ($\boldsymbol{A}_i$) and the vector from the centroid of the cell to the centroid of the adjacent cell that shares that face ($\boldsymbol{c}_i$):

$$\frac{\boldsymbol{A}_i \cdot \boldsymbol{c}_i}{|\boldsymbol{A}_i|\,|\boldsymbol{c}_i|} \tag{III.6.15}$$

The minimal value that results from calculating III.6.14 and III.6.15 for all of the faces is defined as the orthogonal quality for the cell. Therefore, the worst cells will have an orthogonal quality close to 0 and the best cells close to 1. Figure III.6.10 illustrates the relevant vectors and is an example where III.6.15 produces the minimal value and therefore determines the orthogonal quality. Generally, a minimal orthogonal quality > 0.01 is

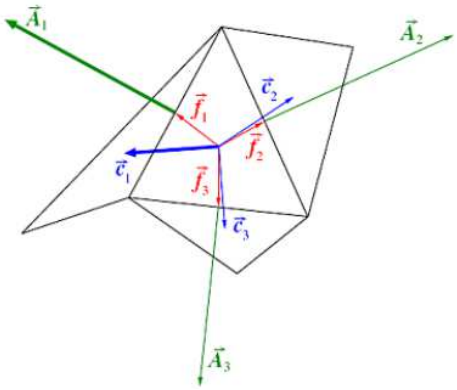

Figure III.6.10: The vectors used to compute orthogonal quality. Figure retrieved from ANSYS® [2013a].

considered acceptable (see [ANSYS®, 2013a]). On Figure III.6.11 we can observe the evolution of the minimum orthogonal quality in function of the time for three consecutive breathing cycles of $\mathbf{Eup}_{15}$. The curve shows that the mesh quality over the cycles does not fall down. It can be observed a decrease of orthogonal quality when the glottal area A_g reaches the maximal values. Nevertheless, when the area A_g starts afterwards to decrease,

the orthogonal quality is again improving. For illustration, see Figure III.6.5, where the glottal area is displayed in its limit positions (at peak inspiratory flow PIF and peak expiratory flow PEF).

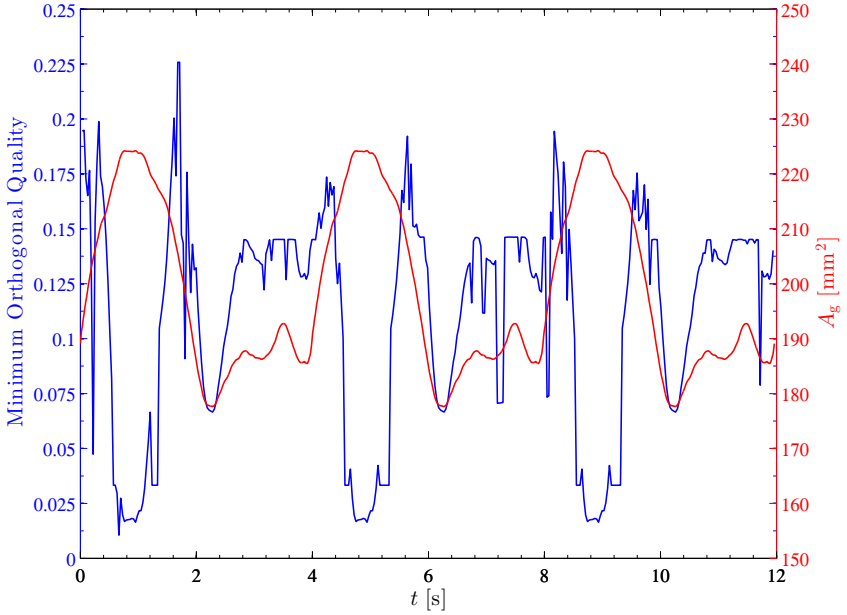

Figure III.6.11: Minimum orthogonal quality within the model and glottal area A_g in function of the time t.

This chapter was dedicated to the methodology applied so as to simulate two-phase flow in a 3D model of human upper airways, including realistic glottal motion and unsteady breathing conditions. In the next chapter, the CFD results obtained for the different simulation cases described in Table III.6.1 are presented.

Chapter III.7

CFD Results

This chapter describes the CFD results deriving from the methodology presented in previous chapter III.6. 6 simulation cases detailed in Table III.6.1 are presented. In the following, results are presented firstly in terms of pressure drop dynamics, thereby offering a comparison with the *in vivo* data described in section II.3.1.2. Next, in section III.7.2, a detailed analysis of the airflow in the upper airways is given, comparing the 6 cases, differing from each other through the breathing type (*eupnea*/*tachypnea*), the glottal wall condition (steady/dynamic) and the nature of the carrier gas (air or He-O_2 mixture). Finally the micro-particle deposition mechanics are discussed in section III.7.3.

7.1 Pressure Drop Dynamics

Human breathing is the result of differences in pressure between the pleural cavity and the atmosphere (see section I.1.1.1). The pressure in the respiratory system with the axial distance from the mouth inlet, and the pressure drop increases with higher flow rates [Zhang and Kleinstreuer, 2004] or different glottal cross-section dimensions [Brouns et al., 2007a]. Consequently pressure drop dynamics has effects on aerosol deposition in the airways. Therefore, the performed simulations enable to study in details the pressure drop in function of different breathing regimes (*eupnea* and *tachypnea*), different glottal dynamics (steady and dynamic) and different carrier gases (air and He-O_2 mixture) in the model of upper airways.

Figure III.7.1 compares the pressure drop variations for different models in function of the distance from the mouthpiece inlet, l. Values of the pressure drops correspond to the difference between the pressure at the mouthpiece inlet, p_{inlet}, and the pressure of the following cross-sectional areas along the center-line of the model, p_{i} (see Figure III.6.2a). Pressure at each cross-section was calculated at the shot-instant of peak inspiration (PIF), and spatially averaged for the cross-section areas.

The shapes of displayed curves are very similar to those reported by [Kleinstreuer and Zhang, 2003; Brouns et al., 2007b] except for the oral cavity region, where in present study

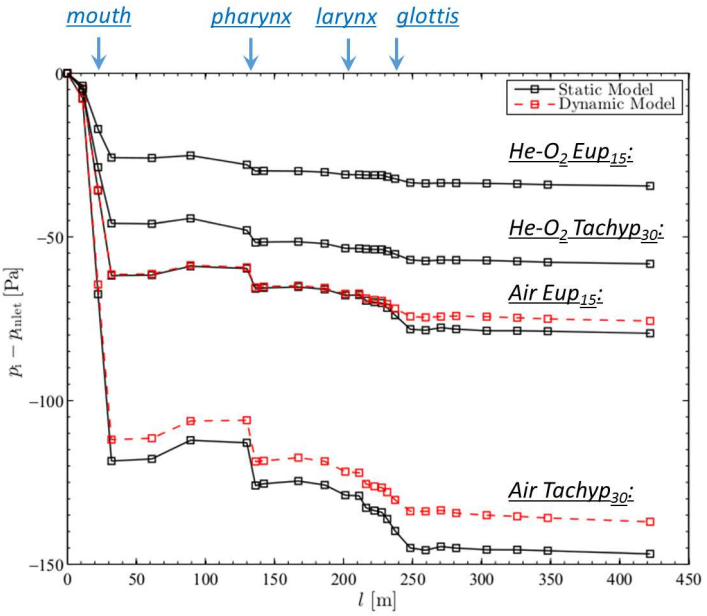

Figure III.7.1: Variations of cross-sectional area-averaged pressure drop in function of the distance from the mouthpiece inlet l. Comparison of different models at the shot-instant of peak inspiration (PIF).

a great pressure drop is caused by tiny mouthpiece diameter. Comparison between static and dynamic model, corresponding to "static" and "dynamic" groups of the *in vivo* study, gives around 5% decrease in pressure drop for case of "dynamic" group in both *eupnea* and *tachypnea* breathing. This is caused by wider glottal opening in case of "dynamic" group during inspiration (see Figure III.6.8). Further, significant pressure drop reduce is present in the models with He-O_2 mixture. In comparison with air, it reaches around 50%. In agreement with previous results presented by Sandeau [2010] the transairway pressure is lower with He-O_2 mixture than with air. In conclusion, unsteady glottal dynamics or He-O_2 mixture as a carrier gas results in lower work of breathing.

The evolution of the pressure drop in function of the flow rate variations over the whole breathing cycle is presented in the Figure III.7.2. The 6 breathing options (see Table III.6.1) are compared using the total pressure drop through the model in function of the flow rate. The shape of the curves is similar to the results of preliminary transglottal pressure *in vivo* measurements (see Figure II.3.2 in section II.3.1.2). In general the pressure drop is higher during inspiration in comparison with expiration. The decrease in pressure drop in expiration is about 38% for static models with air. Similarly, in He-O_2 mixture the decrease of pressure drop during expiration is 24 and 34% for *eupnea* and *tachypnea* task, respectively. In case of model with dynamic glottal walls, the differences between inspiration and expiration rise up to 34 and 50% for *eupnea* and *tachypnea* task, respectively.

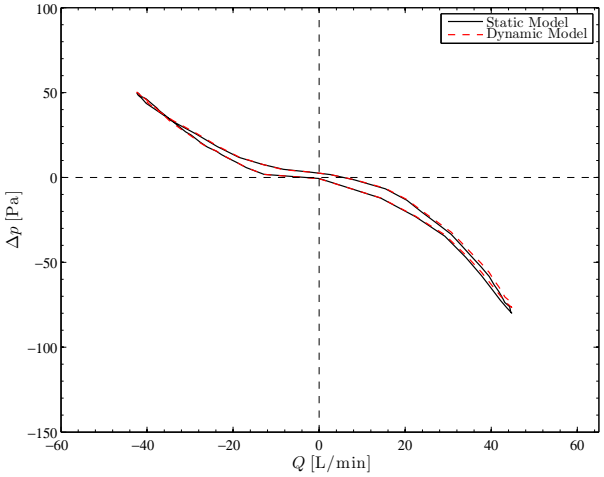

(a) **Eup**$_{15}$; air (cases 1 and 2).

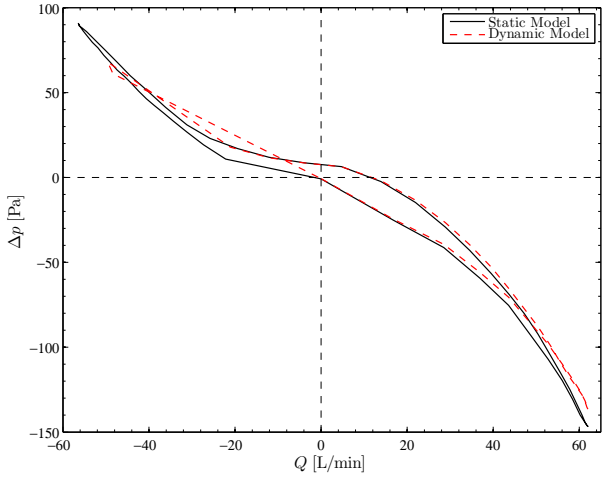

(b) **Tachyp**$_{30}$; air (cases 4 and 5).

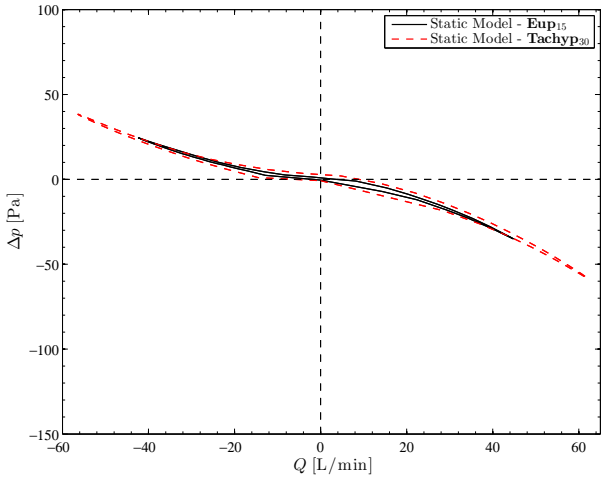

(c) Comparison of **Eup**$_{15}$ and **Tachyp**$_{30}$ static models for He-O_2 mixture (cases 3 and 6).

Figure III.7.2: Variations of pressure drop as a function of the airflow rate during one breathing cycle. Comparison of models with static and dynamic glottal geometries.

7.2 Airflow Dynamics

In the following, each simulated case corresponding to a specific breathing task (**Eup**$_{15}$ or **Tachyp**$_{30}$), specific glottal wall conditions (A_g = const. or $A_g(t)$) and a specific carrier gas (air or He-O_2 mixture) are labelled as in Table III.6.1.

7.2.1 General Flow Features in the Upper Airways

a/ Velocity Magnitude Contours

Development of the velocity field through the mid-sagittal plane of the entire model is displayed on Figure III.7.3 and Figure III.7.4, for shot-instants of peak inspiration PIF

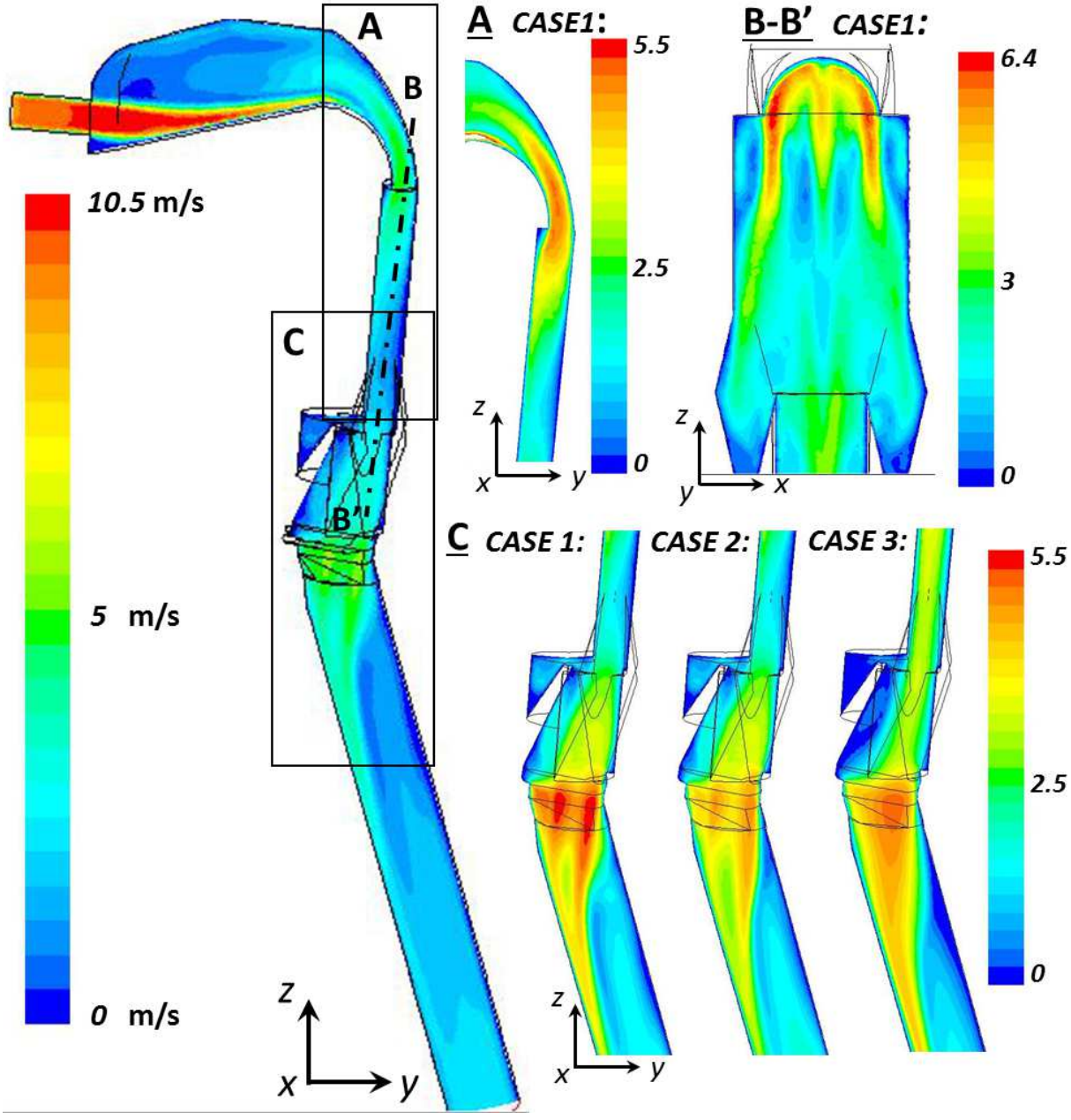

Figure III.7.3: Contours of velocity magnitude $|u|$ [m/s] at the plane $x = 0$. Comparison of case 1, 2 and 3 ($\mathbf{Eup}_{15}$) at peak inspiration PIF.

and peak expiration PEF respectively. Typical flow features are presented for the $\mathbf{Eup}_{15}$

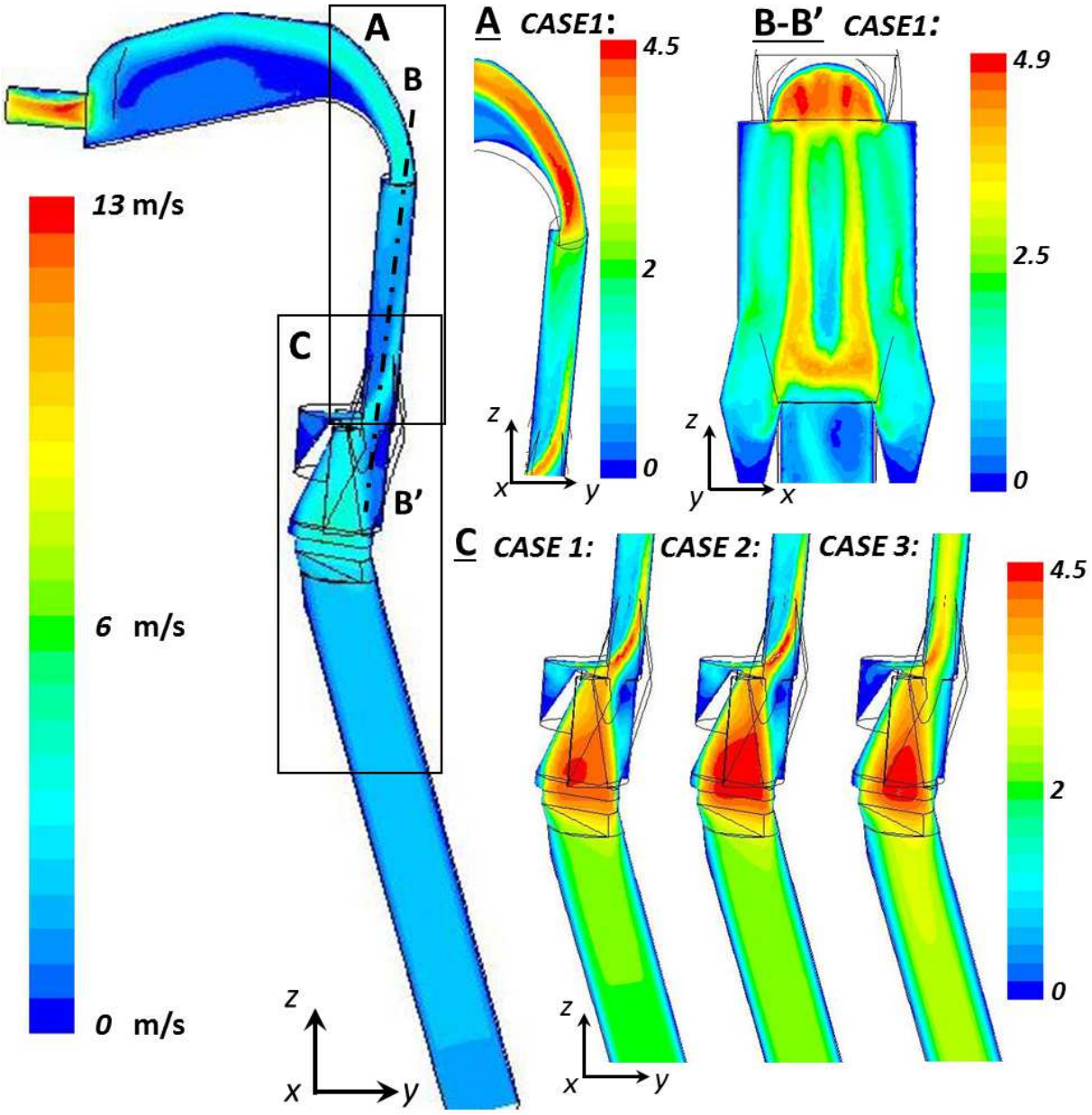

Figure III.7.4: Contours of velocity magnitude $|u|$ [m/s] at the plane $x = 0$. Comparison of case 1, 2 and 3 ($\mathbf{Eup}_{15}$) at peak expiration PEF.

task, case 1 with steady glottal walls and air as carrier gas.

Inspiration

During inspiration (Figure III.7.3), in the nebulizer mouthpiece is formed a high-speed flow that impacts the bottom part of the oral cavity (the tongue, in next referred as tongue plane). Another jet is formed at the oro-pharyngeal area (see detail in panel **A**).

In the plane **B-B'** cutting through the mid-plane of the pharyngeal region, a jet with three branches is created: two symmetrical and one in the middle due to the curvature of the bottom part of the region. Further downstream in the glottal region, the laryngeal jet is generated (see detail in panel **C**). The impact of different breathing conditions on these general flow features is also illustrated in panel **C**. The differences between cases 1, 2 and 3 are displayed. Case 1 in comparison with case 2 reaches the highest speed of the flow, which is caused by a narrower glottal cross-section (see Figure III.6.8a). In both cases 1 and 2 the formation of two jets is observed, that at greater distance stick together. In case 3 with He-O_2 mixture the flow reaches similar velocity amplitudes, but is more stabilized and forms a uniform jet. The maximum velocities in each region correspond to pressure drop described in previous section (Figure III.7.1), lower the pressure drop is, lower the velocity magnitude is. Thus the jet formed in the mouthpiece reaches velocity up to 10.5 m/s. Typical high-speed flows created in the oropharynx and the glottis regions reach maximum velocity amplitude around 6.4 and 5.5 m/s, respectively.

Expiration

A detail view of velocity magnitude contours in the same planes is also provided at the instant of peak expiration PEF in Figure III.7.4. During expiration, the inlet flow from trachea is uniform and stabilized. Note that the formation of the flow instabilities formed at the bronchial bifurcations in the realistic case are not considered (personal communication with Dr. J. Jedelský from Brno University of Technology, Czech republic, October 16, 2014). Two main jets are formed in the glottal area and in the oropharynx, a last one is formed in the mouthpiece. Panel **C** diferentiates the cases 1, 2, and 3. The glottal jet is uniform, it does not branch and impacts the epiglottis so the high-speed flow is skewed towards pharyngeal walls. Further is created the oropharyngeal jet with two branches, that connect in the bend of the soft palate. Similar qualitative trends can be observed whatever the glottal wall condition (case 1 static and case 2 dynamic). In case 3 (He-O_2 mixture), the jet reattachment on the pharyngeal walls does not occur on the same sites as compared to cases 1 and 2 (air).

b/ Turbulence Kinetic Energy

The creation and stabilization of the jets can also be assessed by evaluating the variation of the turbulence kinetic energy amplitudes through the model (see Figure III.7.5). This part presents typical results obtained for case 1 ($\mathbf{Eup}_{15}$, case 1 steady glottal wall, air). However, similar results are obtained for other cases. Four instants for each respiration phase are given. Times t_1, t_2, t_3, and t_4 correspond to $t_1 = t_{\mathrm{PIF}}/2$, $t_2 = t_{\mathrm{PIF}}$, $t_3 = t_{\mathrm{PIF}} + (T_{\mathrm{I}} - t_{\mathrm{PIF}})/2$, $t_4 = T_{\mathrm{I}}$. If we focus on the inspiration phase (Figure III.7.5a), similarly to results of Kleinstreuer and Zhang [2003]; Huang et al. [2013] we observe translation from the laminar to turbulent flow in the region of oral cavity. In comparison with previous works, the studied 3D geometry does not have the inlet mouthpiece parallel with the tongue plane and so the jet directly impacts the tongue wall and significant recirculation zones are created. This causes a significant turbulence kinetic energy peak.

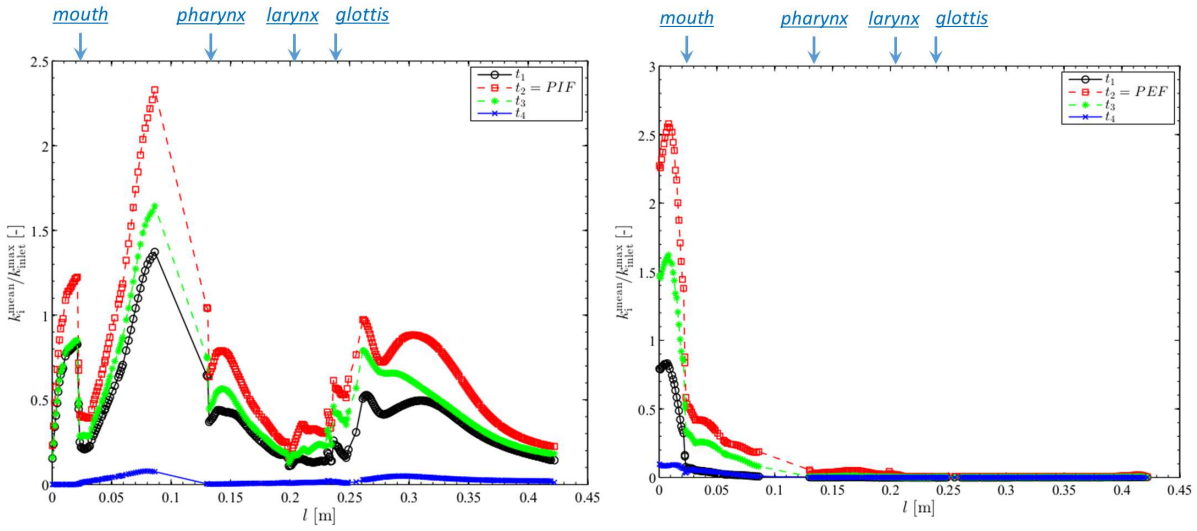

(a) Inspiration.

(b) Expiration.

Figure III.7.5: Variations of area-averaged non-dimensional turbulence kinetic energy $k_{\mathrm{i}}^{\mathrm{mean}}/k_{\mathrm{inlet}}^{\mathrm{max}}$ as a function of the distance from the inlet (case 1). Times $t_1 = t_{\mathrm{PIF}}/2$, $t_2 = t_{\mathrm{PIF}}$, $t_3 = t_{\mathrm{PIF}} + (T_{\mathrm{I}} - t_{\mathrm{PIF}})/2$, $t_4 = T_{\mathrm{I}}$.

Further downstream, the flow stabilizes, but due to the jet produced in the oropharynx (see detail on panel *A*, Figure III.7.3) we observe a second smaller peak of turbulent kinetic energy, that again stabilizes passing trough the pharynx. Further, the airstream passes through geometry with significant cross-section area changes. In consequence it causes drastic changes in turbulence kinetic energy. Downstream the glottis, the two laryngeal jet produce the third increase in turbulence kinetic energy with two peaks. When the first jet, created closer to the anterior wall of trachea, impacts the anterior wall of trachea, the first peak appears. Later downstream, the second jet, formed closer to posterior wall, impacts the anterior wall and the fourth peak appears. Peaks with connected recirculation zones will have a significant effect on particle deposition. The transitional and turbulent flow in the mouth-throat region corresponds with findings of other studies [Matida et al., 2006; Lin et al., 2007; Xi et al., 2008].

During expiration (Figure III.7.5b), as mentioned in previous paragraph, the flow enters stabilized. The turbulent kinetic energy is low and the laminar to turbulent transition appears in the oro-pharyngeal region (see detail *A* on Figure III.7.4). In conclusion, during expiration, the turbulence kinetic energy in the oral region is in our geometry much more important than that created in the laryngeal region.

c/ Wall Shear Stress

When the jets impact the walls of the model, it has crucial effect on the particle deposition by the inertial impaction, thus the impaction sites are considered for further research. The wall shear stress amplitude increases with shear rate, that is the result of the velocity

gradient. Thus, with high velocity gradient the wall shear stress is rising and therefore is considered to be a good representative of the jet flow impaction and recirculated flow [Nithiarasu et al., 2008]. The important places with high wall shear stress amplitude are displayed on Figure III.7.6 for inspiration peak PIF. The highest amplitude (0.9

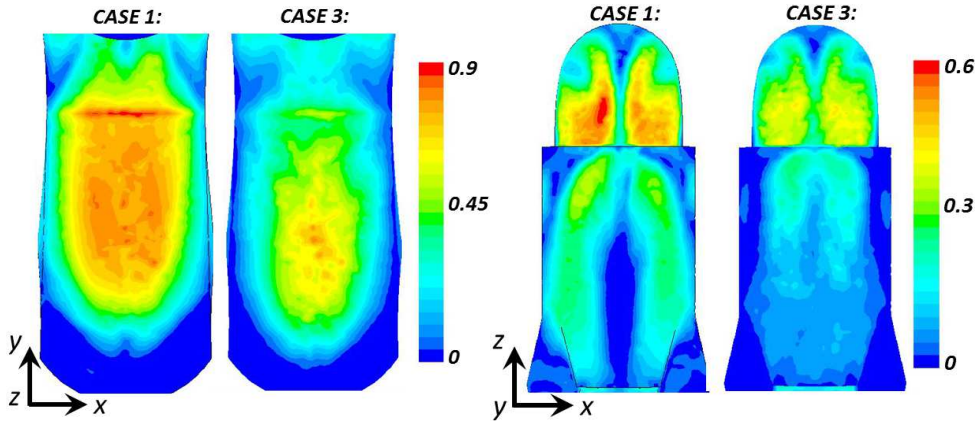

(a) Tongue plane.

(b) Oropharyngeal area.

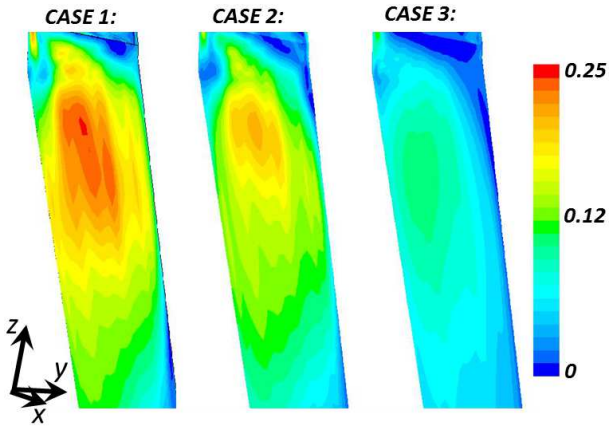

(c) Subglottal area (trachea).

Figure III.7.6: Comparison of wall shear stress at the walls of the model [Pa]. Special interest was put on the regions, where the jets are impacting the wall. Displayed results correspond to $\mathbf{Eup}_{15}$ task at peak inspiration PIF.

Pa) of the wall shear stress is found in the tongue plane, where the site of high speed impaction is the largest in comparison with other places of the model (Figure III.7.6a). In the zone of oropharyngeal jet occurs second site of impaction (Figure III.7.6b) and the wall shear stress rises up to 0.6 Pa. Finally, when glottal jet impacts the trachea wall (Figure III.7.6c) the wall shear stress rises up to 0.25 Pa. The glottal jet impaction on the anterior wall of the trachea was also reported in several previous studies [Cui and Gutheil, 2011; Zhang and Kleinstreuer, 2011; Elcner et al., 2013].

Case 1 with air and case 3 with He-O_2 mixture are compared. Simulation with He-O_2 mixture results in 25% decrease of wall shear stress. Detail on impact of different glottal dynamics is given in panel (c). The sites of highest wall shear stress values are found in

correlation with the most dense deposition sites. Note that in case 2, with moving glottal walls, the wall shear stress occurs at smaller amplitudes. This is result of the laryngeal jet that reaches in case 2 smaller speed (compare with panel **C** on Figure III.7.3.

7.2.2 Laryngeal jet under different breathing conditions

In this section the interest is put on the glottal region and cross section further downstream. A detail view is given to observe the influence of the moving glottal geometry and different carrier gases.

Figure III.7.7 and Figure III.7.8 show the velocity magnitude contours for different simulations of $\mathbf{Eup}_{15}$ and $\mathbf{Tachyp}_{30}$, respectively. Superposed vectors of secondary flow represent the tangential velocity. Each column represents one simulation case: case 1 on the left with steady glottal geometry and air, case 2 with mobile glottal geometry and air, and case 3 with steady glottal geometry and He-O_2 mixture, respectively.

The results of flow velocity and structure simulated during the $\mathbf{Eup}_{15}$ breathing task are illustrated on Figure III.7.7. At the glottal inlet area (l = 238.9 mm) the velocity magnitude reaches around 5 m/s. The secondary flow vectors direct towards the glottal central plane. In cases 1 and 2 a formation of two jets is observed: one faster close to the posterior plane and one slower close to the anterior plane. In the case 3 with He-O_2 mixture the flow structure is more uniform. Nevertheless, note that the airstream is influenced by secondary flow, that performs higher velocity towards the central plane. At the glottal outlet plane the form of the jet starts to be evident and the speed of the flow rises to its maximum (5.5 m/s). Further at the distance 0.5 AP_g, in cases 1 and 2 the high speed flow created in the anterior region of the glottal constriction impacts the tracheal wall. On contrary from the previous simulations with simple tube geometry model (see Figure III.5.9) the laryngeal jet impacts the anterior wall of the trachea. This is a result of inertia effect due to geometry of the laryngeal region, that directs the flow towards the anterior region (see Figure III.7.3, detail **C**), and is in agreement with previous studies [Jayaraju et al., 2007; Elcner et al., 2013]. This observation points out the importance of considering the interactions between the entire upper airways geometry and glottal configuration. The second laryngeal jet, closer to posterior wall, is directed by secondary flow towards the anterior wall too. In case 3, the jet looks axisymetrical, but the secondary vectors are forcing the flow towards the anterior wall. In air cases (1 and 2) at the distance of $2AP_g$ both jets are connected and impact the anterior wall. In case 3 the single jet in He-O_2 mixture impacts the anterior wall at the same distance $2AP_g$. Finally at the distance of $5AP_g$ the flow starts to be stabilized and uniform.

There are not observed significant differences between the flow in cases 1 and 2. In steady case 1 the glottal constriction is narrower and thus the flow speed is slightly higher.

In comparison with $\mathbf{Eup}_{15}$ breathing task the structure of the flow is similar in $\mathbf{Tachyp}_{30}$ breathing. The flow reaches higher levels of the velocity amplitude, but the jet formation has the same characteristics. The flow in cases 3 and 6 with He-O_2 mixture in the laminar regime is more uniform, but as well is characterized by the jet shift towards the anterior

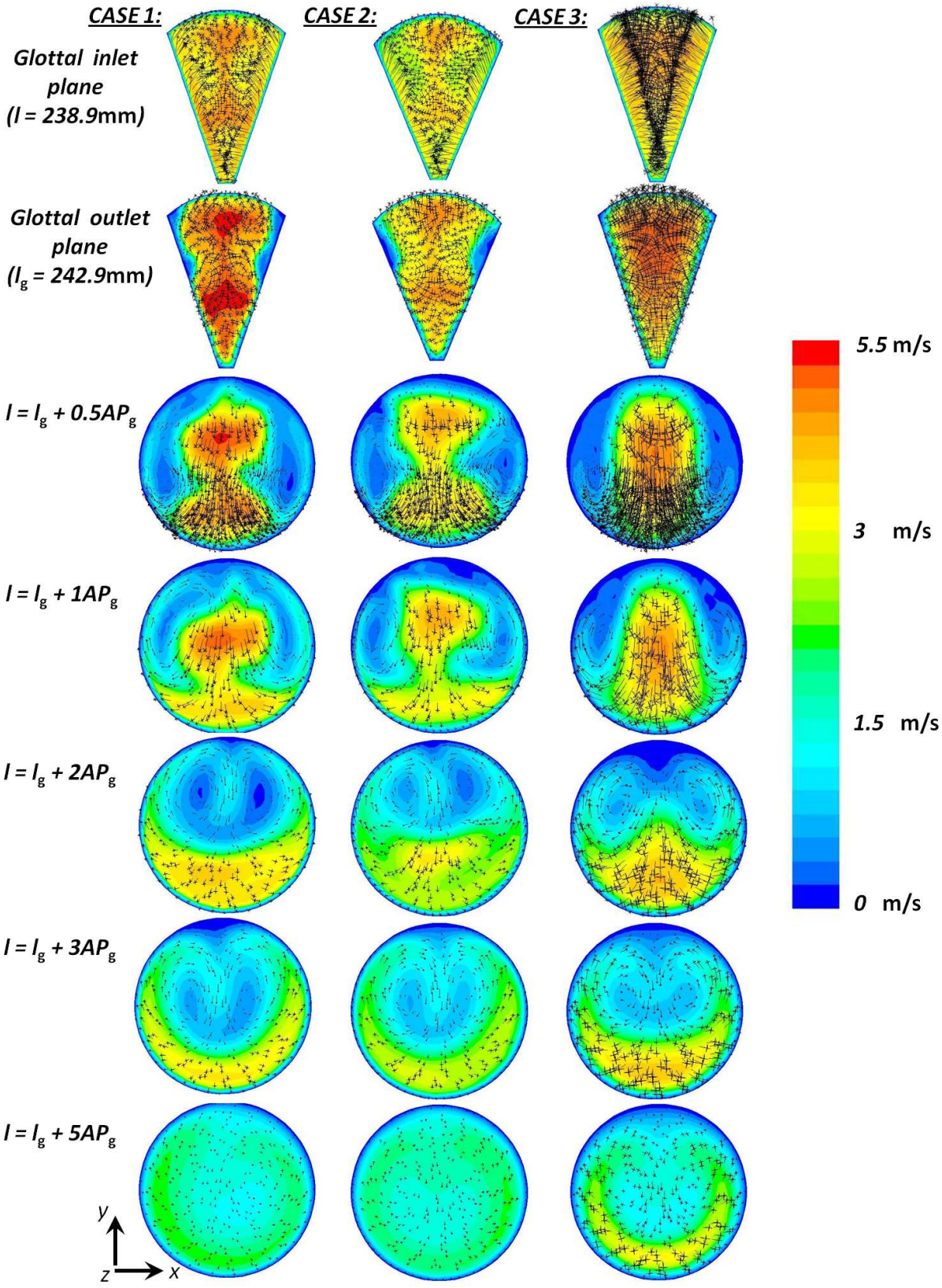

Figure III.7.7: Contours of velocity magnitude $|u|$ [m/s] and vectors of secondary flow (tangential velocity) for glottal plane and subsequent cross-sections at the shot-instant of peak inspiration. Comparison of cases 1, 2, and 3 ($\mathbf{Eup}_{15}$).

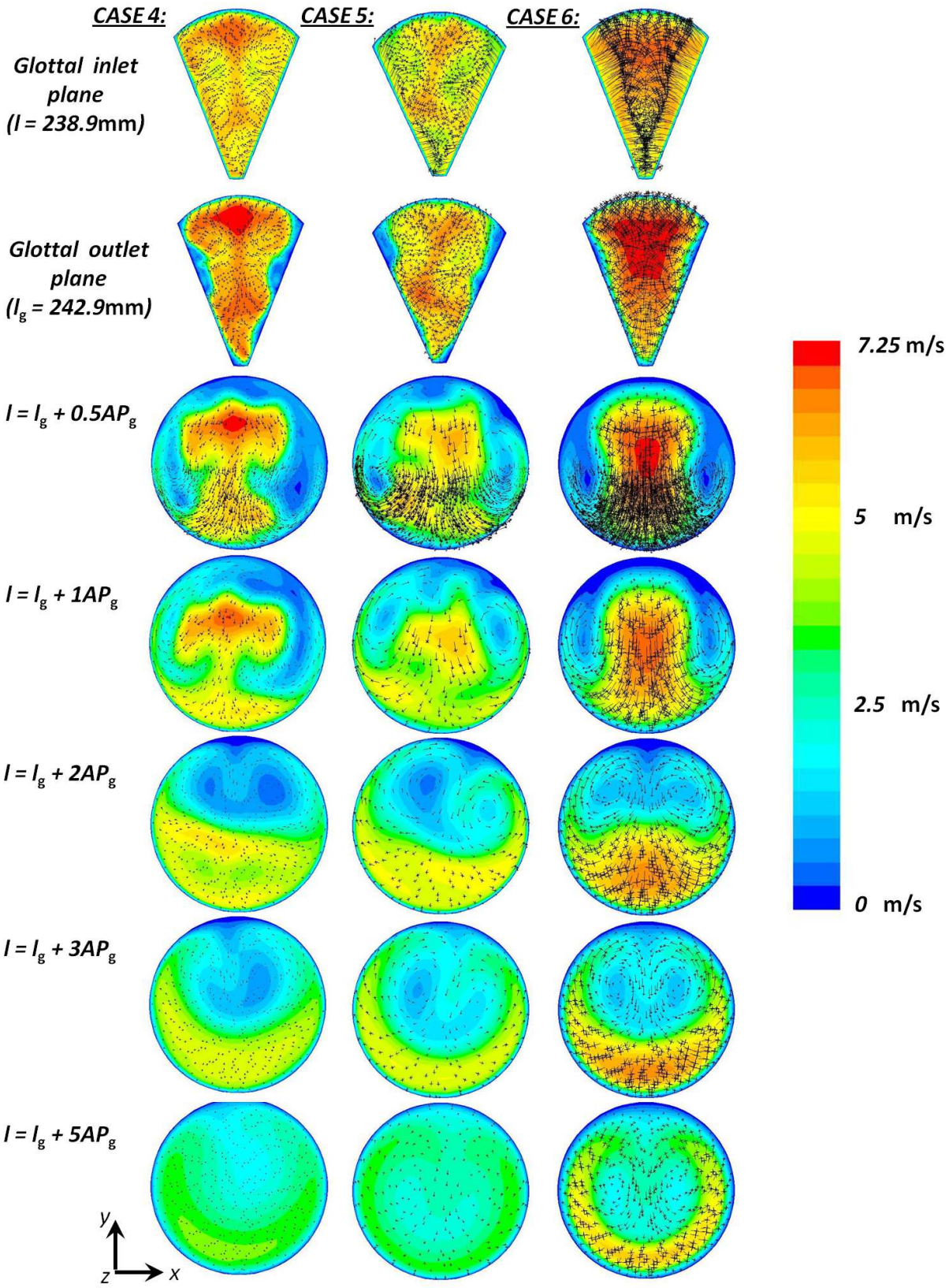

Figure III.7.8: Contours of velocity magnitude $|u|$ [m/s] and vectors of secondary flow (tangential velocity) for glottal plane and subsequent cross-sections at the shot-instant of peak inspiration. Comparison of cases 4, 5, and 6 ($\mathbf{Tachyp}_{30}$).

wall. Observed is also that the high-speed flow stabilizes further after greater distance of $5AP_g$ from the glottal outlet. Similarly Heenan et al. [2003]; Brouns et al. [2007b] observed that the flow structure is very similar in the UA for flow rates of 15 and 30 L/min.

Lastly, Propre Orthogonal Decomposition (POD) technique was applied to understand the coherence structures in turbulence and their spectral signature in a deterministic manner (for details on this technique please refer to Holmes et al. [1998]; Pastur et al. [2005]). POD was developped by Lumley [1967] and in the past was applied to study the flow field within the human airways by Lin et al. [2007].

The existence of moving boundary in the present study could register a significant impact on the dynamic behavior of the solution. Thus, the POD was applied to mid-sagittal plane of the laryngeal zone for the static and dynamic glottal wall conditions of $\mathbf{Eup}_{15}$ task and the interval 0.5s around the PIF. Comparison between cases 1 and 2 was observed. For the application of POD with moving boundaries, we used the method introduced by Utturkar et al. [2005] which consists in interpolation of the solution at each time step onto a fixed uniform grid.

Figure III.7.9 displays the POD statistical results. On the right panel is displayed a

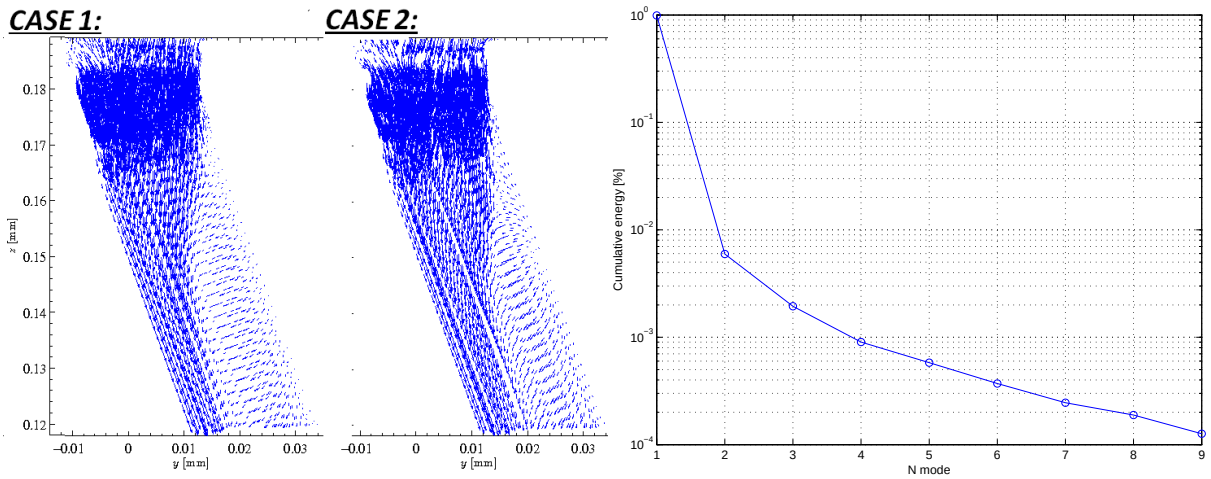

(a) Comparison of cases 1 and 2.

(b) Cumulative energy of the POD modes.

Figure III.7.9: POD analysis results of the flow-field in the mid-sagittal laryngeal plane ($\mathbf{Eup}_{15}$ breathing task, air).

velocity field of the first (the strongest) mode. On the left panel is plotted the cumulative energy of the 9 modes evaluated. In both cases 1 and 2, almost 100% of the energy considers the first mode and thus, this is the most representative of the studied flow-field. Comparing the results of the first mode on the left panel with the contours of velocity magnitude (see panel **C** on Figure III.7.3) the flow-field has similar structure. Likewise, considering cases 1 and 2 no differences in the distribution of energies between POD modes are found. Therefore the results confirm the conclusion that simulations with static or dynamic glottal variations do not show significant differences on the airflow dynamics

within the laryngeal area.

7.3 Aerosol Deposition

The aim of this study was to describe the micro-particle deposition in the upper airways under realistic breathing conditions. The methodology on the aerosol injection was detailed in section III.6.3 and section III.6.2.2, particles of 1, 3, 5, and 10 µm were injected into the model during the inspiration phase.

7.3.1 Effects of non-steady airflow

Aerosol transport under non-steady airflow To visualize the transport of the particles through the upper airways model, Figure III.7.10 displays the particles at different shot instants of the breathing cycle. The breathing cycle corresponds to $\mathbf{Eup}_{15}$ task (case 2, unsteady glottal walls) as shown in Figure III.6.8a. The illustration case of 5 µm particles is chosen here. The particles are colored according to their velocity magnitude $\mid u \mid$. At the beginning of the inspiration phase (see $t_1 = 0.08$s on the Figure III.7.10), the individual aerosol injections are apparent in the mouthpiece region. The aerosol follows the high-speed flow from the mouthpiece (for the detail on the flow structure, see Figure III.7.3). Further, the particles impact the tongue plane and follow towards the walls of the soft palate ($t_2 = 0.10$s). At this moment a part of aerosols continues downstream the model and a part recirculates backflow into the mouth cavity (see t_2, t_3, and t_4). At instant $t_5 = 0.19$s, the flow of particles impacts the anterior wall of trachea. Later, at the peak inspiratory flow PIF (t_6), the particles are escaping from the trachea by the outlet wall Ω_o and reach the highest speed around 5 m/s in the oropharynx and in the region downstream the glottis. At the end of inspiration phase, when the flow rate Q is close to 0 m/s, all the particles are distributed through the whole model and their speed is close to 0 m/s (see t_7). When expiration begins, the particles are transported backwards towards the mouth cavity, escape by the inlet wall Ω_i and around t_9 is noticeable a jet up to 5 m/s in the oropharyngeal region. Finally, around the time $t_{10} = 2.63$s a negligible amount of particles stays in the model and recirculates in the mouth cavity until the end of the cycle at $t = 4$s.

Aerosol deposition under non-steady airflow Figure III.7.11 and Figure III.7.12 illustrate the temporal deposition fractions (intervals of 0.1s) of the 5 µm particles during one breathing cycle ($\mathbf{Eup}_{15}$ task, case 2 with dynamic glottal geometry) on the walls of the model.

Local deposition fractions in Figure III.7.12 are differentiated according to 4 regions defined in Figure III.6.3b: mouth cavity, oropharynx, larynx, and trachea. The *temporal deposition fraction* is defined as the ratio of momentary deposited mass in a given region, to the total injected mass of aerosols during one breathing cycle into the model.

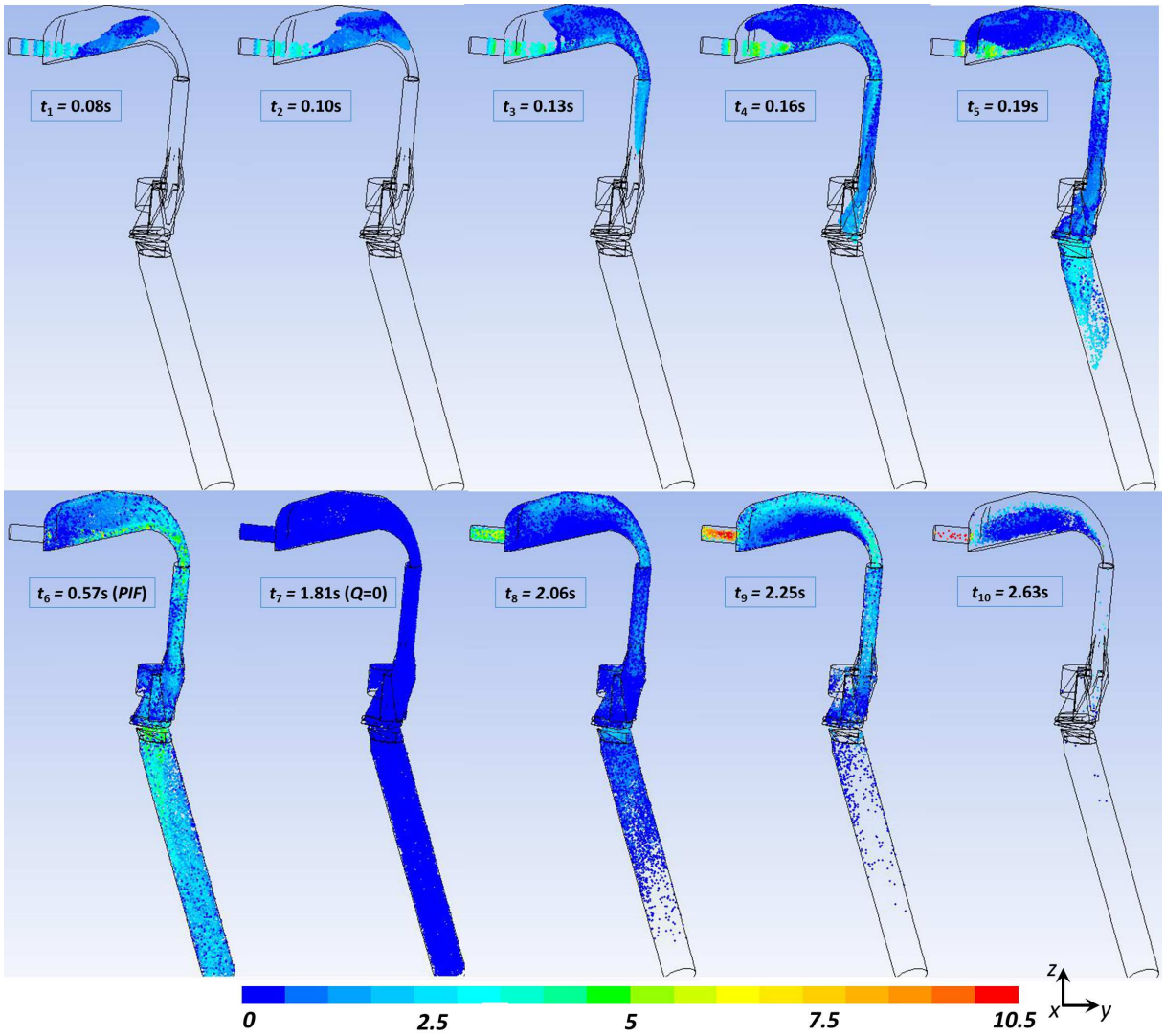

Figure III.7.10: Discrete phase particles plot at different times during the cycle. The particle color corresponds to its velocity magnitude $\mid u \mid$ [m/s].

The variation of deposition in function of time shows consistency with the inlet flow rate Q. Only a few particles is deposited on the walls of the model before the instant $t_1 = 0.08$s (see Figure III.7.10). Indeed, in the beginning of the inspiration the flow speed is low and only few particles is present in the model. The peak deposition is reached just before the peak inspiratory flow PIF ($t_6 = 0.57$s), and further decreases until the beginning of the expiration phase ($t_7 = 1.81$s), when the injection stops. The deposition is the lowest within the smallest flow rates (< 5 L/min) and again rises when the expiration flow rate rises above 10 L/min, until all the aerosols escape or deposit ($t_{10} = 2.63$s). Note that, no deposition is observed during expiration in the region of trachea (compare with shot-instants t_8, t_9, and t_{10} on Figure III.7.10). If the model included the bronchial bifurcations, there would be particles transported from bronchus through the trachea

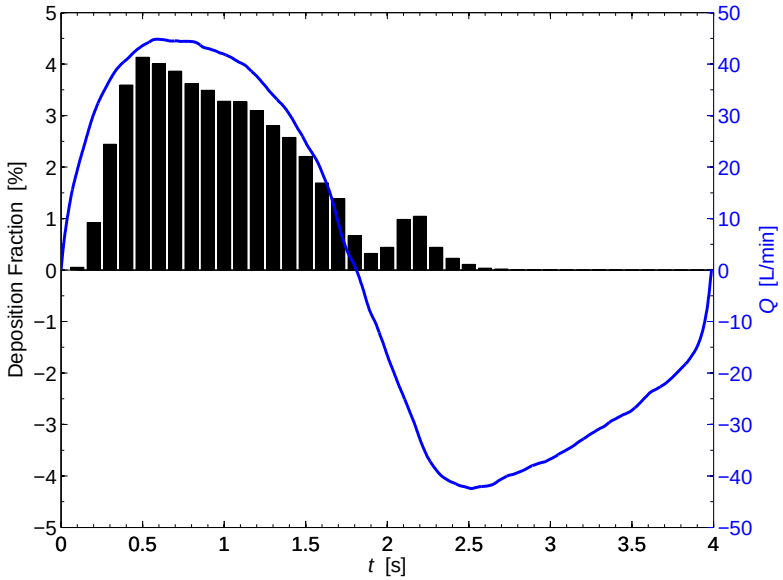

Figure III.7.11: Inlet airflow rate and temporal deposition fractions in the entire model during $\mathbf{Eup}_{15}$ breathing task simulation, case 2 with dynamic glottal geometry.

and fraction of deposited particles would increase in this area. The periods with very low flow rates could be important for deposition of sub-micrometer particles, for which sedimentation and diffusion is becoming the dominant deposition mechanism. In total, the highest temporal deposition fractions are observed within the oropharynx region, results on the deposition fraction over the whole breathing cycle are given in next section.

7.3.2 Deposition spots within the model

In this section, the deposition spots are compared for 2 different particle diameters, 1 and 10 μm. For schematic illustration, Figure III.7.13 displays deposited particles in function of the time for 1 and 10 μm particles ($\mathbf{Eup}_{15}$ task, case 2). At the instant $t_1 = 0.2$s, in both cases, the particles deposited mainly in the bend of the soft palate.

At the instant $t_2 = 0.3$s first particles are deposited in the trachea. Further at the peak inspiratory flow (t_3) the main deposition spots are highlighted. 1 μm particles main deposition sites are observed in the oropharynx and trachea. 10 μm particles main deposition sites are found mainly in the oropharynx. Final deposition with all particles is illustrated on last image at instant t_4. Other cases and particle diameters point to similar deposition sites.

One of the important findings of the airflow dynamics, in previous section, were the results on wall shear stress, that in accordance with work of Nithiarasu et al. [2008] indicated the site of airflow jets impaction. Those impaction sites are important for the particle deposition by inertial impaction and the findings of Taherian et al. [2011] confirms the correlation between concentration of the particles within the high stress

regions. Therefore, the main deposition areas are viewed in detail on Figure III.7.6 in order to investigate the impaction sites of the airflow jets and evaluate the particle deposition.

On Figure III.7.14 , resulting deposited particles after one breathing cycle are displayed for the mouth cavity and oropharynx. The superior view of the tongue wall (Figure III.7.14a) is compared with wall shear stress on this surface (Figure III.7.6a). In particular for 10 μm particles, the shape of deposition area corresponds to the area with the highest wall shear stress. Similarly the deposition in oropharynx (Figure III.7.14b) is compared with wall shear stress distribution on the oropharyngeal walls (Figure III.7.6b). Recognized are two important sites with high wall shear stress values. Consequently, in those locations are observed higher depositions of 10 μm particles. Therefore, wall shear stress seems to be indicative for deposition of bigger particles, that principal motion mechanism is the inertial impaction. The summary of data on regional deposition over the whole cycle will be detailed later on Figure III.7.17.

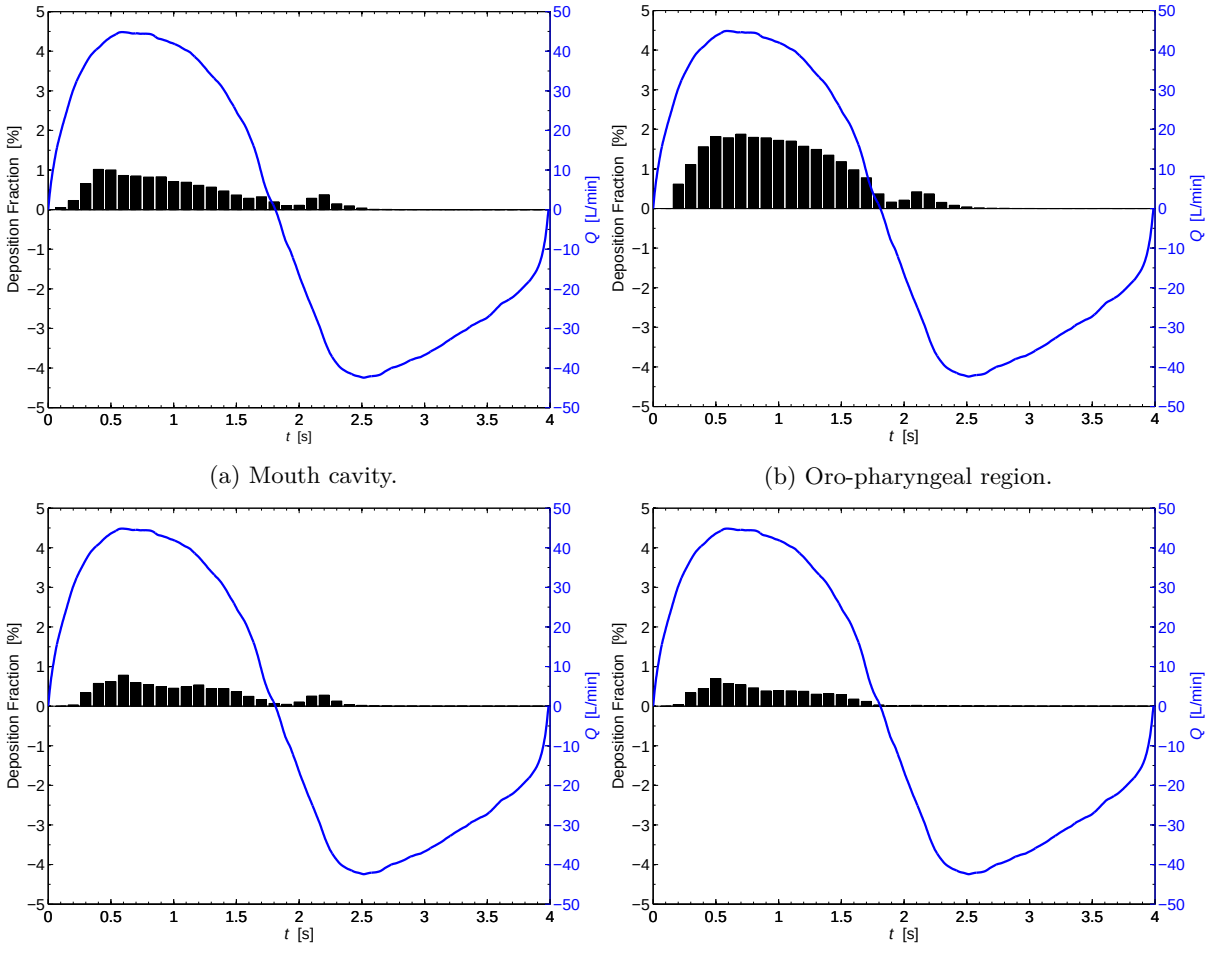

(a) Mouth cavity.

(b) Oro-pharyngeal region.

(c) Larynx.

(d) Trachea.

Figure III.7.12: Inlet airflow rate and temporal deposition fractions in different parts of the model during **Eup**$_{15}$ breathing task simulation, case 2 with dynamic glottal geometry.

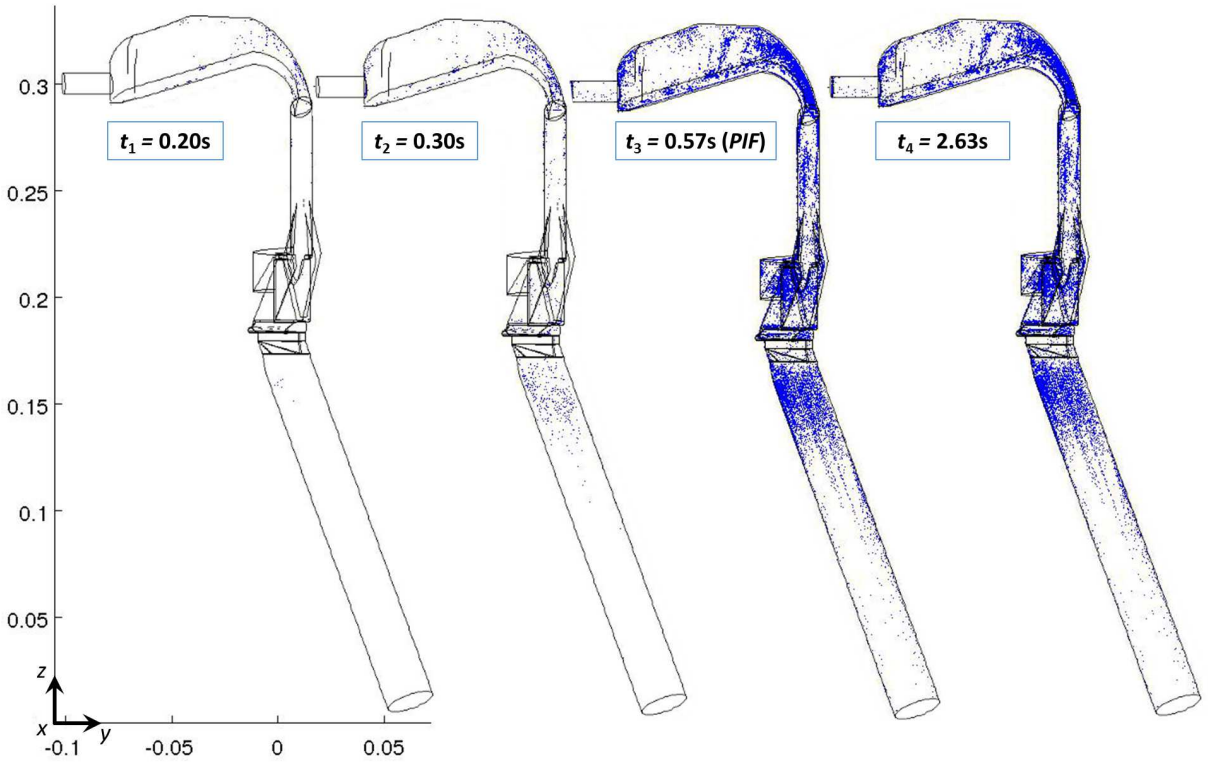

(a) 1 µm particles.

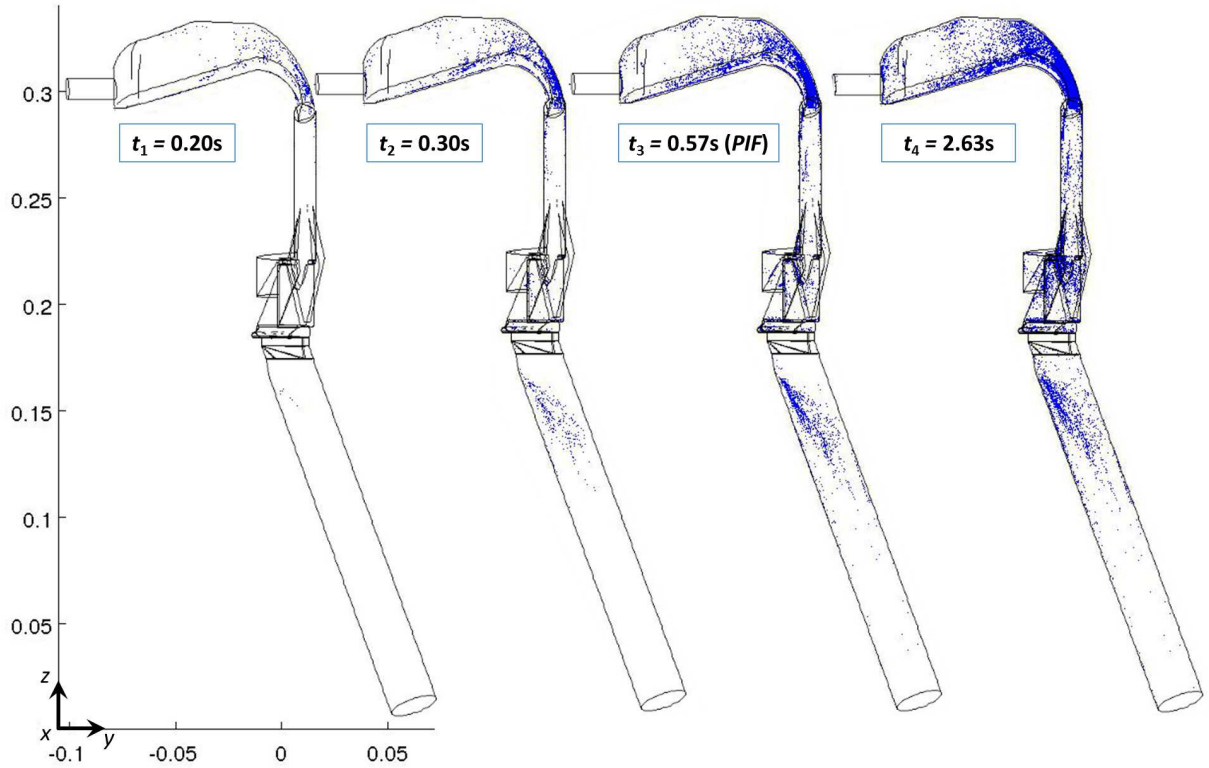

(b) 10 µm particles.

Figure III.7.13: Illustration of particles deposited during the breathing cycle (**Eup**$_{15}$ breathing task simulation, case 2 with dynamic glottal geometry).

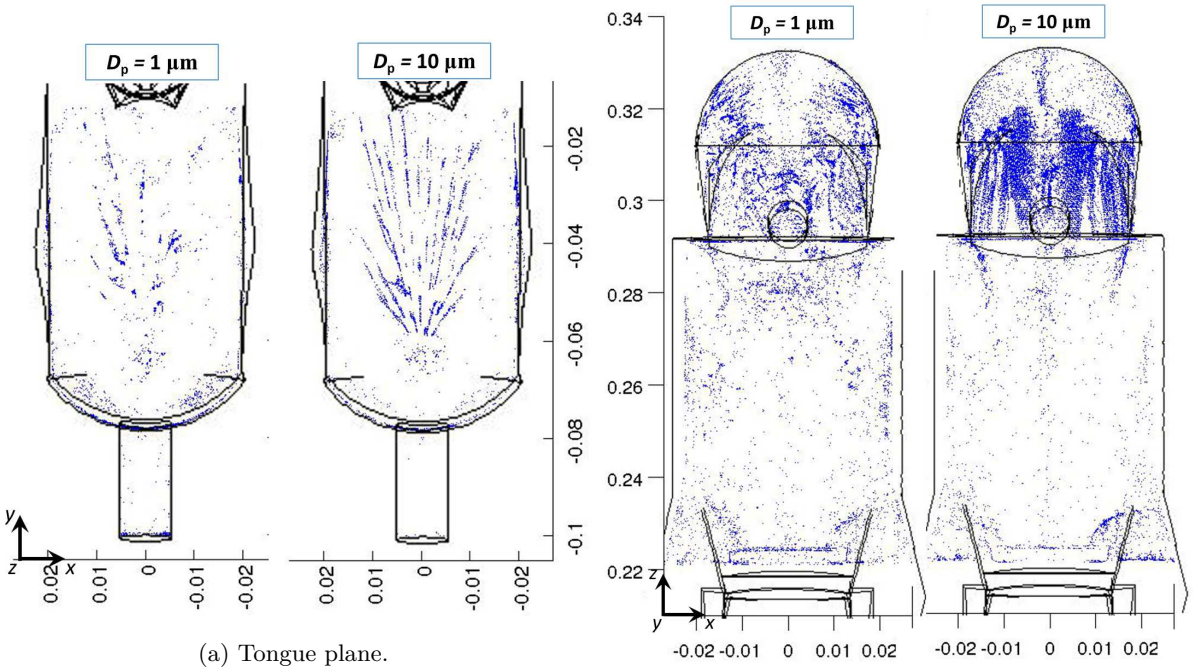

(a) Tongue plane.

(b) Oropharynx.

Figure III.7.14: Illustration of deposited particles on different walls of the model (**Eup**$_{15}$ breathing task simulation, case 2 with dynamic glottal geometry).

7.3.3 Impact of steady and dynamic glottal variations in the trachea region

From deposition illustration on Figure III.7.13 is notable that deposition in the trachea is important for smaller particles ($D_p = 1\,\mu m$). Thus to evaluate the influence of steady and dynamic glottal variations on the particle deposition in this region, results of particles with 1 µm diameter are studied. Figure III.7.15 represents the deposition distribution of 1 µm particles in the entire trachea (regions defined in Figure III.6.3b) in function of the angle around the tracheal central axis (**Eup**$_{15}$ breathing task). As already reported above, the tracheal airflow (see Figure III.7.7) impacts the tracheal anterior part. Similarly, the flow of particles displayed on Figure III.7.10 impacts the tracheal anterior wall. As a result on Figure III.7.15 is observed that particles are deposited mainly in the anterior region of the tracheal tube. Comparison between cases 1 and 2 with static and dynamic glottal variations do not show significant discrepancies. Thus, the glottal dynamic variations does not perform significant influences to the deposition dynamics.

Deposition distribution within the trachea Another characteristics for the deposition in the trachea is the connection of the deposition with the site of the laryngeal jet impaction. As reported on Figure III.7.7 the first one of two laryngeal jets impacts the trachea wall at the distance of $1AP_g$, the second at the distance of $2AP_g$ from the glottal plane. On Figure III.7.13 is observed a free space between the glottal plane and the site with the deposited particles in the trachea. Figure III.7.16 presents the distribution of the

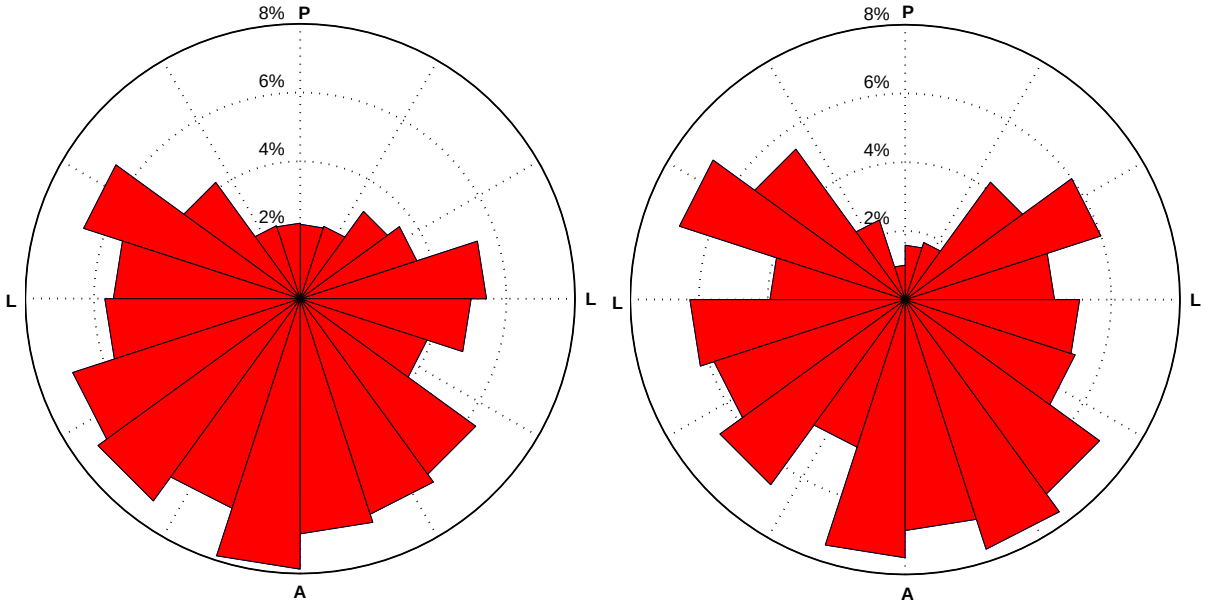

(a) Case 1 with static glottal geometry.

(b) Case 2 with dynamic glottal geometry.

Figure III.7.15: Deposition distribution of 1 μm particles in trachea in function of the angle around the central axis, **Eup**$_{15}$ breathing task simulation (P - posterior, A - anterior, and L - lateral reference plane).

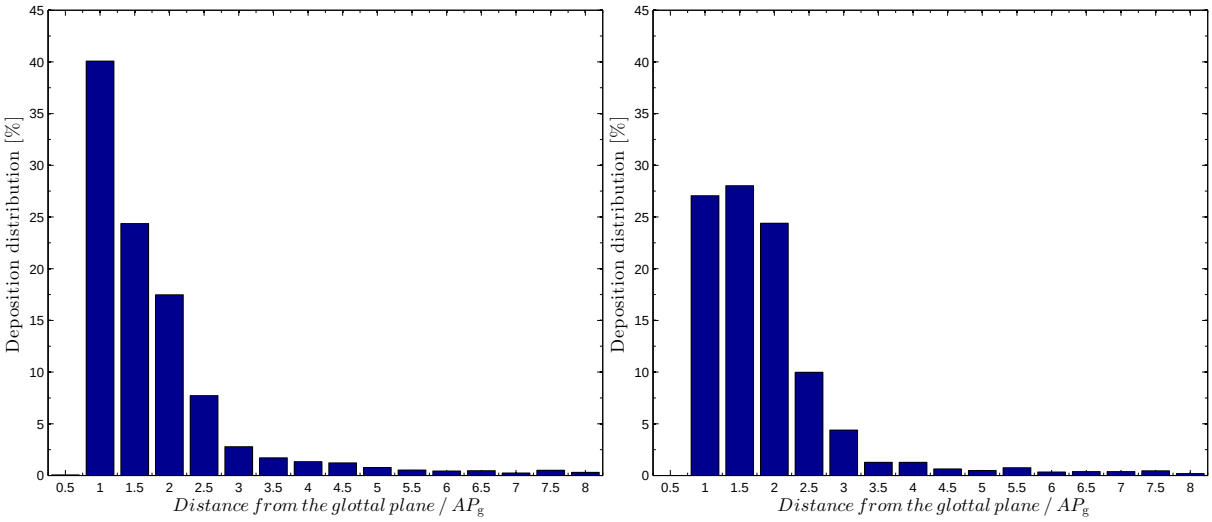

(a) $D_p = 1$ μm.

(b) $D_p = 10$ μm.

Figure III.7.16: Deposition distribution in trachea in function of the distance from the inlet, **Eup**$_{15}$ breathing task, case 2 ($AP_g = 22.1$ mm).

particles in the trachea in function of the distance from the glottal plane. For both particle diameters 1 and 10 μm at the distance between 0 and $0.5AP_g$, the deposition is close to zero. 1 μm particles are mainly deposited at the distance between 0.5 and $1AP_g$

from the glottal plane. 10 μm particles deposition is slightly more spread and the peak deposition is located at the distance between 1 and $1.5AP_g$. In conclusion, bigger particles have higher inertia and so do not follow the flow streamlines perfectly and are deposited in further distance in comparison with small particles.

7.3.4 Summary on deposition results within the upper airways for the 6 cases

The variations of other particle diameters (1, 3, and 10 μm) and other simulation cases (1, and 3 - 6) are marked with similar characteristics as the ones detailed previously for case 2. Note that, only differences in particle velocity amplitude or deposition can be found. Therefore, on Figure III.7.17 are displayed regional and total deposition efficiencies in function of particle diameter, and different simulation cases over the entire breathing cycle. First column summarizes deposition fractions in different regions of the model (according to sections defined in Figure III.6.3b), and second column gives the deposition efficiencies for the entire model. The *deposition efficiency* is defined as the ratio of the number of particles trapped by the walls of the model to the total number of particles released in the mouthpiece during one breathing cycle.

Comparing the deposition fractions in different regions of the model, the highest fraction in all cases and for all studied diameters is deposited within the oropharyngeal region. In the following, if not specified else, the cases with air as a medium (cases 1, 2 and 4, 5) are discussed.

Regional deposition fractions Particles with diameter 1, 3, and 5 μm result in similar deposition characteristics in the mouth cavity, laryngeal, and tracheal regions (see left column on Figure III.7.17). In the mouth cavity and larynx the deposition reaches around 10% of all particles injected into the model. In cases 3 and 6 with He-O_2 mixture, in comparison with air, the deposition is about two times less, around 6% in the mouth cavity and about 3% in the larynx.

In the trachea is for all diameters deposited the smallest fraction. Within this region is significant the difference between *slow breathing* task $\mathbf{Eup}_{15}$ and *rapid breathing* task $\mathbf{Tachyp}_{30}$, when in former case the deposition gets up to 6% (less than 2% in He-O_2 mixture), but in the later one up to 3% (less than 0.5% in He-O_2 mixture).

Regarding the deposition in the oropharynx significant differences between different particle diameters are found. The highest deposition is reached during *rapid breathing* task $\mathbf{Tachyp}_{30}$. Bigger the particles are, higher the difference is. Thus, for 1 μm particles in *slow* and *rapid breathing* the deposition is slightly less and slightly above 20%, repectively. On the other side, for 3 μm particles the deposition reaches more than 25% and more than 35% for *slow* and *rapid breathing*, respectively. In He-O_2 mixture in both breathing regimes the results come to about 12% of deposited mass in this region.

For particle's diameter 10 μm, the values in the mouth cavity and oropharynx are much higher (see panel (g) on Figure III.7.17). Because the main deposition mechanism in upper airways is inertial impaction, higher deposition with bigger particle diameter can

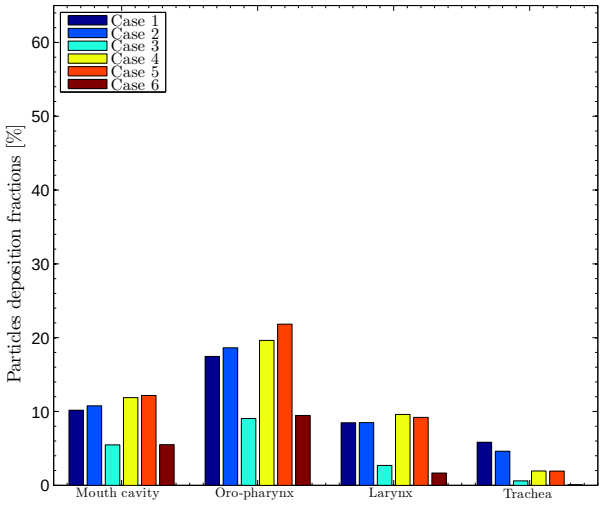

(a) $\boldsymbol{D_p = 1\,\mu m}$. Deposition fractions in different sections.

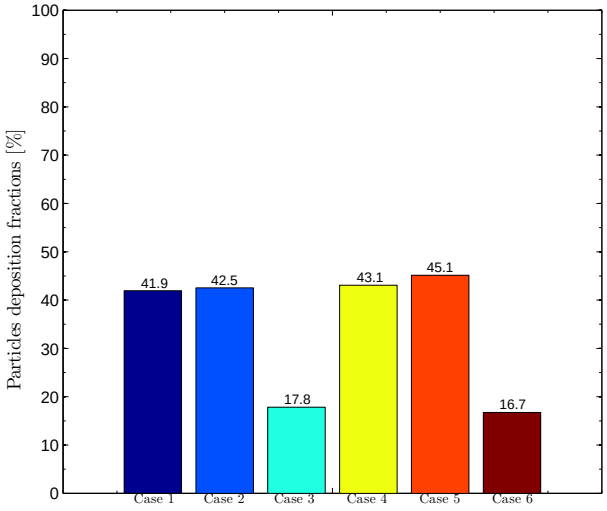

(b) $\boldsymbol{D_p = 1\,\mu m}$. Total deposition fractions.

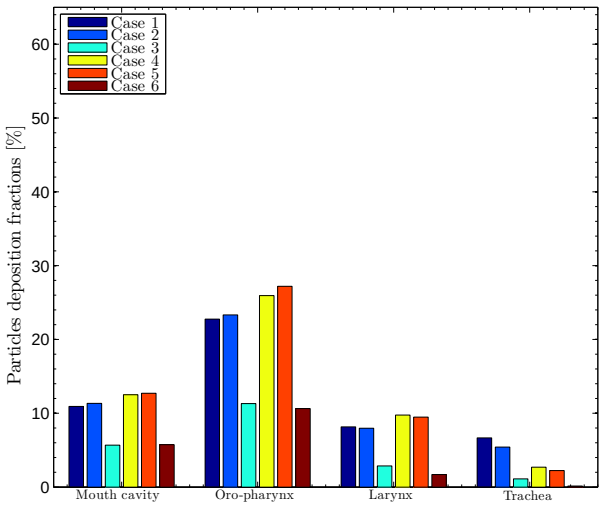

(c) $\boldsymbol{D_p = 3\,\mu m}$. Deposition fractions in different sections.

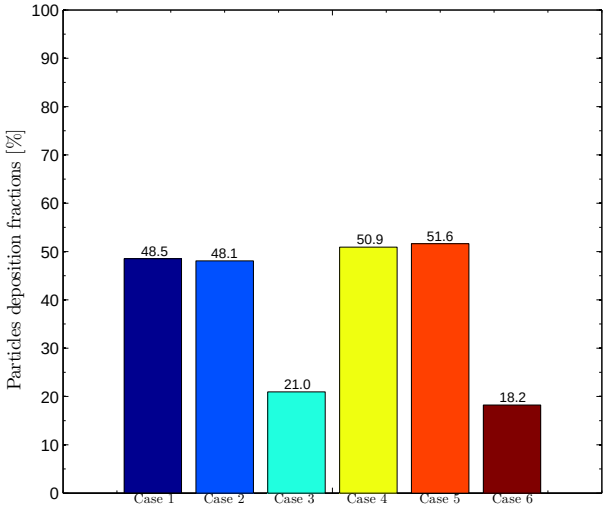

(d) $\boldsymbol{D_p = 3\,\mu m}$. Total deposition fractions.

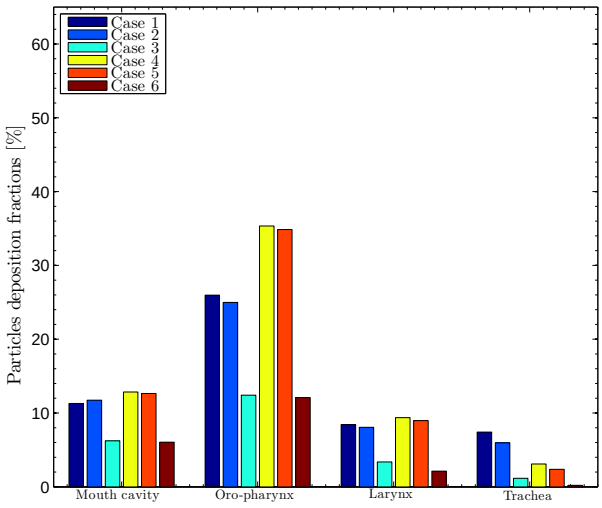

(e) $\boldsymbol{D_p = 5\,\mu m}$. Deposition fractions in different sections.

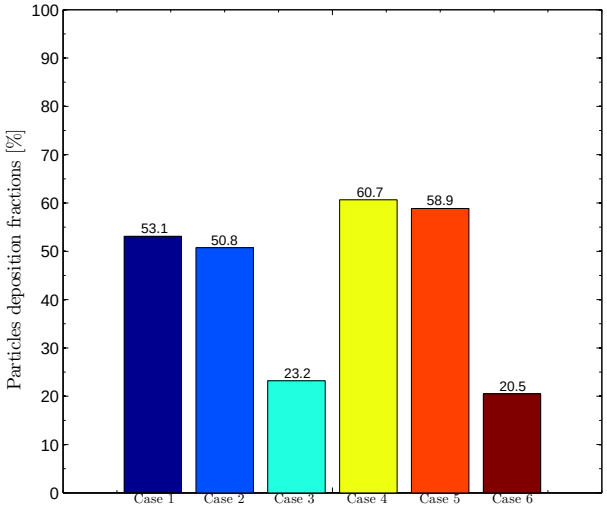

(f) $\boldsymbol{D_p = 5\,\mu m}$. Total deposition fractions.

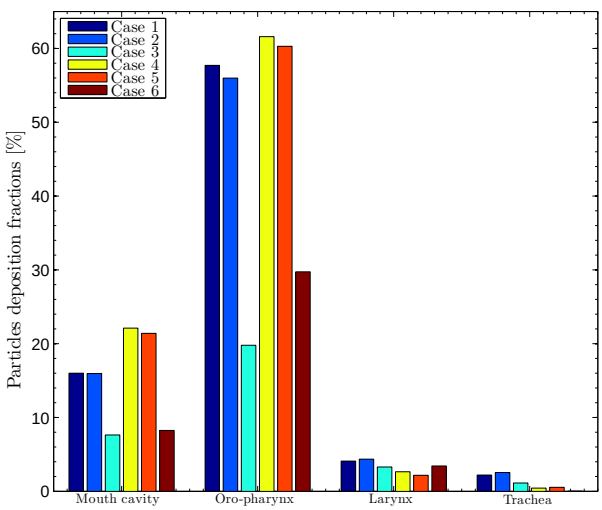

(g) $\boldsymbol{D_p = 10\,\mu m}$. Deposition fractions in different sections.

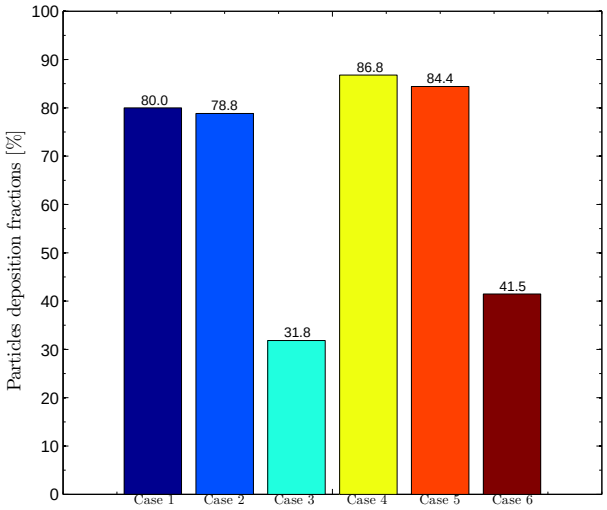

(h) $\boldsymbol{D_p = 10\,\mu m}$. Total deposition fractions for particle diameter.

Figure III.7.17: Comparison of deposition fractions in different sections of the model for simulated cases 1 to 6.

be explained using the Stokes number *Stk* (Equation I.1.13), where D_p is found in the numerator. Therefore the deposition reaches up to 16%/22% (for *slow/rapid breathing*) and 58%/62% (for *slow/rapid breathing*) in the mouth cavity and in the oropharynx, respectively. In He-O_2 mixture the deposition is more than two times smaller, around 8%, in the mouth cavity with no differences between the breathing regimes. Likewise in the oropharynx the deposition is around 20%/30% (for *slow/rapid breathing*). On contrary, the depositions in the larynx and in the trachea are minor, less than 5%.

Total deposition fractions Figure III.7.18 reports the total deposition efficiencies over the entire model vs. the particle diameter D_p. The graph is summary of the left column on the Figure III.7.17. Results of all 6 simulation cases are compared. A distinction between results of air and He-O_2 mixture simulations is notable. The flow with He-O_2 mixture exhibits low Reynolds number and results in laminar flow. Thus, in He-O_2 mixture the deposition is in all cases more than two times smaller in comparison with air, that is in agreement with the literature [Darquenne and Prisk, 2004; Sandeau et al., 2010; Miyawaki et al., 2012; Katz et al., 2014]. Significant difference of He-O_2 mixture deposition is found between 1, 3, and 5 µm particles on one side and 10 µm particles on the other side. While for the former the deposition is reduced with *rapid breathing*, for the latter the deposition is enhanced with *rapid breathing*, in comparison with *slow breathing*. The discrepancy is discussed more in the next paragraph.

Comparing *slow* and *rapid breathing* (**Eup**$_{15}$ and **Tachyp**$_{30}$) slight increase (at maximum 8%) in deposition efficiency is found for *rapid breathing*. Concerning the differences between simulations with static and dynamic glottal area (compare case 1 with case 2 and case 4 with case 5 in the left column on Figure III.7.17), only negligible differences

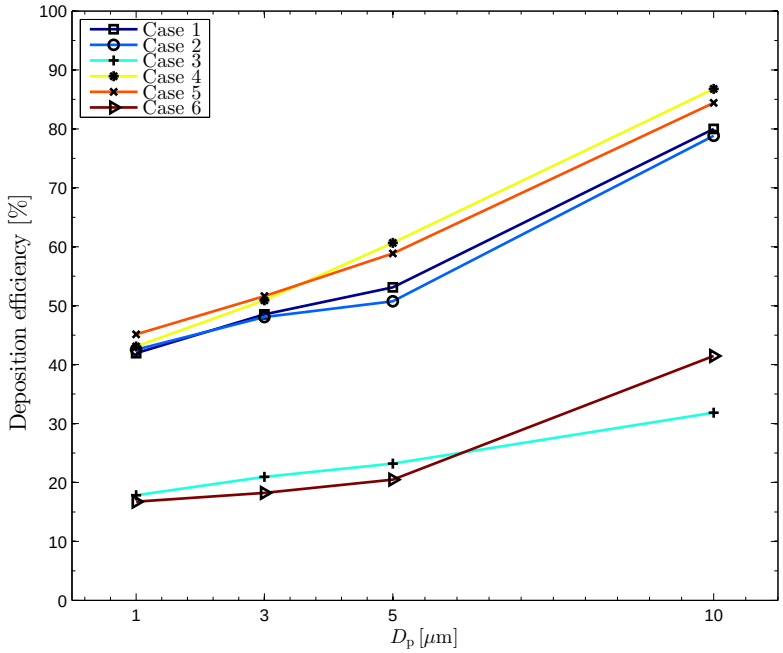

Figure III.7.18: Particle deposition efficiency in function of the particle diameter.

(around 2%) are observed. Nevertheless, note that the highest differences between models with steady and dynamic glottal geometry are found in the oropharynx. And whereas small particles of 1 and 3 µm show slightly smaller deposition in cases of static glottis, on contrary particles of 5 and 10 µm result in higher deposition in cases of static glottis.

Impaction parameter The resulting data on Figure III.7.18 are slightly scattered depending on the breathing task. In order to reduce scatter of the data, the impaction parameter $D_p^2\overline{Q}$ is chosen for better representation. Impaction parameter is usually used as a deposition parameter in previous studies, because it incorporates the effects of varying airflow rate and the particle diameter. Similar to *in vitro* study at non-steady airflow of Golshahi et al. [2013], airflow rate $\overline{Q}$ is calculated as the average inspiration flow rate (32 L/min for $\mathbf{Eup}_{15}$, group 2 and 45 L/min for $\mathbf{Tachyp}_{30}$, group 2).

Comparing the air results on Figure III.7.18 and on Figure III.7.19a the latter show similar tendency of the deposition efficiency, for all six simulations. For He-O_2 mixture in the previous Figure III.7.18 was observed different characteristics between 1, 3, and 5 µm particles on one side and 10 µm particles on the other side. On the contrary, on Figure III.7.19a the data of *slow* and *rapid breathing* demonstrate similar trend. The deposition efficiency shows similar tendency In function of the impaction parameter for both types of breathing.

Comparison with results of three *in vitro* models presented for air by Golshahi et al. [2013] is superposed on the graph. The results show big spread of data depending on the model. Models are displayed on Figure III.7.19b and noticeable differences in the geometries are

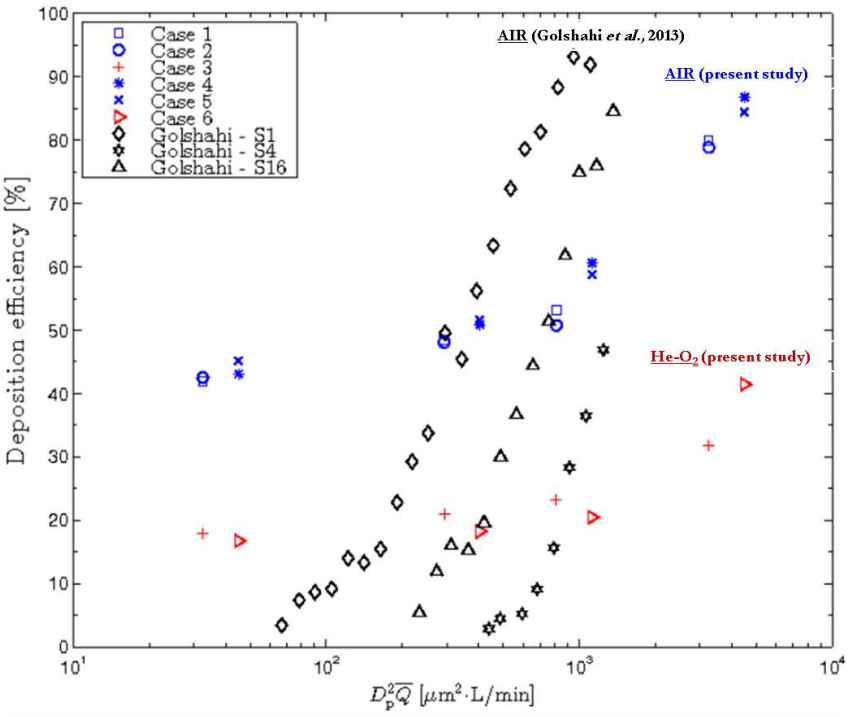

(a) Particle deposition efficiency in function of the impaction parameter. Comparison with Golshahi et al. [2013].

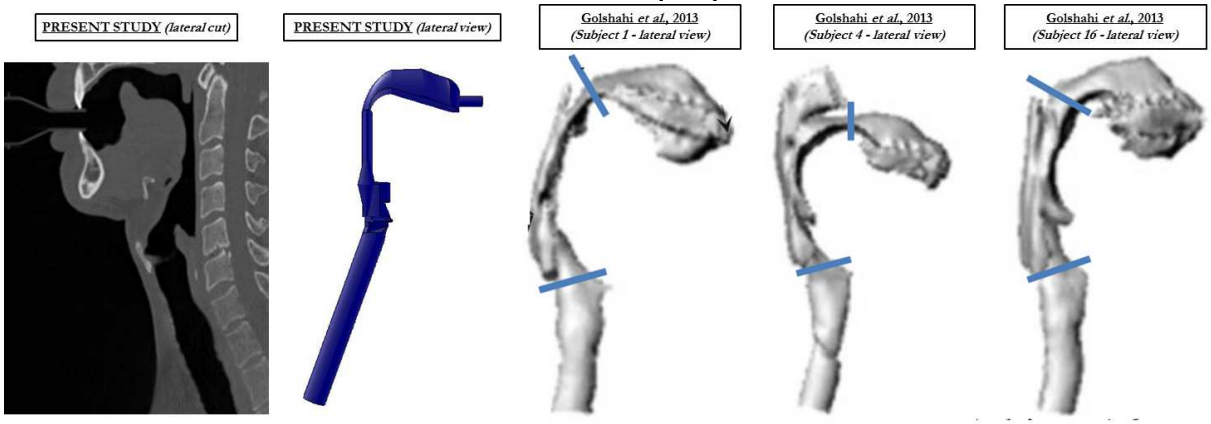

(b) Comparison of present model geometry with models of 3 subjects studied by Golshahi et al. [2013].

Figure III.7.19: Comparison of present study with Golshahi et al. [2013].

evident between those models and also in comparison with our model. Golshahi et al. [2013] presented results on particles diameter in the range between 0.5 and 6.7 μm. Our data in the range between 10^2 and 10^3 of $D_p^2\overline{Q}$ (that correspond to particle diameter 3 and 5 μm) are found within the results of their *in vitro* models. For higher values data of present study are in the range of deposition efficiencies 80 and 90%, that correspond to the highest deposition efficiencies of Golshahi et al. [2013]. Finally the deposition efficiencies of the smallest impaction parameters between 30 and 40 result in much higher values than

would be expected from measured results by Golshahi et al. [2013]. Taking into account the scatter of Golshahi et al. [2013] results depending on different model geometries, it is suggested that such a difference could be caused by this reason. In particular, the small geometry of the present mouthpiece generates very thin jet flow, that can lead to higher deposition for micrometer particles within the upper airways, as was described in Lin et al. [2001].

Summary

Several items can be highlighted to summarize the methodology and the results presented in the Part III.

- An averaged 3D geometry of the human upper airways has been designed based on: (i) the HRCT-scans of a male adult obtained from the pilot study described in Conway et al. [2012]; and (ii) the laryngoscopic images of glottal motion elaborated in the Part II. The time-varying laryngeal area has been developed through 2D and 3D steps, considering a rectangular constriction and a simplified tubular geometry, respectively. Finally the glottal region geometry has been integrated into the 3D averaged model of upper airways.

- CFD simulations were conducted implementing conditions resulting from *in vivo* measurements in the Part II: (i) time-varying glottal wall motion of one breathing cycle; and (ii) unsteady oral airflow rates, together with unsteady aerosol injection of one breathing cycle. In total, six simulation cases were performed in this thesis, differing from each other through different conditions: (i) the breathing regime (*eupnea*/*tachypnea*); (ii) the glottal wall condition (steady/dynamic); and (iii) the carrier gas (air or He-O_2 mixture). During the inspiration phase, aerosol particles with diameter 1, 3, 5, and 10 µm, were injected into the model.

- For each simulation case, the numerical data post-processing comprised several different analysis. (i) Concerning the flow dynamics: study of the airflow field including pressure drop evolution, turbulence distribution through the model and wall shear stress on the regions of jet impaction. (ii) Concerning the unsteady aerosol dynamics: study of particle flow over one breathing cycle and temporal aerosol depositions. (iii) Finally, concerning the aerosol deposition efficiency: study of deposition in different parts of the model and for different particle sizes.

- Regarding the airflow dynamics, three regions forming important jet structures were observed: one in the mouthpiece, second in the oropharyngeal bend and last in the glottal area. Consequently the created high-speed airstream caused jet impaction and recirculation zones in the mouth cavity, in the pharynx and in the trachea, respectively. The wall shear stress (WSS) is considered to be a good representative of the jet impaction and recirculated flow. Thus, the WSS was studied at the impaction sites and later compared with the aerosol deposition distribution in those regions. No significant differences in airflow dynamics were observed between the two simulation

cases: (i) steady glottal walls (group of subjects with unvarying glottal opening); and (ii) unsteady glottal walls (subjects with moving glottal walls).

- Inertial impaction is the most important deposition mechanism within the upper airways and thus the deposition is primarily dependent on the particle size and airflow speed (*i.e.*, Stokes number). Concerning the former one, particles with diameter 1, 3, and 5 μm result in similar deposition distributions over the model. The results showed high correlation between jet impaction sites and aerosol deposition regions, in particular for 10 μm particles. The highest deposition fractions were found in the oropharyngeal region, where for 10 μm particles it reaches up to 60% of the total mass of the particles injected into the model. During *eupnea*, the deposition efficiency reaches around 42%, 49%, 53% and 80% for 1, 3, 5 and 10μm particles, respectively. In comparison with previous CFD works is found higher deposition for particles of 1 and 3 μm. It has been suggested that the increase can be a result of applied variable upper airways geometries and dimension of the mouthpiece. Other important parameter is the nature of the carrier gas. The flow with He-O_2 mixture exhibits low Reynolds number and results in laminar flow. Thus, for He-O_2 mixture the deposition reaches two times smaller values than for air.
- For *slow* and *rapid breathing* (*eupnea* and *tachypnea* respectively) the results of aerosol deposition in upper airways exhibit similar characteristics in both air and He-O_2 mixture. Concerning the aerosol deposition in air, the fraction is higher for *tachypnea* breathing. On the contrary in He-O_2 mixture for 1, 3, and 5 μm particles the deposited fraction is higher in *eupnea* than in *tachypnea*. Only for 10 μm particles the deposited fraction is increased in *tachypnea*.
- The impact of the glottal motion was found to have negligible effects on the deposition dynamics. The deposition fraction does not significantly differ between the two simulation cases: (i) steady glottal walls (group of subjects with unvarying glottal opening); and (ii) unsteady glottal walls (subjects with moving glottal walls). Therefore, in normal breathing conditions the glottal motion can be neglected. However, further research should be performed on the glottal motion influence in specific breathing conditions, *e.g.* when inhaling aerosols. In those conditions the glottis movement may lead to different deposition characteristics.

Conclusions

The aim of this study was to investigate the conditions of human breathing in the upper airways region of the respiratory system and to examine their influence on airflow dynamics and on aerosol transport and deposition. The human respiratory system and the breathing characteristics represent a complex biomechanical problem. During inhaled therapies, the upper airways' morphology can act as an unwanted filter, which limits the amount of drug delivered to the lungs. The glottis, defined by the vocal-fold aperture, causes upper airways to narrow in a minimal cross section, which is determinant on aerosol deposition.

The observations made in the previous works on healthy subjects during breathing found the following glottal features: (i) the glottal area progressively increases during inspiration and narrows during expiration; and (ii) in some cases, the glottis can remain constantly opened whatever the breathing task. However, the quantitative description of the glottal motion in time has been barely studied and the glottal dynamics and its interaction with the breathing airflow rate was poorly described, which yielded to controversial results. Thus, the first general purpose of this thesis was to investigate the time-variations of the glottal area during breathing, together with the synchronized breathing airflow pattern.

Experiments and Computational Fluid Dynamics (CFD) simulations are an efficient tool to predict the respiratory airflow dynamics and aerosol transport and deposition in the human upper airways. However, up to now the data on the realistic breathing conditions (glottal motion and oral airflow rate) were missing and thus, the impact of glottal motion on airflow and aerosol deposition in the human upper airways was often discarded from the numerical and experimental studies. Early *in vitro* studies were mainly carried out under steady flow conditions, with a static glottis. As well the previous *in silico* studies were performed assuming the following approximations: (i) a mean constant inhalation flow rate (15 to 60 L/min); (ii) quasi-steady flow conditions; (iii) simple tubular geometry in the glottal area; and (iv) to our knowledge, a single study considered an oscillatory flow and glottal movement conditions (approximated by sinusoidal functions) [Renotte et al., 2000]. Thus, the second general purpose of this thesis was to predict the effects of a dynamic glottis and realistic airflow conditions on the aerosol deposition within the upper airways using three-dimensional simulations.

This thesis presents research and findings from two different domains: the human physiology and the mechanics of the two-phase flow in the upper airways. To gain understanding on the realistic breathing conditions, an *in vivo* study was performed. The characteristics of the airflow rate and the glottal dimensions variations were measured in collaboration with medical practitioners from *La Timone Adult Hospital* in Marseille, France and *Speech and Language Laboratory* (LPL) in Aix-en-Provence, France. Afterwards, the measured data were integrated into a complementary *in silico* study.

***In vivo* study**

An experimental protocol was developed to examine 20 healthy subjects in a clinical study to investigate: (i) the respiration airflow rate, and (ii) the vocal folds movement

characteristics during breathing. Therefore, oral airflow measurements were achieved by means of EVA2^{TM} system developed at the LPL and synchronized laryngoscopic video recording was realized using a flexible nasofibroscope. Several different breathing tasks were studied in order to investigate glottal dynamics in different conditions: *eupnea*, *tachypnea*, *hyperpnea* (*slow*, *rapid*, and *deep breathing*, respectively), *apnea* and a apecific task mimicking aerosol inhalation.

For all subjects the data processing comprised: (i) the detection of a mean breathing airflow rate per gender for two breathing tasks *eupnea* (performed at 15 cycles/min), and *tachypnea* (performed at 30 cycles/min); (ii) the extensive analysis of the laryngeal images recorded during those two major tasks. These tasks are altogether representative of *slow* and *rapid breathing*. A customized methodology was developed to extract time-variations of the glottal area in each case.

During *eupnea*, for males, the peak value of glottal area decreased from 217.32 ± 53.8 mm^2 (mean ± SD) during inspiration, to 178.1 ± 34.6 mm^2 during expiration. For females, the peak glottal area changes from 189.21 ± 31.6 mm^2 during inspiration to 168.23 ± 30.8 mm^2 during expiration. The mean value over the whole cycle, was found at 196.14 ± 41.9 mm^2 for males, and 177.37 ± 26.7 mm^2 for females. During *tachypnea* the average glottal area is about 8.4% and 0.3% larger for male and female, respectively.

The recorded data showed that glottal and airflow dynamics during breathing differ from sinusoidal signal. The glottal motion seems related to the airflow dynamics during inspiratory phase, but no correlation is observed during expiratory phase. Glottal variations depending on the subject can have "steady" or "dynamic" behavior. Thus, testing the correlation of glottal and airflow rate time-variations, subjects with "static" or "dynamic" glottis during an average breathing cycle were sorted.

Finally, average breathing cycle of a group of subjects with "static" and with "dynamic" characteristics provided input data to conduct the realistic numerical simulations of laryngeal airflow and particle deposition in the model of upper airways.

In silico study

An averaged 3D geometry of the human upper airways has been designed based on: (i) the High-Resolution Computerized Tomography (HRCT) scans of a male adult obtained from the pilot study described in Conway et al. [2012]; and (ii) the laryngoscopic images of glottal motion elaborated in the *in vivo* study. Next, the main task was to implement realistic respiration airflow conditions and realistic movement of the vocal cords within the model.

In total 6 transient simulations of the breathing cycle were performed, 4 with air and 2 with He-O_2 mixture. The boundary conditions were based on the results from the *in vivo* study: (i) the breathing regime (*eupnea* or *tachypnea*); and (ii) the glottal characteristics ("static" or "dynamic"). During the inspiration phase, aerosol particles with diameter 1, 3, 5, and 10 μm, were injected into the model.

The predicted important flow phenomena such as laryngeal jet, recirculation zones, secondary flows patterns are in agreement with the previous *in silico* studies. On the contrary, the small geometry of the present mouthpiece generates very thin jet flow, that can increase the deposition efficiency of the model.

The deposition in upper airways is primarily dependent on the particle size and airflow speed (*i.e.*, Stokes number). Concerning the former one, particles with diameter 1, 3, and 5 μm result in similar deposition distributions over the model. The results showed high correlation between jet impaction sites and aerosol deposition regions, in particular for 10 μm particles. The highest deposition fractions were found in the oropharyngeal region, where for 10 μm particles it reaches up to 60% of the total mass of the particles injected into the model.

During *eupnea*, the deposition efficiency reaches around 42%, 49%, 53% and 80% for 1, 3, 5 and 10μm particles, respectively. In comparison with previous CFD works is found higher deposition for particles with 1 and 3 μm diameter. It has been suggested that the increase can be a result of applied variable upper airways geometries and dimension of the mouthpiece. Other important parameter is the nature of the carrier gas. The flow with He-O_2 mixture exhibits low Reynolds number and results in laminar flow. Thus, for He-O_2 mixture the deposition reaches two times smaller values than for air. These findings consider important conclusions for clinicians, to determine the therapeutic efficiency of drugs administration during inhalation therapy.

The CFD results on airflow dynamics and aerosol transport and deposition demonstrated negligible differences between "static" and "dynamic" glottal characteristics. Therefore, in normal breathing conditions the glottal motion can be neglected.

Perspectives

Concerning the *in vivo* study, nasofiberscopy is an invasive technique to examine the glottal region. The patient is in an uncomfortable condition, which may influence the glottal behavior. Better alternative would be examination using non-invasive techniques, *e.g.* HRCT scan, nevertheless, currently this technique does not provide sufficient image time-resolution.

Further research should be performed on the glottal motion influence in specific breathing conditions, *e.g.* when inhaling aerosols. In those conditions the glottis movement may lead to different deposition characteristics.

Concerning the *in silico* study, future investigation should be orientated on the development of the more realistic upper airways geometry including bronchial bifurcations. The comparison of aerosol deposition results with the previous studies suggest important influence of different geometries on the aerosol deposition. Thus, several realistic geometries should be investigated together with the breathing conditions, in order to provide statistically significant data. In addition, concerning the geometry, interest should be put on the pharyngeal compliance, that can be significant especially in disease.

The study of the particle deposition dynamics in the respiratory tract should be extended also to sub-micrometric particles. Both sub-micron and microparticles are an important subject not only in the field of pharmaceutics, but also regarding the ambient air pollution. Therefore, further application of the present study on the deposition of airborne particles in the respiratory tract would help to study the health effects of aerosol air pollution.

Bibliography

Agarwal, M., Scherer, R. C., and Hollien, H. (2003). The false vocal folds: Shape and size in frontal view during phonation based on laminagraphic tracings. *Journal of Voice*, 17(2):97–113.

Agertoft, L. and Pedersen, S. (1993). Importance of the inhalation device on the effect of budesonide. *Archives of Disease in Childhood*, 69(1):130–133.

Akerlund, L., Kitzing, P., Petersson, G., and Linder, H. (2014). Dysphonia - examination technique. Available at http://www.dysphonia.certec.lth.se/.

Alipour, F., Berry, D. A., and Titze, I. R. (2000). A finite-element model of vocal-fold vibration. *The Journal of the Acoustical Society of America*, 108(6):3003–3012.

Alipour, F., Brucker, C., D Cook, D., Gommel, A., Kaltenbacher, M., Mattheus, W., Mongeau, L., Nauman, E., Schwarze, R., Tokuda, I., and others (2011). Mathematical models and numerical schemes for the simulation of human phonation. *Current Bioinformatics*, 6(3):323–343.

Altman, P. L. and Dittmer, D. S. (1971). *Respiration and circulation*. Federation of American Societies for Experimental Biology, Bethesda, Md.

ANSYS®(2013a). *ANSYS Fluent Meshing User's Guide*. Release 15.0. ANSYS, Inc., Canonsburg, USA.

ANSYS®(2013b). *ANSYS Fluent Theory Guide*. Release 15.0. ANSYS, Inc., Canonsburg, USA.

ANSYS®(2013c). *ANSYS Fluent UDF Manual*. Release 15.0. ANSYS, Inc., Canonsburg, USA.

Baier, H., Wanner, A., Zarzecki, S., and Sackner, M. A. (1977). Relationships among glottis opening, respiratory flow, and upper airway resistance in humans. *Journal of Applied Physiology*, 43(4):603–611.

Bailly, L. (2009). *Interaction entre cordes vocales et bandes ventriculaires en phonation: exploration in-vivo, modélisation physique, validation in-vitro*. Université du Maine. Doctoral thesis.

Bailly, L., Henrich, N. B., Müller, F., Rohlfs, A.-K., and Hess, M. (2014). The ventricular-fold dynamics in human phonation. *Journal of Speech, Language, and Hearing Research*, 57:1219–1242.

Bailly, L., Henrich, N. B., and Pelorson, X. (2010). Vocal fold and ventricular fold vibration in period-doubling phonation: physiological description and aerodynamic modeling. *The Journal of the Acoustical Society of America*, 127(5):3212–3222.

Bailly, L., Pelorson, X., Henrich, N. B., and Ruty, N. (2008). Influence of a constriction in the near field of the vocal folds: Physical modeling and experimental validation. *The Journal of the Acoustical Society of America*, 124(5):3296–3308.

Ball, C. G., Uddin, M., and Pollard, A. (2008). High resolution turbulence modelling of airflow in an idealised human extra-thoracic airway. *Computers & Fluids*, 37(8):943–964.

Barney, A., Shadle, C. H., and Davies, P. (1999). Fluid flow in a dynamic mechanical model of the vocal folds and tract. i. measurements and theory. *The Journal of the Acoustical Society of America*, 105(1):444–455.

Barrett, J. C. and Clement, C. F. (1988). Growth rates for liquid drops. *Journal of Aerosol Science*, 19(2):223–242.

Beaty, M. M., Wilson, J. S., and Smith, R. J. H. (1999). Laryngeal motion during exercise. *The Laryngoscope*, 109(1):136–139.

Becker, S., Kniesburges, S., Müller, S., Delgado, A., Link, G., Kaltenbacher, M., and Döllinger, M. (2009). Flow-structure-acoustic interaction in a human voice model. *The Journal of the Acoustical Society of America*, 125(3):1351–1361.

Bělka, M., Lízal, F., Jedelský, J., and Jícha, M. (2013). Analysis of fiber deposition using automatic image processing method. *EPJ Web of Conferences*, 45:01011.

Benchetrit, G. (2000). Breathing pattern in humans: diversity and individuality. *Respiration physiology*, 122(2-3):123–129.

Benchetrit, G., Shea, S. A., Dinh, T. P., Bodocco, S., Baconnier, P., and Guz, A. (1989). Individuality of breathing patterns in adults assessed over time. *Respiration Physiology*, 75(2):199–209.

Benninger, C., Parsons, J. P., and Mastronarde, J. G. (2011). Vocal cord dysfunction and asthma. *Current Opinion in Pulmonary Medicine*, 17(1):45–49.

Berry, D. A., Herzel, H., Titze, I. R., and Krischer, K. (1994). Interpretation of biomechanical simulations of normal and chaotic vocal fold oscillations with empirical eigenfunctions. *The Journal of the Acoustical Society of America*, 95(6):3595–3604.

Bisgaard, H. (1995). A metal aerosol holding chamber devised for young children with asthma. *European Respiratory Journal*, 8(5):856–860.

Boiron, O., Deplano, V., and Pelissier, R. (2007). Experimental and numerical studies on the starting effect on the secondary flow in a bend. *Journal of Fluid Mechanics*, 574:109–129.

Brancatisano, T., Collett, P. W., and Engel, L. A. (1983). Respiratory movements of the vocal cords. *Journal of Applied Physiology*, 54(5):1269–1276.

Brancatisano, T. P., Dodd, D. S., and Engel, L. A. (1984). Respiratory activity of posterior cricoarytenoid muscle and vocal cords in humans. *Journal of Applied Physiology*, 57(4):1143–1149.

Brouns, M., Jayaraju, S. T., Lacor, C., De Mey, J., Noppen, M., Vincken, W., and Verbanck, S. (2007a). Tracheal stenosis: a flow dynamics study. *Journal of Applied Physiology*, 102(3):1178–1184.

Brouns, M., Verbanck, S., and Lacor, C. (2007b). Influence of glottic aperture on the tracheal flow. *Journal of biomechanics*, 40(1):165–172.

Brown, J. S., Gordon, T., Price, O., and Asgharian, B. (2013). Thoracic and respirable particle definitions for human health risk assessment. *Particle and Fibre Toxicology*, 10:12.

Busetto, L., Calo', E., Mazza, M., De Stefano, F., Costa, G., Negrin, V., and Enzi, G. (2009). Upper airway size is related to obesity and body fat distribution in women. *European Archives of Oto-Rhino-Laryngology*, 266(4):559–563.

Cain, C. C. and Otis, A. B. (1949). Some physiological effects resulting from added resistance to respiration. *The Journal of aviation medicine*, 20(3):149–160.

Calabrese, P., Dinh, T. P., Eberhard, A., Bachy, J. P., and Benchetrit, G. (1998). Effects of resistive loading on the pattern of breathing. *Respiration Physiology*, 113(2):167–179.

Campbell, A. H., Imberger, H., and Jones, B. M. (1976). Increased upper airway resistance in patients with airway narrowing. *British Journal of Diseases of the Chest*, 70:58–65.

Caselles, V., Kimmel, R., and Sapiro, G. (1997). Geodesic active contours. *International Journal of Computer Vision*, 22(1):61–79.

Česenek, J., Feistauer, M., Horáček, J., Kučera, V., and Prokopová, J. (2013). Simulation of compressible viscous flow in time-dependent domains. *Applied Mathematics and Computation*, 219(13):7139–7150.

Chang, H. K. (1989). *Respiratory Physiology: An Analytical Approach*. Dekker.

Chen, Y., Maksym, G., Brown, T., and Deng, L. (2013). Determination of glottic opening fluctuation by a new method based on nasopharyngoscopy. *The Chinese journal of physiology*, 56(1):52–57.

Cheng, Y.-S., Zhou, Y., and Chen, B. T. (1999). Particle deposition in a cast of human oral airways. *Aerosol Science & Technology*, 31(4):286–300.

Childers, D. G., Hicks, D. M., Moore, G. P., Eskenazi, L., and Lalwani, A. L. (1990). Electroglottography and vocal fold physiology. *Journal of Speech, Language and hearing research*, 33(2):245–254.

Childers, D. G., Naik, J. M., Larar, J. N., Krishnamurthy, A. K., and Moore, G. P. (1983). Electroglottography, speech, and ultra-high speed cinematography. *Vocal fold physiology: Biomechanics, acoustics and phonatory control*, pages 202–220.

Chisari, N. E., Artana, G., and Sciamarella, D. (2011). Vortex dipolar structures in a rigid model of the larynx at flow onset. *Experiments in Fluids*, 50(2):397–406.

Cisonni, J., Van Hirtum, A., Pelorson, X., and Willems, J. (2008). Theoretical simulation and experimental validation of inverse quasi-one-dimensional steady and unsteady glottal flow models. *The Journal of the Acoustical Society of America*, 124(1):535–545.

Coates, A. L. and Ho, S. L. (1998). Drug administration by jet nebulization. *Pediatric Pulmonology*, 26(6):412–423.

Cohen, B. S. and Asgharian, B. (1990). Deposition of ultrafine particles in the upper airways: An empirical analysis. *Journal of Aerosol Science*, 21(6):789–797.

Cohen, B. S., Xiong, J. Q., Fang, C. P., and Li, W. (1998). Deposition of charged particles on lung airways. *Health Physics*, 74(5):554–560.

Conway, J., Fleming, J., Majoral, C., Katz, I., Perchet, D., Peebles, C., Tossici-Bolt, L., Collier, L., Caillibotte, G., Pichelin, M., Sauret-Jackson, V., Martonen, T., Apiou-Sbirlea, G., Muellinger, B., Kroneberg, P., Gleske, J., Scheuch, G., Texereau, J., Martin, A., Montesantos, S., and Bennett, M. (2012). Controlled, parametric, individualized, 2-D and 3-D imaging measurements of aerosol deposition in the respiratory tract of healthy human subjects for model validation. *Journal of Aerosol Science*, 52:1–17.

Cotes, J. E., Chinn, D. J., and Miller, M. R. (2009). *Lung Function: Physiology, Measurement and Application in Medicine*. John Wiley & Sons.

Crowe, C. T., Schwarzkopf, J. D., Sommerfeld, M., and Tsuji, Y. (2011). *Multiphase Flows with Droplets and Particles, Second Edition*. CRC Press.

Cui, X. G. and Gutheil, E. (2011). Large eddy simulation of the unsteady flow-field in an idealized human mouth-throat configuration. *Journal of Biomechanics*, 44(16):2768–2774.

Darquenne, C. (2012). Aerosol deposition in health and disease. *Journal of Aerosol Medicine and Pulmonary Drug Delivery*, 25(3):140–147.

Darquenne, C. and Prisk, G. K. (2004). Aerosol deposition in the human respiratory tract breathing air and 80:20 heliox. *Journal of Aerosol Medicine*, 17(3):278–285.

Darquenne, C., van Ertbruggen, C., and Prisk, G. K. (2011). Convective flow dominates aerosol delivery to the lung segments. *Journal of Applied Physiology*, 111(1):48–54.

Decker, G. Z. and Thomson, S. L. (2007). Computational simulations of vocal fold vibration: Bernoulli versus Navier-Stokes. *Journal of Voice*, 21(3):273–284.

Dekker, E. (1961). Transition between laminar and turbulent flow in human trachea. *Journal of Applied Physiology*, 16(6):1060–1064.

Deverge, M., Pelorson, X., Vilain, C., Lagrée, P.-Y., Chentouf, F., Willems, J., and Hirschberg, A. (2003). Influence of collision on the flow through in-vitro rigid models of the vocal folds. *The Journal of the Acoustical Society of America*, 114(6):3354–3362.

Dockery, D. W. and Pope, C. A. (1994). Acute respiratory effects of particulate air pollution. *Annual Review of Public Health*, 15(1):107–132.

Dollinger, M., Kobler, J., A. Berry, D., D. Mehta, D., Luegmair, G., and Bohr, C. (2011). Experiments on analysing voice production: Excised (human, animal) and in vivo (animal) approaches. *Current Bioinformatics*, 6(3):286–304.

Donea, J., Huerta, A., Ponthot, J.-P., and Rodríguez-Ferran, A. (2004). Arbitrary Lagrangian-Eulerian methods. *Encyclopedia of computational mechanics*.

Drechsel, J. S. and Thomson, S. L. (2008). Influence of supraglottal structures on the glottal jet exiting a two-layer synthetic, self-oscillating vocal fold model. *The Journal of the Acoustical Society of America*, 123(6):4434–4445.

D'Urzo, A. D., Rubinstein, I., Lawson, V. G., Vassal, K. P., Rebuck, A. S., Slutsky, A. S., and Hoffstein, V. (1988). Comparison of glottic areas measured by acoustic reflections vs. computerized tomography. *Journal of Applied Physiology*, 64(1):367–370.

Eckel, H. E. and Sittel, C. (1995). Morphometry of the larynx in horizontal sections. *American journal of otolaryngology*, 16(1):40–48.

Elcner, J., Jedelský, J., Lízal, F., and Jícha, M. (2013). Velocity profiles in idealized model of human respiratory tract. *EPJ Web of Conferences*, 45:01025.

England, S. J. and Bartlett, Jr, D. (1982). Changes in respiratory movements of the human vocal cords during hyperpnea. *Journal of Applied Physiology*, 52(3):780–785.

England, S. J., Bartlett, J. D., and Daubenspeck, J. A. (1982). Influence of human vocal cord movements on airflow and resistance during eupnea. *Journal of Applied Physiology*, 52(3):773–779.

Faber, C. E. and Grymer, L. (2003). Available techniques for objective assessment of upper airway narrowing in snoring and sleep apnea. *Sleep & Breathing*, 7(2):77–86.

Fahd, G. (2012). *Création d'une chaine de référence pour la mesure de la pression artérielle*. Aix Marseille Université. Doctoral thesis.

Ferziger, J. H. and Peric, M. (2001). *Computational Methods for Fluid Dynamics*. Springer Berlin Heidelberg.

Finlay, W. H. (2001). *The Mechanics of Inhaled Pharmaceutical Aerosols*. Academic Press, London.

Fleming, J., Conway, J., Majoral, C., Tossici-Bolt, L., Katz, I., Caillibotte, G., Perchet, D., Pichelin, M., Muellinger, B., Martonen, T., Kroneberg, P., and Apiou-Sbirlea, G. (2011). The use of combined single photon emission computed tomography and x-ray computed tomography to assess the fate of inhaled aerosol. *Journal of Aerosol Medicine and Pulmonary Drug Delivery*, 24(1):49–60.

Fourcin, A. J. and Abberton, E. (1971). First applications of a new laryngograph. *Medical & biological illustration*, 21(3):172–182.

Friedrich, G. and Lichtenegger, R. (1997). Surgical anatomy of the larynx. *Journal of Voice*, 11(3):345–355.

Gemci, T., Corcoran, T. E., and Chigier, N. (2000). Dispersion and deposition of inhalation therapy sprays in the larynx and trachea using experimental and numerical methods. In *Eighth International Conference on Liquid Atomization and Spray Systems, Pasadena, CA*.

Gemci, T., Shortall, B., Allen, G. M., Corcoran, T. E., and Chigier, N. (2003). A CFD study of the throat during aerosol drug delivery using heliox and air. *Journal of Aerosol Science*, 34(9):1175–1192.

Ghio, A. and Teston, B. (2004). Evaluation of the acoustic and aerodynamic constraints of a pneumotachograph for speech and voice studies. In *Proceedings of international conference on voice physiology and biomechanics*, pages 55–58.

Golshahi, L., Noga, M. L., Vehring, R., and Finlay, W. H. (2013). An in vitro study on the deposition of micrometer-sized particles in the extrathoracic airways of adults during tidal oral breathing. *Annals of Biomedical Engineering*, 41(5):979–989.

Grgic, B., Finlay, W. H., Burnell, P. K. P., and Heenan, A. F. (2004a). In vitro intersubject and intrasubject deposition measurements in realistic mouth-throat geometries. *Journal of Aerosol Science*, 35(8):1025–1040.

Grgic, B., Finlay, W. H., and Heenan, A. F. (2004b). Regional aerosol deposition and flow measurements in an idealized mouth and throat. *Journal of Aerosol Science*, 35(1):21–32.

Grgic, B., Martin, A. R., and Finlay, W. H. (2006). The effect of unsteady flow rate increase on in vitro mouth-throat deposition of inhaled boluses. *Journal of Aerosol Science*, 37(10):1222–1233.

Grim, M. and Druga, R. (2002). *Základy anatomie: Trávici, dýchací, močopohlavní a endokrinní systém. 3.* Galén.

Guyton, A. C. and Hall, J. E. (2003). *Précis de physiologie médicale.* Piccin, Padoue, 2 edition.

Hankinson, J. L. and Viola, J. O. (1983). Dynamic BTPS correction factors for spirometric data. *Journal of Applied Physiology*, 55(4):1354–1360.

Hansen, J. T. and Koeppen, B. M. (2002). *Netter's Atlas of Human Physiology.* Icon Learning Systems.

Heenan, A. F., Finlay, W. H., Grgic, B., Pollard, A., and Burnell, P. K. P. (2004). An investigation of the relationship between the flow field and regional deposition in realistic extra-thoracic airways. *Journal of aerosol science*, 35(8):1013–1023.

Heenan, A. F., Matida, E., Pollard, A., and Finlay, W. H. (2003). Experimental measurements and computational modeling of the flow field in an idealized human oropharynx. *Experiments in Fluids*, 35(1):70–84.

Henrich, N. B. (2006). Mirroring the voice from Garcia to the present day: some insights into singing voice registers. *Logopedics, Phoniatrics, Vocology*, 31(1):3–14.

Hess, M. M. and Ludwigs, M. (2000). Strobophotoglottographic transillumination as a method for the analysis of vocal fold vibration patterns. *Journal of Voice*, 14(2):255–271.

Heyder, J. and Svartengren, M. U. (2001). Basic principles of particle behavior in the human respiratory tract. In *Drug Delivery to the Lung*, Lung Biology in Health and Disease, pages 21–45. CRC Press.

Higenbottam, T. (1980). Narrowing of glottis opening in humans associated with experimentally induced bronchoconstriction. *Journal of Applied Physiology*, 49(3):403–407.

Hinds, W. C. (1999). *Aerosol Technology: Properties, Behavior, and Measurement of Airborne Particles*. John Wiley & Sons.

Hinze, J. O. (1975). *Turbulence*. McGraw-Hill.

Hofmans, G. C. J., Groot, G., Ranucci, M., Graziani, G., and Hirschberg, A. (2003). Unsteady flow through in-vitro models of the glottis. *The Journal of the Acoustical Society of America*, 113(3):1658–1675.

Hoh, J. F. Y. (2005). Laryngeal muscle fibre types. *Acta Physiologica Scandinavica*, 183(2):133–149.

Hoh, J. F. Y. (2010). Chapter 2.1 - laryngeal muscles as highly specialized organs in airway protection, respiration and phonation. In Stefan M. Brudzynski, editor, *Handbook of Behavioral Neuroscience*, volume 19 of *Handbook of Mammalian Vocalization An Integrative Neuroscience Approach*, pages 13–21. Elsevier.

Holmes, P., Lumley, J. L., and Berkooz, G. (1998). *Turbulence, coherent structures, dynamical systems and symmetry*. Cambridge university press.

Honda, K. and Maeda, S. (2008). Glottal-opening and airflow pattern during production of voiceless fricatives: a new non-invasive instrumentation. *The Journal of the Acoustical Society of America*, 123(5):3738.

Hooper, F. H. (1885). The respiratory function of the human larynx. *New York Medical Journal*, pages 2–8.

Huang, J., Sun, H., Liu, C., and Zhang, L. (2013). Moving boundary simulation of airflow and micro-particle deposition in the human extra-thoracic airway under steady inspiration. part i: Airflow. *European Journal of Mechanics - B/Fluids*, 37:29–41.

Hundertmark-Zaušková, A., Lehmann, R., Hess, M., and Müller, F. (2013). Numerical simulation of glottal flow. *Computers in biology and medicine*, 43(12):2177–2185.

Hurbis, C. G. and Schild, J. A. (1991). Laryngeal changes during exercise and exercise-induced asthma. *The Annals of otology, rhinology, and laryngology*, 100(1):34–37.

Hyatt, R. E. and Wilcox, R. E. (1961). Extrathoracic airway resistance in man. *Journal of Applied Physiology*, 16(2):326–330.

Idel'cik, I. and Meury, M. (1978). *Mémento des pertes de charge coefficients de pertes de charge singulières et de pertes de charge par frottement*. Eyrolles, Paris.

Iheme, L. O. (2011). Frequency domain bandpass filtering for image processing. Technical report, Eastern Mediterranean University, Electrical and Electronic Engineering Department. Available at http://fr.scribd.com/.

Insalaco, G., Kuna, S. T., Cibella, F., and Villeponteaux, R. D. (1990). Thyroarytenoid muscle activity during hypoxia, hypercapnia, and voluntary hyperventilation in humans. *Journal of Applied Physiology*, 69(1):268–273.

Isabey, D. and Chang, H. K. (1981). Steady and unsteady pressure-flow relationships in central airways. *Journal of Applied Physiology*, 51(5):1338–1348.

Isabey, D. and Chang, H. K. (1982). A model study of flow dynamics in human central airways. part II: secondary flow velocities. *Respiration Physiology*, 49(1):97–113.

Isabey, D., Chang, H. K., Delpuech, C., Harf, A., and Hatzfeld, C. (1986). Dependence of central airway resistance on frequency and tidal volume: a model study. *Journal of Applied Physiology*, 61(1):113–126.

Ishizaka, K. and Flanagan, J. L. (1972). Synthesis of voiced sounds from a two-mass model of the vocal cords. *Bell system technical journal*, 51(6):1233–1268.

Issa, R. I. (1986). Solution of the implicitly discretised fluid flow equations by operator-splitting. *Journal of Computational Physics*, 62(1):40–65.

Jackson, A. C., Gulesian, Jr, P. J., and Mead, J. (1975). Glottal aperture during panting with voluntary limitation of tidal volume. *Journal of Applied Physiology*, 39(5):834–836.

Jain, S., Bandi, V., Officer, T., Wolley, M., and Guntupalli, K. K. (2006). Role of vocal cord function and dysfunction in patients presenting with symptoms of acute asthma exacerbation. *Journal of Asthma*, 43(3):207–212.

Jayaraju, S., Brouns, M., Verbanck, S., and Lacor, C. (2007). Fluid flow and particle deposition analysis in a realistic extrathoracic airway model using unstructured grids. *Journal of Aerosol Science*, 38(5):494–508.

Jedelský, J., Lízal, F., and Jícha, M. (2012). Characteristics of turbulent particle transport in human airways under steady and cyclic flows. *International Journal of Heat and Fluid Flow*, 35:84–92.

Jin, H. H., Fan, J. R., Zeng, M. J., and Cen, K. F. (2007). Large eddy simulation of inhaled particle deposition within the human upper respiratory tract. *Journal of Aerosol Science*, 38(3):257–268.

John, W. (2011). Size distribution characteristics of aerosols. In Kulkarni, P., Baron, P. A., and Willeke, K., editors, *Aerosol Measurement*, pages 41–54. John Wiley & Sons, Inc.

Juroszek, B. (2006). Air features in spirometric transducers. *Measurement*, 39(5):466–476.

Karakozoglou, S.-Z., Henrich, N., d'Alessandro, C., and Stylianou, Y. (2012). Automatic glottal segmentation using local-based active contours and application to glottovibrography. *Speech Communication*, 54(5):641–654.

Karnell, M. P. (1989). Synchronized videostroboscopy and electroglottography. *Journal of Voice*, 3(1):68–75.

Katz, I., Pichelin, M., Montesantos, S., Majoral, C., Martin, A., Conway, J., Fleming, J., Venegas, J., Greenblatt, E., and Caillibotte, G. (2014). Using helium-oxygen to improve regional deposition of inhaled particles: mechanical principles. *Journal of Aerosol Medicine and Pulmonary Drug Delivery*, 27(2):71–80.

Katz, I. M., Davis, B. M., and Martonen, T. B. (1999). A numerical study of particle motion within the human larynx and trachea. *Journal of Aerosol Science*, 30(2):173–183.

Katz, I. M. and Martonen, T. B. (1996). Flow patterns in three-dimensional laryngeal models. *Journal of Aerosol Medicine*, 9(4):501–511.

Katz, I. M., Martonen, T. B., and Flaa, W. (1997). Three-dimensional computational study of inspiratory aerosol flow through the larynx: the effect of glottal aperture modulation. *Journal of Aerosol Science*, 28(6):1073–1083.

Khilnani, G. C. and Banga, A. (2008). Noninvasive ventilation in patients with chronic obstructive airway disease. *International Journal of Chronic Obstructive Pulmonary Disease*, 3(3):351–357.

Kleinstreuer, C. and Zhang, Z. (2003). Laminar-to-turbulent fluid-particle flows in a human airway model. *International Journal of Multiphase Flow*, 29(2):271–289.

Kleinstreuer, C. and Zhang, Z. (2010). Airflow and particle transport in the human respiratory system. *Annual Review of Fluid Mechanics*, 42:301–334.

Kniesburges, S., Thomson, S. L., Barney, A., Triep, M., Šidlof, P., Horáček, J., Brücker, C., and Becker, S. (2011). In vitro experimental investigation of voice production. *Current Bioinformatics*, 6(3):305–322.

Kobler, J. B., Rosen, D. I., Burns, J. A., Akst, L. M., Broadhurst, M. S., Zeitels, S. M., and Hillman, R. E. (2006). Comparison of a flexible laryngoscope with calibrated sizing function to intraoperative measurements. *The Annals of otology, rhinology, and laryngology*, 115(10):733–740.

Kovářová, E. and Ždímal, V. (2009). Deposition of inhalants in the human respiratory tract. In *Proceedings of the 10th Annual Conference of the Czech Aerosol Society*, pages 59–60, Čejkovice, Czech Republic. Czech Aerosol Society. ISBN: 978-80-86186-20-7.

Krebs, F., Silva, F., Sciamarella, D., and Artana, G. (2012). A three-dimensional study of the glottal jet. *Experiments in Fluids*, 52(5):1133–1147.

Kucinschi, B. R., Scherer, R. C., DeWitt, K. J., and Ng, T. T. (2006). An experimental analysis of the pressures and flows within a driven mechanical model of phonation. *The Journal of the Acoustical Society of America*, 119(5):3011–3021.

Kuna, S. T., Insalaco, G., and Villeponteaux, R. D. (1991). Arytenoideus muscle activity in normal adult humans during wakefulness and sleep. *Journal of Applied Physiology*, 70(4):1655–1664.

Launder, B. E. and Spalding, D. B. (1974). The numerical computation of turbulent flows. *Computer Methods in Applied Mechanics and Engineering*, 3(2):269–289.

Lin, C.-L., Tawhai, M. H., McLennan, G., and Hoffman, E. A. (2007). Characteristics of the turbulent laryngeal jet and its effect on airflow in the human intra-thoracic airways. *Respiratory Physiology & Neurobiology*, 157(2-3):295–309.

Lin, T.-C., Breysse, P. N., Laube, B. L., and Swift, D. L. (2001). Mouthpiece diameter affects deposition efficiency in cast models of the human oral airways. *Journal of Aerosol Medicine*, 14(3):335–341.

Liu, A. B., Mather, D., and Reitz, R. D. (1993). Modeling the effects of drop drag and breakup on fuel sprays. SAE Technical Paper 930072, SAE International, Warrendale, PA.

Lízal, F., Jedelský, J., Adam, J., Bělka, M., and Jícha, M. (2013). Application of positron emission tomography to aerosol transport research in a model of human lungs. *EPJ Web of Conferences*, 45:01060.

Longest, P. W. and Hindle, M. (2011). Numerical model to characterize the size increase of combination drug and hygroscopic excipient nanoparticle aerosols. *Aerosol Science and Technology*, 45(7):884–899.

Lumley, J. (1967). The structure of inhomogeneous turbulent flows. In Yaglom, A. and Tatarski, V., editors, *Atmospheric turbulence and radio propagation*, pages 166–178. Nauka.

Luo, H., Mittal, R., and Bielamowicz, S. A. (2009). Analysis of flow-structure interaction in the larynx during phonation using an immersed-boundary method. *The Journal of the Acoustical Society of America*, 126(2):816–824.

Martin, S. E., Mathur, R., Marshall, I., and Douglas, N. J. (1997). The effect of age, sex, obesity and posture on upper airway size. *European Respiratory Journal*, 10(9):2087–2090.

Martonen, T. B. and Katz, I. M. (1993). Deposition patterns of aerosolized drugs within human lungs: effects of ventilatory parameters. *Pharmaceutical research*, 10(6):871–878.

Martonen, T. B. and Musante, C. J. (2000). Importance of cloud motion on cigarette smoke deposition in lung airways. *Inhalation Toxicology*, 12 Suppl 4:261–280.

Martonen, T. B., Musante, C. J., Segal, R. A., Schroeter, J. D., Hwang, D., Dolovich, M. A., Burton, R., Spencer, R. M., and Fleming, J. S. (2000). Lung models: strengths and limitations. *Respiratory Care*, 45(6):712–736.

Matida, E. A., Finlay, W. H., Breuer, M., and Lange, C. F. (2006). Improving prediction of aerosol deposition in an idealized mouth using large-eddy simulation. *Journal of aerosol medicine*, 19(3):290–300.

Menon, A. S., Weber, M. E., and Chang, H. K. (1985). Effect of the larynx on oscillatory flow in the central airways: a model study. *Journal of Applied Physiology*, 59(1):160–169.

Menter, F. (1993). Zonal two equation $k - \omega$ turbulence models for aerodynamic flows. In *23rd Fluid Dynamics, Plasmadynamics, and Lasers Conference*. American Institute of Aeronautics and Astronautics.

Menter, F. R., Kuntz, M., and Langtry, R. (2003). Ten years of industrial experience with the SST turbulence model. *Turbulence, heat and mass transfer*, 4:625–632.

Miller, M. R., Hankinson, J., Brusasco, V., Burgos, F., Casaburi, R., Coates, A., Crapo, R., Enright, P., van der Grinten, C. P. M., Gustafsson, P., Jensen, R., Johnson, D. C., MacIntyre, N., McKay, R., Navajas, D., Pedersen, O. F., Pellegrino, R., Viegi, G., Wanger, J., and ATS/ERS Task Force (2005). Standardisation of spirometry. *The European Respiratory Journal*, 26(2):319–338.

Miyawaki, S., Tawhai, M. H., Hoffman, E. A., and Lin, C.-L. (2012). Effect of carrier gas properties on aerosol distribution in a CT-based human airway numerical model. *Annals of Biomedical Engineering*, 40(7):1495–1507.

Mongeau, L., Franchek, N., Coker, C. H., and Kubli, R. A. (1997). Characteristics of a pulsating jet through a small modulated orifice, with application to voice production. *The Journal of the Acoustical Society of America*, 102(2):1121–1133.

Nithiarasu, P., Hassan, O., Morgan, K., Weatherill, N. P., Fielder, C., Whittet, H., Ebden, P., and Lewis, K. R. (2008). Steady flow through a realistic human upper airway geometry. *International Journal for Numerical Methods in Fluids*, 57(5):631–651.

Nomura, H. and Funada, T. (2007). Sound generation by unsteady flow ejecting from the vibrating glottis based on a distributed parameter model of the vocal cords. *Acoustical science and technology*, 28(6):392–402.

Olesik, J. W. and Bates, L. C. (1995). Characterization of aerosols produced by pneumatic nebulizers for inductively coupled plasma sample introduction: effect of liquid and gas flow rates on volume based drop size distributions. *Spectrochimica Acta Part B: Atomic Spectroscopy*, 50(4-7):285–303.

Olson, D. E., Sudlow, M. F., Horsfield, K., and Filley, G. F. (1973). Convective patterns of flow during inspiration. *Archives of Internal Medicine*, 131(1):51–57.

Orlikoff, R. F. (1998). Scrambled EGG: The uses and abuses of electroglottography. *Phonoscope*, 1:37–53.

Ouaknine, M., Fernandes, M., and Giovanni, A. (2000). Visualisation des mouvements vibratoires des cordes vocales en condition d'asymétrie. *Revue de laryngologie, d'otologie et de rhinologie*, 121(5):297–300.

Ounis, H., Ahmadi, G., and McLaughlin, J. B. (1991). Brownian diffusion of submicrometer particles in the viscous sublayer. *Journal of Colloid and Interface Science*, 143(1):266–277.

Painter, R. and Cunningham, D. J. (1992). Analyses of human respiratory flow patterns. *Respiration Physiology*, 87(3):293–307.

Pastur, L. R., Lusseyran, F., Fraigneau, Y., and Podvin, B. (2005). Determining the spectral signature of spatial coherent structures in an open cavity flow. *Physical Review E*, 72(6).

Payne, J., Higenbottam, T., and Guindi, G. (1981). Respiratory activity of the vocal cords in normal subjects and patients with airflow obstruction: an electromyographic study. *Clinical Science*, 61(2):163–167.

Pedley, T. J. (1977). Pulmonary fluid dynamics. *Annual Review of Fluid Mechanics*, 9(1):229–274.

Pelorson, X., Hirschberg, A., Van Hassel, R. R., Wijnands, A. P. J., and Auregan, Y. (1994). Theoretical and experimental study of quasisteady-flow separation within the glottis during phonation. Application to a modified two-mass model. *The Journal of the Acoustical Society of America*, 96(6):3416–3431.

Peterson, J. B., Prisk, G. K., and Darquenne, C. (2008). Aerosol deposition in the human lung periphery is increased by reduced-density gas breathing. *Journal of Aerosol Medicine and Pulmonary Drug Delivery*, 21(2):159–168.

Pickup, B. A. and Thomson, S. L. (2010). Flow-induced vibratory response of idealized versus magnetic resonance imaging-based synthetic vocal fold models. *Journal of the Acoustical Society of America*, 128(3):EL124–EL129.

Plant, R. L. and Hillel, A. D. (1998). Direct measurement of subglottic pressure and laryngeal resistance in normal subjects and in spasmodic dysphonia. *Journal of Voice*, 12(3):300–314.

Pope, C. A., Bates, D. V., and Raizenne, M. E. (1995). Health effects of particulate air pollution: time for reassessment? *Environmental Health Perspectives*, 103(5):472–480.

Pritchard, S. E. and McRobbie, D. W. (2004). Studies of the human oropharyngeal airspaces using magnetic resonance imaging. II. the use of three-dimensional gated MRI to determine the influence of mouthpiece diameter and resistance of inhalation devices on the oropharyngeal airspace geometry. *Journal of Aerosol Medicine*, 17(4):310–324.

Proctor, D. F. and Hardy, J. B. (1949). Studies of respiratory air flow; significance of the normal pneumotachogram. *Bulletin of the Johns Hopkins Hospital*, 85(4):253–280.

Pui, D. Y. H., Romay-Novas, F., and Liu, B. Y. H. (1987). Experimental study of particle deposition in bends of circular cross section. *Aerosol Science and Technology*, 7(3):301–315.

Rattenborg, C. (1961). Laryngeal regulation of respiration. *Acta Anaesthesiologica Scandinavica*, 5(3):129–140.

Renotte, C., Bouffioux, V., and Wilquem, F. (2000). Numerical 3D analysis of oscillatory flow in the time-varying laryngeal channel. *Journal of Biomechanics*, 33(12):1637–1644.

Rodarte, J. R. and Rehder, K. (1986). Dynamics of respiration. In Terjung, R., editor, *Comprehensive Physiology*. John Wiley & Sons, Inc., Hoboken, NJ, USA.

Rogers, K. (2011). *The Respiratory System*. The Rosen Publishing Group.

Rosa, M. O., Pereira, J. C., Grellet, M., and Alwan, A. (2003). A contribution to simulating a three-dimensional larynx model using the finite element method. *The Journal of the Acoustical Society of America*, 114(5):2893–2905.

Roth, A. P., Lange, C. F., and Finlay, W. H. (2003). The effect of breathing pattern on nebulizer drug delivery. *Journal of Aerosol Medicine*, 16(3):325–339.

Rothenberg, M. (1992). A multichannel electroglottograph. *Journal of Voice*, 6(1):36–43.

Roux, E. (2002). Origine et évolution de l'appareil respiratoire aérien des vertébrés. *Revue des maladies respiratoires*, 19(5):601–615.

Rubinstein, I., England, S. J., Zamel, N., and Hoffstein, V. (1989). Glottic dimensions in healthy men and women. *Respiration physiology*, 77(3):291–299.

Ruty, N., Pelorson, X., Van Hirtum, A., Lopez-Arteaga, I., and Hirschberg, A. (2007). An in vitro setup to test the relevance and the accuracy of low-order vocal folds models. *The Journal of the Acoustical Society of America*, 121(1):479–490.

Ruzer, L. S. and Harley, N. H. (2005). *Aerosols Handbook: Measurement, Dosimetry, and Health Effects*. CRC Press.

Sammon, M., Romaniuk, J. R., and Bruce, E. N. (1993). Role of deflation-sensitive feedback in control of end-expiratory volume in rats. *Journal of Applied Physiology*, 75(2):902–911.

Sandeau, J. (2010). *Transport et Dépôt des Particules d'Aérosols Médicaments: Modélisation Physique et Résolution Numérique dans les Voies Respiratoires Extrathoraciques Humaines*. Editions universitaires européennes EUE. Doctoral thesis.

Sandeau, J., Katz, I., Fodil, R., Louis, B., Apiou-Sbirlea, G., Caillibotte, G., and Isabey, D. (2010). CFD simulation of particle deposition in a reconstructed human oral extrathoracic airway for air and helium-oxygen mixtures. *Journal of Aerosol Science*, 41(3):281–294.

Sanders, M. (2007). Inhalation therapy: an historical review. *Primary Care Respiratory Journal*, 16(2):71–81.

Scheinherr, A., Bailly, L., Boiron, O., Legou, T., Giovanni, A., Caillibotte, G., and Pichelin, M. (2012). Glottal motion and its impact on the respiratory flow. *Computer Methods in Biomechanics and Biomedical Engineering*, 15(sup1):69–71.

Scheinherr, A., Bailly, L., Boiron, O., Legou, T., Lagier, A., Caillibotte, G., and Pichelin, M. (2013a). Laryngeal two-phase flow in realistic breathing conditions. *Proceedings of the 19th congress of the European Society of Biomechanics*. Patras, Greece.

Scheinherr, A., Lagier, A., Bailly, L., Boiron, O., Legou, T., Giovanni, A., de la Breteque, B. A., Caillibotte, G., and Pichelin, M. (2013b). Glottal motion and its impact on inhaled aerosol deposition in upper airways. *Journal of Aerosol Medicine and Pulmonary Drug Delivery*, 26(2):A28.

Scherer, R. C., Shinwari, D., Witt, K. J. D., Zhang, C., Kucinschi, B. R., and Afjeh, A. A. (2001). Intraglottal pressure profiles for a symmetric and oblique glottis with a divergence angle of 10 degrees. *The Journal of the Acoustical Society of America*, 109(4):1616–1630.

Scherer, R. C., Titze, I. R., and Curtis, J. F. (1983). Pressure-flow relationships in two models of the larynx having rectangular glottal shapes. *The Journal of the Acoustical Society of America*, 73(2):668–676.

Schlichting, H. (1968). *Boundary-Layer Theory (6th Edition)*. McGraw-Hill, New York, USA.

Schwartz, J. (1993). Particulate air pollution and chronic respiratory disease. *Environmental Research*, 62(1):7–13.

Sciamarella, D. and Le Quéré, P. (2008). Solving for unsteady airflow in a glottal model with immersed moving boundaries. *European Journal of Mechanics - B/Fluids*, 27(1):42–53.

Sciamarella, D., Silva, F., and Artana, G. (2012). Similarity analysis of a glottal-like jet. *Experiments in Fluids*, 53(3):765–776.

Seinfeld, J. H. and Pandis, S. N. (2012). *Atmospheric Chemistry and Physics: From Air Pollution to Climate Change*. John Wiley & Sons.

Semon, F. (1895). *On the Position of the Vocal Cords in Quiet Respiration of Man, and on the Reflex-tonus of Their Abductor Muscles*. Harrison and Sons.

Shadle, C. H., Barney, A. M., and Thomas, D. W. (1991). An investigation into the acoustics and aerodynamics of the larynx. In *Vocal Fold Physiology*, pages 73–82. Singular Publishing Co.

Shea, S. A. and Guz, A. (1992). Personnalité ventilatoire–an overview. *Respiration Physiology*, 87(3):275–291.

Shiba, K. (2009). Chapter 9.1 - Functions of larynx in breathing, vocalization and airway protective reflexes. *Handbook of Behavioral Neuroscience*, pages 373–381.

Shinneeb, A.-M. and Pollard, A. (2012). Investigation of the flow physics in the human pharynx/larynx region. *Experiments in Fluids*, 53(4):989–1003.

Šidlof, P., Doaré, O., Cadot, O., and Chaigne, A. (2011). Measurement of flow separation in a human vocal folds model. *Experiments in Fluids*, 51(1):123–136.

Šidlof, P., Švec, J. G., Horáček, J., Veselý, J., Klepáček, I., and Havlík, R. (2008). Geometry of human vocal folds and glottal channel for mathematical and biomechanical modeling of voice production. *Journal of Biomechanics*, 41(5):985–995.

Spann, R. W. and Hyatt, R. E. (1971). Factors affecting upper airway resistance in conscious man. *Journal of Applied Physiology*, 31(5):708–712.

Šrám, R. J., Binková, B., Dostál, M., Merkerová-Dostalová, M., Líbalová, H., Milcová, A., Rössner, P., Rössnerová, A., Schmuczerová, J., Švecová, V., Topinka, J., and Votavová, H. (2013). Health impact of air pollution to children. *International Journal of Hygiene and Environmental Health*, 216(5):533–540.

Stahlhofen, W., Rudolf, G., and James, A. (1989). Intercomparison of experimental regional aerosol deposition data. *Journal of Aerosol Medicine*, 2(3):285–308.

Stănescu, D. C., Pattijn, J., Clément, J., and van de Woestijne, K. P. (1972). Glottis opening and airway resistance. *Journal of Applied Physiology*, 32(4):460–6.

Stapleton, K. W., Guentsch, E., Hoskinson, M. K., and Finlay, W. H. (2000). On the suitability of $k-\epsilon$ turbulence modeling for aerosol deposition in the mouth and throat: a comparison with experiment. *Journal of Aerosol Science*, 31(6):739–749.

Steinecke, I. and Herzel, H. (1995). Bifurcations in an asymmetric vocal-fold model. *The Journal of the Acoustical Society of America*, 97(3):1874–1884.

Stella, M. H. and England, S. J. (2001). Modulation of laryngeal and respiratory pump muscle activities with upper airway pressure and flow. *Journal of Applied Physiology*, 91(2):897–904.

Stocks, J. and Hislop, A. A. (2001). Structure and function of the respiratory system. In *Drug Delivery to the Lung*, Lung Biology in Health and Disease, pages 47–104. CRC Press.

Story, B. H. and Titze, I. R. (1995). Voice simulation with a body-cover model of the vocal folds. *The Journal of the Acoustical Society of America*, 97(2):1249–1260.

Švec, J. G., Horáček, J., Šram, F., and Veselý, J. (2000). Resonance properties of the vocal folds: In vivo laryngoscopic investigation of the externally excited laryngeal vibrations. *The Journal of the Acoustical Society of America*, 108(4):1397–1407.

Švec, J. G. and Schutte, H. K. (1996). Videokymography: High-speed line scanning of vocal fold vibration. *Journal of Voice*, 10(2):201–205.

Švec, J. G., Šram, F., and Schutte, H. K. (1999). Videokymography: A new high-speed method for the examination of vocal-fold vibrations. *Otorinolaryngologie a foniatrie*, 48:155–162.

Swift, D. L., Montassier, N., Hopke, P. K., Karpen-Hayes, K., Cheng, Y.-S., Su, Y. F., Yeh, H. C., and Strong, J. C. (1992). Inspiratory deposition of ultrafine particles in human nasal replicate cast. *Journal of Aerosol Science*, 23(1):65–72.

Taherian, S., Rahai, H. R., and Waddington, T. (2011). CFD modeling and analysis of pulmonary airways/particles transport and deposition. *Proceedings of the 41st AIAA Fluid Dynamics Conference and Exhibit*.

Tao, C. and Jiang, J. J. (2007). Mechanical stress during phonation in a self-oscillating finite-element vocal fold model. *Journal of Biomechanics*, 40(10):2191–2198.

Templer, J. W., Von Doersten, P. G., Quigley, P. R., Scott, G. C., and Davis, W. E. (1991). Laryngeal airway resistance. the relationships of airflow, pressure, and aperture. *Archives of Otolaryngology–Head & Neck Surgery*, 117(8):867–870.

Tian, L. and Ahmadi, G. (2007). Particle deposition in turbulent duct flows-comparisons of different model predictions. *Journal of Aerosol Science*, 38(4):377–397.

Titze, I. R. (1994). *Principles of voice production*. Prentice Hall.

Titze, I. R., Schmidt, S. S., and Titze, M. R. (1995). Phonation threshold pressure in a physical model of the vocal fold mucosa. *The Journal of the Acoustical Society of America*, 97(5):3080–3084.

Triep, M. and Brücker, C. (2010). Three-dimensional nature of the glottal jet. *The Journal of the Acoustical Society of America*, 127(3):1537–1547.

Triep, M., Brücker, C., and Schröder, W. (2005). High-speed PIV measurements of the flow downstream of a dynamic mechanical model of the human vocal folds. *Experiments in Fluids*, 39(2):232–245.

Utturkar, Y., Zhang, B., and Shyy, W. (2005). Reduced-order description of fluid flow with moving boundaries by proper orthogonal decomposition. *International Journal of Heat and Fluid Flow*, 26(2):276–288.

Vaissière, J., Honda, K., Amelot, A., Maeda, S., and Crevier-Buchman, L. (2010). Multi-sensor platform for speech physiology research in a phonetics laboratory. *The Journal of the Phonetic Society of Japan*, 14(2):65–78.

Van den Berg, J. W., Zantema, J. T., and Doornenbal Jr, P. (1957). On the air resistance and the bernoulli effect of the human larynx. *The Journal of the Acoustical Society of America*, 29(5):626–631.

Wang, Y., Liu, Y., Sun, X., Yu, S., and Gao, F. (2009). Numerical analysis of respiratory flow patterns within human upper airway. *Acta Mechanica Sinica*, 25(6):737–746.

Wells, A. C. and Chamberlain, A. C. (1967). Transport of small particles to vertical surfaces. *British Journal of Applied Physics*, 18(12):1793.

West, J. B. (2007). *Pulmonary Physiology and Pathophysiology: An Integrated, Case-based Approach*. Lippincott Williams & Wilkins.

West, J. B. (2008). *Respiratory Physiology: The Essentials*. Lippincott Williams & Wilkins.

Widdicombe, J. G. and Tatar, M. (1988). Upper airway reflex control. *Annals of the New York Academy of Sciences*, 533:252–261.

Wilcox, D. C. (1998). *Turbulence Modeling for CFD*, volume 2. DCW Industries, Incorporated.

Wong, D., Ito, M. R., Cox, N. B., and Titze, I. R. (1991). Observation of perturbations in a lumped-element model of the vocal folds with application to some pathological cases. *The Journal of the Acoustical Society of America*, 89(1):383–394.

Xi, J. and Longest, P. W. (2007). Transport and deposition of micro-aerosols in realistic and simplified models of the oral airway. *Annals of Biomedical Engineering*, 35(4):560–581.

Xi, J. and Longest, P. W. (2008). Evaluation of a drift flux model for simulating submicrometer aerosol dynamics in human upper tracheobronchial airways. *Annals of biomedical engineering*, 36(10):1714–1734.

Xi, J., Longest, P. W., and Martonen, T. B. (2008). Effects of the laryngeal jet on nano-and microparticle transport and deposition in an approximate model of the upper tracheobronchial airways. *Journal of Applied Physiology*, 104(6):1761–1777.

Xi, J., Si, X. A., Kim, J., Mckee, E., and Lin, E.-B. (2014). Exhaled aerosol pattern discloses lung structural abnormality: A sensitivity study using computational modeling and fractal analysis. *PLoS ONE*, 9(8):e104682.

Xu, G. B. and Yu, C. P. (1985). Theoretical lung deposition of hygroscopic NaCl aerosols. *Aerosol Science and Technology*, 4(4):455–461.

Zhang, Z. and Kleinstreuer, C. (2003). Low-reynolds-number turbulent flows in locally constricted conduits: A comparison study. *AIAA Journal*, 41(5):831–840.

Zhang, Z. and Kleinstreuer, C. (2004). Airflow structures and nano-particle deposition in a human upper airway model. *Journal of Computational Physics*, 198(1):178–210.

Zhang, Z. and Kleinstreuer, C. (2011). Computational analysis of airflow and nanoparticle deposition in a combined nasal-oral-tracheobronchial airway model. *Journal of Aerosol Science*, 42(3):174–194.

Zhang, Z., Kleinstreuer, C., and Kim, C. S. (2002). Micro-particle transport and deposition in a human oral airway model. *Journal of Aerosol Science*, 33(12):1635–1652.

Zheng, X., Bielamowicz, S., Luo, H., and Mittal, R. (2009). A computational study of the effect of false vocal folds on glottal flow and vocal fold vibration during phonation. *Annals of Biomedical Engineering*, 37(3):625–642.

Zheng, X., Mittal, R., Xue, Q., and Bielamowicz, S. (2011). Direct-numerical simulation of the glottal jet and vocal-fold dynamics in a three-dimensional laryngeal model. *The Journal of the Acoustical Society of America*, 130(1):404–415.

Ziethe, A., Patel, R., Kunduk, M., Eysholdt, U., and Graf, S. (2011). Clinical analysis methods of voice disorders. *Current Bioinformatics*, 6(3):270–285.

Annexes

Annex A - Instruction Interface for Clinical Study

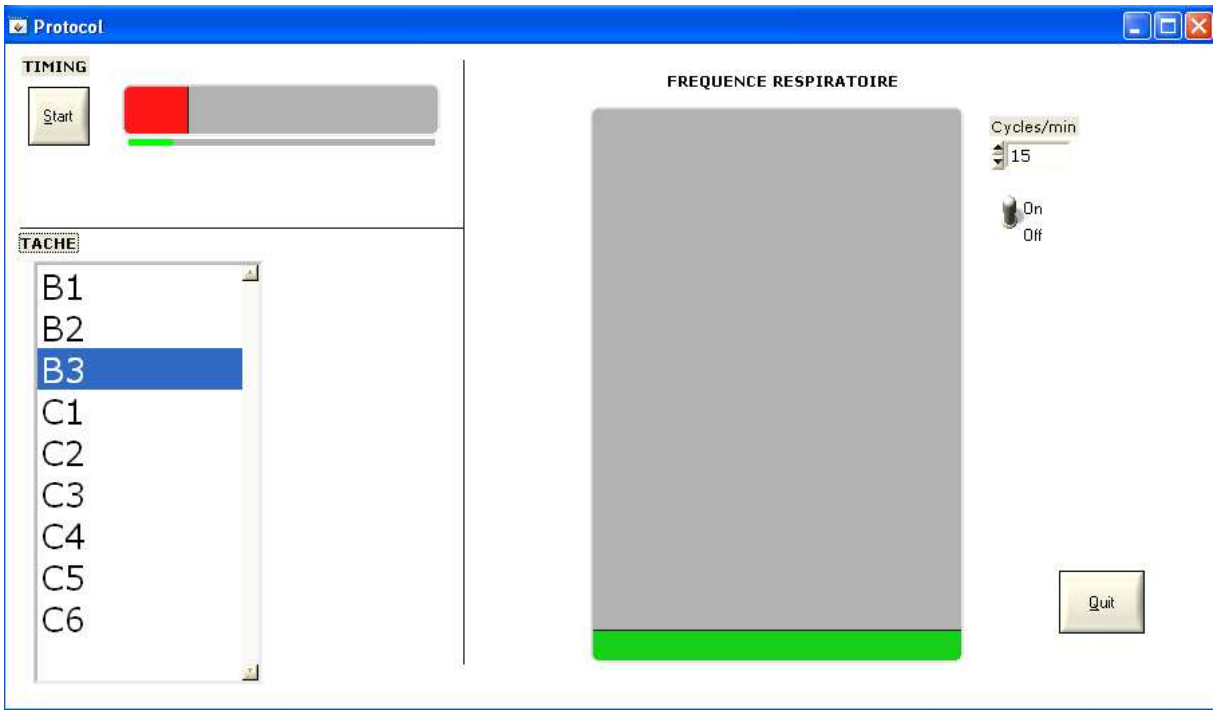

Figure A1: The interface developed to describe the instructions to the subject during the clinical study. It comprises a progress bar to show the subject the duration of the target task, the list of the breathing tasks to realize, and a metronome to help the subject breathing at the target frequency when necessary.

Annex B - 2D Model

Geometry

As a first approximation, a 2D model of the laryngeal area with a rectangular constriction representing the glottal geometry was chosen (see Figure B1). For comparison with the

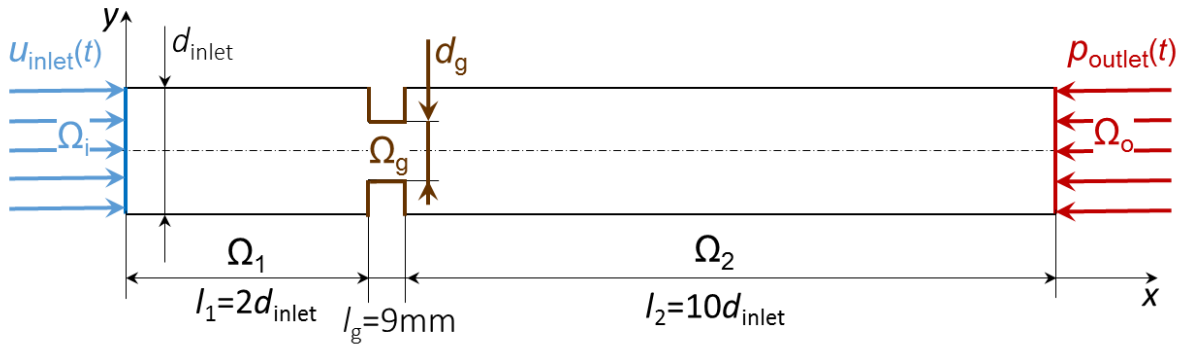

Figure B1: 2D geometry of glottal area including main boundary conditions (see section III.7.3.4).

realistic geometry a frontal cut through male laryngeal region is displayed on Figure B2. The geometry of present study approximates the vocal folds area to the area Ω_g.

The inlet Ω_i dimension is set to d_{inlet} = 21 mm, corresponding to male glottal antero-posterior diameter measured in Friedrich and Lichtenegger [1997]. The region upstream the glottal constriction, Ω_1, was designed as a simple rectangle with length $l_1 = 2d_{inlet}$. Downstream is found the glottal constriction Ω_g with an axial length l_g=9 mm. Finally a rectangular area Ω_2 of length $l_2 = 10d_{inlet}$ follows. This length ensures the stabilization of the glottal jet. The dimension of the glottal constriction d_g is approximated according to *in vivo* values and will be detailed in the Boundary Conditions section.

Mesh Properties

The model was created in GAMBIT 2.4.6., which is a preprocessor to model the geometry and generate the mesh. This model includes moving geometry boundaries, therefore a mesh composed from irregular triangular elements (Tri-Pave meshing scheme) was chosen.

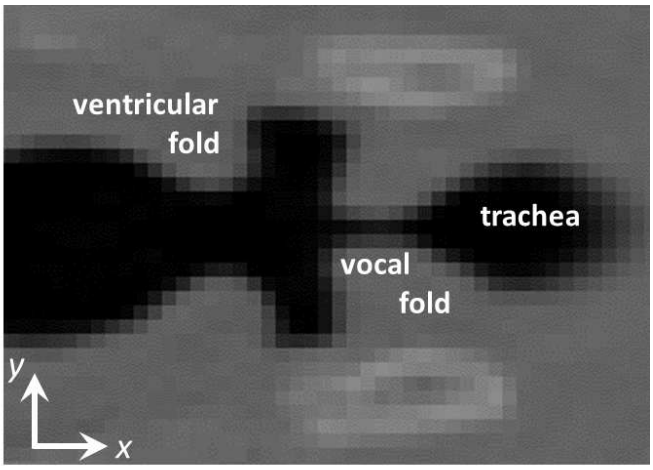

Figure B2: Frontal view on a laryngeal area using HRCT (male volunteer from study of Conway et al. [2012]).

This type of elements is the most convenient for complex geometries and dynamic meshes. Mesh is refined in the region of geometry constriction (see Figure B3). The smallest element size is $\Delta x_{\text{inlet}} = 1$ mm at the inlet and $\Delta x_{\text{g}} = 0.25$ mm at the area of the glottal constriction. This results in a total number of 23 964 elements.

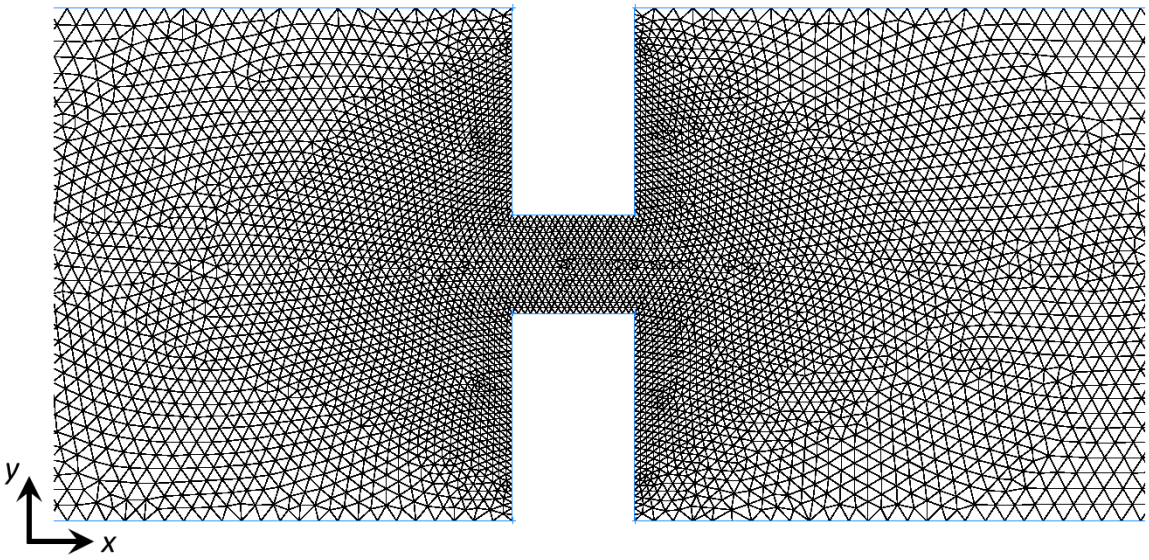

Figure B3: Detail of the mesh around the 2D glottal constriction.

Solution Method

To set the viscosity model of the simulation, Reynolds number (Re) at the glottis area was calculated:

$$Re = \frac{\rho_g u_g d_g}{\eta}\,[-]\,, \tag{III.7.1}$$

where ρ_g is the density of the gas, u_g the flow velocity at the glottal constriction, d_g the glottal width and η the dynamic viscosity of the gas. Mean and maximal Re numbers were calculated using the uniform glottal velocity u_g of the mean cycle and at the instant of peak airflow inlet $t(\overline{Q}_{max})$. The uniform airflow velocity at the inlet u_{inlet} of the model is calculated using the mean airflow rate cycle $\overline{Q}(t)$:

$$\overline{u}_{inlet}(t) = \frac{\overline{Q}(t)}{A_{inlet}}, \tag{III.7.2}$$

where the inlet area is

$$A_{inlet} = \frac{\pi {d_{inlet}}^2}{4}, \tag{III.7.3}$$

and so the glottal velocity $u_g(t)$ is

$$\overline{u}_g(t) = \overline{u}_{inlet}(t)\frac{d_{inlet}}{d_g(t)}, \tag{III.7.4}$$

where $d_g(t)$ is the variation of glottal width (for definition see Figure II.3.4c in II.3.2.2) over the breathing cycle measured in the *in vivo* study (for details see boundary conditions in III.7.3.4). The calculated aerodynamic parameters are summarized in Table B1. Concluding from the values in the table and in analogy with hemodynamic pulsatile flows

	Mean of the breathing cycle	Peak flow inlet PIF
$\overline{Q}$ [L/min]	21.1	33.2
u_{inlet} [m/s]	0.92	1.46
d_g [mm]	8.5	14
u_g [m/s]	2.39	2.29
Re_{max} [-]	1388	2183

Table B1: Aerodynamic parameters in glottal constriction: mean values over the whole cycle and values at the instant of peak airflow inlet $t(\overline{Q}_{max})$

of similar characteristic parameters, the flow unsteadiness induces internal stabilization effects, so that laminar regimes can be observed in spite of peak Re numbers larger than 4000 [Boiron et al., 2007]. Therefore, this preliminary airflow model was employed considering laminar airflow conditions. CFD simulations were conducted using Fluent 6.3.26, assuming an incompressible Newtonian gas (as defined in section III.7.3.4). The Navier-Stokes flow governing equations for laminar regime in primitive variables formulation are:

$$\left.\begin{array}{rcl} \nabla \cdot \boldsymbol{u}(\boldsymbol{x},t) & = & 0 \\ \rho\left[\frac{\partial \boldsymbol{u}(\boldsymbol{x},t)}{\partial t} + \Big(\big(\boldsymbol{u}\,(\boldsymbol{x},t) - \boldsymbol{u}_{grid}\big)\cdot\nabla\Big)\boldsymbol{u}(\boldsymbol{x},t)\right] & = & -\nabla p(\boldsymbol{x},t) + \nabla\cdot\boldsymbol{\tau} \end{array}\right\} \forall[\boldsymbol{x},t] \in \Omega \times [0,+\infty] \tag{III.7.5}$$

with tensor vector:

$$\boldsymbol{\tau} = \eta(\nabla \boldsymbol{u}(\boldsymbol{x}, t) + \nabla^T \boldsymbol{u}(\boldsymbol{x}, t)), \tag{III.7.6}$$

where $\boldsymbol{u}$ and p stand respectively for the instantaneous flow velocity vector and the instantaneous static pressure. The vector $\boldsymbol{u}_{\text{grid}}$ represents the grid velocity of the moving mesh, which is determined for all mesh elements as:

$$\boldsymbol{u}_{\text{grid}} = \frac{\Delta \boldsymbol{y}}{\Delta t}. \tag{III.7.7}$$

The mesh displacement $\Delta \boldsymbol{y}$ was defined at solid walls of Ω_{g} using user defined function. The process is described in next section, and the quality of the mesh over the whole breathing cycle is reported later for final model of upper airways.

The transport equations were solved by means of a finite volume method using first-order time and spatial discretization schemes. The time step of the calculation Δt was set to 10^{-2}s resulting in 353 time steps of the calculation. Iterative convergence was achieved when the dimensionless RMS residuals over the entire flow field were inferior to 10^{-3}, which occurred at each time-step after about 80 iterations. Physical properties of the gas were those of air with the density $\rho = 1.225$ kg/m^3 and dynamic viscosity $\eta_{\text{air}} = 1.7894 \times 10^{-5}$ Pa·s).

The Courant-Friedrichs-Lewy (CFL) number derived for the inlet area using the inlet velocity u_{inlet} at the instant $t(\overline{Q}_{\max})$:

$$CFL_{\text{inlet}} = \frac{\overline{u}_{\text{inlet}^{\max}} \Delta t}{\Delta x_{\text{inlet}}} = 14.5[-]. \tag{III.7.8}$$

Even if $CFL > 1$, calculation converged, so neither mesh dimensions, nor Δt had to be changed.

Boundary Conditions

The boundary conditions for different domains of the model Ω_{i}, Ω_1, Ω_2, Ω_{g}, Ω_{o} (see Figure B1) were set:

- At the inlet face Ω_{i}, the velocity inlet condition was set as $\Omega_{\text{i}} = \overline{u}_{inlet}(t)$. Velocity inlet (see Figure B1) conforms with the preliminary *in vivo* study (see section II.3.1.1). An average of the flow rate over 185 quiet breathing cycles was calculated (*eupnea* cycles of S1, S2, and S3 volunteers). This yielded to the mean respiratory period $\overline{T} = 3.52$s (see Figure B4) and the mean inlet velocity $\overline{u}_{inlet}(t)$ (see III.7.2). The unsteady boundary condition was coded in C programming language using a User Defined Function (UDF) with DEFINE_PROFILE macro. The UDF is a function that can be dynamically loaded within the ANSYS Fluent solver to enhance the standard features of the code [ANSYS®, 2013c].
- On solid walls of Ω_1 and Ω_2 domains was applied a no slip shear boundary condition $\boldsymbol{u}_{\text{wall}} \cdot \boldsymbol{n} = 0$, where $\boldsymbol{u}_{\text{wall}}$ is the velocity vector of the wall motion, here equal to zero and $\boldsymbol{n}$ is the outward normal vector.

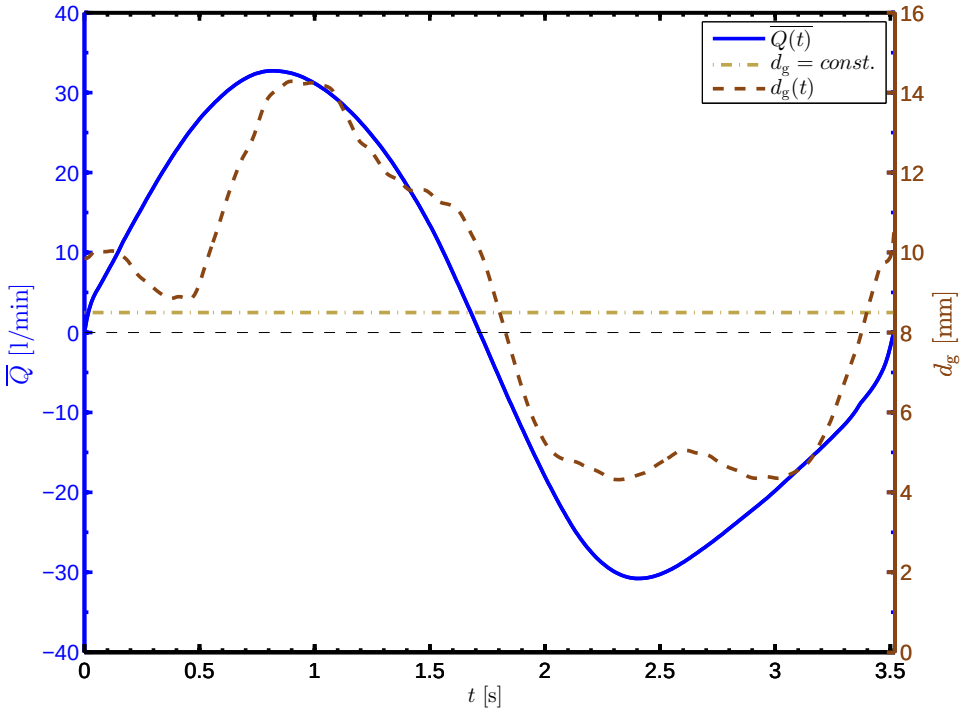

Figure B4: Evolution of airflow rate $\overline{Q}$ [L/min] and glottal width d_g [mm] for steady geometry $d_g = const.$ and unsteady $d_g(t)$. Plotted d_g is typical quiet breathing cycle of S1 (see section II.3.1.1). $\overline{Q}$ is mean of 185 quiet breathing cycles of S1, S2 and S3 and positive $\overline{Q}$ values correspond to inspiration, negative to expiration.

- Deforming motion of solid boundaries in glottal domain Ω_g was set as $\Omega_g = -\frac{1}{2}\frac{dd_g}{dt} \cdot \boldsymbol{n}$. The width of the glottal constriction d_g (see Figure B1) was set according to measured values of glottal width (for definition see Figure II.3.4c in II.3.2.2) in preliminary study (II.3.1.1). Two different cases were simulated:

  i. **Case 1** considers a steady glottal geometry with a mean glottal width $d_g(t) = 8.5$ mm (see Figure B4). This value corresponds to the mean of glottal aperture $d_g(t)$ during typical quiet breathing cycle (subject S1).

  ii. **Case 2** considers a moving glottal geometry $d_g(t)$. The glottal movement measured during typical quiet breathing cycle of subject S1 (see Figure B4) was chosen (see section II.3.1.1).

  The unsteady boundary condition of solid walls in Ω_g was loaded and compiled to ANSYS Fluent solver using a UDF with DEFINE_GRID_MOTION macro written in C language. The x-positions of all nodes were preserved. The y-positions were displaced as following: the mesh nodes at the vertical solid walls had to be moved according to cross-multiplication ($y_{i+1} = y_{t=0} + \Delta l \frac{y_{t=0}}{l}$, where l is the length of the wall at $t = 0$s and $\Delta l = d_{inlet} - d_{g_i} - l$ its change from initial length); the horizontal solid walls in Ω_g were moved according to $d_g(t)$.

- The interior elements were displaced according to the movement of the walls in Ω_g by remeshing method of the ANSYS Fluent solver. This ensures that, when the skewness or size of the mesh elements exceeds specified values the cells are updated.
- A pressure outlet boundary condition was set at outlet domain Ω_o to $p(t) = 0$.

Initial conditions with zero velocities $u_{(t=0)} = 0$ and pressures $p_{(t=0)} = 0$ were assumed at all points. All boundary conditions were set and the simulation was conducted for one breathing cycle.

Results

Case 1 - Steady glottal geometry

Unsteady flow simulation was carried out considering $\overline{Q}(t)$ together with the constant glottal constriction geometry (as explained in section III.7.3.4).

Figure B5a shows the development of the glottal jet at four shot-instants: t_1 and t_2 during inspiration (t_2 corresponds to maximal inspiration velocity), and t_3 and t_4 during expiration phase of breathing (t_3 corresponds to maximal expiration velocity). Table B2 summarizes the main flow parameters for the shot-instant t_3 at the glottal area. Inertial

	Glottal Geometry = mean($d_g(t)$)	Glottal Geometry = $d_g(t)$
d_g [mm]	8.5	4.5
u [m/s]	4.5	10
Re [-]	2608	3069

Table B2: Aerodynamic parameters through glottis constriction at the shot-instant t_3.

effects associated with flow-rate variations yield to the jet instability and fluctuations of the reattachment area during the breathing cycle. The main flow parameters are then summarized and compared to simulation with mobile glottal geometry in Table B2.

Case 2 - Moving glottal geometry

Unsteady flow simulation was carried out considering $\overline{Q}(t)$ and mobile glottal constriction $d_g(t)$ (Figure B4). Figure B5b shows the development of the glottal jet at four shot-instants: t_1 and t_2 during inspiration (t_2 corresponds to maximal inspiration velocity), and t_3 and t_4 during expiration phase of breathing (t_3 corresponds to maximal expiration velocity). In comparison with Figure B5a we observe that the flow speed reaches up to 10 m/s, that is two times higher than in steady glottis simulation. Main flow characteristics are summarized in Table B2.

Note that, despite of the axisymmetric geometries of both models and symmetric movements of the glottal walls, both modeled flows show jet-like structures impacting the

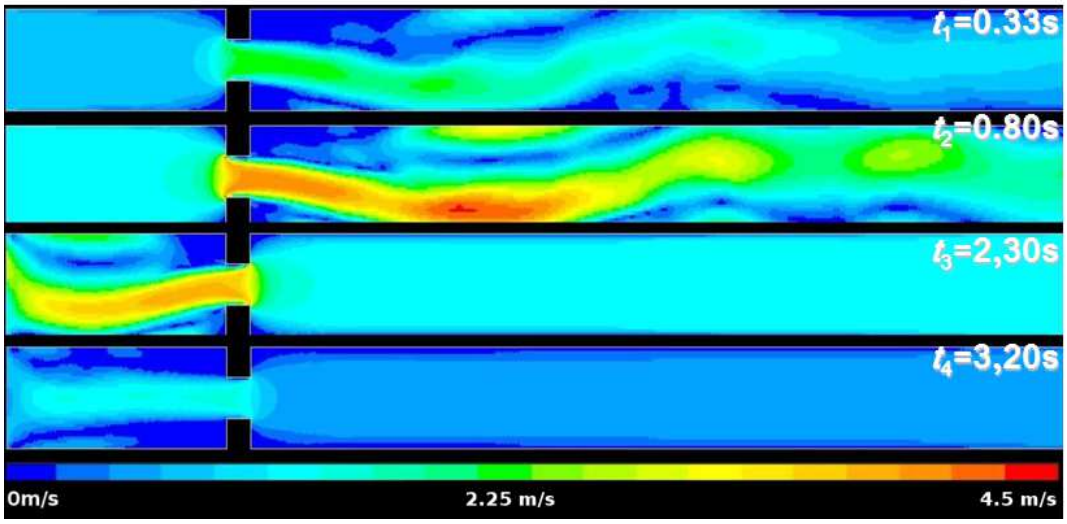

(a) Case 1 - model with steady glottal constriction.

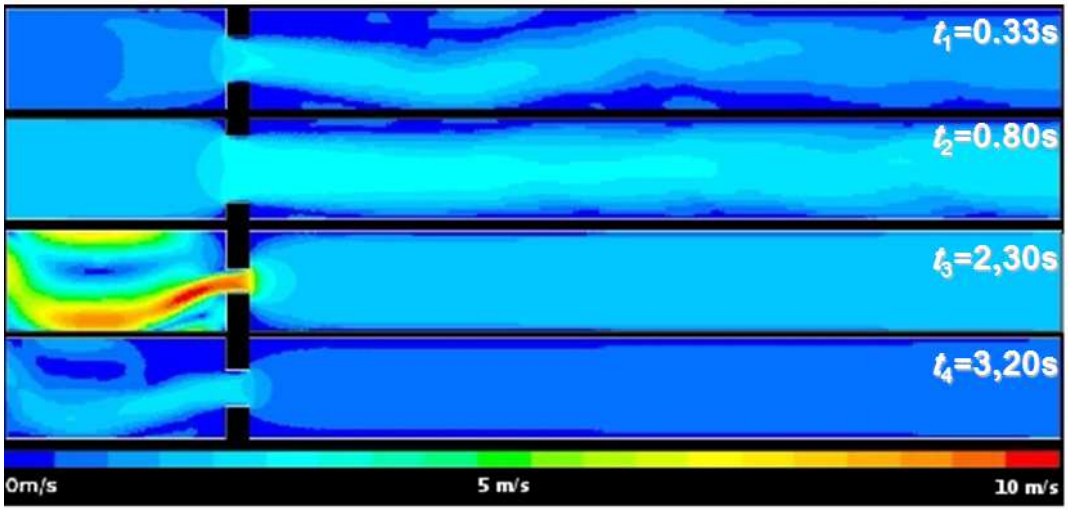

(b) Case 2 - model with moving glottal constriction.

Figure B5: Contours of velocity magnitude $\mid u \mid$. In each panel, the two upper snapshots correspond to inspiration (t_2 corresponds to maximal inspiration velocity) and the two lower snapshots correspond to expiration phase of breathing (t_3 corresponds to maximal expiration velocity). Note the different velocity scales between panel *a* and *b*.

bottom wall (see Figure B5). This phenomenon is called the Coandă effect and was already referred in several studies on glottal jet dynamics (*e.g.*, see recently published work of Česenek et al. [2013]).

The effect of glottal movement on the flow speed can be viewed on the Figure B6, where the glottal velocity u_g is plotted in function of time t. The glottal velocity u_g is defined by Equation III.7.4. Both cases, with steady (yellow curve) and unsteady glottis geometry (brown curve), are plotted for the entire breathing cycle. We observe that during inspiration (t_1 and t_2) the glottal constriction in Case 1 is narrower than in Case 2 and

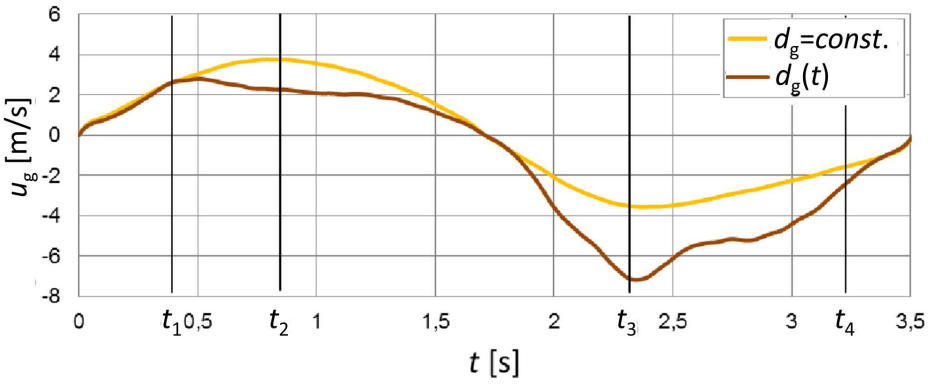

Figure B6: Evolution of the glottal velocity during simulated breathing cycle for steady (yellow curve) and unsteady (brown curve) cases.

so the velocity in Case 1 exceeds the velocity of unsteady simulation with moving glottis. On the contrary, during expiration the glottis significantly narrows in Case 2 and so the created jet has two times higher velocity compared to Case 1.

On Figure B7a is displayed the pressure drop in function of the distance from the inlet

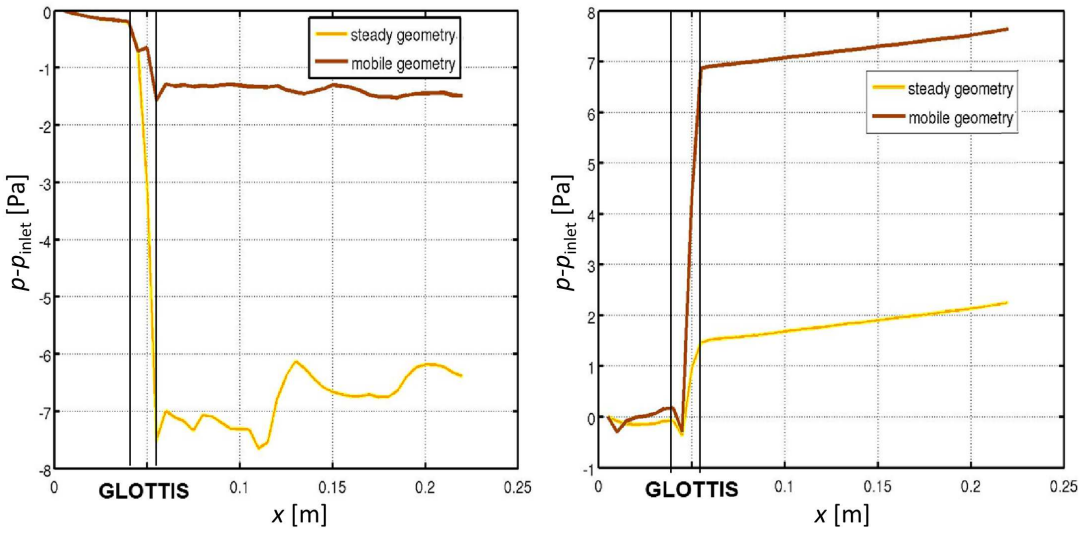

(a) Shot-instant t_2, peak inspiration.

(b) Shot-instant t_3, peak expiration.

Figure B7: Variations of pressure drop as a function of the axial distance from the inlet.

in shot-instant t_2 during inspiration. Pressure dynamics for steady and unsteady cases are compared. There is observed a 4 times higher pressure drop for the steady geometry. This is caused by the narrower glottal constriction in comparison with the unsteady geometry. Similarly Figure B7b represents the pressure drop dynamics in shot-instant t_3 during expiration. In this case the glottal constriction is narrower in unsteady case and consequently the pressure drop is 4 times higher than in unsteady case.

Annex C - User Defined Functions

```c
#include "udf.h"
#include "math.h"
#include "alfa.h"
#define  RADIUS    0.01105  /* glottal radius */

DEFINE_GRID_MOTION(motion_glottis_middle, domain, dt, time, dtime) /* attention dt isn't delta time */
{
#if !RP_HOST
  Thread *tf = DT_THREAD (dt);
  face_t f;
  Node *node_p;
  real c, x1, y1, x,  y ;
  double  x_B1, x_B2, y_B1, y_B2, x_A, y_A, alfa1, alfa2, alfa1_prim, alfa2_prim, y_C1, y_C2, k, l,
y_E1, y_E2, x_prim1, x_prim2, x_prim3, x_prim4, x2_prim, y2_prim, y_prim1 ;
  double  y_prim2, y_prim3, y_prim4, D, d1 , d2 , d1_prim , d2_prim, x_F, y_S;
  int n;
  int one_message=0;
  int st0, st1;

  SET_DEFORMING_THREAD_FLAG (THREAD_T0 (tf));
  begin_f_loop (f, tf)
    {
      f_node_loop (f, tf, n)
        {
          node_p = F_NODE (f, tf, n);
          c = (time / dtime);

          st1 = ((int)(c + 0.5))%N_ALFA;
          st0 = (st1 - 1)%N_ALFA;

          x1 = NODE_X(node_p);
          y1 = NODE_Y(node_p);

          y_S = 0.001742004;
          x_A = RADIUS * sin( 5.0/180.0*M_PI );
          y_A = -RADIUS * cos( 5.0/180.0*M_PI ) + y_S;

          x_B1 = RADIUS * sin( alfa[st0] );
          y_B1 = RADIUS * cos( alfa[st0] ) + y_S;

          x_B2 = RADIUS * sin ( alfa[st1] );
          y_B2 = RADIUS * cos ( alfa[st1] ) + y_S;

          if (NODE_POS_NEED_UPDATE (node_p))
                        {
              NODE_POS_UPDATED (node_p);

              alfa1 = atan((x_B1-x_A)/(-y_A+y_B1));
              alfa2 = atan((x_B2-x_A)/(-y_A+y_B2));

              y_C1 = x_A/tan(alfa1);
              y_C2 = x_A/tan(alfa2);

              alfa1_prim=atan(x1/(-y_A+y_C1+y1));
              alfa2_prim=alfa1_prim*alfa2/alfa1;

              y_E1=y_A-y_C1;
              y_E2=y_A-y_C2;

              /* line through the original point */
              k = (y1 - y_E1)/x1;     /* line direction determinated by y_E1 & original mesh point */
              l =  y_E1/k;            /* sustitution */

              /* Discriminant of the quadratic equation (line equation inside of circle equation)*/
              D = (-2*l/k - 2*y_S)*(-2*l/k - 2*y_S) - 4*(1/k/k+1)*(l*l+y_S*y_S-RADIUS*RADIUS);

              /* cross-points of original line and circle */
              y_prim1=(-(-2.0*l/k-2.0*y_S) + sqrt(D))/2.0/(1.0/k/k+1.0);
              y_prim2=(-(-2.0*l/k-2.0*y_S) - sqrt(D))/2.0/(1.0/k/k+1.0);
              x_prim1 = y_prim1/k - l;
              x_prim2 = y_prim2/k - l;
```

```
                /* line through the new point */
                x_F=-y_E2*tan(alfa2_prim);
                k = -y_E2/x_F;
                l = y_E2/k;

                /* Discriminant of the quadratic equation (line equation inside of circle equation)*/
                D = (-2*l/k - 2*y_S)*(-2*l/k - 2*y_S) - 4*(1/k/k+1)*(l*l+y_S*y_S-RADIUS*RADIUS);

                /* cross-points of new line with the circle*/
                y_prim3=(-(-2.0*l/k-2.0*y_S) + sqrt(D))/2.0/(1.0/k/k+1.0);
                y_prim4=(-(-2.0*l/k-2.0*y_S) - sqrt(D))/2.0/(1.0/k/k+1.0);
                x_prim3 = y_prim3/k - l;
                x_prim4 = y_prim4/k - l;

                /* length of new lines */
                if (y_prim1>=y_S)
                                { /* length of the secant */
                    d1=sqrt((y_prim1-y_prim2)*(y_prim1-y_prim2)+(x_prim1-x_prim2)*(x_prim1-x_prim2));
                                  /* length of the part to the mesh point */
                    d1_prim=sqrt((y_prim1-y1)*(y_prim1-y1)+(x_prim1-x1)*(x_prim1-x1));
                                }
                else
                                {
                    d1=sqrt((y_prim2-y_prim1)*(y_prim2-y_prim1)+(x_prim2-x_prim1)*(x_prim2-x_prim1));
                    d1_prim=sqrt((y_prim2-y1)*(y_prim2-y1)+(x_prim2-x1)*(x_prim2-x1));
                                }


                if (y_prim3>=y_S)
                                {
                    d2=sqrt((y_prim3-y_prim4)*(y_prim3-y_prim4)+(x_prim3-x_prim4)*(x_prim3-x_prim4));
                                }
                else
                                {
                    d2=sqrt((y_prim4-y_prim3)*(y_prim4-y_prim3)+(x_prim4-x_prim3)*(x_prim4-x_prim3));
                                }

                d2_prim=d1_prim*d2/d1;
                x2_prim=d2_prim*sin(alfa2_prim);
                y2_prim=sqrt(d2_prim*d2_prim-x2_prim*x2_prim);

                if (y_prim3>=y_S)
                                {
                    x = x_prim3-x2_prim;
                    y = y_prim3-y2_prim;
                                }
                else
                                {
                    x = x_prim4-x2_prim;
                    y = y_prim4-y2_prim;
                                }

                NODE_X(node_p) = x;
                NODE_Y(node_p) = y;


                if (one_message==0) /* condition enables only one printf in a loop = in one time step */
                                {
                    Message("x1:%f, y1:%f, \n", x1, y1);
                    one_message=one_message+1;
                                }
                      }
        }
    }
  end_f_loop (f, tf);
#endif
}
```

```c
#include "udf.h"
#include "math.h"
#include "alfa.h"
#define  RADIUS    0.01105  /* glottal radius */

DEFINE_GRID_MOTION(motion_subglottis, domain, dt, time, dtime) /* attention dt is not delta time! */
{
  #if !RP_HOST
  Thread *tf = DT_THREAD (dt);
  face_t f;
  Node *node_p;
  real c, x1, y1, z1, x,  y, z_B, z_K, x_A, alfa_K ;
  double  x_B1, x_B2, y_B1, y_B2, y_A, alfa1, alfa2, alfa1_prim, alfa2_prim, y_C1, y_C2, y_E1, y_E2,
x_prim1, x_prim2, x_prim3, x_prim4, x2_prim, y2_prim, y_prim1 ;
  double  y_prim2, y_prim3, y_prim4, k, l, D, d1 , d2 , d1_prim , d2_prim, x_F, y_S, y_B01, x_B01,
x_B02, y_B02, delta_z, delta_y, alfa_B1, alfa_B2 ;
  int n, st0, st1 ;

  SET_DEFORMING_THREAD_FLAG (THREAD_T0 (tf));
     begin_f_loop (f, tf)
      {
        f_node_loop (f, tf, n)
          {
            node_p = F_NODE (f, tf, n);
            c = (time / dtime);
            st1 = ((int)(c + 0.5))%N_ALFA;
            st0 = (st1 - 1 )%N_ALFA;

            x1     = NODE_X(node_p);
            y1     = NODE_Y(node_p);
            z1     = NODE_Z(node_p);

            alfa_K = 0.909299984;
            x_B01 = RADIUS * sin( alfa[st0] );                  /* points in the higher plane */
            y_B01 = RADIUS * cos( alfa[st0] ) + 0.001742004;
            z_B   = 0.17968;

            x_B02 = RADIUS * sin ( alfa[st1] );
            y_B02 = RADIUS * cos ( alfa[st1] ) + 0.001742004;

            z_K = 0.17368;
            delta_z = z_B - z1;
            delta_y = tan(20.0/180.0*M_PI) * delta_z;           /* shift of the circle ceter */
            y_S = 0.001742004 + delta_y;

            x_A = 0.000963071;
            y_A = -0.009265947 + delta_y;

            alfa_B1=(alfa[st0]-alfa_K)/(z_B - z_K)*z1 + alfa_K - (alfa[st0]-alfa_K)/(z_B - z_K)*z_K;
            alfa_B2=(alfa[st1]-alfa_K)/(z_B - z_K)*z1 + alfa_K - (alfa[st1]-alfa_K)/(z_B - z_K)*z_K;

            x_B1 = RADIUS * sin( alfa_B1 );
            y_B1 = RADIUS * cos ( alfa_B1 ) + y_S;

            x_B2 = RADIUS * sin( alfa_B2 );
            y_B2 = RADIUS * cos ( alfa_B2 ) + y_S;

              if ( NODE_POS_NEED_UPDATE (node_p))
             {
              NODE_POS_UPDATED (node_p);

              alfa1=atan((x_B1-x_A)/(-y_A+y_B1));
              alfa2=atan((x_B2-x_A)/(-y_A+y_B2));

              y_C1=x_A/tan(alfa1);
              y_C2=x_A/tan(alfa2);

              alfa1_prim=atan(x1/(-y_A+y_C1+y1));
              alfa2_prim=alfa1_prim*alfa2/alfa1;

              y_E1=y_A-y_C1;         /* y_A is negative, but y_C1 positive => summation */
              y_E2=y_A-y_C2;
```

```
                /* line through the original point */
                k = (y1 - y_E1)/x1;    /* line direction determinated by y_E1 & original mesh point */
                l =  y_E1/k;           /* sustitution */
                /* Discriminant of the quadratic equation (line equation inside of circle equation)*/
                D = (-2*l/k - 2*y_S)*(-2*l/k - 2*y_S) - 4*(1/k/k+1)*(l*l+y_S*y_S-RADIUS*RADIUS);

                /* cross-points of original line and circle */
                y_prim1=(-(-2.0*l/k-2.0*y_S) + sqrt(D))/2.0/(1.0/k/k+1.0);
                y_prim2=(-(-2.0*l/k-2.0*y_S) - sqrt(D))/2.0/(1.0/k/k+1.0);
                x_prim1 = y_prim1/k - l;
                x_prim2 = y_prim2/k - l;

                /* line through the new point */
                x_F=-y_E2*tan(alfa2_prim);
                k = -y_E2/x_F;
                l = y_E2/k;
                /* Discriminant of the quadratic equation (line equation inside of circle equation)*/
                D = (-2*l/k - 2*y_S)*(-2*l/k - 2*y_S) - 4*(1/k/k+1)*(l*l+y_S*y_S-RADIUS*RADIUS);
                /* cross points of new line with the circle*/
                y_prim3=(-(-2.0*l/k-2.0*y_S) + sqrt(D))/2.0/(1.0/k/k+1.0);
                y_prim4=(-(-2.0*l/k-2.0*y_S) - sqrt(D))/2.0/(1.0/k/k+1.0);
                x_prim3 = y_prim3/k - l;
                x_prim4 = y_prim4/k - l;

                if (y_prim1>=y_S)   /* length of new lines */
                  { /* length of the secant */
                    d1=sqrt((y_prim1-y_prim2)*(y_prim1-y_prim2)+(x_prim1-x_prim2)*(x_prim1-x_prim2));
                    /* length of the part to the mesh point */
                    d1_prim=sqrt((y_prim1-y1)*(y_prim1-y1)+(x_prim1-x1)*(x_prim1-x1));
                  }
                else
                  {
                    d1=sqrt((y_prim2-y_prim1)*(y_prim2-y_prim1)+(x_prim2-x_prim1)*(x_prim2-x_prim1));
                    d1_prim=sqrt((y_prim2-y1)*(y_prim2-y1)+(x_prim2-x1)*(x_prim2-x1));
                  }


                if (y_prim3>=y_S)
                  {
                    d2=sqrt((y_prim3-y_prim4)*(y_prim3-y_prim4)+(x_prim3-x_prim4)*(x_prim3-x_prim4));
                  }
                else
                  {
                    d2=sqrt((y_prim4-y_prim3)*(y_prim4-y_prim3)+(x_prim4-x_prim3)*(x_prim4-x_prim3));
                  }

                d2_prim=d1_prim*d2/d1;
                x2_prim=d2_prim*sin(alfa2_prim);
                y2_prim=sqrt(d2_prim*d2_prim-x2_prim*x2_prim);

                if (y_prim3>=y_S)
                  {
                    x = x_prim3-x2_prim;
                    y = y_prim3-y2_prim;
                  }
                else
                  {
                    x = x_prim4-x2_prim;
                    y = y_prim4-y2_prim;
                  }

                NODE_X(node_p) = x;
                NODE_Y(node_p) = y;
                NODE_Z(node_p) = z1;
              }
          }
      }
  end_f_loop (f, tf);
#endif
}
```